ASSESSMENT OF THERMALLY ENHANCED GEO-ENERGY PILES AND WALLS

O. A. A. ELKEZZA

PHD

2023

Assessment of Thermally Enhanced Geo-Energy Piles and Walls

Omar A Ahmed ELKEZZA

Submitted for the Degree of
Doctor of Philosophy

School of Engineering
Faculty of Engineering and Informatics
University of Bradford
2023

Abstract

Omar A Ahmed Elkezza

Assessment of Thermally Enhanced Geo-Energy Piles and Walls

Keywords: geo energy piles and walls, graphTHERM concrete, thermally enhanced soils, Geopolymer concrete, phase change materials (PCM) heat exchanger, PCM impregnated light weight aggregate.

Geo-energy piles and walls have long been recognized as a promising way to reduce carbon dioxide emissions while providing renewable energy. However, enhancing the thermal performance of these structures has remained a significant challenge. This thesis evaluated five different approaches to improving the thermal performance of geo-energy piles and walls, through a series of experiments using a fully instrumented testing rig. The first approach involved adding graphTHERM powder to concrete to double its thermal conductivity, boosting heat transfer efficiency by an impressive 50% to 66%. The second approach tested slag-based geopolymer concrete as a sustainable construction material for geo-energy piles and walls, reducing CO2 emissions by 44.5% while improving thermal performance by 14% to 21%. The third approach involved testing thermally enhanced soils at the geo-energy structures/soil interface, resulting in an 81% improvement in heat transfer efficiency. The fourth approach utilized innovative phase change material (PCM) heat exchangers that increased heat transfer efficiency by 75% and 43% in heating and cooling operations, respectively. Finally, incorporated PCM-impregnated light weight aggregates at the interface of the structure soil, significantly increasing temperature difference and reducing thermal deformation of geo-energy structures.Overall, these innovative approaches made a significant contribution to enhancing the thermal performance of geo-energy piles and walls. However, approaches four and five, which involve utilizing PCM heat exchangers and PCM-impregnated LWA's, respectively, showed extra benefits in dropping the thermal effect on soils and reducing the thermal damage on those structures. These techniques offer great promise for improving the thermal performance of geo-energy structures.

Acknowledgements

I would like to express my heartfelt gratitude to my parents, my wife, and my siblings for their unwavering support and belief in me during my PhD research journey. Their encouragement and love have been a constant source of strength and motivation for me throughout this challenging but rewarding journey.

I would also like to extend my deepest appreciation to Professor Mostafa Mohamed for his guidance, mentorship, and invaluable insights that have greatly contributed to the success of my research. His expertise and dedication have been instrumental in shaping my academic and professional development.

I am also deeply grateful to Mr John Hornby and Mr Steve Robinson for their assistance and support during the lab work. Their technical expertise and willingness to share their knowledge have been invaluable in the smooth execution of my research.

Finally, I am also truly grateful to all of my friends for their support and belief in me. Without their encouragement and support, this journey would not have been possible. Thank you from the bottom of my heart.

Table of Contents

List of Figures

List of Tables

Abbreviations

GES	Geo energy structure
GEP	Geo energy pile
GEW	Geo energy wall
GSHP	Ground source heat pump
HE	Heat exchange
HP	Heat pump
XRD	x-ray diffraction
LDPE	Low density polyethylene
HDPE	High density polyethylene
OPCC	Ordinary Portland cement concrete
GPC	Geopolymer concrete
EAFS	electric arc furnace slag
FA	Fly ash
CTE	Coefficient of thermal expansion
PCM	Phase change material
EST	Excess in soil temperatures
C-S-H	Calcium silicate hydrate
PCM LWA’S	Coated impregnated lightweight aggregates
LECA	Lightweight expanded clay aggregate
LEP	Lateral earth pressure
MDUW	Maximum dry density
OMC	Optimum moisture content

Notations

Q	The rate of heat transfer watts
c_p	Specific heat capacity j/kg.k
c_v	Volumetric heat capacity Mj/m^3.k
U	The overall heat transfer coefficient
h_f	Heat transfer coefficient w/m^2.k
Nu	Nusselt number
R_e	Reynolds number
P_r	Prandtl number
f_D	Darcy friction factor
$C_1 \& C_2$	Factors in Eq.4.4
$\mathcal{V}_{f,i}$	Velocity field m/sec
A	Area m^2
ʋ	Kinematic viscosity
$\dot{m}$	The mass flow rate of circulating fluid kg/sec
dh	Hydraulic diameter of pipe (m)
e	Absolute surface roughness m
$\varepsilon_{\text{thermal}}$	Thermal strain
L	Specimen thickness (m)
q	Thermal energy dissipated into the ground (W)
T_{in}	Inlet temperature (◦C)
T_{out}	Outlet temperature (◦C)
ρ_thermal	Thermal stress
E	Modulus of elasticity

Greek

λ	Thermal conductivity W/m.K
μ	Dynamic viscosity Ns/ m^2
ρ	Density kg/m^3
∇	Represents the divergence operator
ΔT	Is the temperature difference between inlet and out let ^{o}C

Subscripts

f	Fluid
g	Ground
i	inner
o	outer
c	concrete
w	water
P	Pipe

Chapter 1: Introduction

1.1 Background

Climate change is one of the critical issues globally affect environmental, economic and society. In Europe there are more than 160 million buildings that consumes more than 40% of the total energy usage (Thomas & Rees., 2009). For example; in the Uk domestic heating accounts for almost quarter of the UK energy uses which accounts for about 15% of the total carbon emissions. Currently burning fossil fuels is the most common method for generating energy in the UK accounts for about 83% of the total energy produced, while 17% is supplied from renewable energy source (ECUK., 2015). Nevertheless, fossil fuels are a depleting source of energy and contribute significantly to elevating carbon emission and greenhouse effect. Widespread use of renewable energy sources is, therefore, essential for the UK and Europe to meet their carbon emission and neutralisation targets and in particular to meet its net zero carbon target.

In the recent years, the utilisation of the shallow geothermal energy for heating of buildings is spreading rapidly in Europe and around the world. Ground source heat pump (GSHP) is the will know and the wide spread technology the uses the thermal energy to provide sustainable heating and cooling energies. Two standard systems can be used for extracting/rejecting the heat from/to the ground, (i.e. open loop and closed loop). The former system uses water source (lakes or rivers) and pumps it directly into the heat pump, while the latter uses fluid carrying pipes laid either horizontally or vertically (Kovačević et al., 2012). The closed GSHP system is fundamentally made of two components, namely a Heat Pump (HP) and a Heat Exchanger (HE). A HP circulates a coolant fluid in the HE e.g. in pipes that are laid either horizontally or vertically into ground to either extract heat from or reject heat into the ground. Due to the high cost of vertical drilling and the need for a large ground area for placing horizontal HE (loops), the HE pipes are recently being installed within the foundation elements of the structures and buried infrastructures. These structures are currently known as geo-energy structures (GES) e.g. energy piles, energy diaphragm walls and tunnel energy lining (Suryatri-

yastuti et al., 2012). The analysis and design of geo energy piles have been developed for both thermal aspects (Pahud, 2008; Loveridge and Powrie, 2013; Alberdi-Pagola et al., 2018) and the geomechanical considerations that caused by the temperature changes within the pile (Di Donna and Laloui. 2014; Mimouni and Laloui, 2015; Rotta and Laloui, 2016). However, the implementation of energy wall mainly has been accompanied by numerical methods (Bourne-Webb et al., 2016; Narsilio et al., 2016; Di Donna et al., 2016; Barla et al., 2018; Rammal et al., 2018; Di Donna et al., 2021).

The efficiency of geo energy pile depends on many design parameters such pile geometry, pipe configuration and numbers, thermal properties of concrete, fluid flow rate and thermal properties, ground characteristics (Zahraa et al., 2021). Most of these parameters have been studied by (Lee and Lam, 2013; Loveridge and Powrie, 2014; Kavanaugh and Rafferty, 2014; Park et al., 2015; Luo et al., 2016; Caulk et al., 2016; Cui and Zhu, 2017; Laloui and Loria, 2020; Zhao et al., 2017; Noorollahi et al., 2018; Huang et al., 2018; Park et al., 2018). However, published work would indicate that the thermal properties of concrete and ground characteristics have given less attention. Guo et al. (2010); Li et al. (2018); Kong et al. (2019) have assessed the enhancement of the concrete thermal conductivity by using graphite powder. Nonetheless, there was no evaluation of the effect of this thermal enhancement on the concrete's compressive strength and there was also a lack of physical measurements of the pile performance. Furthermore, research studies on evaluating the effect of adjacent soil properties on the performance of GESs seem scarce and existing ones are carried out numerically (Qi et al., 2020; Bourne-web et al., 2020).

Even though the efficiency of geo-energy piles were examining thoroughly, limited laboratory investigations were carried out to study the use of diaphragm walls as a geo-energy structure and to the best of my knowledge, there are only two experimental work were conducted to study the geo energy walls (Kurten et al., 2015; Dong et al., 2019). And none of these studies have investigated the effect of concrete thermal conductivity and adjacent soil properties on the thermal performance of geo energy walls.

In addition, over the last decade the use of thermal energy storage (TES) has been widespread in building applications, Phase Change Materials (PCMs) are

commonly used to increase the thermal energy storage due to the ability of absorb and/or release latent heat due to its solid-liquid phase translation (Peng et al., 2020). This motivated the researcher to investigate the use of PCM to enhance the TES in GSHP's applications. Therefore, several studies were performed using the PCM as a thermal storage system in GSHP's applications but with different approaches including: i. using PCM with horizontal HE (Benli, 2011; Dehdezi et al., 2012; Bottarelli et al., 2015; Pu et al., 2019), ii. Using PCM with vertical GHE (Wang et al., 2014; Li et al., 2016; Qi et al., 2016; Chen et al., 2017; Kong et al., 2017), iii. encapsulating PCM inside the energy pile (Hen et al., 2018; Musa et al., 2020; Yang et al., 2021; Cao et al., 2022; Bao et al., 2022) and iv. using a PCM slurry as a heat transfer fluid (Kong et al., 2017; Pu et al., 2019). Based on the critical review which done by the author, the majority of the research studies were carried out numerically to assess the effects of incorporating PCM in the backfill material for GHE. There were only four studies that experimentally evaluate the influence of incorporating the PCMs into GEP using three different techniques (Olawoore, 2020; Mousa et al., 2020; Yang et al., 2021; Bao et al., 2022). However, to the best of the authors' knowledge there are no available laboratory studies in the open technical literature to date into applying PCM in geo-energy wall (GEW).

1.2 Research significance

Recently, geo-energy piles and walls are considered to be an effective solution to extract/ reject thermal energy from/ to the ground and provide a sustainable energy source to meet the UK targets for Co_2 emission reduction. However, its interaction with the surrounding soils, and the enhancement of its thermal performance still not thoroughly covered. Therefore, the results obtained from this thesis are more likely to provide engineers and researcher with an innovative approaches in how to enhance the thermal performance and the interaction with the surrounded soil of geo-energy structures without detrimental effect on its mechanical properties. In addition, the outcomes would also offer a greater grasp in how to enhancing the thermal energy storage of GES for designers and research who work in the related area.

1.3 Research Aim and Objectives

The main aim of this research is to enhance the thermal performance of geo-energy piles and walls through enhancing i. Thermal properties of concrete, ii. Thermal properties of GES/soil interface and iii. Thermal energy storage of those structures. The main objectives of this study are summarised below:

- To enhance the thermal conductivity of concrete using graphTHERM, and evaluate the effect of this enhancement on the thermal performance of geo energy piles (GEP) and geo energy walls (GEW).
- To produce thermally conductive Geopolymer concrete and to study the feasibility of using for using this concrete for geo energy piles and walls applications.
- To use highly conductive fillers (graphTHEM and MF carbon fibre) to enhance the thermal properties of GES/Soil interface and assess its influence on the thermal performance of GEP and GEW.
- To increase the thermal energy storage (TES) of GEP and GEW using PCM heat exchanger and evaluate the associated effects on the thermal performance of GEP and GEW.
- To use the coated PCM impregnated LWA's to enhance the TES of GES/Soil interface and evaluate the thermal efficiency improvement of GEP and GEW.

1.4 Outline of the Thesis

In addition to the introduction chapter, this thesis contains seven more chapters. The aims and objectives, research significance, and research methodology have been obviously set out in this chapter.

CHAPTER TWO provides a summary of the physical concepts required to understand the heat transfer behaviour of soils. Also, gives an overview for the ground source heat pumps types and components. Ended with delivers the heat transfer mechanism of geo energy piles and walls.

CHAPTER THREE highlights the impacts of using thermally enhanced concrete on the thermal performance of geo-energy structures and interaction between the

thermo-active-structures and adjacent dry and partly saturated soils. graph-THERM concrete have been used to form GEP and GEW. Thermal performance comparison with GEP and GEW made from conventional concrete were carried out.

CHAPTER Four studies the thermal performance of geo energy structures (pile and walls) made of geopolymer concrete. The environmental impact of GPC (geopolymer concrete) piles and walls was also assessed by comparing the CO2 emissions with those resulted from OPCC (ordinary Portland cement concrete) piles and walls. In this chapter four prototypes of geo energy structures prepared from normal and geopolymer concretes were tested; two piles and two walls. Moreover, numerical model was developed using COMSOL finite element modelling, and validated with the experimental findings.

CHAPTER FIVE investigates the feasibility of improving the thermal performance of GES through the addition of conductive additives to adjacent soils at the soil-structure interface. Two additives named graphTHERM and carbon fibre are experimented to enhance the thermal properties of soil placed around the geo-energy experimental models within predetermined areas.

CHAPTER SIX experimentally examine the thermal performance of geo-energy piles and walls fabricated with Phase Change Materials (PCMs) heat exchangers. Four prototype concrete geo-energy piles and walls were casted and tested using two different types of heat exchangers including standard heat exchangers and PCM heat exchangers. The PCM heat exchangers utilised in the current study was filled using two types of PCM with different melting points of 26^{o}C and 42^{o}C for geo-energy piles and walls respectively. The thermal performance was experimentally assessed for 100 hrs of continuous operation under cycles of cooling and heating.

CHAPTER SEVEN look at the effect of enhancing the thermal energy storage of soils around GEP and GEW through using innovative coated PCM impregnated LWA's. and assessing the thermal performance for 100 hrs of continuous operation under cycles of cooling and heating.

Finally, **CHAPTER EIGHT** concludes the main findings of this research. as well as offers some recommendations to be considered in the future research.

Chapter 2: Physical concepts

2.1 Introduction

The energy is referring to the ability of doing work and work is usually expressed in mechanics terms as the force applied to body causes a displacement of that body. Both energy and work are scalars and have the same units, kgm^2/s^2 or Joules (J). The conservation of energy low is applied so; energies cannot be destroyed or created but it can be transferred from one form to others. The common forms of energy are potential, kinetic, thermal, sound, gravitational, light, and electromagnetic energy.

Thermal energy can be transferred to/from ground energy system by the collision of the ground particles due to random movement of the atomic particles caused by the change of the ground system temperature (Loveridge, 2012). The expressions that usually used for ground energy are the heat transfer rate or on other words power which, normally given symbol (Q), and measured with units of watts (W) or joules per sec (J/s).

With the neglect of heat that transferred by the phase change, heat can be transferred in soils via three main mechanisms known as: conduction, convection and radiation. These processes are thoroughly discussed in the coming sections.

2.2 Heat transfer mechanism

2.2.1 Conduction

When anybody subjected to a change in temperature, the heat will be transported from the hot region to the cold region. This heat transfer occurs as a result of the vibration of the atomic particles and the collisions between the particles which caused by the temperature increase (Rees et al., 2000; Loveridge, 2012). Fourier's law defined the heat transfer at steady state by proportional relationship between the temperature change (gradient) and the heat transfer rate as following:

$$\frac{q}{A} \propto \frac{dT}{dx} \tag{2.1}$$

Using a proportionality constant,

$$Q = \lambda A \frac{dT}{dx} \tag{2.2}$$

Where, Q is the heat transfer rate, A is the cross-section area that perpendicular to the direction of heat movement. dT and dx representing the temperature gradient and λ is the thermal conductivity. As for the electrical conductivity, a thermal resistance (R) to the heat transfer can also be defined. This concept combined both geometric properties (area A and length L) and the thermal conductivity into single parameter:

$$R = \frac{\Delta T}{Q} = \frac{L}{A\lambda} \tag{2.3}$$

In complex geometries, the thermal resistance usually in terms of shape factor, S_f and thermal conductivity:

$$R = \frac{1}{\lambda . S_f} \tag{2.4}$$

All the previous equations are used when the heat transferred at the steady states. When the heat transfer is unsteady the gradient of temperature varies with time, then become essential to look at general approach. This is known as the diffusion heat equation:

$$\frac{d^2T}{dx^2} = \frac{\rho' C'}{\lambda} \frac{dT}{dt} = \frac{1}{\alpha} \frac{dT}{dt} \tag{2.5}$$

Where, α stands for the thermal diffusivity measured with unit (m^2/s), and it measures how quickly the material transfer the heat. $\rho' \; and \; C'$ are the material density and specific heat capacity, respectively.

2.2.2 Convection

“Convection “is the transfer of thermal energy from or to the body by physical movement of the surrounding fluid which transfers the energy with its mass. On other words, changing the fluid temperature leads to a change in density at the contact zone and controls the fluid flow. Convection can be free or forced. Forced convection occurs when fluid passes over surface with different temperature. This

type of convection, sometimes named advection which is commonly occurs in ground energy system due to the ground water movement. Newton's law gave the following description for convection:

$$\frac{Q}{A} = h\,(T - T_F) \tag{2.6}$$

Where; T_f and T are the temperatures of the fluid and the pipe that flowing in, respectively, and h is the coefficient of the heat transfer in W/m^2 K.

2.2.3 Radiation

In the form of electromagnetic radiation, all bodies considered to radiate their thermal energy due to the raise of temperature. The heat waves that travels through the spaces and get absorbed by other atoms. This absorbed energy is depending upon the absorptivity of the body and the intensity of the radiation. The Stefan-Boltzmann law described the heat that radiated from black body (thermal radiator) as function of its temperature:

$$\frac{Q}{A} = \sigma . r T^4 \tag{2.7}$$

Where Q the rate of heat transfer in watts, σ is a constant given by Stefan-Boltzmann 5.699×10-8 in $W/m^2\ K^{\ 4}$.

2.3 Heat transfer in soils

in soils and rock, the heat can be transferred by three processes (conduction, convection and radiation). However, conduction is considered to be dominant process in dry soils whereas when ground flow is present, convection also contributes to the heat transfer mechanism (Rees et al., 2000). Fig. 2.1 shows the conditions where convection and radiation can possibly become significant, which mainly at large soil particles when the pore spaces occupies a large space to allow the water easily pass. The water movement may also be worthy in fine soil particles. The processes of heat transfer mechanisms are discussed below.

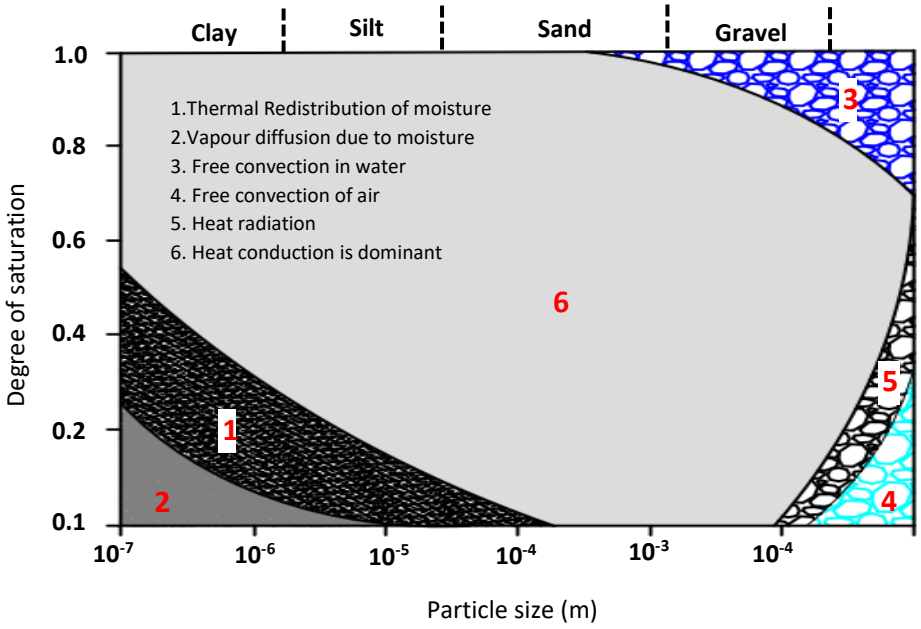

Fig. 2.1. Heat transfer mechanism by particle size and saturation (redrawn from Farouki,1986)

2.3.1 Soils Conduction

The soil constituents are given the highest thermal conductivity in comparison with the other soil components (air and water), therefore being the preferable path to transfer heat by conduction see Table 2.1. However, occupied water and air in the soil pores also play a significant role in soil thermal conductivity, as heat flow through soil solids is restricted by contacts between particle.

Table 2.1. Thermal conductivity for some of the soil constituent

Material	Thermal conductivity (w/m.k)
Quartz	7.7
Kaolinite	2.64
Illite	1.85
Water	0.60
Ice	2.22 @ 0 °c
Air	0.024
Mica	1.6 - 3.5
Garnet	3.1 - 5.5
pyroxene	3.5 - 5.7
chlorite	5.2
Olivine	3.2 - 5
Feldspar	1.4 – 2.5
Plagioclase	1.5 - 2
Amphibole	2.8 - 4
Pyroxene	3.5 – 5.7

Data from Farouki,1986, Cote and Conrad, 2005 and Banks, 2008

2.2.2 Soils convection

In soils free convection can be only take place when the pore space are some millimetres in size (Farouki,1986). A study carried out by Martynov (1959),

showed that the free convection in soils can become more significant at more than 30°C temperature gradients and above this high temperature gradient an increase in the overall thermal conductivity can be obtained due to the free convection. It reported that the thermal energy storage in soils can be affected by free convection for soils with coefficient of permeability greater than 10^{-5} m/s for both horizontal and vertical flows (Hellstrom, 1991). However, The soil layers decreases the vertical hydraulic conductivity which leads to create neutral obstruction to this process.

Forced convection in soils is possible to occur when air or water are forced to migrate through the soil particles due to the deference in pressure, e.g. Ground water movement. Farouki (1986), demonstrated that the thermal conductivity of soil mass can be increased by 20% when convection process is occurred.

Convection mainly consists of two processes: diffusion between soil particles and advection caused by the transport of fluid through pores. These two processes are companied in one equation named the diffusion-advection equation:

$$\frac{\rho' C'}{\lambda'}\frac{dT}{dt} = \frac{d^2T}{dx^2} + \frac{d^2T}{dy^2} - \frac{\rho_w C_w}{\lambda'}\upsilon\frac{dT}{dx} \tag{2.8}$$

Thermal properties of soil that used in this expression is:

$$\rho' C' = n\rho_w C_w + (1-n)\rho_s C_s \tag{2.9}$$

$$\lambda' = n\lambda_w + (1-n)\lambda_w \tag{2.10}$$

Where ρ_w, ρ_s is the density of water and solids, λ' thermal conductivity, n is the porosity and C_w, C_s is the specific heat capacity of water and solids.

The relative importance of advection versus heat diffusion is measured by the dimension less Peclent number which presents the ratio of the rate of advection by the flow to the rate of diffusion of the same flow. Domenico and Schwartz (1990) gave the Peclent number for heat transport in ground water as:

$$Pe = \frac{Lv\rho_w c_w}{\lambda'} \tag{2.11}$$

where, L is the length and v is the velocity,

2.2.3 Soils radiation

Apart from the coarse soils, the radiation in soils can be neglected (Rees et al., 2000). However, the only available information about the radiation in soils is illustrated by Fillion et al. (2011), they experimentally showed that the radiation can has a positive impact in the thermal conductivity of porous material in corresponding with the particle size. They revealed that radiation come to be important for d_{10}> 10mm, and the heat transfer ability doubled its value when d_{10} become greater than 200mm.

2.3 Thermal properties of soils

2.3.1 Soil thermal conductivity

The thermal conductivity of soils is defined as the amount of heat transferred through a unit area of soil in unit time due to the effect of thermal gradient (Alrtimi, 2014). Nusier and Abu-Hamdeh (2003) revealed that the thermal conductivity of soil is mainly related to the heat conduction between soil particles and which is affected by several parameters such as moisture content, density, mineralogy, particles size and the volumetric proportion of the soil constituent. So, the thermal conductivity of soils is so sensitive to its physical properties.

In soils, the thermal conductivity is measured by either steady state methods or transient methods. The steady state methods measure the thermal conductivity considering the heat flux through the soil is constant. Whereas, the transient or unsteady state methods measure the thermal conductivity at different times before reaching the steady state situation. Table 2.2 summaries the most used available methods to determine the thermal conductivity.

Table 2.3 shows the thermal conductivity values for the common rocks and soils in the UK .The data presented in Table 2.3 obtained from two different tests, the Divided bar method (laboratory steady state method), was used for rocks, while

Table 2.2. Summary of methods used to determine thermal conductivity of soils

1.Steady state methods		
1.1 Longitudinal heat flow		
Method	Details	Reff
1.1.1 Hot plate methods	In these methods, samples are placed between two flat plates presents hot plate and cold plate . The temperature difference creates a temperature gradient across the sample. furrier's law for unidirectional heat flow can be applied to evaluate the thermal conductivity of soils.	BS 874:1986
1.1.2 Heat flow meter apparatus	Is an approximate technique measuring the thermal conductivity of a material based on the thermal conductivity of reference material. It is commonly used to estimate the thermal conductivity of insulating materials.	ASTM C 518 (2004)
1.2 Radial heat flow methods		
Method	Details	Reff
1.2.1 Concentric cylinder method	The theory of this method is to radially heat the sample, rather than longitudinally as in the hot plate method. In most cases, the device consists of an inner heating cylinder (heating source) and an outer cooling cylinder (sink). This process is also suitable for powdery or granular materials.	ASTM E 1225 (2004)
1.2.2 Concentric spheres	This method is used to avoid the heat loss associated with the protected hotplate and concentric cylinder method. In this method, the heat generator is placed in the core of a spherical sample and all flow is conducted through a control volume.	Barrios et al., 2008
2. Transient method		
Method	Details	Reff
2.1 Transient hot wire method	In this method, a thin wire is embedded in the centre of a soil sample. The wire heats the soil sample until reach the equilibrium. After reaching equilibrium, a constant power is applied to the heating wire. Thermocouples are used to measure the radial temperature difference across the soil sample.	ASTM C 1113
2.2 Thermal needle method (single probe)	It can be considered to be the fastest and easiest method available for measuring soil thermal properties. Mostly used to measure the thermal conductivity of soils	ASTM C177
2.3 Dual probe method	Based on the theory of infinite linear heat source and radial heat transfer in an isotropic medium with uniform initial temperature. This technique consists of two stainless steel needles connected in parallel and separated by a gap. One of needle is the source heater (thermal probe) and the other needle contains the temperature sensor (sensor probe). It can measures both the thermal conductivity and volumetric heat capacity of any soil mass. Thermal diffusivity is calculated as the ratio between thermal conductivity and heat capacity.	Nusier and Abu-Hamdeh, 2003

Transient needle probe was used for measuring the thermal conductivity of soils. However, no data about the density and the moisture content of the tested samples are provided, but given information about the boreholes sources.

Table 2.3. Thermal conductivity values for some of the UK lithology's (Dowing and Gray,1986)

Formation	Number of tests	λ w/m.k
London Clay	5	2.45 ±0.07
Lambeth – sandy mudstone	4	2.33 ± 0.04
Lambeth – mudstone	10	1.63 ± 0.11
Chalk	41	1.79 ± 0.54
Upper Greensand - sandstone	18	2.66 ± 0.19
Gault – sandy mudstone	32	2.32 ± 0.04
Gault – mudstone	4	1.67 ± 0.11
Kimmeridge Clay	58	1.51 ± 0.09
Oxford Clay	27	1.56 ± 0.09
Mercia Mudstone	225	1.88 ± 0.03
Sherwood Sandstone	64	3.41 ± 0.09
Westphalian Coal – sandstone	37	3.31 ± 0.62
Westphalian Coal – siltstone	12	2.22 ± 0.29
Westphalian Coal – mudstone	25	1.49 ± 0.41
Westphalian Coal – coal	8	0.31 ± 0.08
Millstone Grit	7	3.75 ± 0.16
Carboniferous limestone	14	3.14 ± 0.13
Old Red Sandstone	27	3.26 ± 0.11
Hercynian Ganites	895	3.30 ± 0.18
Basalt	17	1.80 ± 0.11

2.3.2 Specific heat capacity of soils

Specific heat capacity of soil is the amount of thermal energy that rises its temperature by one degree (Bank, 2008). The specific heat capacity of soil solids is approximately 800j/kg.k, this value is enough to classify the soil as a highly heat storage material. The specific heat of any soil affected by varies parameters moisture content and soil composition. Soil solids have less specific heat capacity than water. Thus, wet soils always have higher specific heat capacity value than dry ones. Abu-Hamdeh (2003) illustrated that the specific heat of the soils increases by the increase of its moisture content. Kopp's Law can be adopted to calculate the specific heat capacity of soils based on the mass fraction the specific heat capacity of the soil components.

$$c_p = \frac{1}{m}\left(c_s.m_s + c_w.m_w + c_a.m_a\right) \tag{2.12}$$

If m_s, m_w and m_a are the mass fraction and C_s, C_w and C_a the specific heat capacities of solids, water, and air respectively.

2.3.3 Thermal diffusivity of soils

Thermal diffusivity (α) measures how rapid is the heat to transfer in soils. It calculated as thermal conductivity divided by the soil specific heat capacity and density, it is measured in m^2/s

$$\alpha = \frac{\lambda'}{\rho . c_p} \tag{2.13}$$

2.3.4 Thermal Effusivity of soils

Thermal effusivity (β), is also named as the heat storage coefficient, is calculated as following:

$$\beta = \sqrt{\lambda . \rho . Cp} \tag{2.14}$$

where

β = Thermal effusivity (J/ $s^{0.5}$ m^2 K)

Soil with high thermal effusivity indicates both large thermal conductivity and thermal storage capacity. Ghauman (1985) pointed out that materials with high thermal effusivity can rapidly dissipate the heat. Whereas, materials with a low thermal effusivity has more ability to hold heat considerably longer.

2.4 Factors influencing the thermal properties of soils

The thermal properties of soils are known as the thermal conductivity, specific heat capacity and thermal diffusivity and mainly affected the heat transfer and storage in soils. The thermal properties of soils are influenced by many parameters which categorized into two groups: those which are related to the soil composition such as particle size and mineralogical composition and those which can be easily controlled like moisture content, soil density and temperature of soil (Abu-Hamdeh et al., 2001).

2.4.1 Moisture content

The influence of moisture content on thermal conductivity in soils and has been extensively studied (Farouki, 1986; Tarnawski et al. 2000; Krishnaiah and Singh, 2003; Nusier and Abu- Hamdeh, 2003; Sakaguchi et al., 2007; Hall and Allinson, 2009). These studies clearly show that the soil thermal conductivity increases with the increase of its moisture content.

It is known that soils are consists of two or three-phase substances. In dry soils, air have occupied the voids between the soil particles, the thermal conductivity of the air is considerably lesser than that for the other elements, so heat is more likely to transfer through the contact points between the soil particles. The inclusion of water is soils allows the water to fills the pores and provides water bridges between soil particles (Hall and Allinson, 2009). The water bridges leads to enhanced the heat transfer from one particle to another. For all soils, the relationship between thermal conductivity and moisture content shows two distinct phases. At first phase, the thermal conductivity remarkable increases as the water content increases, then the rate of increase become more steady with further increase of moisture (Mohamed et al., 2015).

depending on dry density and moisture content Kersten (1949) suggested two empirical equations for predicting the thermal conductivity of two different types of soils. The first equation is to be used for silt and clay soils that containing more than 50% silt and clay (Eq. 2.15) and the second equation is for sandy soils (Eq. 2.16).

$$\lambda = 0.1442.\,[0.9\log w - 0.2] * 10^{0.6243\,\gamma_d} \quad \text{for silts and clay} \quad (2.15)$$

$$\lambda = 0.1442.\,[0.7\log w + 0.4] * 10^{0.6243\,\gamma_d} \quad \text{for sandy soils} \quad (2.16)$$

Where ρd is the dry density in $g/cm3$.

In partially saturated state, Johansen (1975) proposed a model to calculate the thermal conductivity of soils. This model introduces the concept of using the Ker-

sten number ke, which depends on the soils saturation degree. The thermal conductivity of the soil, giving by Johansen's Eq. 2.17, can be assessed by linear interpolation between saturated and dry thermal conductivities.

$$\lambda = (\lambda_{sat} - \lambda_{dry}).\, ke + \lambda_{dry} \tag{2.17}$$

Tong et al. (2009) established an equation to calculate the thermal conductivity of soil taken into account the effects of moisture content, the saturation degree, pressure, porosity, and temperature as following

$$\lambda = \eta_1 .(1-n)k_2 + (1-\eta_2).[1-\eta_1 .(1-n)]^2 * \left[\frac{(1-n).(1-\eta_1)}{\lambda_s} + \frac{nS_r}{\lambda_w} + \frac{n(1-S_r)}{k_g}\right]^{-1} + \eta_2\left[(1-n).(1-\eta_1)\lambda_s + nS_r k_w + n.(1-S_r)\lambda_g\right] \tag{2.18}$$

Where; λ_w, λ_s and λ_g are the thermal conductivities of water, solid, and gas, respectively, n is the soil porosity. η_1 is a fitted for pore structure of solid and gas mixture, [0< η_1 (n)<1], η_2 is coefficient depending on the soil saturation degree (S_r), porosity and temperature, [0<η_2 (n,Sr,T)<1].

2.4.2 Dry density

It is known that the increase in the soil density leads to increase its conductivity to heat (Smith, 1942). When the soil density increased the porosity and the air avoids are reduced resulting, more soil particles are filled into a unit volume and, therefore, more contacts between particles occurs which offers more heat flow paths causing an increase in the soil thermal conductivity.

The link between the soil densities and their thermal conductivity has been extensively investigated. Kersten (1949) proposed empirical equation developed from thermal conductivity tests using 19 different soil types in dry conditions. The thermal conductivity for silt and clay and for only sand is expressed as:

$$\lambda = \&\{(0.9\log w - 0.2) \times 10^{0.6242\rho_d - 3.4628}\} \times 418.6\ (silt\ \&\ clay) \tag{2.19}$$

$$\lambda = \&\{(0.7\log w + 0.4) \times 10^{0.6242\rho_d - 3.4628}\} \times 418.6\ (sand) \tag{2.20}$$

Where; where λ is the thermal conductivity of the soil (Wm^{-1} K^{-1}), w is the moisture content (%), and ρ_d is the dry density (g/cm^3).

Thermal conductivity at the saturated condition, λ_{sat}, and that after air drying, λ_{dry}, are calculated using Eqs. (2.21) and (2.22), respectively. The thermal conductivity of soil under unsaturated conditions is defined in Eq. (2.23) using the thermal conductivities of soil under saturated and air-dried conditions, and Kersten number Ke, as following:

$$\lambda_{sat} = 0.57^{n} \cdot \lambda_{s}^{1-n} \quad (2.21)$$

$$\lambda_{dry} = \frac{137\rho_d + 64.7}{2700 - 947\rho_d} \quad (2.22)$$

$$\lambda_{unsat} = (\lambda_{sat} - \lambda_{dry})K_e + \lambda_{dry} \quad (2.23)$$

$$K_e = \{0.7\log(S_r/100) + 1.0\} \text{ for coarse} \quad (2.24)$$

$$K_e = \{\log(S_r/100) + 1.0\} \text{ for fine} \quad (2.25)$$

Here, λ_{sat}, λ_{dry}, and λ_{unsat} are the thermal conductivity of the saturated condition, that of the air-dried condition, and that of the unsaturated condition, respectively (Wm^{-1} k^{-1}), K_e is the Kersten number, n is the porosity, ρ_d is the dry density (g/cm^3), and S_r is the degree of saturation (%).

several empirical equations were produced by Singh and Devid (2000) to estimate thermal resistivity for dry and saturated soils. Those equations have been calibrated using data generated from the transient needle method. It was observed that the absolute error between the thermal conductivity values calculated from the equations and the experimental measurements was less than 15-20%. Nusier and Abu-Hamdeh (2003) experimentally evaluated the thermal conductivity value of two soils classified as sand and loam with respect to its density using dual probe method. They concluded that the thermal conductivity increased with increasing bulk density for both soils.

Several relationships have been presented to describe the relationship between dry density of soils and thermal conductivity e.g. (Farouki, 1986; Krishnaiah and Singh, 2003; Chen, 2008). However, the presented was obtained for a few soils

types and cannot be considered as standard values for other soil types. This is due to the fact that the thermal conductivity of the soil is influenced by many other factors such as particle size, mineralogy, water content.

Elminshawy et al. (2017) studied the effect of compaction level on porosity and void ratio for a small laboratory scale EPAHE (earth pipe air exchanger) system with 150 mm diameter and 1500 mm length copper pipe; it was discovered that the thermal performance of EAPHE system and air temperature can be enhanced by increasing the soil compaction level (density).

2.4.3 Mineralogy of Soil

It is known that soils are made up of solid grains which surrounded by pores (voids) filled with water (saturated soil) or air (dry soil) or both (partially saturated). The soil mass constituents and its fraction volume have significant influence on-the thermal conductivity of soil. For example, sands with high quartz content (like silica sand) commonly more conductive to heat than the other types of sand where is more content of pyroxene and plagioclase feldspar (Farouki, 1986). The thermal conductivity of some important soil components is given in Table 2.1. Most of the soils are made up of one or more minerals such as quartz, clay minerals, and organic materials mixed with water and air. the quartz has the highest thermal conductivity and air has the lowest. The fact that sands have higher thermal conductivity than clay is justified by the different in the mineralogical composition between sand and clay.

2.4.4 Particle size

The porosity and density of any soil are strongly connected with the particle size distribution. Consequently, the thermal conductivity of soils is directly affected by this property. Several researchers have provided the significance of the heat transfer through and between the contact of any soil particles eg. (Farouki, 1986; Tarnawski et al., 2002; Krishnaiah and Singh, 2003). They highlighted that in dry soils, the conduction by particle contact is the main mechanism that influences conduction. The thickness of water layer (film) a rounding soil particles is influenced by Particle size. The quantity of water required to create water coating is directly depending on specific surface area of the particles. Since the specific

surface area of Clay particles are higher than that of the sands, therefore more water is required to make the water film around the particles (Sepaskhah and Boersma., 1979).

An explanation for this property provided by Tavman (1996), when the particle size decreases, more grains are necessary to reach the same porosity consequently the thermal resistance between those grains rises. Nusier and Abu-Hamdeh (2003) also concluded that sand had always higher thermal conductivity values than loam and clay soil at all densities.

2.4.5 Temperature of soil

The temperature can in somehow effected the thermal conductivity measurements. In soils, all minerals show a decrease in thermal conductivity with increasing temperature (Brandon and Mitchell, 1989). The heat transfers through minerals crystalline is thought to occur by both pressure and longitudinal waves, which become less harmonic as temperature increases. On the other hand, the water and gases thermal conductivity increases with boosting temperature (Rooyen and Winterkorn, 1957). Gases and general liquids collisions between molecules is the rolling phenomena for heat transfer. Consequently, the increase in molecular collisions caused by temperature increase leads to an increase in the thermal conductivity.

The influence of temperature on the thermal conductivity of soils have been not thoroughly studied. A few studies showed that an increase in the soil temperature slightly increases the thermal conductivity and this increase is strong related with water content (Tarnawski et al., 2002; Sakaguchi et al., 2007; Hamuda, 2009).

2.5. Ground source heat pump system

ground source heat pump is typically a mechanical equipment that uses to increase/ decrease the temperature of the thermal energy that extracted or dissipated from the ground, by running fluid through burred close or open loop pipes. These heat pumps can extract the stored heat in the ground and used to heat the buildings during the winter and reject heat into ground to cool buildings in summer. Its work mechanism is quite similar to that of refrigerator. The ground source heat pumps, are consists of main four components known as: Evaporator, Condenser, Compressor and Expansion valve see Fig. 2.2. In heating cycles, fluid is

circulated through the heat pump that is buried in the ground or inside geo-energy structures, this fluid absorbs or releases the heat from/to the ground and is collected into the evaporator which contains a heat transfer liquid. Inside the evaporator, the heat transfer liquid absorbs the thermal energy (heat) from the fluid that was in the ground heat exchanger which rises the temperature of the heat transfer liquid. Then the higher temperature heat transfer liquid is circulated in the compressor which converts the compressed liquid to high pressure and temperature liquid. in the condenser, the vapour heat transfer liquid transfers its heat to heat the buildings (under floor heating , radiators and heating the water for daily use). Commonly, the ground heat exchanger GHE could be installed in two ways, either as an open loop or a closed loop (Suryatriyastuti et al., 2012; singh et al., 2019), to reject/extract heat energy to/from the ground. The open loop extract water from the source of water (e.g. aquifer or river), by pumping it to the heat pump system, and then pumps it back to the water source at some distance apart do avoid any interaction between inlet and out let. Open loop solutions are considered to be an unfavourable option owing to their costly maintenance requirements caused by clogging, which may occur due to the pollution in the water source (Suryatriyastuti et al., 2012).

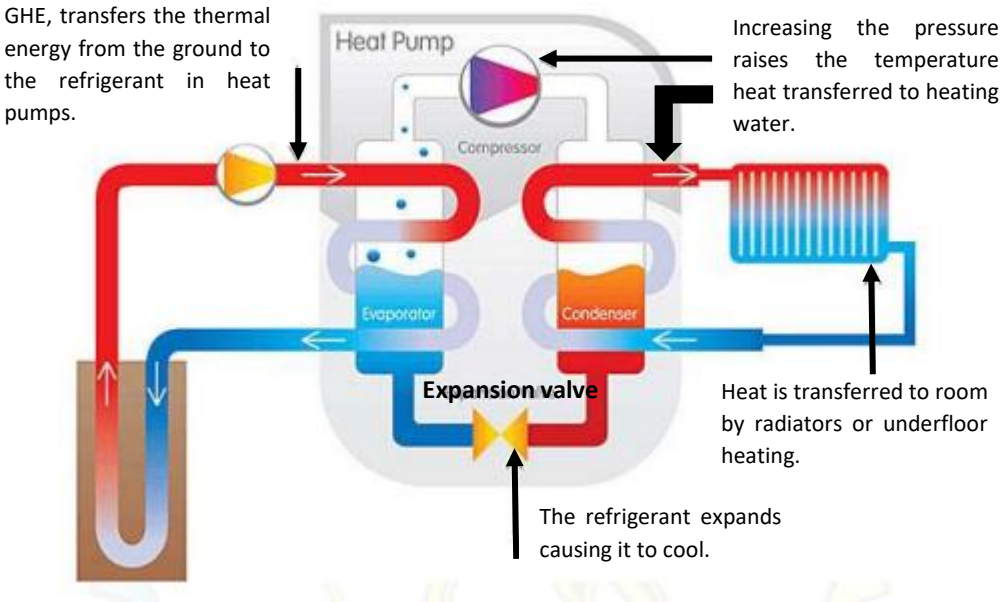

Fig. 2.2. Ground source heat pump components and mechanism (Olawoore, 2019).

Whereas the closed loop system runs constant fluid mass in a closed pipes network, installed either vertically or horizontally (Akrouch, 2014; Suryatriyastuti et

al., 2012; Zagorscak and Thomas, 2016; Kovačević et al., 2013). Due to the high cost of vertical drilling and the large ground area needed for placing horizontal GHE (loops), the GHE pipes are recently being installed within the foundation elements of the structures. Heat exchangers in structures foundation that is planned to be built can significantly lower the costs and provide new opportunities to widespread use of this technology (Brandl, 2006; Bourne-Webb et al., 2016; Soga and Rui, 2016; Brandl, 2016; Loveridge et al., 2020). Currently, all types of underground structures, such as tunnel anchors and linings, slabs, piles and diaphragm walls can be employed to exchange heat with the ground (Loria, 2020). Fig. 2.3 illustrates the types of the ground heat exchangers that commonly uses with the GSHPS.

2.5.1. Energy efficiency of heat pump

The efficiency of the ground heat pump is measured by the coefficient of performance (COP) which is defined as the ratio between the given energy (heat output) by the pump to drive energy (electrical energy input). For instant, the use of ground source heat pump with COP=4, means that each 4kW of heat provided by the pump needs 1kW of the electrical energy to derive the pump.

2.6. Heat transfer in GEO-Energy piles

In a geo- energy pile, heat transfers from/to the surrounded ground by heat transfer processes named as convection and conduction. In cooling modes, the heat transfers by convection from the fluid in side (GHE) to the pipe wall, then conducted to the concrete which transfer that heat to the surrounded soils by conduction (dry soils) and both conduction and convection in the saturated and partly saturated soils. Fig. 2.4 demonstrates the process of heat transfer across GEPs. The temperature gradient between the circulated fluid and the soil derives the heat to be transferred to the soil in cooling modes (operation during summer), and vice versa in winter. The concept of thermal resistance is applied to solve the heat transfer equation for GEP as following:

$$Q = \frac{T_1 - T_5}{R_T} \tag{2.26}$$

$$R_T = R_{Fuid} + R_{Pipe} + R_{Concrete} + R_{Ground} \tag{2.27}$$

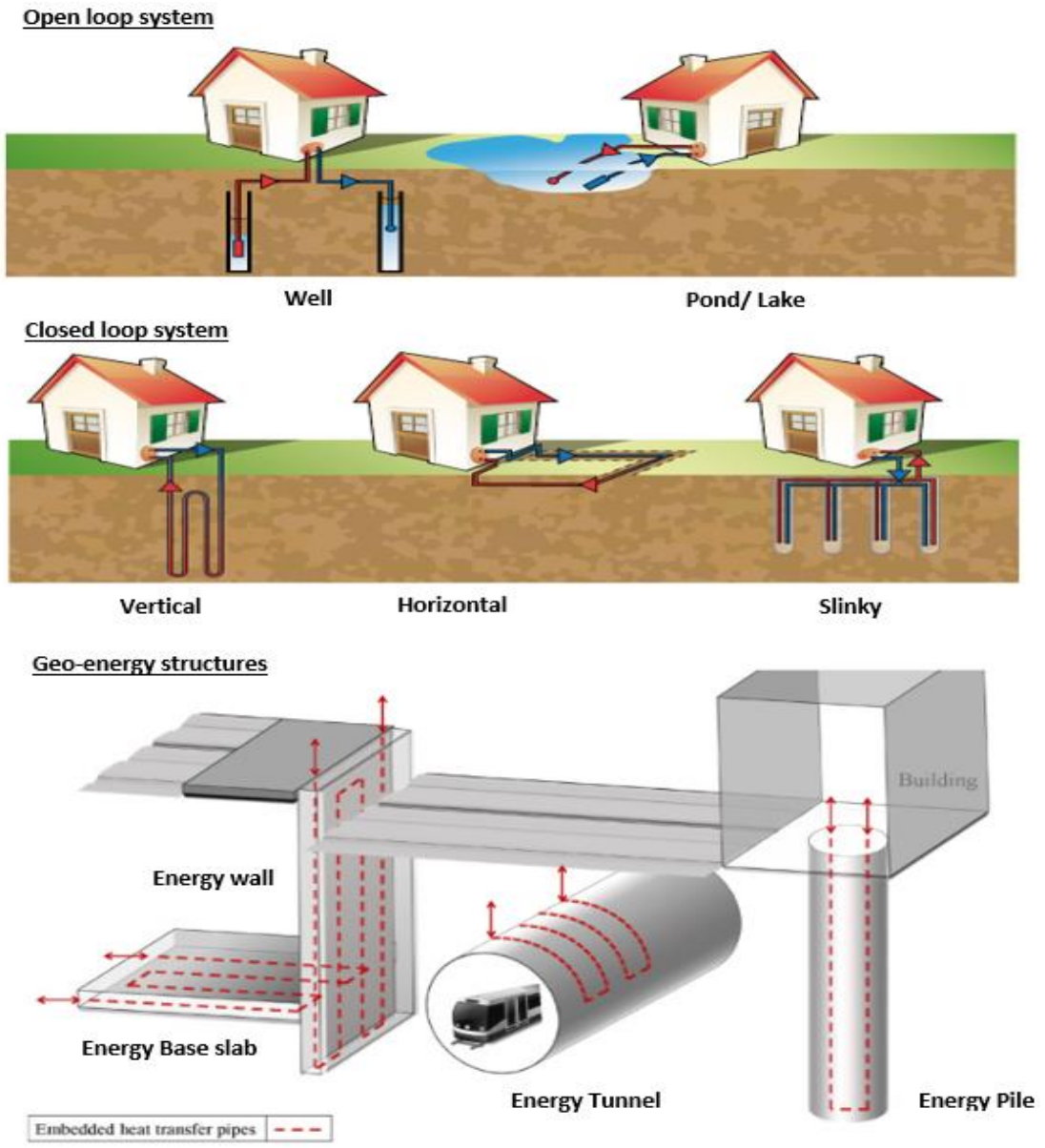

Fig. 2.3. Different types of ground heat exchangers.

Where; Q is the heat transfer rate, T_1 and T_5 are fluid and soil temperature, R_{fluid} ,R_{pipe}, $R_{concrete}$, R_{ground} are the thermal resistance of fluid, pipe, concrete and grounds, respectively. (Faizal et al., 2016; Rui Assunção, 2014).

R_{fluid} is generally calculated by assuming that the pipe wall has uniform temperature using the following expression:

$$R_{fluid} = \frac{1}{2n\pi r_i h_i} \tag{2.28}$$

Where *n* is the number of pipes in GEP, r_i is the internal radius of the pipe and h_i is the coefficient heat transfer of the fluid circulated in the pipe, h_i can be calculated using Nusselt number (represents the ratio between convection and conduction) as following:

$$h_i = \frac{Nu\ \lambda_{fluid}}{2r_i} \tag{2.29}$$

$$Nu = 1.86 * (Re.)^{\frac{1}{3}}.(\frac{2r_i}{L})^{\frac{1}{3}}.(\frac{\mu}{\mu_W})^{0.14} \tag{2.30}$$

The thermal resistance of the conduction through the pipe Wall can be calculated by the theory of hollow cylinder with constant temperature at the outer and inner surfaces as following:

$$R_{pipe} = \frac{\ln\left(\frac{r_0}{r_i}\right)}{2n\pi k_p} \tag{2.31}$$

Where; r_0, k_p are the pipe outer diameter and the pipe thermal conductivity.

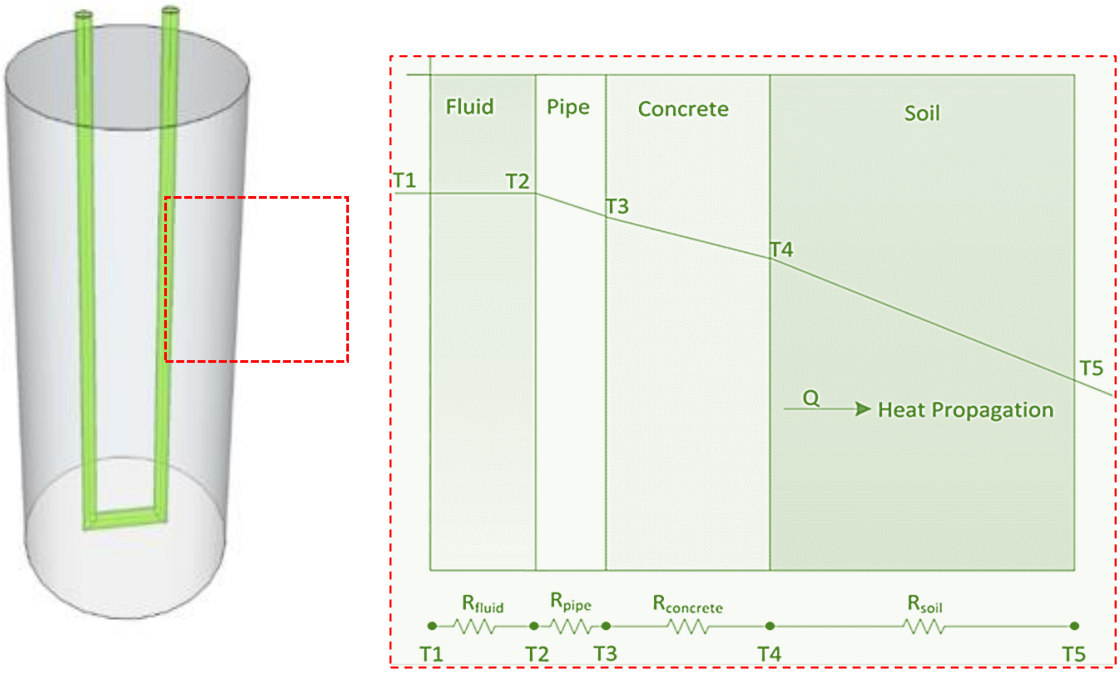

Fig. 2.4. Temperature drop between running fluid and ground for geo-energy pile (Faizal et al., 2016).

The thermal resistance of concrete is considered to be more difficult to be calculated, however, Shonder & Beck (2000), proposed a formula for calculation of thermal resistance of hollow cylinder which can be used as concrete pile. two radiuses named as r_p, r_{eff}, where r_p is the pipe radius and r_{eff} is the effective radius and it's a function of the number of pipes inside the geo energy piles and r_o the outer radius of the heat exchanger.

$$R_{concrete} = \frac{\ln \frac{r_p}{r_{eff}}}{2\pi k_c} \tag{2.32}$$

Where; R_p is pile radius , k_c is thermal conductivity of the concrete and $r_{eff} = r_0\sqrt{n}$,n donates the number of pipes.

The surrounded soil thermal resistance is estimated by the equation proposed by (li et al. 2018) as following:

$$R_S = \frac{\ln\left(\frac{r_S}{r_{ps}}\right)}{2\pi k_s} \tag{2.33}$$

Where; r_s is soil radius, r_{ps} is the distance between the pipe and the soil and k_s is soil thermal conductivity.

2.7. Heat transfer in GEO-Energy walls

The heat transfer for energy walls depends on many factors, such as influences from heat exchangers and influence from the geometric of the wall as well as effects of difference materials (concrete, soil ……etc). Generally, two main heat transfer process monitored, conduction and convection. As the liquid is circulated in the heat exchanger it transfers the heat to the pipe wall by convection, then the heat is transferred through the pipe wall to the concreate (wall body) by conduction. Finally, this heat conductes from the concrete to the surrounded ground by conduction (Rui manual, 2014). Kurten et al. (2014) developed an approach based on a model evaluated by (koschenz and drer, 1999) to analytically analysis the heat transfers on concrete based on its thermal resistance, Kurten model considers the heat to be transfers in the wall systems in two dimensions X and Y whereas, at the insulation layer the heat will be transferred in one dimensional. Fig. 2.5 represents the geometry of Kurten model and Table 2.4 gives a description of the nations in Fig. 2.5.

Commonly, the thermal resistance model is normally used to analyse the heat exchange rate on the bore holes and energy piles considers the thermal resistances to be connected in series .in contrast , for energy diaphragms the extracted or dissipated heat flows to or from outside (soils) and the inside (basement) and this needs to be considered. This process can be evaluating by form of a delta connection as shown in Fig. 2.6. From outer wall of pipe T_3, the heat flows towards the soil as well as towards basement, this can be expressed by means of the analogy to electrical circuit, the delta connection can be transformed to star network which easier for numerical Implementation.

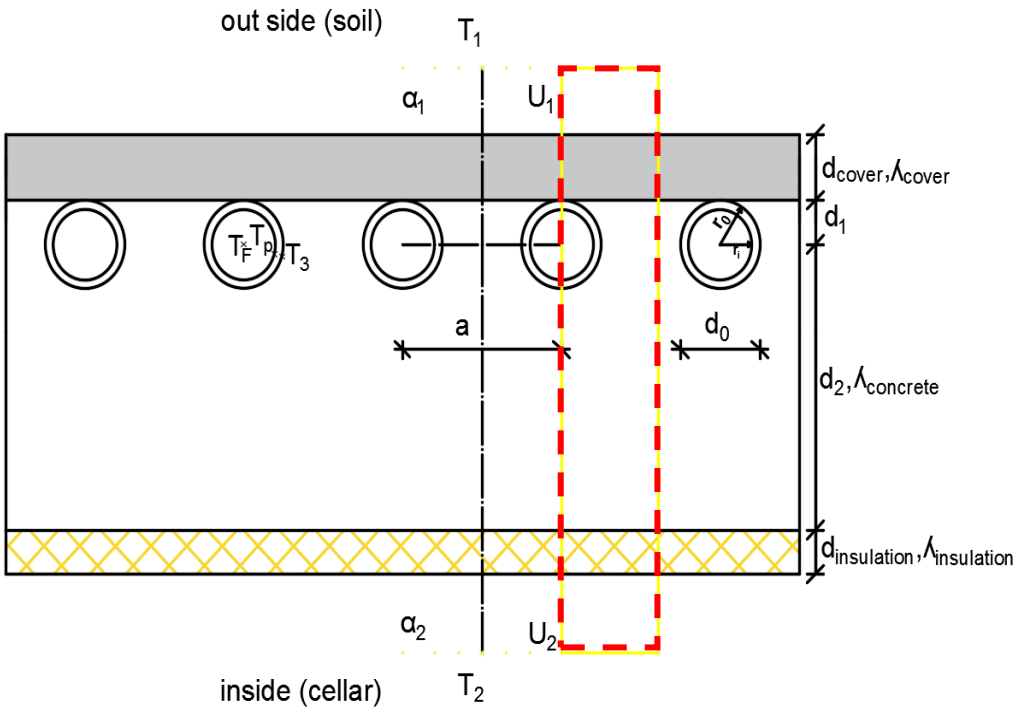

Fig. 2.5. Heat transfer through the energy walls (Kurten, 2015).

Table 2.4. Notations for Fig. 2.5 parameters.

$\boldsymbol{\lambda_c}$	Concrete thermal conductivity, (w/mk)	$\propto_1$	Coefficient heat transfer outside (w/m^{2}k)
$\boldsymbol{\lambda_L}$	Conduction layer thermal conductivity, (w/mk)	$\propto_2$	Coefficient heat transfer inside (w/m^{2}k)
$\boldsymbol{\lambda_{is}}$	Insulation layer thermal conductivity, (w/mk)	U_1	Overall heat transfer coefficient outside (w/m^{2}k)
$\boldsymbol{\lambda_p}$	Thermal conductivity of pipes, (w/mk)	U_2	Overall heat transfer coefficient inside (w/m^{2}k)
d_1	Distance from pipe centre to the cover layer (m)	a	Distance between the pipes (m)
d_2	Distance from pipe centre to the insulation layer (m)	d_0	Pipe outside diameter (m)
d_L	Thickness of the heat conduction layer (m)	di	Pipe inner diameter (m)
d_{IS}	Thickness of the heat conduction layer m		
T_1	Outside temperature (soil) ^{o}c		
T_2	Inside temperature (cellar) ^{o}c		
T_F	Fluid temperature heat carrier ^{o}c		

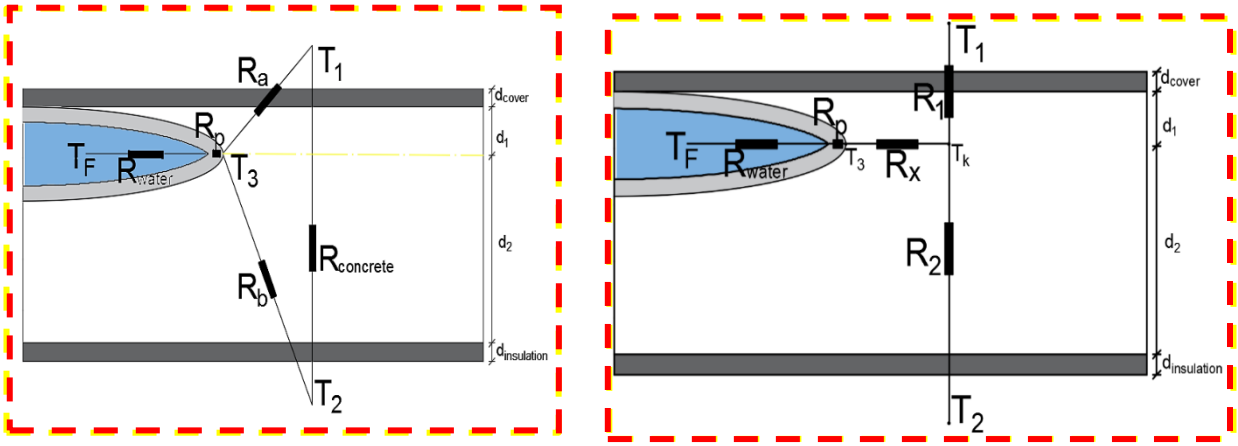

Fig. 2.6. Thermal resistance diagram for energy wall.

Fig. 2.6 shows the star connection T_3 is the start temperature the pipe outer surface, T_k is the average structural component temperature and it can evaluated via a "structure resistance" R_x . Using the core temperature T_k helps to calculate the heat flow towards inside Q_2 and outside Q_1. By applying the law of one dimensional heat conduction Q_1 and Q_2 ca be calculated by:

$$Q_1 = \frac{1}{R_1}.(T_k - T_1) \quad \text{with } R_1 = \frac{1}{U_1} \tag{2.34}$$

$$Q_1 = \frac{1}{R_2}.(T_k - T_2) \quad \text{with } R_2 = \frac{1}{U_2} \tag{2.35}$$

The heat transfer coefficients U1 and U2 can be calculated as follows:

$$\text{U1}= \left[\frac{1}{\propto_1} + \frac{d_{cover}}{\lambda_{cover}} + \frac{d_1}{\lambda_c}\right]^{-1} \quad \& \quad \text{U2}= \left[\frac{1}{\propto_2} + \frac{d_{insulation}}{\lambda_{insulation}} + \frac{d_2}{\lambda_c}\right]^{-1}$$

The overall heat flow for the System **Q** to Outside (Soil) And Inside (Cellar) Is**:**

$$\boldsymbol{Q_{TO\ SOIL}} = \frac{T_F - T_3}{R_W + R_P} + \frac{1}{R_X}.(T_3 - T_K) - \frac{1}{R_2}.(T_K - T_2) \tag{2.36}$$

$$\boldsymbol{Q_{TO\ CELLAR}} = \frac{T_F - T_3}{R_W + R_P} + \frac{1}{R_X}.(T_3 - T_K) - \frac{1}{R_1}.(T_K - T_1) \tag{2.37}$$

The heat transfer rate between the wall of pipe and the circulated fluid can be described by the thermal Resistance of from convection R_w and the thermal resistance through the pipe wall R_P it can be determined by the known correlation from the thermodynamics (Vdi-warmeatlas, 2006).

$$R_P = \frac{1}{2.\pi.\lambda_P.L}.\ln\left(\frac{d_0}{d_i}\right) \tag{2.38}$$

$$R_w = \frac{1}{h.\pi.d_i.L} \qquad \text{with} \qquad h_i = \frac{Nu\ \lambda_{fluid}}{2r_i} \tag{2.39}$$

2.7.1 Structural resistance Rx

The structural resistance R_X is the main important parameter of Kurten model, that's because this thermal resistance takes into account the geometry of the pipe layer and the multi-layered structural part as presented before in Fig 2.5, in energy walls, a 2D heat flow is more likely to occurs in the layer of the pipes and only 1D heat flow in the insulation layer is assumed. Kurten model mathematically calculated the structural resistance R_X this derivation was detailed in (Kurten, 2015) and given the formula for the structural resistance as following:

$$R_x = \frac{(a - d_0).(1 - \Phi)}{(U_1 + U_2).(d_0.(1 - \Phi) + a.\Phi)} \tag{2.40}$$

With

$$\Phi = \frac{2.\pi.\lambda_{concrete}.\Gamma}{a.(U_1 + U_2)} \tag{2.41}$$

Where: -

$$\Gamma = \left[\ln\left(\frac{a}{\pi.d_0}\right) + \frac{2\pi.\lambda_c}{a.(U_1+U_2)} + \sum_{s=1}^{\infty}\frac{g_1(s)+g_2(s)}{s}\right]^{-1} \tag{2.42}$$

$$g_1(s) = -\frac{\left(\bar{U}_2/\lambda_C\right)a - 2\pi s}{\left(\bar{U}_2/\lambda_C\right)a + 2\pi s}.e^{-(4\pi s/a)d2}.[1 + g_2(s)] \quad (2.43)$$

$$g_2(s) = \frac{\left(\lambda_C + \frac{\lambda_L}{N_1} - \frac{\lambda_L}{N_2}\right)(e^{-(4\pi s/a)d1} - R)}{\lambda_C(1+R) + (\frac{\lambda_L}{N_2} - \frac{\lambda_L}{N_1})(1-R)} \quad (2.44)$$

$$N_1 = 1 - \frac{\left(\bar{U}_1/\lambda_L\right)a + 2\pi s}{\left(\bar{U}_1/\lambda_L\right)a - 2\pi s}.e^{-(4\pi s/a)dL} \quad (2.45)$$

$$N_2 = 1 - \frac{\left(\bar{U}_1/\lambda_L\right)a - 2\pi s}{\left(\bar{U}_1/\lambda_L\right)a + 2\pi s}.e^{-(4\pi s/a)dL} \quad (2.46)$$

$$R = -\frac{\left(\bar{U}_2/\lambda_C\right)a - 2\pi s}{\left(\bar{U}_2/\lambda_C\right)a + 2\pi s}.e^{-(4\pi s/a)(d_1+d_2)} \quad (2.47)$$

$$\bar{U}_1 = \propto_1 ,, \qquad \bar{U}_2 = \left[\frac{1}{\propto_1} + \frac{d_{IS}}{\lambda_{IS}}\right] \quad (2.48)$$

2.8. Summary

This chapter provide a review of the main physical concepts that are essential to understand the heat transfer mechanism in soil and the definitions of thermal properties of soil. A significant amount of understanding has been accumulated on the parameters that effecting the heat transfer. The ground sources heat pump components and mechanism as well as the analytical approach for the heat

transfer mechanisms for geo energy piles and walls are also covered in this chapter. The following five chapters, present and discuss different thermal enhancement approaches for geo-energy piles and walls.

Chapter 3: The Influence of the Thermally Enhanced Concrete on the Performance of Geo-Energy Piles and Walls.

3.1 Highlights

- Enhancing the thermal conductivity of concrete was found to significantly improve the performance of geo-energy structures.
- The heat transfer efficiency of energy pile and energy diaphragm wall made from thermally enhanced concrete was significantly improved by 50% and 66% respectively.
- Adding 36% of graphTHERM powder to the concrete by weight of cement was found to double the thermal conductivity of concrete without detrimental effects on the compressive strength.
- The stiffness of the graphTHERM concrete was higher by 15% more than that measured for normal concrete.

3.2 Introduction

Critical analysis of heat transfer mechanisms in geothermal energy piles has demonstrated that there are four key factors affecting the thermal performance of geothermal energy piles which are: i. geometrical optimisation, ii. introduction of a Nanofluid as a coolant/circulating fluid, iii. pipe materials and iv. concrete heat transfer enhancement (Faizal et al., 2016). Geometrical optimisation mainly focuses on the pile dimensions depth, diameter, concrete cover, etc. as well as the pipe configuration [number of pipes and pipe arrangements]. Kwag and Krarti (2013) numerically demonstrated that increasing the pile length led to an increase in the heat exchange rate. It was also revealed that when the distance between U-tube loops or shanks space was increased, the extracted and dissipated energy was considerably enhanced. Similarly, Kaltreider et al. (2015) showed that the heat transfer was remarkably higher when larger tube shanks were used. It was also noted that enlarging the pile diameter resulted in a lower concrete thermal resistance ($R_{concrete}$) for a single U-tube configuration (Loveridge and Powrie, 2014). The double U-shaped pipes were found to produce a better thermal performance than a single U-tube (Li et al., 2014; Gashti et al., 2014). Increasing the

number of pipes inside the energy piles was found to provide an enhanced mechanism to extract more heat from the ground. Jalaluddin et al. (2011) indicated that enhanced coaxial heat exchanger tubes gave an improved heat transfer with the surrounding ground. In other words, increasing the length of the HE pipes inside the foundation elements of the structure increased the extracted heat. Zarrella et al. (2013) pointed out that the helical shaped HE also led to an improvement in the thermal performance and was considered to provide more heat transfer than U-tube shaped HE due to providing higher heat transfer area than the conventional U-tube HE. The geometrical parameters of GEPs were largely governed by the imposed mechanical load of the superstructure rather than the building energy demand. Nevertheless, to enhance the thermal performance, an increase in the pile length and/or pile diameter might be necessary, hence a coupled mechanical and thermal assessment of the GEPs is required to optimise the use of the sub-structural elements of the structures. Lyu et al. (2020)'s proposed a novel heat exchanger configuration for a geo-energy pile, which called a deeply penetrating 1-U-shaped configuration and compared its heat transfer performance with a traditional 1-U-shaped and 1-W-shaped configuration. It was revealed that the proposed deeply penetrating 1-U-shaped HE provided superior improvement on the total heat transfer rate giving an increase of 122% when compared with the traditional 1-U-shaped configuration [a single U-tube shaped] and of 55% when compared with 1-W-shaped [a single W-tube shaped] configuration. An optimisation exercise of double-U-tube borehole heat exchanger (BHE) was carried out using the Taguchi Method to rank the most influential parameters on the extracted and rejected heat (Kumar and Murugesan, 2020). Eight parameters were studied including borehole temperature, inlet temperature, borehole radius, half centre distance, grout thermal conductivity, soil thermal conductivity and mass flow rate. The optimization exercise indicated that during heat rejection and extraction (cooling and heating), the inlet temperature and borehole temperature are found to be the most influential parameters on the heat transfer rate, followed by the mass flow rate, centre distance and thermal conductivity of the grouting material. BHE tube radius did not influence the heat transfer rate for cooling mode. In heating mode, the thermal conductivity of soil was found to be the less influential parameter on the heat transfer rate.

Several studies examined the effect of mixing nanoscale particles with the circulating fluid to enhance its thermal properties. It was proven that a significant increase in thermal properties of fluid occurred with a small concentration of particles (Das et al., 2006). Ghozatloo et al. (2014)'s tests on Graphene/water fluid with a concentration of 0.050, 0.075 and 0.100% by weight revealed that the thermal conductivity of the circulating fluid increased when increasing the graphene concentration up to a particular concentration of 0.075%. For example, measurements taken at 25 °C illustrated that with the addition of 0.05, 0.075 and 0.10% of graphene by weight in water, the thermal conductivity was increased by 15%, 29.2% and 12.6% respectively. Godson et al. (2014) found that the overall heat transfer coefficient of nanofluids made of silver and water mix was higher than that of water. Furthermore, it was shown that the pressure drop in the case of this nanofluid was higher compared to that observed for the base fluid due to an increase in viscosity, hence more pumping power was needed. Although nanofluids showed a remarkable improvement in thermal conductivity, it did not result in a significant impact on the overall thermal exchange energy (Cecinato and Loveridge, 2015).

Due to being the interface element between the circulating fluid and surrounding concrete, pipe material should carefully be selected because of the impacts of its thermal resistivity on controlling the heat transfer, durability and cost effectiveness (Noorollahi et al., 2018). To investigate the effect of pipe material, Selamat et al. (2016) carried out experiments on pipes made of three different types of material: high density polyethylene (HDPE), copper, and a composite (cooper and LDPE coating) and with a thermal conductivity of 0.41, 387.6 and 1.19 W/m.K respectively. The heat exchange rate was found to be 206.4, 232.2 and 209.6 W/m respectively. As a result, the copper pipe was revealed to improve the operational efficiency by 16%. Another investigation Raymond et al. (2015) using three different types of pipe material: plastic with a thermal conductivity of 0.24 W/m.K, steel with a thermal conductivity of 57 W/m.K and copper with a thermal conductivity of 395 W/m.K, showed that the heat exchange rate (W) for the three pipes was 933.96, 939.89, 939.92 kWh/year respectively. Consequently, the study suggested that the type of the pipe material had no major effect in the system performance which is contradictory to the outcomes of (Selamat et al., 2016). Furthermore, by comparing the thermal performance of the steel pipes with that of the

HDPE pipes, it was observed that the performance of the steel pipes was higher. This was attributed to the fact that its thermal resistance was about 7% less than that of the HDPE pipes. In addition, it was reported that due to higher heat exchange rate in the case of steel pipes, a higher soil temperature around the steel pipe was experienced (Cao et al., 2016). Improving the thermal properties of HDPE using different types of conductive fillers such as metallic oxide, non-oxides, graphite and other similar materials was assessed. Dorrian and Mumm (2011) developed a pipe with a higher thermal conductivity of 0.85 W/m.K by the addition of a blend of 20% HDPE, 5% thermoplastic elastomer and 75% zinc oxide. The results revealed that using the thermally enhanced pipe material reduced pipe length by almost less than half whilst increasing the extracted heat by 100%. Ye et al. (2006) experimentally evaluated HDPE filled with expanded and colloid graphite. The thermal conductivity of HDPE pipes increased with the increase in the graphite content whilst expanded graphite led to twice as high thermal conductivity values compared to those measured for HDPE filled with colloid graphite. It is reasonable to highlight that the key considerations for the selection of the pipe material would be dependent on the cost, corrosion resistance, durability and its thermal properties. Hence, HDPE pipes become a sensible choice due to their low cost, corrosion resistance and easy installation.

Several studies were carried out aiming at either increasing the compressive strength of concrete or reducing the thermal conductivity of concrete for insulation purposes. Nevertheless, limited investigations were performed to improve the thermal conductivity of concrete (Li et al., 2018). It is, therefore, crucial that the use of novel composite materials is explored to enhance the thermal properties of concrete without losing sight of any potential impacts on the load carrying capacity of structural elements such as the piles. Guo et al. (2010) examined the addition of graphite to improve the thermal conductivity of concrete and pointed out that at room temperature, with an increase in the graphite content, the thermal conductivity of concrete rapidly increased. In another study, a series of graphite concrete specimens were prepared by mixing cement, sand, water, water-reducing agent, and different volumetric content of powdered graphite (0%, 5%, 10%, 15%, and 25%). The results indicated that the addition of graphite powder clearly enhanced the thermal conductivity, especially for concrete specimens

with graphite contents of more than 15%. The measured thermal conductivity results were used in a numerical modelling using finite element analysis to investigate the performance of geo-energy pile made of graphite concrete. The results demonstrated the ability of graphite concrete to enhance the heat transfer characteristics of energy piles and showed that a higher graphite content was more beneficial to the heat transfer process. However, the study did not include any field or large-scale experimental measurements (Li et al., 2018). Similar numerical study by Kong et al. (2019) on heat transfer characteristics of graphite concrete was used to thermally enhance energy pile and the results indicated that the heat transfer capacity of the graphite concrete energy pile was higher by 6.5% than that measured on a typical concrete energy pile. Nonetheless, there was no evaluation of the effect of this thermal enhancement on the concrete's compressive strength and there was also a lack of physical measurements of the pile performance.

Even though the efficiency of geo-energy piles were studied by several authors e.g. (Bao et al., 2019 and Cecinato and Loveridge, 2015) limited laboratory investigations were carried out to study the use of diaphragm walls as a geo-energy structure. Kurten et al. (2015) developed a semi-analytical model that was used to evaluate the effects of several factors including ground temperature, inlet temperature, flow rate and thermal conductivity of soil. The model was validated using experimental results and its results showed that the pipe thickness cover, flow rate and inlet temperature are the most important factors which affected extraction of heat using such a structure. However, the results of another numerical study carried out by Di Donna et al. (2016) to evaluate the most influential parameters on the performance of heat exchange using embedded walls revealed that the thermal conductivity of concrete and ground temperature caused significant impacts on the geo-energy wall performance. The behaviour of the geo-energy wall was assessed by a finite element model carried out by Sterpi et al. (2017) to highlight the wall's geotechnical and structural response. The results suggested that the thermally induced effects on the structure were not negligible and could be observed partly in the form of additional displacements and variations of the internal actions. Bourne-Webb et al. (2016) also performed numerical simulations to study the mechanical response of the geo-energy walls under different environment conditions and found that the seasonal changes affected the thermal expansion value for the wall and the

soils, hence it should be considered in the design process. Dong et al. (2019) proved through experimental and numerical investigations that a short-term heating of the wall showed a substantial temperature gradient across the wall thickness resulting in a significant stress and strain variation within the wall during the first few hours. Di Donna et al. (2017) published results of the first study on the efficiency of diaphragm walls and found that the concrete thermal conductivity had major effects on the long-term performance of geo-energy diaphragm walls and recommended to carefully design the concrete mix to maximise the thermal conductivity of wall material.

In light of the aforementioned critical review of the key parameters affecting the performance of geo-energy structures, it is reasonable to conclude that extensive research studies have been conducted on geo-energy structures with a focus on optimising the geometry of geo-energy structures, heat exchanger coil types and design. However, published work would seem to indicate that less attention has been given to the concrete thermal properties' effect on the performance of the energy piles and diaphragm walls. Consequently, this chapter reports the outcomes of an experimental investigation conducted using a large-scale fully instrumented laboratory rig for assessing the effects of enhancing the concrete thermal conductivity using graphTHERM addition on the thermal performance of geo-energy structures including piles and walls. The primary objectives of this chapter are to: i. Optimise the content of graphite to achieve a significantly improved thermal conductivity with minimal/no adverse impact on strength, ii. Assess the heat transfer capacity of geo-energy structures e.g., pile and walls utilising thermally enhanced concrete in dry and partly saturated grounds and iii. Study the thermal expansion and lateral earth pressure on the geo-energy structure.

3.3. Experimental materials and methods

In order to enable the investigation process of geo-energy structures using thermally enhanced concrete, a fully instrumented testing rig was designed and manufactured to run the heat transfer experiments consisting of three main parts, a testing tank, geo-energy structure and a data acquisition system. Details of the materials used in this experimental programme are demonstrated and discussed hereafter.

3.3.1. Materials

3.3.1.1. Sand

Standard building sand was chosen to simulate the ground soil in this experimental study due to its availability and cost effectiveness. The particle size distribution of the sand was determined in accordance with BS1377: Part 2 and is shown in Fig. 3.1. The sand was found to have a mean particle size of 0.24 mm and its characteristic diameters are illustrated in Fig. 3.1. The coefficients of uniformity (Cu) and curvature (Cc) were determined and found to be 1.38 and 0.89 respectively. As a result, the sand used was classified as a poorly graded fine to medium sand. The specific gravity (Gs) of the sand was determined using the pycnometer method as specified by BS1377:2, 1990 and found to be 2.65.

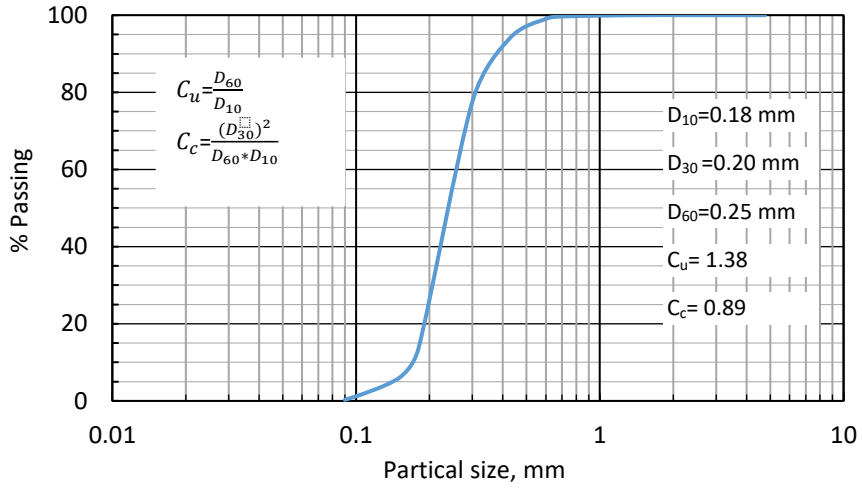

Fig. 3.1. Particle size distribution of the used sand.

A standard Proctor Compaction Test was performed according to BS1377-4:1990 in order for the maximum dry unit weight and optimum moisture content of the sand to be determined. The compaction test revealed that the maximum dry unit weight and optimum moisture content are 18.15 kN/m^3 and 11% respectively. In addition, direct shear tests were performed in compliance with BS 1377 part 7 under a range of normal stresses between 70 and 250 kPa to generate data for the normal stress shear stress relationships. Based on the acquired data, the friction angle for the sand was found to be 34.8° Table 3.1.

Table 3.1. Main properties of the used sand.

Parameter	Value	Test Method
Mean particle size, D50 (mm)	0.24	BS.1377:2, 1990
Coefficient of Uniformity, Cu	1.38	
Coefficient of Curvature, Cc	0.89	
Specific gravity, Gs	2.65	BS.1377:2, 1990
Maximum dry unit weight (kN/m^3)	18.15	BS.1377:4, 1990
Optimum water content (%)	11	BS.1377:4, 1990
Angle of friction angle, φ (degrees)	34.8	BS.1377:7, 1990
Hydraulic conductivity (m•s^{-1})	2.7x10^{-4}	BS.1377:6, 1990

3.3.1.2. Graphite powder

In this study, a special type of the graphite powder called “graphTHERM” was used to enhance the thermal conductivity of the concrete as it has a less effect on hydration of the concrete besides its high thermal conductivity. The selected graphite powder was developed by Georg H. Luh GmbH and had a high thermal conductivity of more than 100 W/m.K. Based on the data sheet provided by the supplier, graphTHERM was manufactured to be used as a filling material to increase the thermal conductivity without causing significant adverse impacts on the mechanical properties. Table 3.2 presents the main properties of graphTHERM powder as provided by the supplier.

Table 3.2. Main properties of graphTHERM.

Property	Value
Carbon (%)	Min 99.9
Ash (%)	Min 0.01
Iron (ppm)	100
Tapped density (g/cm^3)	0.85 – 1
Thermal conductivity, for cylindrical prepared sample of 1.85 gm.cm-3 and w/c=10% (W/m.K)	100
Surface area (m^2/g)	6.5-10
D10 (µm)	10 – 14
D50 (µm)	18 – 25
D90 (µm)	30 – 45

3.3.1.3. Concrete batches

All concrete batches were designed in compliance with the British Standards, BS 8500. Portland limestone cement (CEM II/A-LL 52.5R), manufactured by Hanson UK in accordance with BS EN 197-1:2000 was used in this study. A mix of natural coarse aggregates (NCA) with a maximum particle size of 10 mm and natural fine aggregate (NFA) with a maximum particle size of 5 mm were used in this research. The NCA particles had predominantly angular shapes. The properties of the coarse and fine aggregates were conformed to the standard requirement limits of BS EN 882. A water/cement (w/c) ratio of 0.45 was chosen to achieve a target compressive strength ranging between 45 - 48 MPa after 28 days. The proportions of the concrete constituents were kept constant for all concrete mixes in this study, the graphite powder was added to the concrete mix as a ratio of the cement by weight. It is imperative to note that the graphite powder was not used as a replacement material in the concrete. The concrete batches were prepared by mixing cement, NFA, NCA, water and graphite powder (graphTHERM). The graphTHERM was added with different weight contents of 0%, 10%, 20%, 30%, 40% and 50% by weight of the cement. The materials were mixed in a mechanical pan type mixer for 2-3 min in order for a homogenous mix to be achieved prior to adding the predefined amount of water. The mix was then poured in special cylindrical moulds with an internal diameter of 100 mm and a height of 50 mm as well as in 100 mm cubical moulds. The former was used to create specimens with an appropriate size for measuring thermal conductivity using a hotplate testing setup, whereas the latter was used to produce standard concrete cubes for assessing the compressive strength of thermally enhanced concrete. Both cylindrical and cubical concrete specimens were cured for 28 days in a water bath followed by 2 days in a drying room with an ambient temperature of 24°C. It was important to dry out the specimens due to the sensitivity of thermal conductivity measurement to moisture content. Afterward, these samples were utilised to determine the optimum graphTHERM content. Subsequently, the optimum percentage of the graphTHERM was used to produce further concrete samples for evaluating the thermal expansion coefficient and concrete stiffness. Also, concrete prisms with dimensions of 40 x 40 x 160 mm were used to evaluate the concrete

thermal expansion coefficient in accordance with TI-B 101 (94), whereas cylindrical concrete samples with a diameter of 100 mm and height of 200 mm were used to determine the concrete stiffness in accordance with EN 1992-1-2, 2004.

3.3.2. Experimental methods

3.3.2.1. Hot plate setup

Hot plate tests were carried out according to the British Standards - BS EN 12664: 2001 to measure the thermal conductivity on cylindrical concrete samples prepared with different percentages of graphite powder by weight of cement. Fig. 3.2 shows a schematic drawing of the hot plate test. The concrete sample was sandwiched between flat hot and cold plates as shown in Fig. 3.2. Due to the temperature difference, a thermal gradient was created through the sample. The heat flux, which is defined as the amount of the input heat power passing through the cross-sectional area of the specimen, can be determined from the power input and the cross-sectional area of the specimen. By knowing the temperature drop, heat flux and length of the specimen, Fourier's law of unidirectional heat transfer can be applied to calculate the thermal conductivity (k) in W/m.K as given by Eq. (3.1).

$$k = \frac{Q.L}{A.\Delta T} \tag{3.1}$$

Where; Q is the heat flux (w/m^2), ΔT is the temperature drop (°C), L is the specimen thickness (m) and A is the cross-sectional area of the concrete sample (m^2). It is worth noting that the setup was calibrated by measuring the thermal conductivities of sample materials such as wood, aluminium and brass with known thermal conductivity. The results of the calibration exercise showed that the maximum error in the thermal conductivity measurement was found to be 3%. In addition, measurements were taken on three identical samples and the average value was reported hereafter for each concrete mix.

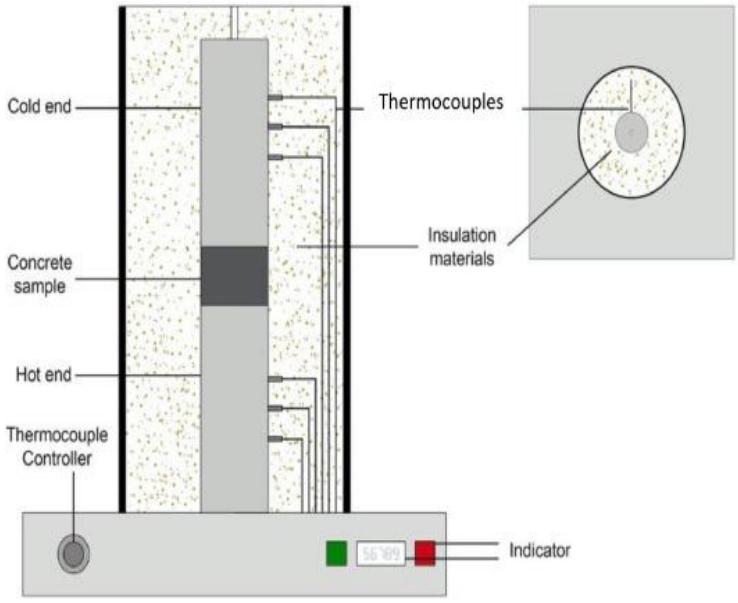

Fig. 3.2.Schematic drawing of the hot plate test experimental setup.

3.3.3. Heat transfer experiments

A Fully instrumented heat transfer testing rig with internal dimensions of 1 m x 1 m x 1 m was designed and manufactured. Figs. 3.3 and 3.4 show schematic diagrams of the testing rig and configuration of the geo-energy pile and wall respectively. The tank walls are fully insulated to minimise the effect of the ambient air temperature. A drainage system was installed at the base of the tank to uniformly introduce and drain groundwater over the whole cross-section area of the tank. The drainage system included perforated pipes, manifold, gravel bed, a filter sheet and a well. The perforated pipes and manifold were surrounded by a gravel bed that was wrapped by a synthetic filter sheet to prevent washing out of fine sand particles and to avoid blockage of the drainage system. The drainage system (manifold) related to an external well to regulate and maintain the water level inside the tank at pre-determined levels.

Two different embedded geo-energy structures were examined in this study a concrete energy pile and concrete energy wall**.** The geo-energy pile was formed with external dimensions of 900 mm in height and 150 mm in diameter. The pile was placed in the centre of the tank and surrounded by sand. A U-shaped heat exchanger [HE] made out of nylon with a total length of 1700mm and outer and

inner diameters of 8 mm and 6 mm respectively was embedded symmetrically inside the concrete pile.

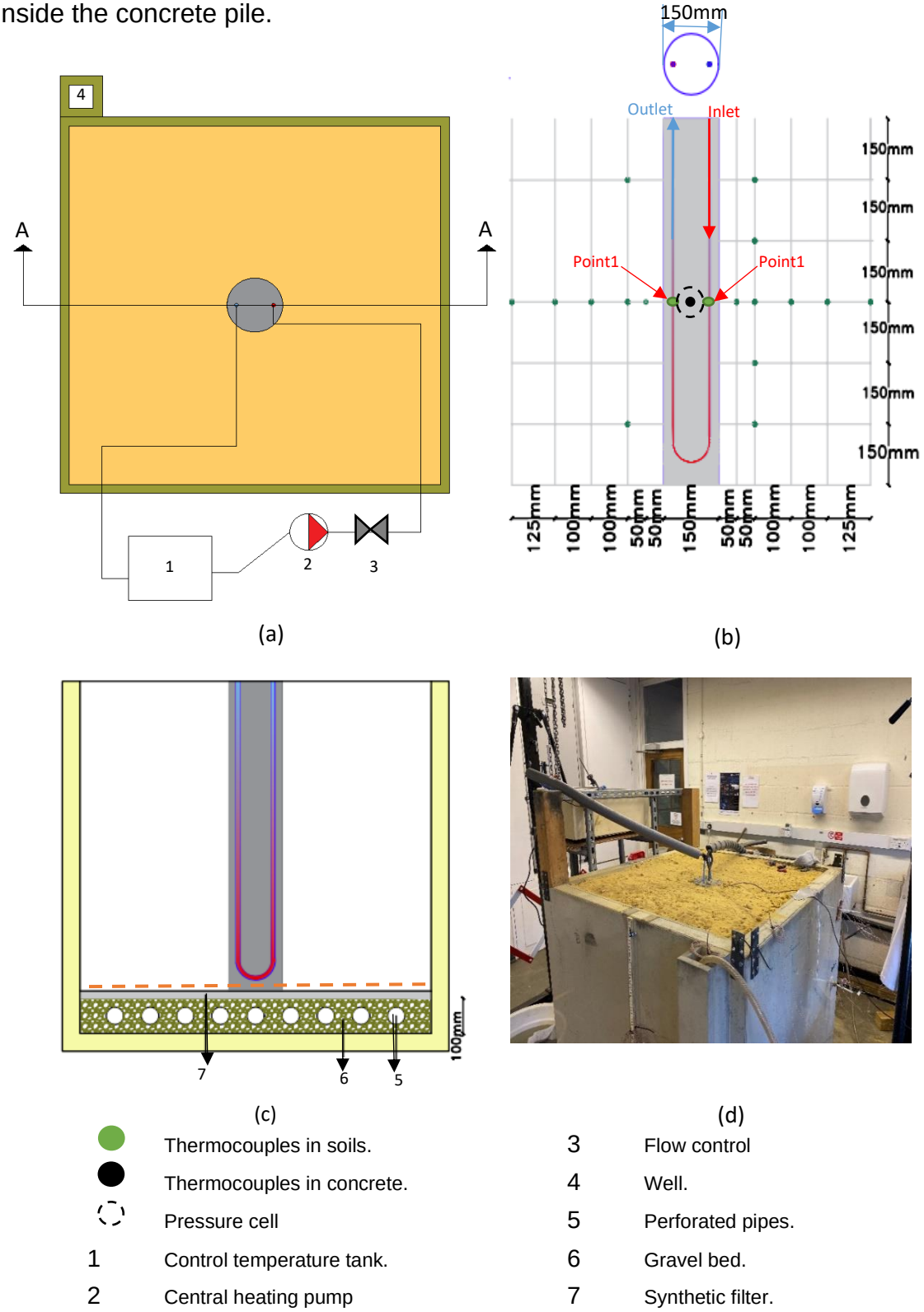

Fig. 3.3. Schematic diagram of the experimental rig for energy pile tests; a) Plan view, b) Location of thermocouples, c) Vertical cross section of the testing tank and d) Image of real testing rig.

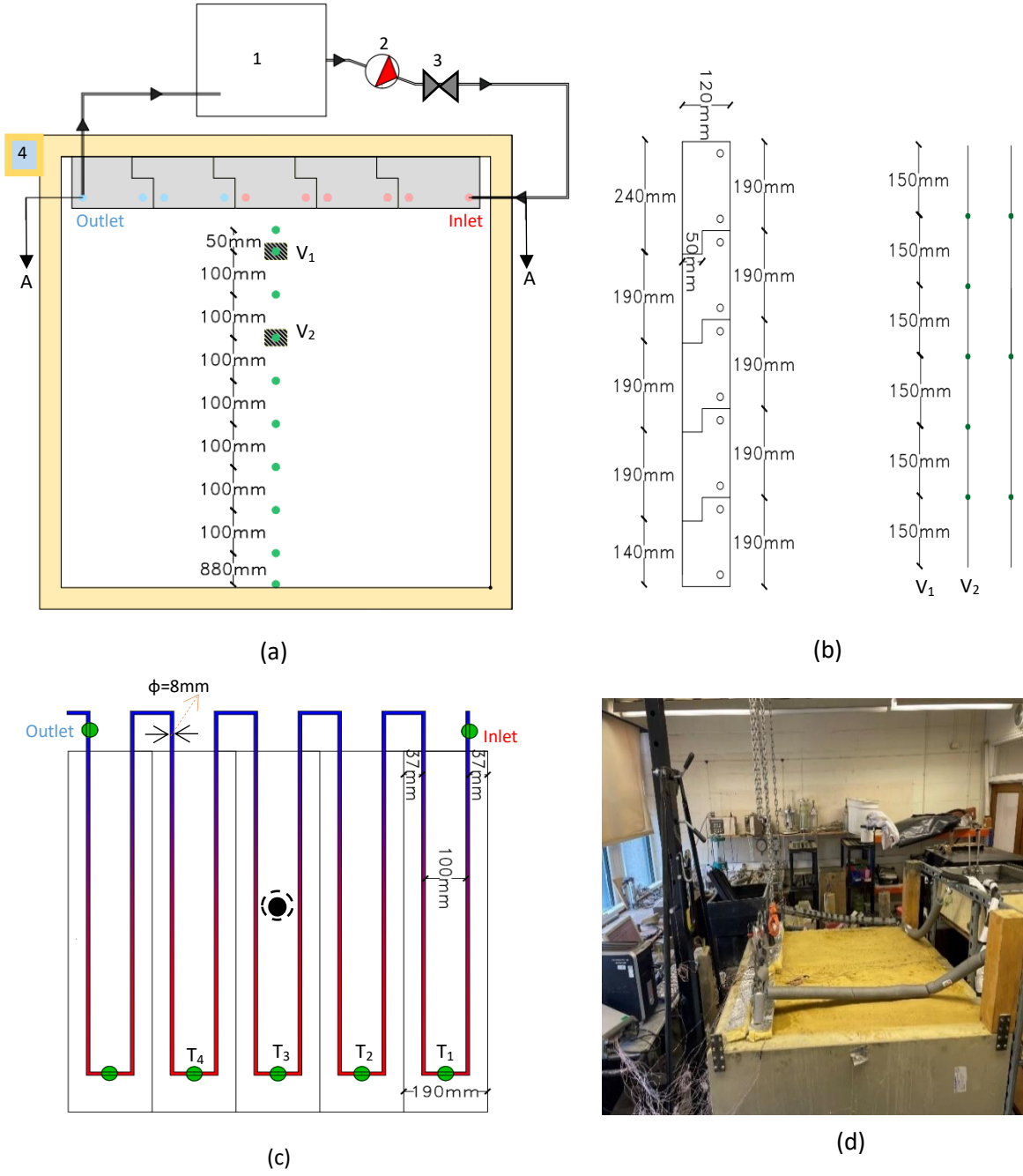

●	Thermocouples in soils.	3	Flow control
●	Thermocouples in concrete.	4	Well.
◌	Pressure cell	5	Perforated pipes.
1	Control temperature tank.	ϕ	Pipe diameter
2	Central heating pump		

Fig. 3.4. Schematic diagram for the experimental rig for energy wall test; a) Plan view, b) Dimensions of wall and location of thermocouples, c) Arrangement of heat exchanger and d) Image of real testing rig.

The concrete energy wall was constructed in 5 segments that were interlocked together to form an embedded wall as shown in Fig. 3.4b. Each segment of the concrete wall had dimensions of 900 mm in height, 190 mm in width and 120 mm in depth. A nylon U-shaped heat exchanger was embedded in each segment resulting in a total heat exchanger tube length of 9900 mm. In order to fasten the HEs precisely in predefined locations inside the energy piles and walls, metal cages were manufactured and fitted inside the casting mould prior to casting of wet concrete. The centre to centre spacing between the two legs of the U-shaped HE was maintained at 100 mm in the energy piles and walls. After casting the concrete, the energy model structures were cured for 28 days by covering them with wet sheets that were frequently wetted with water to maintain consistent curing conditions.

Upon completion of curing period, the geo-energy pile was installed in the centre of the testing tank which is located in control temperature room and the ambient temperature was kept constant of about 21^{o}C. To measure the lateral earth pressure on the pile and the wall, an earth pressure cell was installed at a pre-determined location which was at mid-height of pile or the centre point of the wall. The earth pressure cell was placed during the sand filling stage of the tank as shown in Fig. 3.3b and Fig. 3. 4c. A T-type thermocouple was fastened at mid height of the pile and at the centre point of the wall to measure the temperature of the concrete during the test. The illustrative drawings in Figs. 3.3b, 3.4a and 3.4b show the location of sensors. The soil temperature was measured at several vertical and horizontal sections. A total of 23 T-type thermocouples were utilised for measuring the vertical and horizontal soil temperature profile, fluid temperature inside the heat exchanger, inlet and outlet temperature and the ambient temperature. A total of 27 T-type thermocouples were required in tests involving the geo-energy wall. All thermocouples were calibrated prior to their use and the accuracy of the measurements were found to be ± 0.25°C. After the installation of all devices and sand-filling completed, a mix of degradable glycol-water ratio 1 part glycol to 3 parts of water was circulated in the HE that was embedded inside the energy structure with a target temperature of 52°C. The flow rate of the circulating fluid was controlled using a peristaltic pump at a rate of 67 l/h (which presenting laminar flow with Reynolds number of 510) throughout the tests. In total 6 experiments were carried out including 4 tests on energy piles and 2 tests on energy

walls with the fixed and variable parameters demonstrated in Table 3.3. The first two tests were conducted on piles that were made from normal concrete and graphite concrete and installed in dry sand beds as illustrated in Table 3.3. Two more tests were then performed whilst the sand surrounding the pile was partly saturated with water by maintaining the water level inside the tank at 500 mm above the base resulting in a steady hydrostatic water pressure. This is an attempt to simulate a real-world scenario where geo-energy piles are installed in grounds where groundwater table is stagnant at a particular level. The final two experiments were carried out on energy walls made of normal and thermally enhanced concrete materials but installed in a similar ground to the previous two tests in which sand was partly saturated with water. It should be noted that test coding was developed to reflect test conditions. For example, a test code W-NW-1 indicated a normal concrete wall installed in a partly saturated sand whereas test code W-GW-2 indicated an energy wall made out of graphite concrete in partly saturated sand. Table 3.3 illustrated the fixed and variable parameters in each experiment alongside with the test coding. Measurements were taken every 10 second by the data acquisition system and saved automatically on the computer. An hourly average was then determined and presented hereafter.

Table 3.3. Fixed and variable parameters for heat transfer experiments.

	Series	Test coding	Fixed parameters	Variable parameters
Energy piles	1	D-NP-1	DS, FR = 67 l/h, IT = 52.14 °C	NP
		D-GP-2	DS, FR = 67 l/h, IT = 52.41 °C	GP
		W-NP-3	FR = 67 l/h, PSS, IT = 52.01 °C, WL = 500 mm	NP
		W-GP-4	FR = 67 l/h, PSS, IT = 52.52 °C, WL = 500 mm	GP
Energy walls	2	W-NW-1	PSS, WL = 500 mm, FR = 67 l/h, IT = 53.18 °C	NW
		W-GW-2	PSS, WL = 500 mm FR = 67 l/h, IT = 52.35 °C	GW

where; DS = Dry Sand, PSS= Partly Saturated Sand, FR = Flow Rate, WL= Water Level and IT = Inlet Temperature, NP= normal concrete pile, GP= graphTHERM concrete pile, NW= normal concrete wall, GW= graphTHERM concrete wall.

3.3 Results and discussion

This section is organised to present and discuss the measurements taken for the thermal conductivity and thermal heat capacity of sand and the thermal conductivity of concrete before assessing the behaviour of the geo-energy structures under different conditions. The effect of adding thermal enhancement material on the concrete thermal conductivity is presented and discussed. These results are then utilised to support the discussion of the influence of the thermally enhanced concrete on the performance of geo-energy structures e.g. piles and walls.

3. 3.1. Thermal properties of sand soil

A KD2 Pro thermal analyser device was utilised to measure the thermal properties including thermal conductivity and thermal capacity of the sand used. Both dry and wet sand samples were prepared with a constant dry unit weight of 18.15 kN/m^3 under a static load. Samples of the wet sand were prepared with varying water contents of 1%, 3%, 5%, 10%, 20% and 30% and were compacted to the same dry unit weight. Upon compaction of the sand samples, needles of the KD2 Pro thermal analyser device were inserted carefully into the prepared sample to measure the thermal conductivity and volumetric thermal heat capacity. Average values of three measurement readings were taken for each sample. Fig. 3.5 presents the thermal conductivity measurements on sand samples as a function of water saturation. The degree of saturation was determined based on the actual measurement of the water content at the end of the test. The results clearly show a correlation between increases in thermal conductivity and increasing water saturation. The thermal conductivity of dry sand was found to be 0.36 W/m.K. Careful inspection of the data shown in Fig. 3.5 revealed that the relationship between thermal conductivity and degree of saturation shows two distinct phases. The first phase is characterised by a remarkable increase in the thermal conductivity values from 0.36 to 2.6 W/m.K with a slight change in the water saturation while in the second phase, the thermal conductivity values increased from 2.6 to 3.5 W/m.K over a wide range of water saturation. This could be attributed to the gradation of the sand used and its water retention properties resulting in a high suc-

tion head at low degrees of water saturation, which in turn caused improved bonding between the particles and enhanced conductive heat transfer capability. Also shown in Fig. 3.5 are the measured values for the volumetric heat capacity of the sand as a function of the degree of water saturation. It is clear that the volumetric heat capacity (C_v) increased linearly with the degree of saturation which is consistent with previous observations by (Yadav and Saxena, 1973; Ghuman and Lal, 1985 and Abu-hamdeh, 2003).

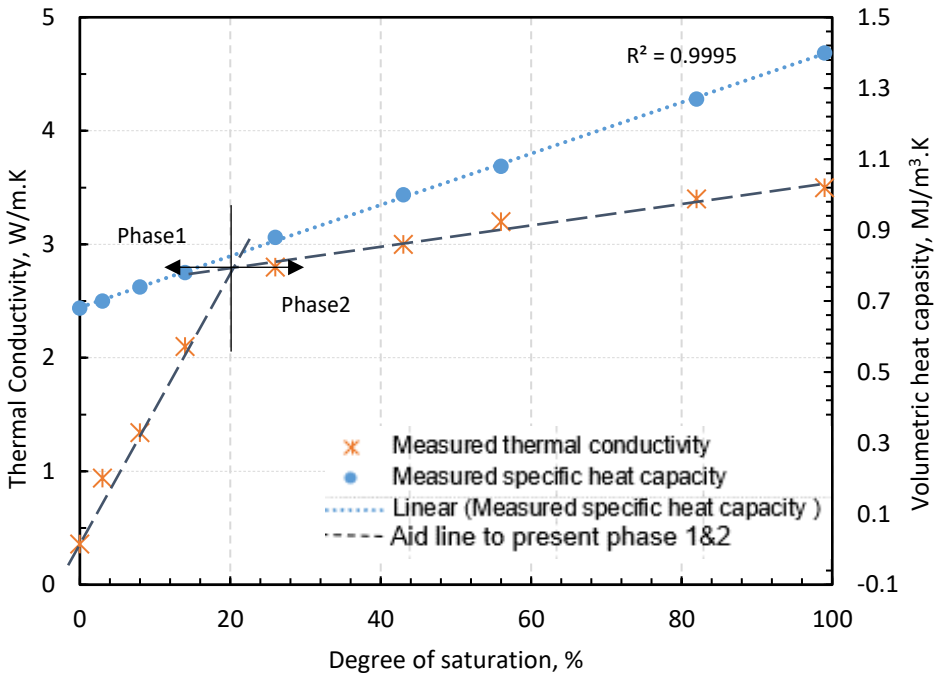

Fig. 3.5. Measured thermal conductivity of sand as a function the degree of water saturation

3.3.2. Thermal conductivity, strength and stiffness of concrete

The attained results for the thermal conductivity of concrete samples prepared with 0%, 10%, 20%, 30%, 40% and 50% graphite (graphTHERM) content of cement weight and tested at room temperature are presented in Table 3.4. It should be noted that the data presented in Table 3.4 represents the average value of the thermal conductivity attained from tests on three identical concrete samples whilst batch 1 was carried out as a control test. Consequently, the degree of improvement was determined in comparison to the results attained from the control test. It can be observed that the highest thermal conductivity value was recorded

for a concrete made with a graphite content of 50%. The measured thermal conductivity was 3.10 W/m.K which was more than double that obtained on a normal concrete sample (1.44 W/m.K). The enhanced thermal conductivity could fundamentally be attributed to the higher thermal conductivity value of the graphTHERM which was typically 100 W/m.K but also to the particle size of graphTHERM, which is , smaller than that of the cement, could have contributed to filling of the tiny voids between the aggregates thereby resulting in an improved packing of particles and a higher density concrete. In other words, replacing the air voids in the concrete with higher thermal conductivity particles could result in a significant increase in the thermal conductivity of concrete (Meng and Khayat, 2016 and Arora et al., 2018).

The data plotted in Fig. 3.6 suggest that the relationship for the thermal conductivity of concrete as a function of graphite powder content took the form of an S-shape curve characterised by three distinct regions. With the addition of up to 10.5% of graphite powder by the weight of cement, a moderate degree of improvement in the thermal conductivity can be observed in region 1. Whereas in region 2, a remarkable degree of improvement in the thermal conductivity of concrete was recorded with the increase in the graphite powder content up to 35.5%. Any further increase in the graphite content above 35.5% led to another moderate degree of improvement in the thermal conductivity of concrete. Results reported by Qingwen et al. (2018) suggested that in order to observe a positive change in the value of the thermal conductivity of concrete, more than 15% of graphite should be added to the concrete. No optimum value for the graphite content was suggested by the study, nor was the impact on the mechanical behaviour assessed.

Data for the influence of graphTHERM content on the measured compressive strength of concrete after 28 days of curing were also plotted in Fig. 3.6. It was observable that the addition of graphTHERM powder to the concrete mix resulted in a considerable degree of improvement in the compressive strength of concrete up to 10% graphTHERM content. A more than 10% addition of the graphTHERM powder led to a gradual but slight decline in the measured compressive strength. However, the measured compressive strength was still higher than that recorded in the control test on normal concrete with 0% graphTHERM powder content. The

results revealed that adding more than 45% of graphite powder resulted in achieving a lower strength below that recorded for the normal concrete with zero graphite powder content.

Table 3.4. Thermal conductivity of concrete mixed with different percentages of graphite

Batch number	Graphite Content %	Room Temperature °C	Thermal Conductivity W/m.K	Degree of improvement %
1	Zero	24.4	1.44	-
2	10	24.7	1.60	11
3	20	25.9	2.10	45
4	30	24.6	2.64	83
5	40	24.3	2.97	106
6	50	24.8	3.10	115

Strengthening of concrete by incorporation of graphite powder was previously reported and interpreted by (Dimov et al., 2018). Graphite powder would interact with cement in the presence of water to produce Calcium Silicate Hydrate (C-S-H) which is different to that produced in the case of normal concrete and would affect the morphology of the hydration. These changes promote a growth of C-S-H along the graphite particles which enhanced the bond strength of the cement. Results for the microstructure of graphite-concrete taken by X-ray diffraction (XRD) indicated the modification of cement crystals upon graphite incorporation, more specifically to calcium aluminoferrite, calcium carbonate, tri- and di-calcium silicate as well as calcium aluminate (Dimov et al. 2018). The microstructural changes in the crystals at the early stage of hydration are responsible for the strength growth at late stages e.g 28 days.

In order for an optimum graphite content to be determined for geo-structural applications, both aspects of the compressive strength of concrete and thermal conductivity were taken into consideration. From Fig. 3.6, it was very clear that there is a range for the graphite content which can result in enhancing both thermal conductivity and concrete compressive strength over those recorded for normal concrete. Bottom line was that addition of graphite powder should not reduce the

strength of concrete. The results suggested that addition of 36 % of graphite powder content to concrete material was effective in terms of enhancing the thermal conductivity by 100 % (top of region 2) whilst resulting in a better compressive strength of graphite concrete which was 10 % higher than that attained for the control test on normal concrete without any graphite powder.

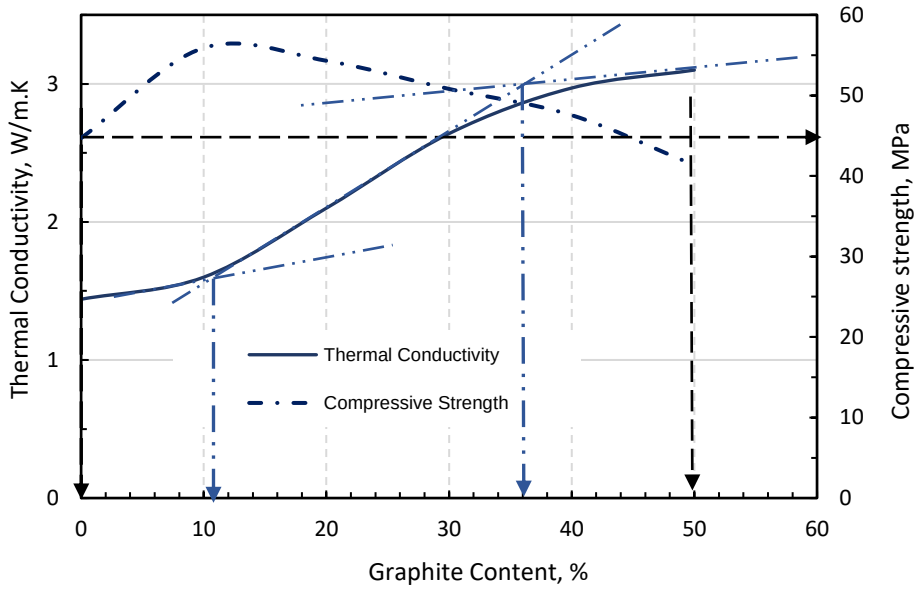

Fig. 3.6. Thermal conductivity and compressive strength of concrete as a function of the graphite content.

Stiffness of normal concrete and graphTHERM concrete prepared with an optimum value of graphite powder was measured on cylindrical samples with a diameter of 150 mm and length of 300 mm. Samples were cured in a water bath for 28 days and air dried for 24 hours prior to testing. Strain gauges were fastened on the sample surface in the longitudinal direction as shown in Fig. 3.7 b and c. Fig. 3.7a shows recorded data for the applied stress and measured strain on samples made from normal concrete and graphTHERM concrete. The modules of elasticity (E) was determined from the measured data in accordance to EN 1992-1-2,2004. The results revealed that the stiffness of the graphTHERM concrete and normal concrete was found to 32 GPa and 27.8 GPa respectively. It is clear that the stiffness of graphTHERM concrete is 15 % great than that measured for the normal concrete. The increase in stiffness of graphTherm concrete could be attributed to combining C-S-H which has a Young's modulus E of 23.8 GPa with graphite particles with E value of 2000 GPa (Tanabe et al., 2008 and

Dimov et al., 2018). This would lead to a considerable increase in the elasticity modulus of the graphite-concrete. Moreover, addition of graphite powder assists with the reduction in the concrete porosity as it extends the size range of microscale dimension of the particles and increases the packing density for the mix (Sbia et al., 2015 and Arora et al., 2018).

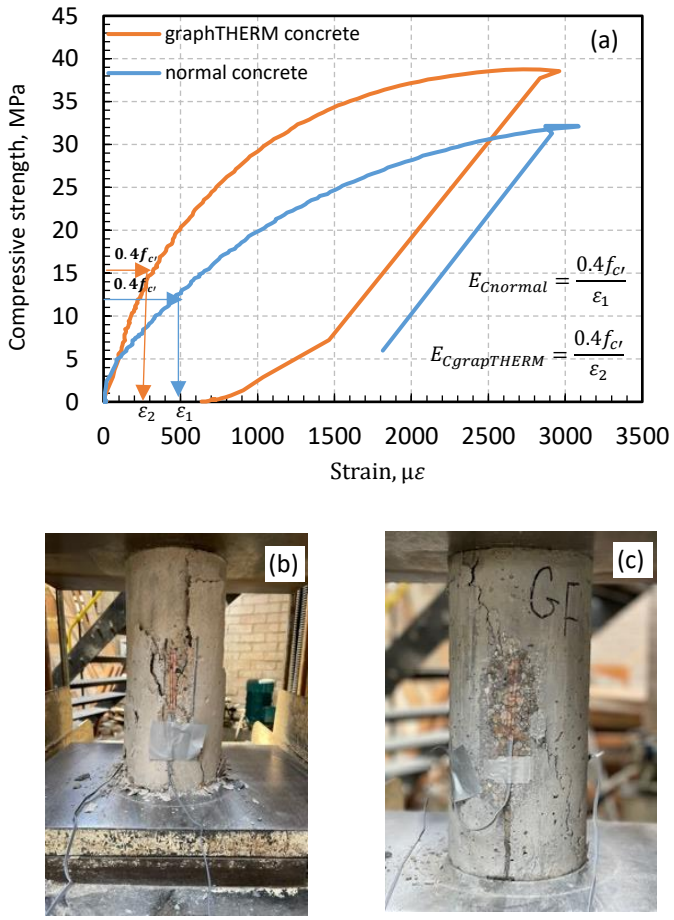

Fig. 3.7. Cylinder compressive strength vs strain for normal concrete and graphTHERM concrete.

3.3.3 Heat transfer experiments for energy pile

3.3.3.1 Heat transfer experiments for energy pile

Throughout all tests, the circulating was continually pumped at flow rate of rate of 67 l/h (which presenting laminar flow with Reynolds number of 510) and fluid temperature was recorded at the inlet and outlet points of the HE that was embedded in the model geo-energy pile. The inlet-outlet temperature difference

Δt would indicate the highest amount of heat energy that the pile was able to dissipate into the soil. Fig. 3.8 presents the temperature difference between inlet and outlet from the four tests and evidently demonstrates that test W-GP-4 in which the energy pile made of graphite concrete and installed in partly saturated sand gave the highest temperature difference. On average a difference of about 3 °C was recorded after reaching steady state conditions in comparison to a measured temperature difference on normal concrete pile in partly saturated sand of 2 °C, indicating a degree of improvement of 50% while the degree of improvement in temperature deference between inlet and outlet decreased to 31% when the piles were tested in dry soil conditions. These findings provide reliable evidence that the thermal performance of geo-energy pile increased when the graphite concrete was used which could be attributed to the higher thermal conductivity of graphite concrete than that of normal concrete as illustrated in Fig. 3.8.

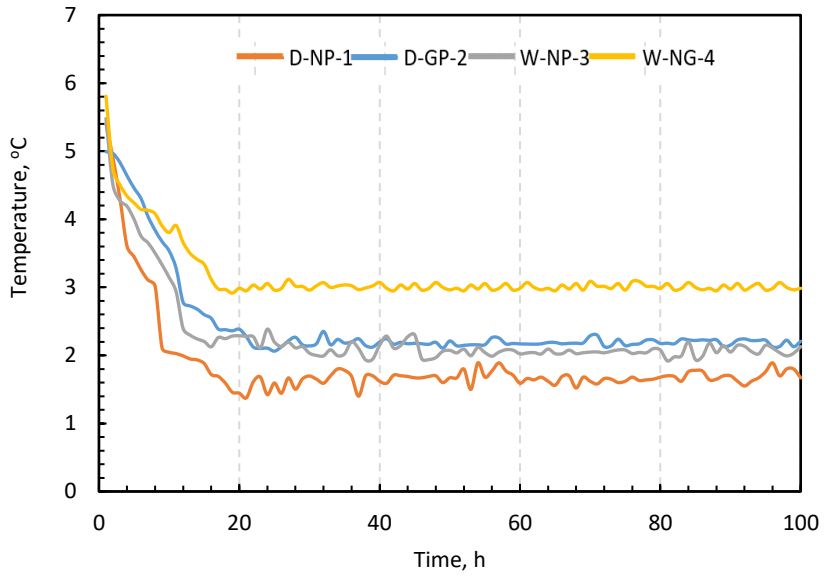

Fig. 3 8. Measured temperature difference between inlet and outlet

In addition, as illustrated in Fig. 3.3, the circulating fluid temperature was measured at two more points; points 1 and 2 inside the HE at a distance of 450 mm and 1450 mm from the inlet point respectively. The total length of pipe within the HE was 1700 mm. Data for the measured temperature, the temperature difference from that measured at the inlet point and the percentage of temperature dissipation at the two points after reaching steady state conditions are presented

in Table 3.5. The data demonstrates that the fluid temperature flowing in the HE reduced by about 20% and 90% of the total dissipated temperature at points 1 and 2 respectively. To evaluate the effect of water saturation on the liquid temperature dissipation, the temperature difference

$\Delta t_{1\text{-}2} = T_1 - T_2$ was determined and presented in Table 3.5. The results clearly showed for energy piles with normal concrete tests D-NP-1 and W-NP-3 that saturating the sand up to mid height of the pile caused a 37% increase in the temperature difference between points 1 and 2. This could be attributed predominantly to the fact that the soil in the bottom half of the tank was fully saturated with water leading to remarkably higher thermal conductivity and heat capacity. To confirm this observation, measurements for the thermal conductivity and volumetric thermal heat capacity of soil were taken on samples at predetermined heights after the completion of the tests W-NP-3 and W-GP-4. In addition, samples were extracted precisely at the same predetermined heights for determination of water content and density. Fig. 3.9 presents water distribution inside the testing tank which confirms that sand in the bottom half of the tank is fully saturated with water. Notably, there is a significant drop in the degree of saturation in the top 300 mm of the sand reaching an almost dry condition at the surface of the sand. Then, the obtained value of the soil degree of saturation was used in conjunction with Fig. 3.5 to measure the thermal conductivity and heat capacity of the sand along the tank height. Also, presented in Fig. 3.9, is the measured thermal conductivity against the degree of saturation. The measurements reveal that thermal conductivity and heat capacity retained high values in the bottom half of the tank and decreased gradually towards the sand surface (top of the tank).

Table 3.5. Circulating fluid temperature along the heat exchanger

TEST CODE	INLET POINT	POINT 1 (T_1)			POINT 2 (T_2)			POINT2 - POINT1	OUTLET POINT		DISSIPATED ENERGY
	T_i	T_1	Δt_1	HD	T_2	Δt_2	HD	Δt_{1-2}	T_O	Δt_3	q
	°C	°C	°C	%	°C	°C	%	°C	°C	°C	watts
D-NP-1	52.14	51.76	0.39	23	50.65	1.52	92	1.11	50.49	1.65	113.50
D-GP-2	52.41	51.97	0. 44	20	50.46	1.95	90	1.51	50.25	2.16	148.65
W-NP-3	52.01	51.6	0.46	22	50.07	1.94	95	1.53	49.96	2.05	141.10
W-GP-4	52.52	51.75	0.77	25	49.58	2.94	96	2.17	49.45	3.07	211.27

where; T_i = inlet temperature, T_1 = Circulating fluid temperature at 450 mm, T_2 = Circulating fluid temperature at 1450mm, T_O = Outlet temperature, $\Delta t_1 = T_i - T_1$, $\Delta t_2 = T_i - T_2$, $\Delta t_3 = T_i - T_O$, $\Delta t_{1-2} = T_1 - T_2$, HD = percentage of heat dissipation, q = dissipated energy.

Fig. 3.10 shows the change in the soil temperature measured at five points along the depth of the pile at 150 mm, 300 mm, 450 mm, 600 mm and 750 mm in the inlet side and at three points at 150 mm, 450 mm and 750 mm in the outlet side. All measurements were taken at 100 mm away from the pile in both inlet and outlet sides as shown in Fig. 3.3. With the increase in the experimental time, the soil temperature increased until reaching steady state conditions after 20 h from the onset of the test.

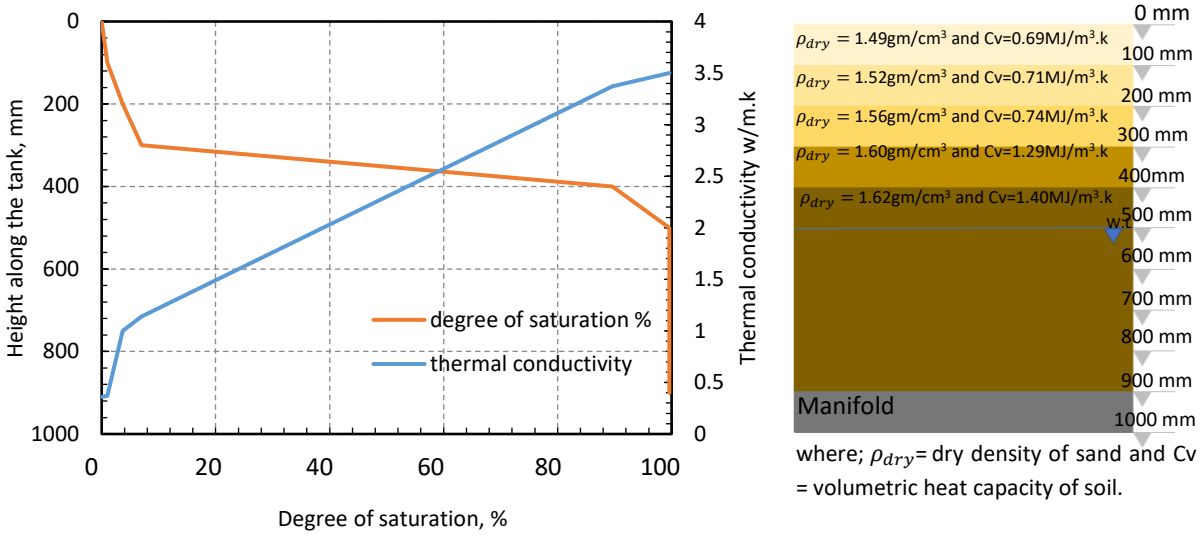

Fig. 3.9. Measured degree of saturation and thermal properties along the experimental tank.

Fig. 3.10 therefore shows the results of the vertical profile of soil temperature after reaching steady state conditions. The maximum soil temperature recorded

at 750 mm for D-GP-2 test is found to be around 33 °C which reduced by 2 °C in W-GP-4, recording 31°C. It was evident that the temperature gradient was much steeper at the top half of the pile which suggested that most of the dissipated heat was recorded in the lower soil layers of the tank where the sand has a higher specific heat capacity value due to being saturated. Tests in which geo-energy piles were installed in dry sands showed a higher soil temperature along the vertical profile. Furthermore, the gradient of soil temperature in tests performed on normal and graphite concrete piles installed on partly saturated sand demonstrated a considerable reduction in the soil temperature in comparison to that measured in dry sand. Comparing the vertical temperature profiles recorded on the four geo-energy piles illustrated that the temperature gradient in the adjacent soil was strongly affected by the concrete thermal characteristic. It was obvious that the dissipation of heat from the graphTHERM concrete pile did not cause the soil temperature to increase to the normal concrete pile level despite the fact that it enabled a higher heat dissipation. To calculate the dissipated heat, Eq. (3.2) was used:

$$q = \dot{m} c_p (T_{out} - T_{in}) \tag{3.2}$$

where; q is the thermal energy dissipated into the ground (watts), $\dot{m}$ is the mass flow rate (kg/s), Cp the spesific heat capacity (J/kg. K) and Tinlet and Toutlet are the inlet and outlet temperatures respectively. For dry tests, D-NP-1 and D-GP-2, the calculated dissipated heat was about 113.50 watts and 148.6 watts respectively, while for partly saturated soil tests, the dissipated heat was about 141.10 watts for W-NP-3 and 211.27 watts for W-GP-4. Fig. 10 also shows that the soil temperature was elevated on both sides of the pile due to dissipation of heat via the HE. Tests D-NP-1 and D-GP-2 that were carried out in dry soil conditions, showed higher soil temperature. On the other hand, results from tests W-NP-3 and W-GP-4 indicated that a lower soil temperature was recorded in comparison with those measured for dry soil. This phenomenon could be attributed to the fact that the specific heat capacity is different for dry and saturated sand. Specific heat capacity is defined as the amount of energy to unit increase in the temperature of a unit mass of material. Therefore, it needed more energy to be rejected from the geothermal pile to observe an identical change in temperature in the

saturated sand. These results are in consensus with previous work carried out by (Mohamed et al., 2 015; Kramer, 2013 and Bao et al., 2019).

The horizontal soil temperature profile at mid-height of the pile (450 mm below the soil surface) measured on both inlet and outlet sides are shown in Fig. 3.11. As can be seen in Fig. 3.11, due to the high temperature gradient between the pile and the surrounding soil, the soil temperature has increased until reaching steady state conditions. The maximum increase in the soil temperature from its initial state (20 ± 1°C) was recorded at~15°C in tests carried out on dry sand. This could be attributed to its lower heat capacity and thermal conductivity (Kramer, 2013; Faroki, 1986 and Alrtimi et al., 2014). Whereas, when the energy pile was installed in a partly saturated sand, the maximum soil temperature difference was found to be 10 °C resulting in a reduction of 33%. In addition, with the increase in the radial distance from the pile, there was a significant decrease in the soil temperature. The maximum temperature changes at 50 mm, 100 mm, 200 mm, 300 mm and 425 mm away from the pile surface were 14.5 °C, 10.6 °C, 6.50 °C, 3.64 °C and 1.68 °C respectively. Hence, the temperature reached a relatively stable state at approximately 300 mm on both sides, which was as twice as the pile diameter.

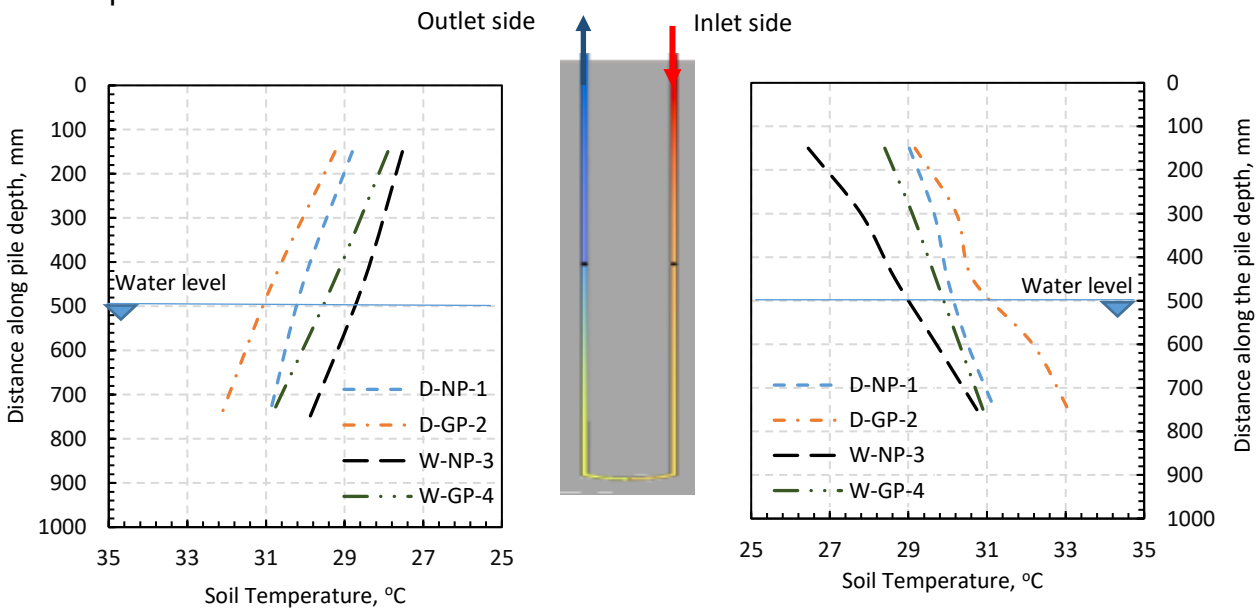

Fig. 3.10. Vertical temperature profile of the soil at 100 mm away from the pile.

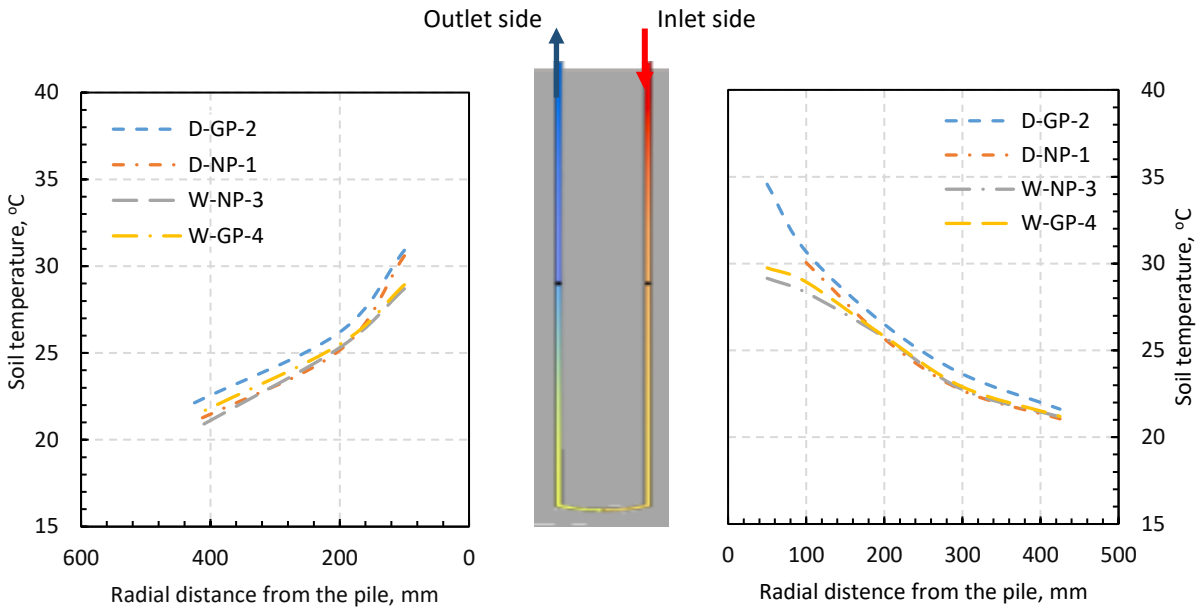

Fig. 3.11. Soil horizontal temperature profile at mid-height of the pile.

Fig. 3.12a and b showed the lateral earth pressure measured at mid-height of the pile. The lateral pressure cell was placed at the pile-soil interface of the pile in the inlet side. The data were captured from tests on geo-energy piles made from normal concrete and graphTHERM concrete and installed in dry sand and partly saturated sand. The initial values of the lateral earth pressure were approximately 4.8 kPa and 5.79 kPa on piles installed in dry and partly saturated sand beds respectively. The lateral earth pressure was slightly increased by circa 10 Pa after running the experiment for 20 h. This could be attributed to the induced thermal expansion due to heating that in turn led to an increase in the lateral earth pressure at the soil-pile interface. To ascertain the observed behaviour, the thermal strain due to thermal expansion of the pile was calculated in accordance with EN 1992-1-2 as given by Eq. (3.3).

$$\varepsilon_{thermal} = \Delta T * CTE \tag{3.3}$$

where; CTE is the coefficient of thermal expansion for concrete and ΔT is the temperature difference on concrete which was measured during the test. To accurately calculate the thermal strain, it was crucial to determine the coefficient of

thermal expansion. Experiments were conducted in accordance with TI-B 101 (94) on samples of normal concrete and graphTHERM concrete with an optimum percentage of graphTHERM. The coefficient of thermal expansion was found to be 2.002 x 10^{-6} $^{o}C^{-1}$ and 5.024 x10^{-6} $^{o}C^{-1}$ for graphTHERM concrete and normal concrete respectively. Fig. 3.13 illustrates that the increase in pile temperature led to an increase on the thermal strain. The calculated thermal strain of the normal concrete pile was 45% higher than that for the graphTHERM concrete pile. This could be attributed to the coefficient of thermal expansion of the normal concrete which was determined experimentally and found to be about 2.5 times greater than that measured for graphTHERM concrete.

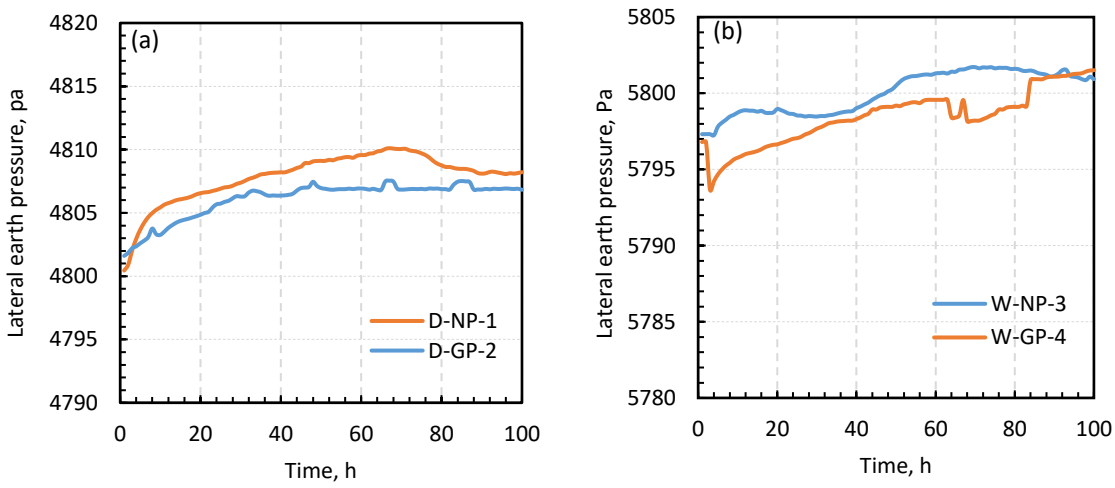

Fig. 3.12. Lateral earth pressure for (a) dry soil tests and b) partly saturated soil tests.

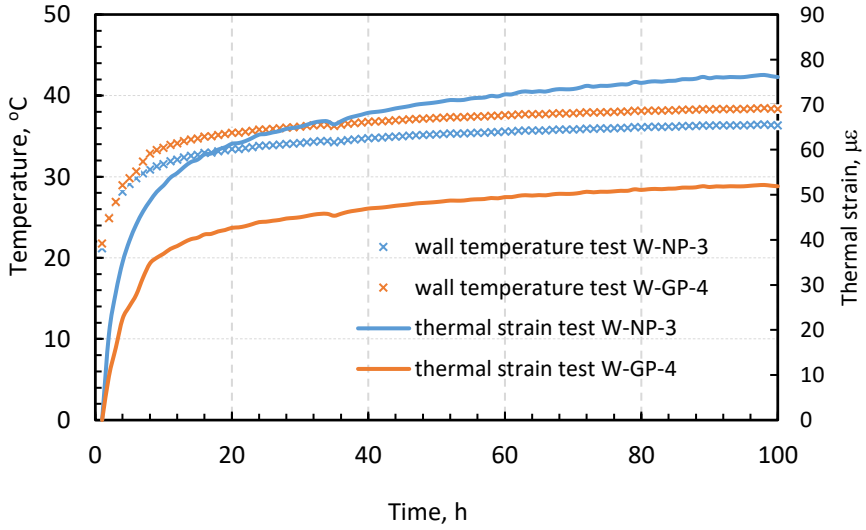

Fig. 3.13. Pile temperature against thermal strain for W-NP-3 and W-GP-4.

3.3.3.2 Heat transfer through geo-energy walls

Tests W-NW-1 and W-GW-2 were carried out using geo-energy walls made from normal concrete and thermally enhanced concrete, installed in partly saturated sand. Temperature measurements taken for the circulating fluid were recorded at the inlet and outlet points of the heat exchanger. Fig. 3.14 presents data for the inlet-outlet temperature difference measured on normal and graphTHERM concrete geo-energy wall. The data evidently demonstrate that the graphTHERM concrete wall (W-GW-2) produced a higher temperature dissipation of 9.67 °C compared with a temperature difference of 6 °C dissipated by the normal concrete wall after reaching steady state conditions. These results illustrate that the thermal performance of geo-energy walls increases by 66% when graphite concrete was used. This may be attributed to the fact that inclusion of graphite powder in the concrete contributed significantly to fill the tiny voids with highly thermal conductive material resulting in a considerable reduction in the degree of porosity and improvement in its thermal conductivity as suggested by (Arora et al., 2018). This led to the dissipation of more heat to adjacent soils which in turn enhanced the performance of heat pumps.

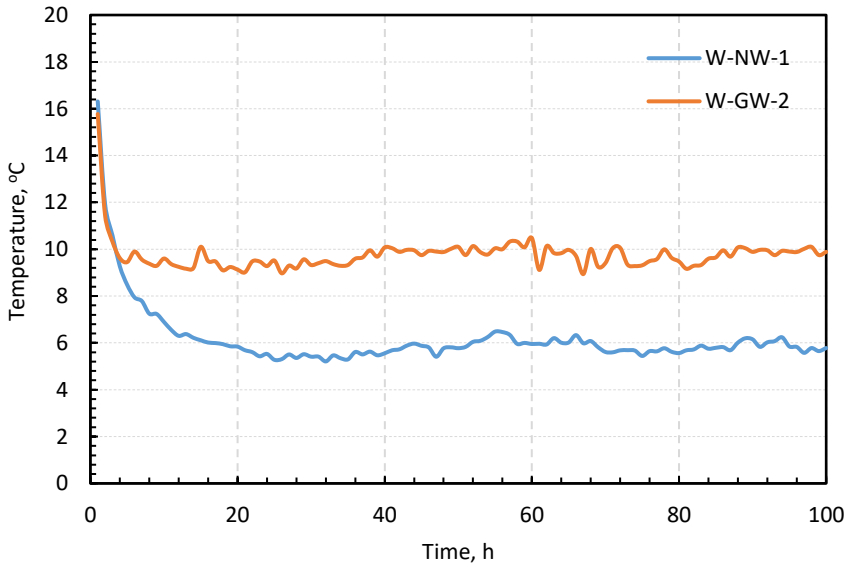

Fig. 3.14. Temperature difference (inlet-outlet).

In addition to measuring inlet and outlet temperatures, temperature measurements were taken at 4 more points: P1, P2, P3 and P4 at a distance of 900 mm, 2950 mm, 4950 mm and 6950 mm along the 9900mm long heat exchanger

(see Fig. 3.4c). Fig. 3.15a and b shows data for the temperature measurements at the six points from tests on geo-energy walls made from normal concrete and thermally enhanced concrete respectively. The results show that the temperature drops from that recorded at the inlet T_i was almost the same in both tests W-NW-1 and W-GW-2. The measured fluid temperature was reduced by about 11% at P_1 and 70% at P_4 as illustrated in Table 3.6. The fluid temperature gradient along the embedded heat exchanger was considered to decline uniformly.

Table 3.6. Circulating fluid temperature along the heat exchanger.

TEST CODE	INLET POINT	POINT 1			POINT 4			OUTLET POINT	
	T_i	T_1	Δt_1	HD	T_4	Δt_4	HD	T_O	Δt_6
	°C	°C	°C	%	°C	°C	%	°C	°C
W-NW-1	53.81	53.05	0.76	13	50.29	3.52	61	47.98	5.82
W-GW-2	52.35	51.45	0. 90	10	46.16	6.19	67	42.67	9.67

where; Ti = inlet temperature, T_1= liquid temperature at 900 mm, T_4= liquid temperature at 6950mm, T_O=outlet temperature, $\Delta t_1 = T_i - T_1$, $\Delta t_4 = T_i - T_4$, $\Delta t_6 = T_i - T_O$, HD = percentage of heat dissipation.

The vertical soil temperature profiles measured at two vertical sections V1 and V2, located at 100 mm and 300 mm away from the experimented energy wall as shown in Fig. 3.3. Measurements of temperature along V1 were taken at a depth of 150 mm, 300 mm, 450 mm, 600 mm, and 750 mm, while those along V2 were recorded at 150 mm, 450 mm and 750 mm. Data for the temperature measurements taken at two vertical sections namely V1 and V2 were plotted in Fig. 3.16 after reaching steady state conditions. The data show clearly that the soil temperatures at section V1 were significantly higher than those measured further away at section V2. Furthermore, it can be observed that the influence of the graphTHERM concrete energy wall (W-GW-2) on the soil temperature was significant in comparison with that produced by the geo-energy wall made from normal concrete (W-NW-1). This reflects principally the ability of each type of wall to dissipate heat into the surrounding soil. Eq. (3.2) was used to calculate the dissipated heat from the energy walls and found that, W-GW-2 dissipated heat of about 665.53 watts, while W-NW-1 dissipated 400.53 watts. Hence, the graphite concrete wall dissipated more than 50% heat to adjacent soils which would result in a higher temperature variation in the surrounding soils.

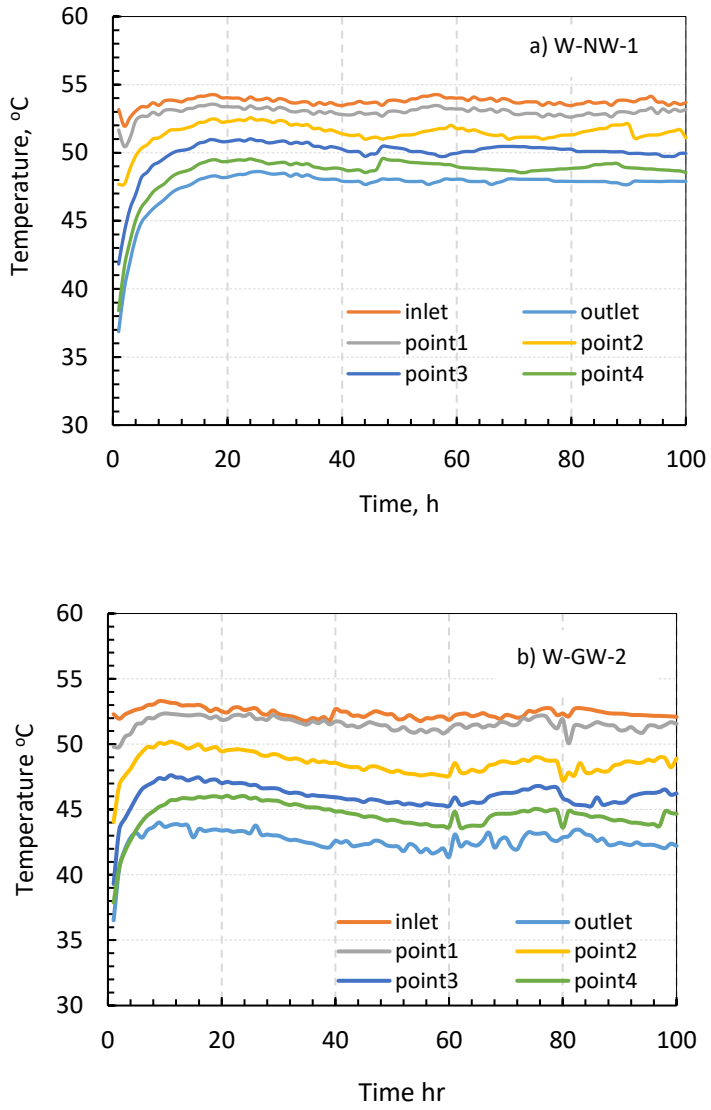

Fig. 3.15. Circulating fluid temperature along the heat exchanger a) normal concrete wall and b) graphTHERM concrete wall.

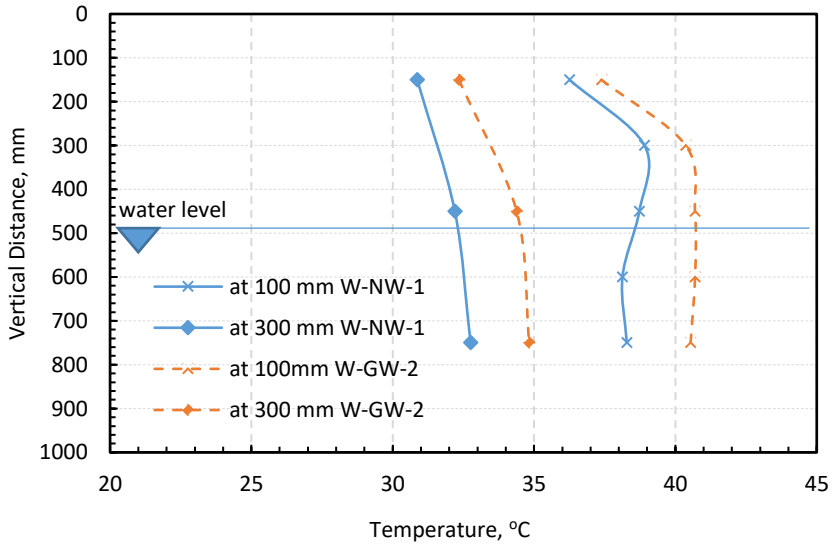

Fig. 3.16. Vertical soil temperature profile for W-NW-1 and W-GW-2.

The horizontal soil temperature profile measured at mid-height of the wall is presented in Fig. 3.17. Soil temperature was measured at 50 mm, 100 mm, 200 mm, 300 mm, 400 mm, 500 mm, 600 mm and 880 mm away from the wall. It was observed that an interference region between the wall and soil can be considered as the most affected region in the experimental tank. From the results of the two tests, a soil-wall interference region was identified to be around 400 mm. Initially, the soil temperature was 21°C which was increased intensely to reach almost 41.5 °C at 50 mm away from the wall after reaching steady state conditions for graphTHERM concrete wall. For the same measurement point the temperature gradient reduced by 2 °C to be almost 38 °C when the normal concrete was used. The figure also indicated the steady state soil temperature reduced when increasing the horizontal distance from the wall.

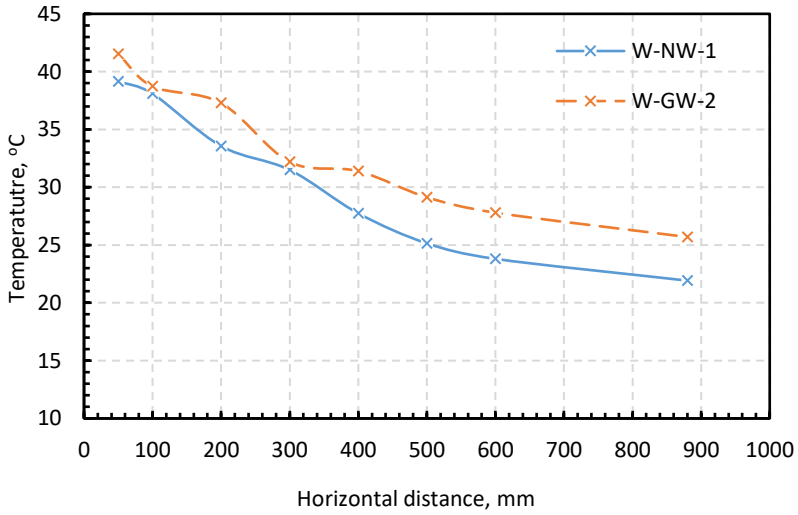

Fig. 3.17. Horizontal soil temperature profile for W-NW-1 and W-GW-2.

Fig. 3.18 shows the measured lateral pressure at mid-height of the wall in case of a normal concrete and graphite concrete wall. The experimental results are evidence that heating the geo-energy wall induced thermal expansion which in turn increased the lateral earth pressure applied on the wall surface. In other words, the lateral earth pressure increased with the increase in wall temperature irrespective of the concrete type until reaching almost a constant value after running the tests for 40 hours. The maximum lateral earth pressure was double that measured at the onset of the experiment. According to Dong et al. (2019), the

increase in lateral earth pressure could have a significant contribution to the vertical stress within a wall. In the case of the graphTHERM concrete wall, the excess lateral earth pressure was 8 kPa to 13.8 kPa whilst for normal concrete wall, 8 kPa to 15 kPa. The results suggest that the graphTHERM concrete wall produced 8% lower lateral earth pressure than that measured on a normal concrete wall. To explain this behaviour, Eq. (3.3) was utilised to determine the thermal strain for both walls as a function of temperature. Data for the thermal strain were presented in Fig. 19 and demonstrate that when the temperature of the wall increased, the correspondingly strain increased. For normal concrete wall the maximum thermal strain was founded to be 119 με while for the grapTHERM concrete wall, the maximum thermal strain was reduced by 41% to 84 με. This suggested that the Coefficient of thermal expansion for graphTHERM concrete is 2.5 times less than that measured for the normal concrete. In contrast with the pile, the wall generated a higher lateral earth pressure which could be attributed to the relative volume of concrete used for the construction of pile and wall. So, the pile, when subjected to thermal load, would slightly expand, but due to the cylindrical shape of the pile, adjacent sand would arch around it partially absorbing the effect of thermal expansion. Whereas, in case of geo-energy walls, the lateral expansion is greater than that observed on piles and the whole wall would push the sand unidirectionally, thus producing a higher lateral earth pressure. One should note that it is essential that further investigations are carried out to evaluate the effect of graphTHERM concrete on the thermally induced elongation for geo-energy piles and walls and the thermally induced bending for the geo-energy wall to be in line with the recent studies on concrete geo-energy structures by (Nicholison et al., 2014; Mimouni and Laloui., 2015; Loria and Laloui. 2016; Loria and Laloui.2017; Pagol et al. 2018; Dong et al. 2019; Loveridge et al.2020; Ravera et al. 2020; Loria, 2020; Shao et al. 2021 and Sailer et al. 2021).

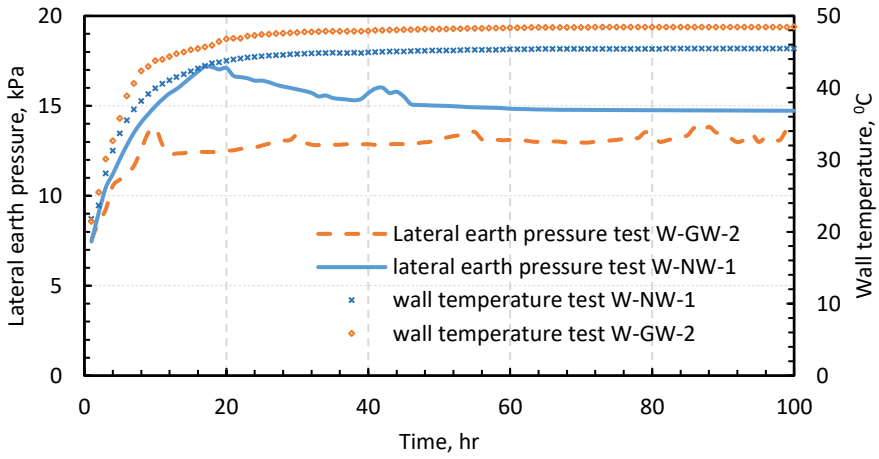

Fig. 3.18. Lateral earth pressure on walls made out of normal concrete and graphite concrete.

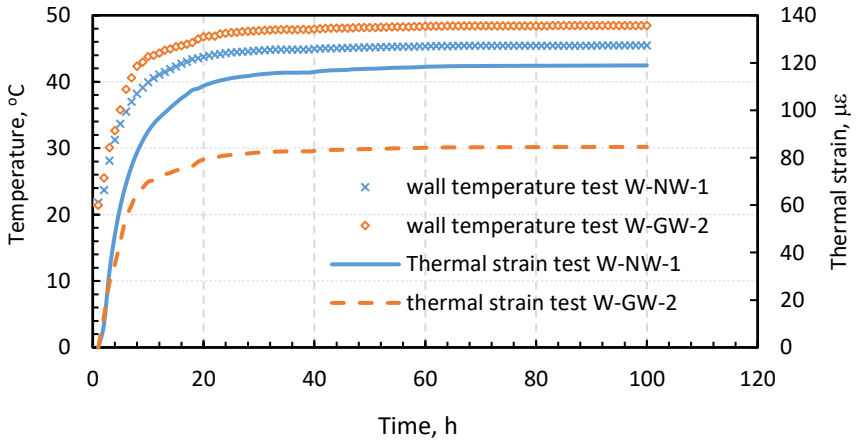

Fig. 3.19. Wall temperature and thermal strain versus time.

3.4. Summary and findings

A comprehensive experimental investigation was carried out to assess the influence of using thermally enhanced concrete in the construction of two geo-energy structure applications e.g. energy piles and energy diaphragm walls. Based on the experimental results, the following conclusions could be drawn out;

- The thermal conductivity of graphite-concrete was significantly improved in comparison to that obtained for normal concrete under the same environmental temperature. An improvement of about 11%, 45%, 83%, 100% and 115% was recorded when 10%, 20%, 30%, 40% and 50% of graphTHERM powder was added to the concrete respectively.

- Considerable improvements in the compressive strength of concrete was achieved when grahpTHERM powder was added to concrete. The peak for the compressive strength of graphite concrete was recoded with the addition of 10% graphite powder. Adding more than 45% of graphite powder to the concrete resulted in achieving a compressive strength that was lower than that of normal concrete.

- The results suggested that adding 36% of graphite powder to the concrete enhanced the thermal conductivity by 100% in addition to achieving 10% higher concrete compressive strength.

- The thermal performance of energy pile was remarkably improved by incorporating graphTHERM into concrete whether placed in dry or partly saturated sand. The degree of improvement was found to be 31% and 50% when the geo-energy pile was installed in dry and partly saturated sand respectively.

- The thermal efficiency of geo-energy wall diaphragms was increased by 66% when graphTHERM was added to the concrete.

- The stiffness of the graphTHERM concrete was higher by 15% more than that measured for normal concrete.

- The coefficient of thermal expansion of graphTHERM concrete was found to be 2.5 times less than measured for normal concrete. Therefore, the graphTHERM concrete geo-energy structures would experience less thermal expansion which in turn could lead to less lateral earth pressure.

Chapter 4: Feasibility of using Geo-polymer concrete for Geo-energy piles and walls applications

4.1 Highlights

- The geopolyemer concrete can be used as sustainable concrete for the construction of the geo energy structures due to its ability to produce less co_2 emissions.
- Electric arc furnace slag (EAFS), can be used to produce a higher thermal conductivity geo- polymer concrete.
- The stiffness and the coefficient of thermal expansion (CTE) of geo-polymer concrete were 11% and 17%, respectively lesser than those measured for the same compressive strength normal concrete.
- The heat transfer efficiency of energy pile and energy diaphragm wall made from geo- polymer concrete was improved by 14% and 21% respectively.
- The CO2 emissions associated with the production of geopolymer concrete was 44.5% smaller than that for normal concrete.

4.2 Introduction

Reinforced concrete is typically the most material applied in GES constructions (Brandl, 2006) owing to its ability in providing high heat-conducting and high thermal storage capability. It is well known that cement is the most frequent material used to produce concrete, however, cement is considered a harmful material in terms of sustainability since the production of cement contributes to causing around 6% of the global CO_2 emissions (Amran et al., 2020; Hamada et al.,2020), in addition to consuming a large amount of energy. In order to mitigate such detrimental effects, sustainable alternative materials are incorporated to replace the conventional cement in concrete (Das et al., 2020, Alhawat et al., 2022). Geopolymer (GPC) is a novel construction material that can be applied in engineering applications with a full replacement for cement binder in concrete (Tayeh et al., 2021; Zinkaah et al., 2022). Geopolymer is classified as an inorganic material and belongs to the family of alkali-activated materials, synthesized by activating a variety of raw aluminosilicate materials that are rich in alumina and silica (e.g., fly ash, red mud, slag and metakaolin) through highly concentrated alkali activation to form a polymeric structure ranging from amorphous to semi-crystalline. Geopolymer has effectively replaced conventional cement in various construction

applications such as precast bridge decks, fire resistance material, and pavements. Recently, geopolymer is being gained more attention as an appropriate material for developing sustainable concrete, offering several benefits over conventional concrete in terms of mechanical, durability, high fire resistance and thermal properties. Moreover, geopolymer has exhibited greater environmental performance by minimising footprint emissions in addition to the ability to integrate waste materials as sources for geopolymer (Weil et al., 2009). Despite having similar mechanical and durability properties to those of conventional concrete, the thermal properties, namely thermal conductivity, and specific heat may differ significantly from those found in normal concrete. The thermal properties of concrete are crucial for designing buildings to provide thermal storage as well as restrict or improve thermal movement. The thermal performance of concrete can be affected by changing the quantities of components, which have varied thermal conductivity and thermal specific heat properties. These two characteristics govern the level of heat stored in the material used as well as the heating rate that can be transferred into/out of the material used. Accordingly, relatively limited research has been conducted on the thermal performance of geopolymer concrete. According to the previous finding, geopolymer concrete generally exhibits lower thermal conductivity in comparison with other conventional building materials (Aguilar et al., 2010; He et al., 2020). Rashad et al. (2019) demonstrated that geopolymer mortar had a lower heat conductivity (0.930 W/(m·k) in comparison to cement mortar (1.400 W/(m.K). In a different study, Snell et al. (2017) indicated that the thermal conductivity and the specific heat of geopolymer paste are substantially lower than that found in cement paste and more equivalent to those measured in silica sand and granite. However, the thermal performance of geopolymer is heavily influenced by the characteristics of the materials used (e.g. chemical composition, the quantity of soluble alumina and silica, and the particle size of precursors). Previous studies indicated that the low thermal conductivity of fly ash-based geopolymer, especially in comparison with that found in geopolymer prepared from metakaolin (Kong et al., 2007; Guerrieri et al., 2010; Zhao et al., 2011). This is probably can be attributed to the low porosity and the change in the pore structure of geopolymer matrix. Investigations conducted by Nikliоć et al. (2016) showed that geopolymer paste offered higher thermal conductivity when fly ash was partially replaced by steel slag (up to 40%). This can be clearly

ascribed to the extensive content of iron in steel slag particles, having high thermal conductivity reaching around 15 W/m.K. Conversely, the inclusion of fiber in geopolymer matrix seems one of the most efficient ways to enhance the thermal insulation and reduce the thermal conductivity of geopolymer. Samal et al. (2015) examined the thermal conductivity of several fiber reinforcements in metakaolin-based geopolymer under increasing temperature conditions. The findings indicated that the highest thermal conductivity recorded at 250°C did not exceed 0.700 W/m.K, which is highly comparable to that typically found in conventional concrete (lower than 0.750 W/m.k. This can be explained by the high porosity of fibre, resulting in the existence of high levels of air in geopolymer, and thus reducing the rate of heating transfer through geopolymer. Aside from adding fibre, Lee et al. (2016) stated that adding the aluminium powder to fly ash-based geopolymer can decrease the thermal conductivity and apparent density of the matrix. This is mainly due to the reactions between aluminium powder and sodium hydroxide in geopolymer slurry, forming hydrogen, which in turn results in increasing porous structures inside geopolymer mortar.

Interestingly, the change in thermal conductivity can also be associated with the ratio of Si/Al molar as it tends to rise with increasing Si/Al molar ratios (Kamseu et al., 2012). This mostly is related to increasing the content of silica, which can be useful for enhancing the thermal conductivity by strengthening the produced polysilicates. The thermal conductivity of geopolymer tends to reduce with lower geopolymer density (He et al., 2020). The type of aggregate used in concrete has also a significant impact on the thermal conductivity of concrete. Evidently, lightweight aggregate has lower thermal conductivity due to its higher porosity and reduced density, which is mostly filled by air in concrete, increasing the heat insulation of structures.

The concrete effect on the thermal performance of geo-energy structures has been extensively studied (Li et al., 2018; Kong et al., 2019). The influence of graphite powder on the thermal conductivity was carried out by Li et al. (2018), and the results then used in developing numerical modelling using finite element analysis to investigate the performance of geo-energy piles made of graphite concrete. The results demonstrated the ability of graphite concrete to enhance the heat transfer characteristics of energy piles and showed that a higher graphite

content was more beneficial to the heat transfer process. A similar numerical study was carried out by Kong et al. (2019) on the heat transfer characteristics of graphite concrete to thermally enhance energy in piles. The results indicated that the heat transfer capacity of the graphite concrete energy pile was higher by 6.5% than that measured in a typical concrete energy pile. Nonetheless, there was no evaluation of the effect of this thermal enhancement on the concrete compressive strength, in addition to the lack of physical measurements of the pile performance.

It can be concluded that concrete is one of the key parameters that need to be highly considered during the design of geo-energy structures. Also, geopolymers are thermally stable under exposure to high temperatures. Geopolymer has a low mass loss and a low expansion ratio and thermal conductivity. Furthermore, the thermal characteristics of geopolymers are directly connected to the geopolymer ingredients and raw materials. Accordingly, the literature showed that there are relatively limited studies were carried out on the thermal characteristics of geopolymer concrete, while the applicability of geopolymer concrete as a construction material for geo-energy piles has not been investigated yet, Therefore, the current chapter aims to fill the research gab by experimentally and numerically exploring the potential use of geopolymer concrete in enhancing the thermal performance of geo-energy piles and walls using a large-scale fully instrumented laboratory rig. For comparative purposes, piles and walls were prepared from conventional and geopolymer concretes with similar compressive strengths. Moreover, a 2D finite element model was developed and validated for-geo energy piles using COMSOL Multiphysics by using the data obtained from the experiments.

4.3 Experimental programme

In order to accurately investigate the thermal performance of GPC geo-energy structures, a fully instrumented testing rig was designed and manufactured to run the heat transfer experiments consisting of three main parts, a testing tank, geo-energy structure and a data acquisition system. Details of the materials used in this experimental approach are demonstrated and discussed in the following sections.

4.3.1 Materials

4.3.1.1 Sand

Standard building sand was selected to simulate the ground soil in this experimental study further details about the physical, geotechnical and thermal properties of this sand can be found in and section 3.3.1.1.

4.3.1.2 Normal concrete

The concrete mixtures were designed with water/cement (w/c) ratio of 0.45 to achieve a target compressive strength ranging between 45 - 48 MPa after 28 days. Different samples were prepared to measure the thermal conductivity of concrete, compressive strength, thermal expansion coefficient and stiffness further information about the normal concrete batches is presented in section 3.3.1.2 of this thesis.

4.3.1.3 Geopolymer concrete

The Geopolymer concrete batches were designed to achieve a target compressive strength of 45MPa. The main components used in producing geopolymer mixtures were by mixing fly ash (FA), electric arc furnace slag (EAFS), sodium hydroxide, sodium silicate, coarse and fine aggregates. The FA meets the requirements of BS EN 450-1 and is classified as category N (known as class F according to ASTM 618). Table 4.1 presents the chemical composition of FA used in this study. EAFS is a by-product of steel making, produced during the production of the steel. The chemical composition of EAFS was obtained from the supplier and presented in Table 4.2. The alkaline activator used was consisted of sodium hydroxide (NaOH) with amorality of 14 and sodium silicate solution (Na_2Sio_3), having a ratio of Na_2Sio_3/NaOH. Off note, the NaOH and sodium silicate solution were mixed before being added to the concrete. Additionally, naphthalene named Oscreed 893 superplasticizer and additional water was added to the mixture to improve the workability. The composition of GPC is shown in Table 4.3. Four geopolymer concrete mixes were designed and tested to evaluate the effect of EAFS on the thermal conductivity of geopolymer concrete. For all mixes, the total binders were kept constant of 400kg/m^3. EAFS% was taken

as 0.1, 0.2, 0.3, and 0.4 of the total binders and other proportions were kept constant, with Na_2Sio_3/NaOH ratio of 2.5 as described in Table 4.3. The mixes were prepared with the same fine and coarse aggregates used earlier in normal concrete. Firstly, all dry materials were mixed together for two minutes before adding the alkaline activator, the additional water and superplasticizer for around 5 mins. Then the mix was poured in the moulds prepared to measure the mechanical and thermal properties, namely thermal conductivity, coefficient of thermal expansion, compressive strength, and concrete stiffness.

Table 4.1. Chimical and phisical analysis of fly ash.

Element	Units	Weight	property
Loss in Ignition	%	3.90	
Fineness	%		27.6
Particle Density	Kg/m^3		2304
28 days Activity Index	%		84
90 days Activity Index	%		100
Initial setting time, sample	Minutes		205
Cl	%	0.01	
Sulfuric Anhydride So_3	%	0.78	
Calcium Oxide CaO	%	4.48	
SiO_2, Al_2O_3, FeO_3	%	83.66	
Na_2O	%	2.72	
Magnesium Oxide MgO	%	1.57	
Phosphate PO_4	%	0.35	

Where, activity index is defined by ASTM C 311 (1998), as the ratio of the compressive of mortar mixed with 20% fly ash (by weight of binder) to control mortar.

Table 4.2. Physical and chemical properties of electric arc furnace slag (EAFS)

Element	Units	Weight	property
SiO_2	%	17.96	
Al_2O_3	%	7.96	
Fe/$FeO_/$ Fe_2O_3	%	31.58	
CaO	%	32.52	
MgO	%	4.56	
MnO	%	3.8	
Na_2O+K_2O	%	0.2	
TiO_2	%	0.59	
Relative Density	Kg/m^3		3500
P_2O_5	%	0.58	
SO_3	%	0.25	
Loss in Ignition	%	-	
Specific gravity			3.01

Table 4.3. Mixture properties of GPC and OPCC

Ingredient	OPCC proportions kg/m³	GPC-Mix1 proportions kg/m³	GPC-Mix2 proportions kg/m³	GPC-Mix3 proportions kg/m³	GPC-Mix4 proportions kg/m³
Cement	343	-	-	-	-
Flay ash	-	360	320	280	240
Slag	-	40	80	120	160
NaOH (14 M)	-	66.5	66.5	66.5	66.5
Na_2SiO_3	-	163	163	163	163
Coarse aggregate 10mm	1199	1209	1209	1209	1209
Fine aggregate	783	650	650	650	650
Water	155	20	20	20	20
Super plasticiser	-	10	10	10	10
weight	2480	2518.5	2518.5	2518.5	2518.5

Where, EAFS ratio for GPC-Mix1, GPC-Mix2, GPC-Mix3, and GPC-Mix4 are 0.1, 0.2, 0.3, and 0.4, respectively.

4.3.2 Experimental method

4.3.2.1 Thermal properties of concrete

The Hot plate test was carried out to measure the thermal conductivity of OPCC and GPC samples according to the British Standards - BS EN 12664:2001. More information about this test can be obtained from section 3.3.2.1 of this thesis.

4.3.2.2 Heat transfer experiments

In total 4 experiments were carried out including 2 tests on energy piles and 2 tests on energy walls with the fixed and variable parameters demonstrated in Table 4. 4. The first two tests were conducted on piles using OPCC and GPC as illustrated in Table 4.4. Two more experiments were carried out on energy walls made of OPCC and GPC. It is worth to mentioned that the piles and walls were experimented using the experimental rig that have been explained in section 3.3.3.

Table 4.4. Fixed and variable parameters for GEP and GEW.

Series		Test coding	Fixed parameters	Variable parameters	Notes
GEP	1	OPCC pile	FR = 67 l/h, PSS, IT = 52.49^{O}C, WL=500 mm	OPCC	Normal concrete
		GPC pile	FR = 67 l/h, PSS, IT = 51.67^{O}C, WL=500 mm	GPC	Geopolymer concrete
GEW	2	OPCC wall	FR = 67 l/h, PSS, IT = 53. 78^{O}C, WL=500 mm	OPCC	Normal concrete
		GPC wall	FR = 67 l/h, PSS, IT = 51.59^{O}C, WL=500 mm	GPC	Geopolymer concrete

Where; PSS= Partly Saturated Sand, FR = Flow Rate, WL= Water Level and IT = Inlet Temperature, OPCC= normal concrete, GPC= Geopolymer concrete.

4.4 Assessing CO_2 emissions for OPCC and GPC

The energy that used to deliver the raw materials for OPCC and GPC, is responsible to release CO_2 emissions into the atmosphere. OPC produces a higher emission in comparison with other cementitious materials such as FA, and EAFS. The manufacturing of one kg of OPC produces about 0.73–0.85 gm of CO_2 (Hasanbeigi et al., 2012; Hills et al., 2016; Alsalman et al., 2021). In the current chapter, the value of 0.84 kg-CO_2/kg, was used to calculate the total CO_2 emissions for the production of geo-energy structures (Sanjuán et al., 2020). The other concrete materials such as aggregates and sand are generated relatively low CO_2 emissions. The CO_2 emissions of FA, and EAFS are 0.0196 kg-CO_2/kg, and 0.052 kg-CO_2/kg, respectively. According to several studies (yang et al., 2013; Ghacham et al.,2016). Hammond et al. (2011), the emissions associated with fine aggregate was stated 0.0048 kg-CO_2/kg ,while the coarse aggregate emissions was reported to be 0.0075 kg-CO_2/kg (yang et al., 2013). According the emissions associated with the production, it has been estimated as 0.008 kg-CO_2/kg (yang et al., 2013).

The activating solutions such as sodium hydroxide and sodium silicate, consumes higher energy for their production, and consequently, result in a considerably higher CO_2 emission. Production of sodium hydroxide emissions lead to carbon emission of approximately 1.915 kg-CO_2/kg (Alsalman et al., 2021). This value is computed for 100% concentration of (solids) sodium hydroxide. On the

other hand, production sodium silicate generates lower emissions when compared to that for sodium hydroxide of 1.22 kg-CO2/kg (Alsalman et al., 2021), it is worth to mentioned that this value is for the solid form. Moreover, superplasticizers have an average emission rate of 1.88 kg-CO_2/kg (European Federation of Concrete, 2015). It is worth mentioning that in this study, the emissions related to transportation were assumed to be the same since the materials were collected from similar distances, and thus the impact of such emissions was neglected.

4.5 Numerical model

The physics problem in this numerical model is to simulate the operation of GEP system which can be divided into two categories:

1). Time dependant heat transfer problem, which can be solved to calculate the temperature at each node of the finite element mesh.

2). unsteady fluid flow and convection (forced) problem in pipes, which can be solved by estimating the fluid temperature and the pipe wall temperature along the pipe axis.

In the domains that equipped by solid such as pipe, concrete and soil, pure conduction heat transfer is expected to occur which is governed by the conduction equation in case of no generation of internal heat as following:

$$\rho C_p \frac{\partial T}{\partial t} + \nabla.(-\lambda \nabla T) = 0 \qquad (4.1)$$

Where; $\nabla.$ Represents the divergence operator and λ is the thermal conductivity of the material (pipe wall, concrete and soil). Equation (4.1) is solved for temperature, T. a boundary conditions of a zero-hour temperature of all the module component are applied to the numerical model during the run time and was used to create a matrix which will be solved, for approximately calculate the temperature changes.

The fluid flow and heat transferred from/to fluids in pipes are physically modelled the heat exchanger pipe based in modelling the internal flow and the heat to be transferred through the pipe wall; the solution of the pipe flow and heat transfer problem is provided using built-in equations in COMSOL. In which, pipe flow is evaluated by solving the momentum and continuity equation given by (Branard et al., 1966).

$$\rho_f \left(\frac{\partial_{v\mathcal{F},i}}{\partial t}\right) = -\nabla_{pf} - \mathcal{F}_D \frac{\rho_f}{2dh} |\mathcal{V}_{f,i}|\mathcal{V}_{f,i} \quad (4.2)$$

and

$$\frac{\partial \mathrm{A}_{pi}\rho_f}{\partial t} + \nabla.\left(\mathrm{A}_{pi}\rho_f \mathcal{V}_{f,i}\right) = 0 \quad (4.3)$$

The second term of the right-hand side in Equation (4.2) accounts for pressure drop by viscous shear and the Darcy friction factor f_D represents the pressure drop with respect to the pipe length due to the viscous shear and it can be calculated using Reynolds number, e pipe roughness and dh the hydraulic diameter.

f_D can be assessed using the equation proposed by Churchill, (1997) as following:

$$f_D = 8\left[\left(\frac{8}{R_e}\right)^{12} + (C_1 + C_2)^{-1.5}\right]^{1/2} \quad (4.4)$$

Where; C_1 and C_2 are factors given as:

$$C_1 = \left[-2.457\, ln\left(\left(\frac{7}{R_e}\right)^{0.9} + 0.27\left(\frac{e}{dh}\right)\right)\right]^{16} \quad (4.5)$$

$$C_2 = \left(\frac{37530}{R_e}\right)^{16} \quad (4.6)$$

Equation (4.4) are valid all flow condition, including, laminar or turbulent. Furthermore, e in Equation (4.5) describes the absolute value for pipe surface roughness; and for polyethylene it is given as 3.0 $\times 10^{-6}$m.

Reynolds number, R_e is gives the ratio between the inertial forces to the viscous forces, such that:

$$R_e = \frac{\rho_f \, \mathcal{U} \, dh}{\mu} \tag{4.7}$$

In pipe, the heat transfer is covered by the energy equation as follows:

$$\rho \mathrm{A}_{pi} C_{p,f} \frac{\partial T}{\partial t} + \left(\rho_f \mathrm{A}_{pi} C_{p,f} \mathcal{V}_{f,i} \, . \nabla T \right) = \mathrm{A}_{pi} \, \lambda_f \nabla T + \mathcal{F}_D \frac{\rho_f \mathrm{A}_{pi}}{2dh} \left| \mathcal{V}_{f,i} \right|^3 + \dot{q}_{wall} \tag{4.8}$$

Where; λ_f, $C_{p,f}$ and T are the thermal conductivity, specific heat capacity and temperature of the heat carrier fluid, respectively, and $\dot{q}_{wall}$ denotes to the flux heat per length that extracted or dissipated through the pipe wall to the surrounding domain and given by:

$$\dot{q}_{wall} = U P_p \, (T_C - T_0) \tag{4.9}$$

Where; U is the coefficient heat transfer in the pipe, $P_p = 2\pi r_i$ represents the wetted perimeter and T_C is the temperature of concrete (outer side the pipe surface). Fig.4.1, shows the cross section of the domain of pipe-fluid and demonstrate the temperature gradient across the pipe wall. By considering the internal fluid film resistance and the resistance of the wall, the overall heat transfer coefficientis evaluated as follows:

$$U = \frac{1}{\frac{1}{h_f} + \frac{r_i}{\lambda_p} \ln \left(\frac{r_o}{r_i} \right)} \tag{4.10}$$

Where; h_f is the convection heat transfer coefficient, λ_p thermal conductivity of the pipe and r_i , r_o are internal and external pipe radius, respectively.

$$h_f = Nu \frac{\lambda_f}{2r_i} \tag{4.11}$$

as the ratio of convective to conductive across the pipe wall is given by Nusselt number. And estimated for laminar flow as following:

$$Nu = 1.86 * (R_e P_r)^{1/3} \left(\frac{2r_i}{l}\right)\left(\frac{\mu}{\mu_w}\right)^{0.14} \quad (4.12)$$

Off note, eq (4.12) are valid only with the following condition:

Laminar , $\left\{\left[R_{e_D}\, P_r/(L/D)\right]^{1/3}(\mu/\mu_w)^{0.14}\right\} \geq 2$, uniform surface temperature, 0.48< P_r < 167000.0044 < μ/μ_w < 9.75.

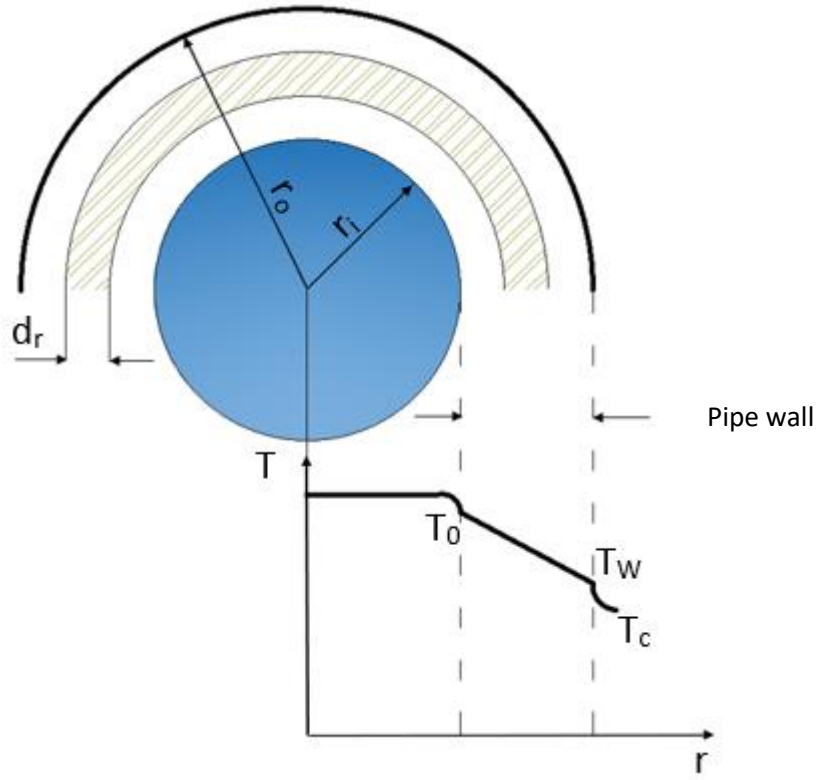

Fig. 4.1. the temperature gradient across the pipe wall.

4.5.1 Geometry and Boundary Conditions

All geometries were assembled with COMSOL as shown in Fig. 4.2 cylindrical concrete pile with a diameter of 150mm and a length of 1m contained a U-shaped heat exchanger with inlet and outlet have been constructed. The inlet and outlet were placed 90^o apart and the heat exchangers were 8mm diameter HDPE tubes with 1mm wall thicknesses placed inside the concrete pile at the centre with a

concrete cover of about 17mm. The distances between the U-tube shanks were kept constant at 100mm, whilst a 425mm ×1000mm soil block was assigned surrounding the pile on the both sides (inlet and outlet side).

The simulation was carried out using finite element mesh with a maximum element size of 0.01 m and a minimum element size of 0.00002 m and a maximum growth rate of 1:1. All boundary conditions were applied using the data collected from the lab experimental data, which were explained previously in section 2.2.3. The ambient temperature of 20^{o}C has been assigned on the top (soil surface) of the module domain while the sides and the bottom have been insulated. Moreover, the inlet temperature and flow rate were kept constant at 53^{o}C and 67l/h, Table 4.5 and Fig 4.2 demonstrate the module parameters.

To simulate the current experimental work two numerical runs were performed, run 1 considers the OPCC geo-energy pile with thermal conductivity of 1.44 w/m.k, whereas run 2 studies the GPC pile with a thermal conductivity value of 1.69 w/m.k. both runs were carried out to simulate the pile operation for 100hrs, and during each run, the increase of soil and concrete temperature and the drop of liquid temperature were calculated.

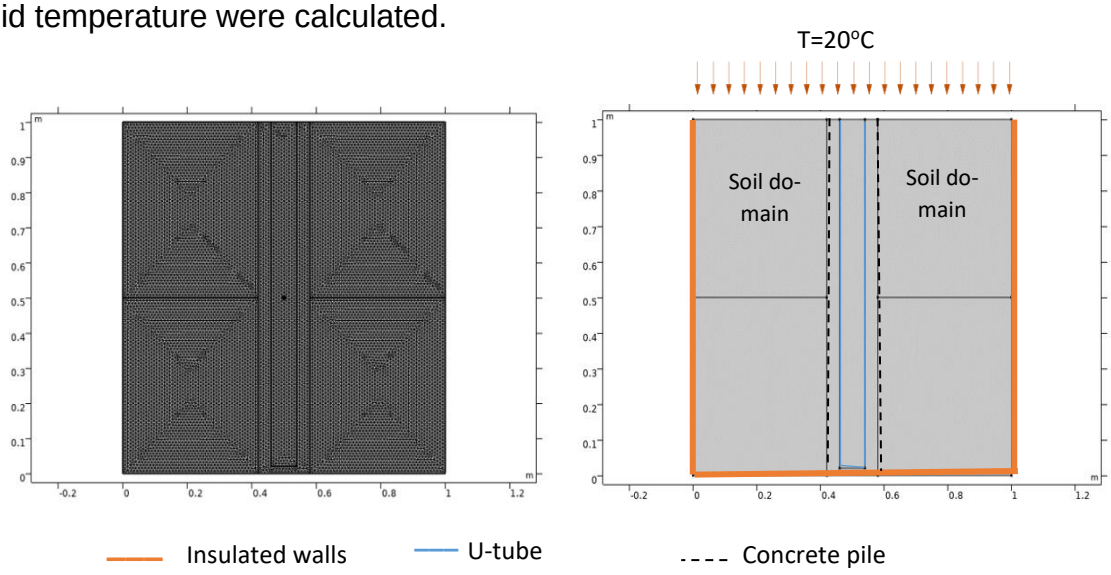

Fig. 4.2. Geometry and boundary conditions of the pile model

Table 4.5. Parameters for the simulation runs.

Parameters	Value	Unit	Note
Initial soil temperature	21	^{o}C	Measured
Coolant inlet temperature, T_i	53	^{o}C	Measured
Soil thermal conductivity, Ks	2.8	w m^{-1} k^{-1}	Measured
Coolant density	1035	Kg m^{-3}	Data sheet

Coolant thermal heat capacity, C_p	3700	J kg^{-1} k^{-1}	Measured
Internal pipe radius, r_i	3	mm	Measured
external pipe radius, r_o	4	mm	Measured
Heat exchanger length, L	1700mm	mm	Measured
Dynamic viscosity, μ	0.0080	Ns m^{-2}	Data sheet
Kinematic viscosity, ư	0.0000076	m^2 s^{-1}	Data sheet
Reynolds Number, R_e	510		Computed
Coolant thermal conductivity	0.457	w m^{-1} k^{-1}	Measured
Pipe thermal conductivity, K_P	0.250	w m^{-1} k^{-1}	Data sheet
Prandtl number, P_r	71		Computed
Nusselt number ($_{laminar}$), N_u	7.029		Computed
Heat transfer coefficient, h_f	527	w m^{-2} k^{-1}	Computed
GPC Thermal conductivity*	1.69	w m^{-1} k^{-1}	Measured
OPCC Thermal conductivity*	1.44	w m^{-1} k^{-1}	Measured
GPC Specific heat capacity	1095.7	J kg^{-1} k^{-1}	Computed
OPCC specific heat capacity	1231.8	J kg^{-1} k^{-1}	Computed
GPC density	2521	Kg m^{-3}	Measured
OPCC density	2480	Kg m^{-3}	Measured

4.5.2 Model application

The 2D numerical model presented above has been utilised to provide a realistic interpretation of the relationship between the thermal conductivity of the concrete and surrounded ground thermal conductivity. This is done through a number of simulations where the thermal conductivity of ground where kept fixed and equal to a value of 2.8 W/mK. And the thermal conductivity of concrete changed between upper limit of Kc=2Ks and lower limit of Kc=0.25Ks. All the other parameters were fixed as shown in Table 4.5. Table 4.6 shows the detailed variable parameters of the simulation runs.

Table 4.6. Parameters values used in the pile simulation.

Run#	Variable Parameter
1	Rc=0.25Rs
2	Rc=0.5Rs
3	Rc=0.75Rs

4	Rc=Rs
5	Rc=1. 5Rs
6	Rc=2Rs

Rc= thermal conductivity of concrete and Rs = thermal conductivity of soil

4.6 Results and discussions

4.6.1 Thermal conductivity, strength, and stiffness of OPCC and GPC

Thermal conductivity and compressive strength results for concrete samples prepared with OPCC and GPC tested at room temperature are illustrated in Table 4.7 and Fig. 4.3. All data presented in Table 4.7 represents the average value of three identical concrete samples. Batch 1 was carried out with OPCC, while batches 2, 3, 4, and 5 were tested with GPC with different ratios of EAFS (0.1, 0.2, 0.3 and 0.4).

According to the obtained results, the thermal conductivity of OPCC is equal to 1.44 W/m.k, whereas for GPC concrete varied between 1.56 to 1.72 W/m.k and reached the peak when EAFS was 0.3 in other words EAFS 30% 0f the total binders. In addition, the thermal conductivity of GPC also increased with increasing EAFS /FA ratio. This increase in the thermal conductivity value could be fundamentally attributed to the higher content of Fe_2O_3 in the EAFS. Zhihe et al. (2014) reported that the higher thermal conductivity of the steel slag is mainly corresponding to the content of Fe_2O_3. Also, Taked et al. (2009) pointed out that the Fe_2O_3 has the higher thermal conductivity among the other synthesized iron oxides (15 W/m.k) demonstrating why slag was previously employed to enhance the thermal conductivity of concrete asphalt mixture (Jiao et al., 2020). The enhancement might also be explained by the higher density of GPC batches, which was 3% higher than made from OPCC, leading to an increase in the thermal conductivity of GPC batches. The relationship between the GPC density and the thermal conductivity was previously discussed by Ali et al. (2020) and Elzeadani (2021), the reduction of concrete density leads to increasing the pore volume of their internal structures, which in turn leads to entrapping air in the mix. Furthermore, data for the influence of EAFS content on the measured compressive strength of GPC after 28 days of air curing were also plotted and presented in

Fig. 4.3 and Table 4.7. It was obvious that the addition of EAFS to the GPC mixes resulted in a considerable degree of improvement in the compressive strength up to EAFS = 0.3, whilst further increase in EAFS content led to a gradual decline in the measured compressive strength. Strengthening GPC by the incorporation of slag was previously reported by Farooq et al. (2021), increasing EAFS content can trigger the increase in the compressive strength of Na_2Sio_3 and NaOH due to the presence of Ca^{+2} ions, which react with the alumina and the silica to form C-A-S-H gel in addition to C-S-H.

Table 4.7. Thermal conductivity of OPCC and GPC batches.

Batch number	EAFS ratio	Room Temperature °C	Thermal Conductivity W $m^{-1}K^{-1}$	Compressive strength MPa
1	-	24.4	1.44	45
2	0.1	24.5	1.56	41.2
3	0.2	24.1	1.61	43.4
4	0.3	24.0	1.69	45.6
5	0.4	24.4	1.72	42.5

Moreover, alkaline activator reaction with the slag considered as an exothermal reaction because heat is generated during the geopolymerization process. Therefore, the increase of EAFS content increased the compressive strength of GPC. Also, it has been reported that the GPC compressive strength improvement with slag addition could be attributed to the formation of gel phase (C-S-H and A-S-H) and the compactness of microstructure (Kumar et al., 2010).

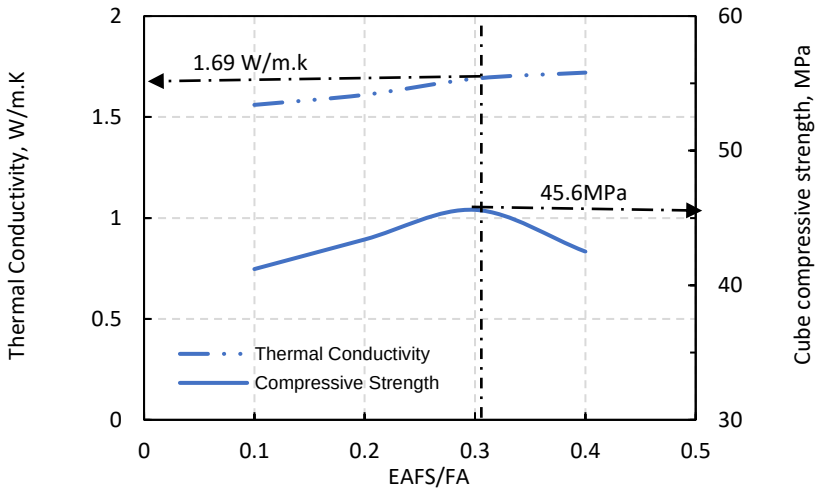

Fig. 4.3. GPC thermal conductivity and compressive strength with respect EAFS/FA ratio.

Due to the sensitivity of the concrete stiffness to the thermo-mechanical behaviour of geo-energy structures. The stiffness of OPCC and GPC batch 4 was measured on cylindrical samples with a diameter of 150 mm and length of 300 mm. Samples were cured in a water bath for 28 days and air dried for 24 hours prior to testing. Strain gauges were fastened on the sample surface in the longitudinal direction as shown in Fig. 4.4 (a) and Fig. 4.4 (c). Fig. 4.4 (b) shows recorded data for the applied stress and measured strain on samples made from OPCC and GPC. The compressive strength presented in Fig. 4.4 (b) is cylindrical compressive strength. The modulus of elasticity (E) was determined from the measured data in accordance with EN 1992-1-2, (2004). The results reveal that the stiffness of the OPCC and GPC was 28.2 GPa and 25.6 GPa, respectively. It is clear that the stiffness of OPCC concrete was 11% greater than that measured for the GPC. This could be caused by the proportion of coarse and fine aggregate in the GPC mixes, which was 6% less than the proportion in OPCC. Nikbin et al. (2014) and Neupane (2016) found a significant increment in the modulus of elasticity with the increase of the proportion of aggregate in GPC mixes.

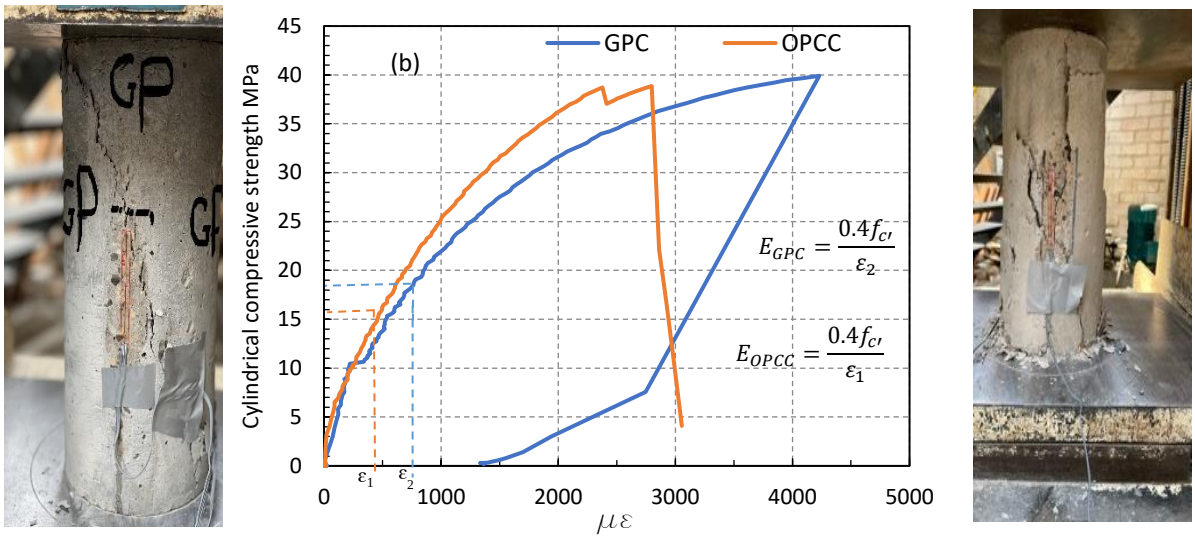

Fig. 4.4. Measured stiffness for OPCC and GPC.

4.6.2 Pile heat transfer tests

For the two pile tests, the circulating fluid temperature was recorded at the inlet, outlet and T_1 points of the HE embedded in the model geo-energy pile as it can be seen in Fig. 3.3b. The inlet-outlet temperature difference $\Delta\mathbf{t}$ represents the amount of heat energy dissipated by the pile into the soil. Fig. 4.5a illustrates the temperature difference between the inlet and outlet for the four tests. It can be obviously observed that GPC pile in which the energy pile made of Geopolymer concrete (GPC) gave the highest differences in temperature. On average, a difference of about 2.37 ^{o}C was recorded after reaching steady-state conditions for the GPC pile test. In comparison to the temperature difference measured on the OPCC pile (2.07 ^{o}C), it can be said that almost 14 % improvement in temperature difference between inlet and outlet was reported in the case of using Geopolymer concrete. These results provide reliable proof that the thermal performance of geo-energy pile tends to enhance when the GPC is used, which could be attributed to the higher thermal conductivity value of GPC than that of OPCC as illustrated in Fig. 4.3. Furthermore, Fig. 4.5b and Table 4.8 demonstrate the circulating fluid temperature measured at a certain point named T_1 inside the HE at a distance of 850 mm from the inlet point of 1700 mm HE, a data for the measured temperature at inlet and outlet, the temperature difference from that measured at the inlet point and the percentage of temperature dissipation at T1 after reaching steady-state conditions. The data demonstrate that the fluid temperature flowing

in the HE reduced by about 52 % and 45 % of the total dissipated temperature at point T1.

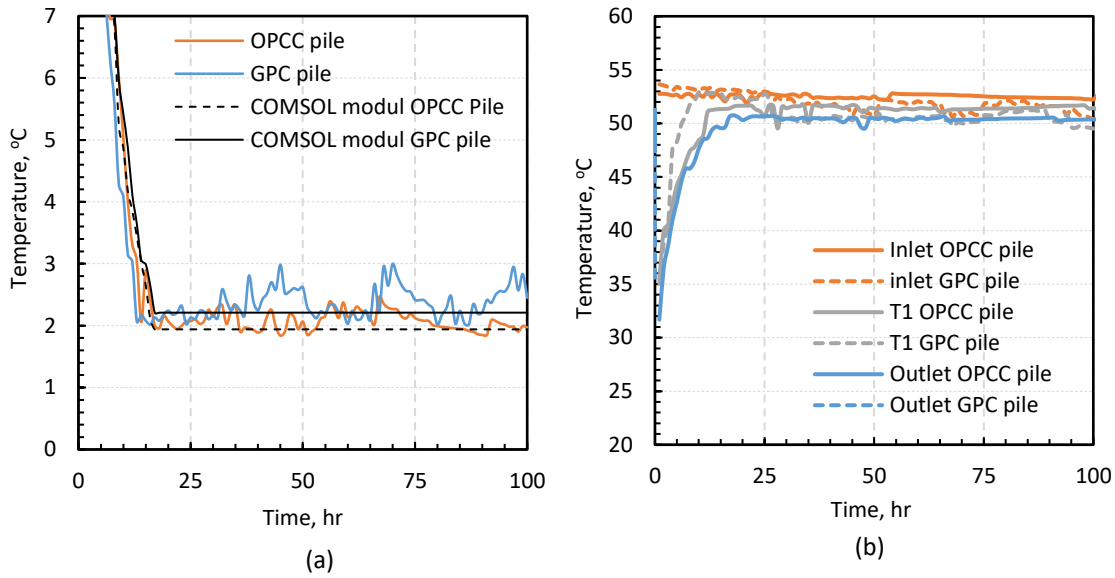

Fig. 4.5. Experimental and numerical temperature difference between inlet and outlet.

Table 4. 8. Circulating fluid temperature along the heat exchanger for pile tests

TEST CODE	INLET POINT	POINT 1 (T_1)			OUTLET POINT		DISSIPATED ENERGY
	T_i °C	T_1 °C	Δt_1 °C	HD %	T_O °C	Δt_{in-out} °C	q watts
OPCC PILE	52.49	51.40	1.09	52	50.41	2.08	143.14
GPC PILE	51.67	50.60	1. 07	45	49.30	2.37	163.10

Where; T_i = inlet temperature, T_1 = Circulating fluid temperature at 450 mm, T_O = Outlet temperature, $\Delta t_1 = T_i - T_1$, $\Delta t_{in-out} = T_i - T_o$, HD = percentage of temperature dissipation, q = dissipated energy.

The heat exchange between the geo-energy structure and soil per unit can be calculated using equation 3.2. It was obvious that the dissipation of heat from the GPC pile is higher than that reported with the OPCC pile by 14%. For OPCC pile and GPC pile, the calculated dissipated heat was about 143.14 watts and 163.10 watts, respectively. As a result of the high temperature gradient between the experimental piles and soil, the soil temperature rapidly increased during the early stage of heating until reaching a certain level, then it maintains almost constant,

showing a steady state. Fig. 4.6 exhibits the change that occurred in the soil temperature in the horizontal direction after reaching steady-state conditions for both piles tests, including OPCC and GPC pile. For both tests, the temperature of sand at the horizontal location was measured at (50mm, 100mm, 200mm, 300mm, 425mm) in both sides of the pile at a constant depth of 450mm from the tank base (see Fig. 3.3b). The maximum temperature change (the temperature at the measured point - initial soil temperature) was observed at 50mm from the pile, recording about 11 ^{o}C and 8 ^{o}C for the GPC and OPCC piles, respectively as seen in Fig. 4.6. This temperature changes then gradually decreased with the increase in the horizontal distance until reaching 1.6 ^{o}C and 1.4 ^{o}C at the boundaries of the experimental tank. In addition, the steady state temperature changes for GPC pile rise by about 8% compared to that of the OPCC pile. This could be attributed to the fact that the amount of dissipated energy from the GPC pile is 14% higher than that found in OPCC pile.

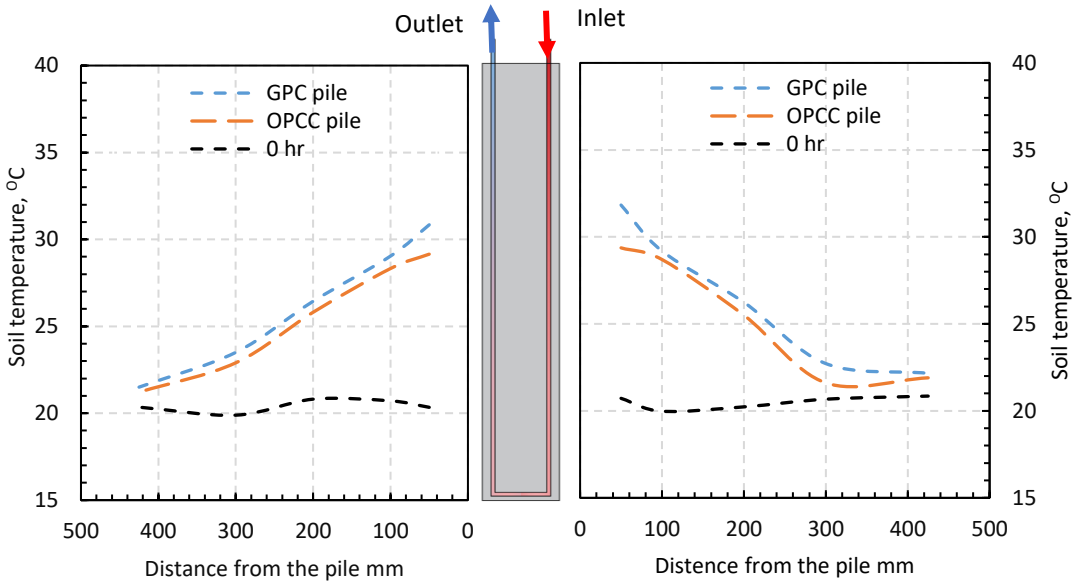

Fig. 4.6.Soil horizontal temperature profile at the mid-height of the pile.

Fig. 4.7 supports the state of increasing soil temperature along with the depth of the pile at predetermined locations at 100mm away from both sides of the pile as shown in Fig. 3.3b. The distribution of the temperature change increased as the depth rose. However, these changes are clearly affected by the water table; in fact, the change in temperature above the water table is more significant than that below the water table. In the case of testing GPC pile, the temperature

change above the WL of soil was 28.30 ^{o}C at 150 mm, 29.47 ^{o}C at 300 mm and 29.73 ^{o}C at 450 mm, whereas below the WL, the temperature changes were less significant, reporting 30.80 ^{o}C at 600 mm and 30.98 ^{o}C at 750 mm. In other words, the temperature of dry/ partially saturated soils showed higher temperature changes compared to those were fully saturated. This can be justified by the fact that saturated sand has greater heat capacity than partially saturated and dry sand. Therefore, it seems that more energy needs to be rejected from the GEP in order to reach the same temperature in the saturated sand (Mohamed et al., 2015; Kramer, 2013; Bao et al., 2019). To confirm this observation, the thermal conductivity and volumetric thermal heat capacity measurements of soil were taken on samples at predetermined heights after the completion of testing GPC and OPCC piles. Samples were extracted precisely at the same predetermined heights to determine water content and density. Fig. 4.8 presents water distribution inside the testing tank, which confirms that sand at the lower half of the tank was fully water-saturated. There was also a significant drop in the degree of sand saturation at 300 mm of the top, turning to an almost dry condition at the surface of the sand. The value obtained from the soil degree of saturation was then used in conjunction to the soil thermal properties provide in Fig. 3.5, to measure the thermal conductivity and heat capacity of the sand along with the tank height, as presented in Fig. 4.8, the measurements revealed that high values of thermal conductivity and heat capacity were stated at the bottom half of the tank, while it gradually reduced towards the sand surface (top of the tank).

Fig. 4.9 shows the lateral earth pressure measured at mid-height of the pile. The lateral pressure cell was placed at the pile-soil interface of the pile on the inlet side. The data was captured from the tests conducted on OPCC and GPC piles, using partly saturated sand. The initial value of the lateral earth pressure was approximately 5.79 kPa. For OPCC pile test, the lateral earth pressure was slightly increased by circa 10 Pa after running the experiment for 20 h to a value of 5.80 kPa, while the later earth pressure for the GPC pile increased by 3 Pa after reaching the steady-state condition. This could be attributed to the induced thermal expansion due to heating, leading to an increase in the lateral earth pressure at the soil-pile interface. To determine the observed behaviour, the thermal strain due to thermal expansion of the pile was calculated in accordance with EN 1992-1-2 as given by Equation 3.3.

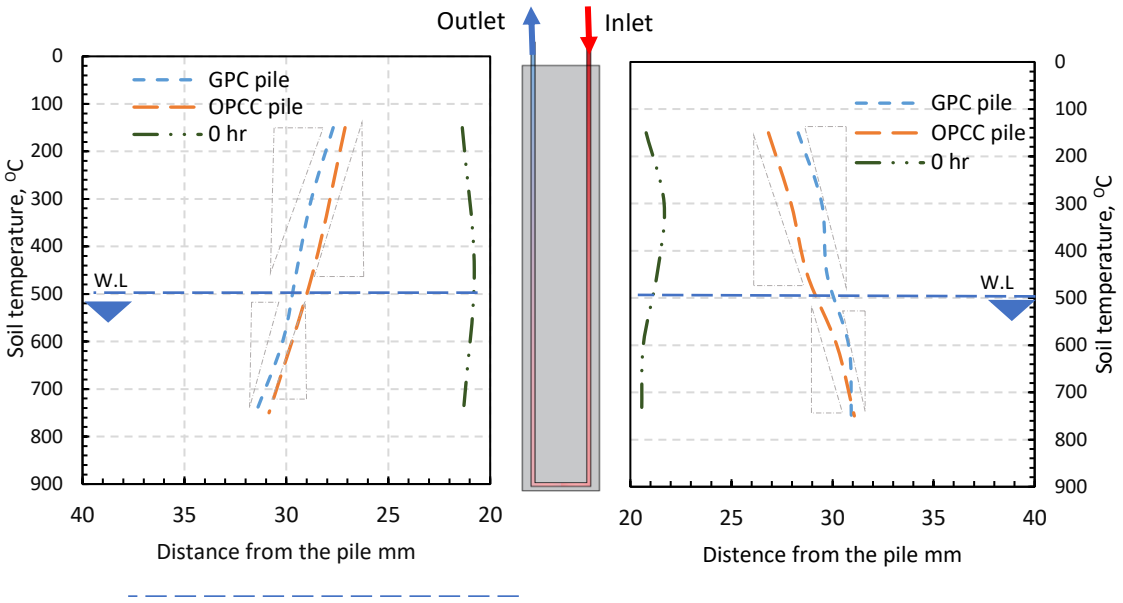

Fig. 4.7. Soil vertical temperature profile at 100mm away from the pile.

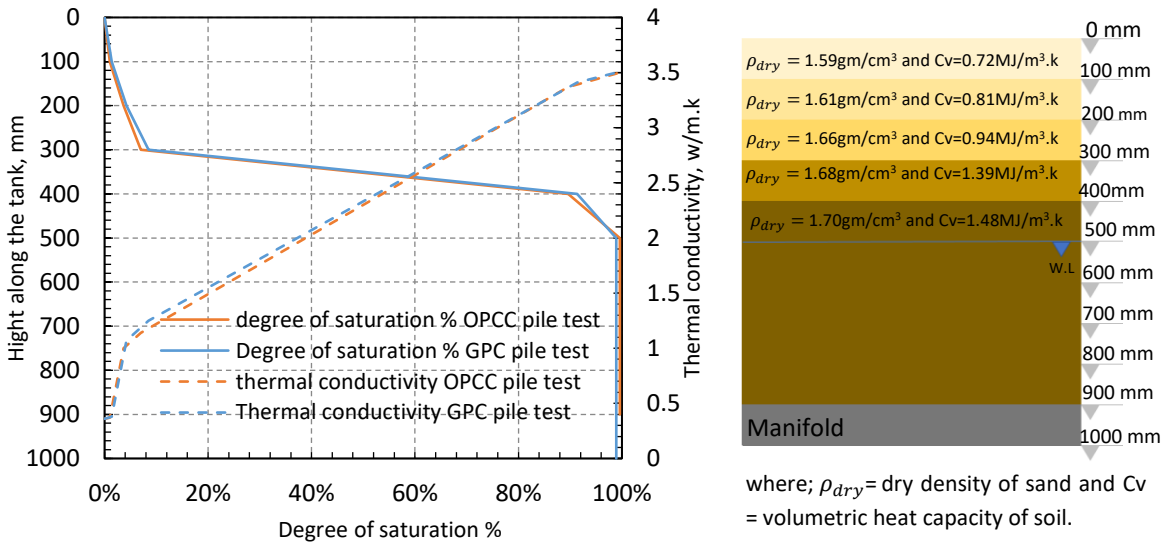

Fig. 4.8. Measured degree of saturation and thermal properties along the experimental tank

To precisely estimate the thermal strain, it was essential to determine the coefficient of thermal expansion. Experiments were conducted in accordance with TI-B 101 (94) on OPCC and GPC samples. The coefficient of thermal expansion was found to be 4.173 x 10^{-6} $^{o}C^{-1}$ and 5.024 x10^{-6} $^{o}C^{-1}$ for GPC and OPCC, respectively. Fig. 4.10 illustrates that the increase in pile temperature led to an increase in the thermal strain. The calculated thermal strain of the OPCC pile was about 2% higher than that measured in GPC pile. This could be attributed to the

difference in CTE between OPCC and GPC, which was experimentally higher in OPCC by 17% in comparison with GPC.

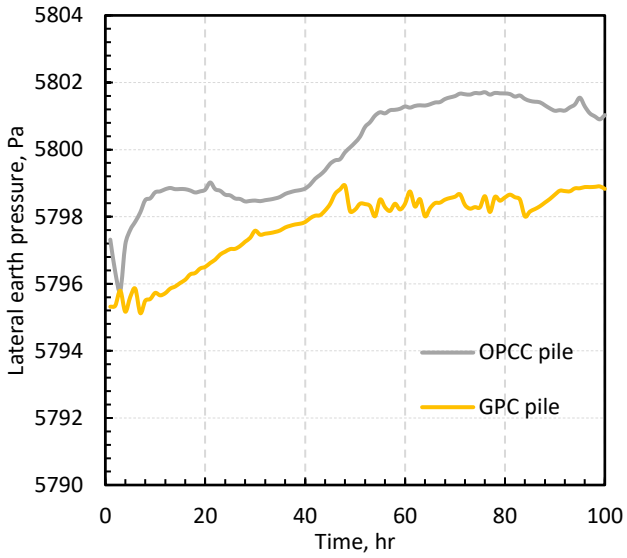

Fig. 4.9.Lateral earth pressure at the pile middle height for OPCC and GPC

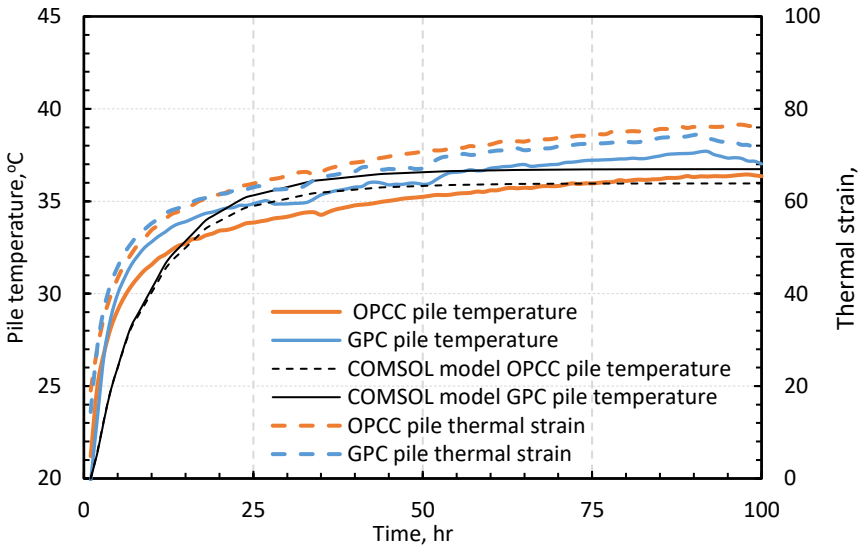

Fig. 4.10.Experimental and numerical pile temperature and calculated thermal strain for OPCC and GPC

4.6.2.1 Validation of pile numerical model

The experimental data of the pile heat transfer tests were utilised to validate the 2D COMSOL pile model. The model was operated for a 100 continuous hrs to evaluate the GEP made of OPCC and GPC. The temperature difference results between inlet and outlet between the modelled data and the experimental data

have been used to assess the model accuracy. For run 1 and run 2, the temperature differences between inlet and outlet were constant of 1.94 ^{o}C and 2.21 ^{o}C respectively, by reaching the steady state. According to the experimental results, the average steady-state temperature difference was 2.07 ^{o}C and 2.37 ^{o}C at the steady-state close, indicating a good agreement in the results. To evaluate the accuracy of the numerical model results, the root mean square error (RMSE) and the maximum error (Errmax) were calculated using Eq. 4.13 and Eq. 4.14, respectively, and the findings were presented in Table 4.9.

$$RMSE = \sqrt{\frac{\left(\Delta_{T\_comsol} - \Delta_{T\_experimental}\right)^2}{n}} \tag{4.13}$$

$$Err_{max} = \frac{\left|\left(\Delta_{T\_comsol} - \Delta_{T\_experimental}\right)\right|}{\Delta_{T\_comsol}} \tag{4.14}$$

Table 4. 9. Δ_T and statistical performance of pile model

Model run	Δ_{T_comsol} ^{o}C	$\Delta_{T\_experimental}$ ^{o}C	RMSE	Errmax
1	1.94	2.07	0.13	0.067
2	2.21	2.37	0.16	0.072

Table 4.9 shows the values of RESE and Err max 7.2% between the COMSOL model and the experimental data. 7.2% maximum error was recorded for run 2 while 6.7% error was found in run 1. These findings showed a strong agreement with the result of the experimental work. The variation of concrete temperature has also been modelled, Fig. 4.10 shows the temperature of concrete variation with time, while Fig. 4.11 and Fig. 4.12 displays the variation of temperature with time for the whole experimental tank (including pile and soil). According to the figures, after one hour of GPC and OPCC GEP continues operation, the temperature of the pile increased by almost 2 ^{o}C, while with further increase in time (e.g., 10 hrs), the change in temperature on OPCC pile was about 8 ^{o}C and for GPC was 9 ^{o}C. By extending the time of running, the pile temperature reached a steady state at 20hrs, then minor changes in the temperature of the pile and soils were noted until the end of the operation. For both runs, a notable excess of GPC

temperature was captured by about 1^{o}C more than OPCC as seen in Fig. 4.10, Fig. 4.11, and Fig. 4.12.

4.6.2.2 The effect of concrete thermal conductivity

The thermal conductivity of concrete has been rated to be the third important parameter that affecting the thermal performance of geo-energy piles (Cecinato and loveridge., 2015). Shafagh et al. (2021) demonstrated that the thermal conductivity of soil is the dominant heat transfer mechanism for buried pipes because it relatively occupied the large volume of the system. Hence, the model has been utilised to provide deep understanding for the relationship between the thermal conductivity of soil and the thermal conductivity of concrete for the geo energy piles applications. The model was simulated for 100h continues operation at constant inlet temperature of 52 ^{o}C and constrained with data presented in Table 4.5.

Simulations were performed for range of concrete thermal conductivities see Table 4.6. the temperature difference between inlet and outlet at each hour of the total run of 100hr, have been calculated and presented in Fig. 4.13. Fig. 4.13 shows concrete thermal conductivity can play an important role in the temperature difference (inlet-outlet) of the geo energy pile. In order to understand Fig. 4.13, the case of Rc=Rs was taken as reference. Below the reference line, the reduction of 25% in thermal conductively (kc) leads to a decrease in $\Delta T_{(in\text{-}out)}$ of about 15%. Whereas further reduction to 75% on Kc value produces 70% reduction in $\Delta T_{(in\text{-}out)}$. On the other hand, above the reference line, an increase of 50% of Kc leads to enhance $\Delta T_{(in\text{-}out)}$ by 35%. Therefore, the results recommended to control the thermal conductivity of concrete to be equal or greater than the value of Ks.

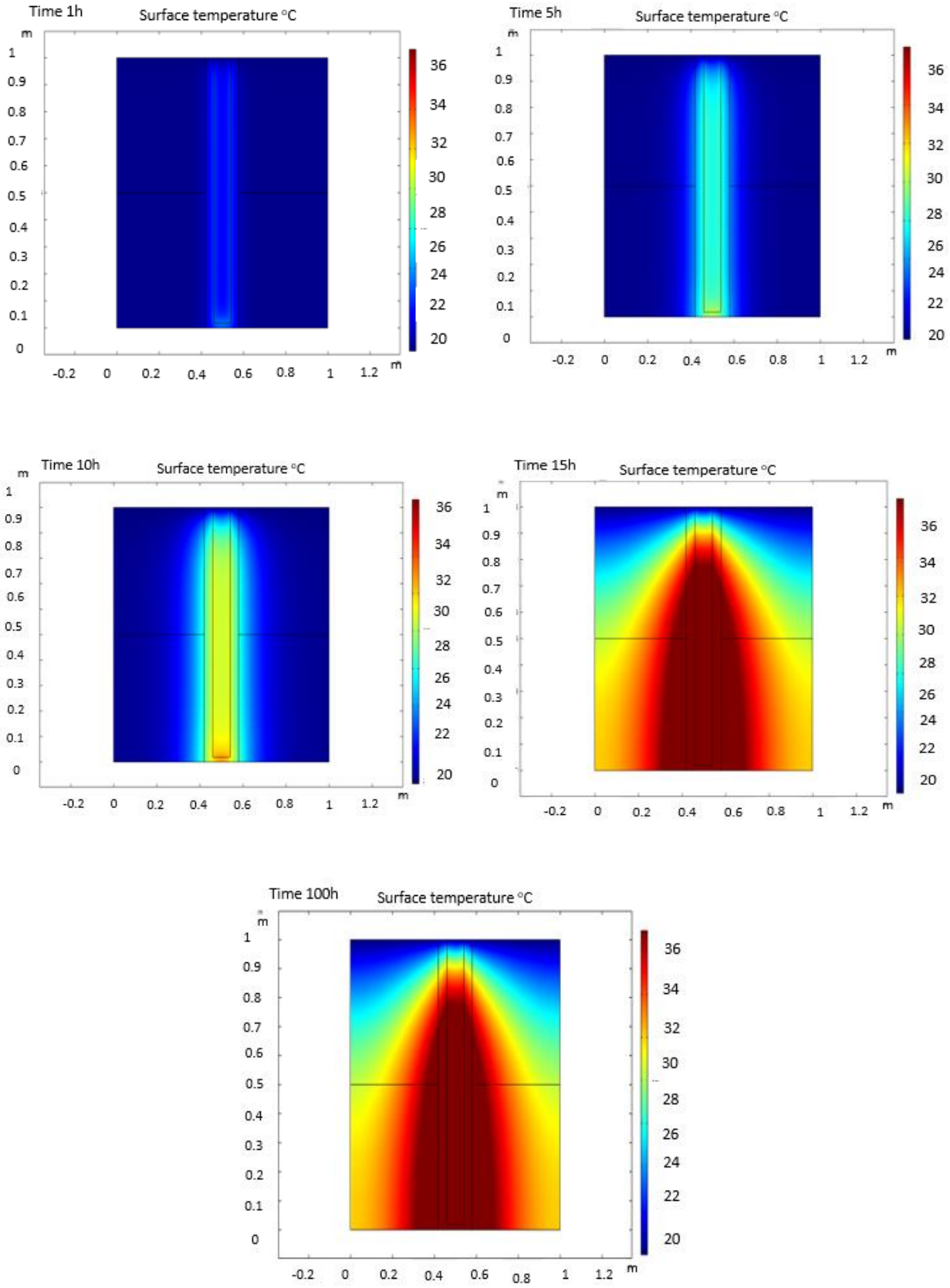

Fig. 4.11. Modelled temperature variation of OPCC pile test

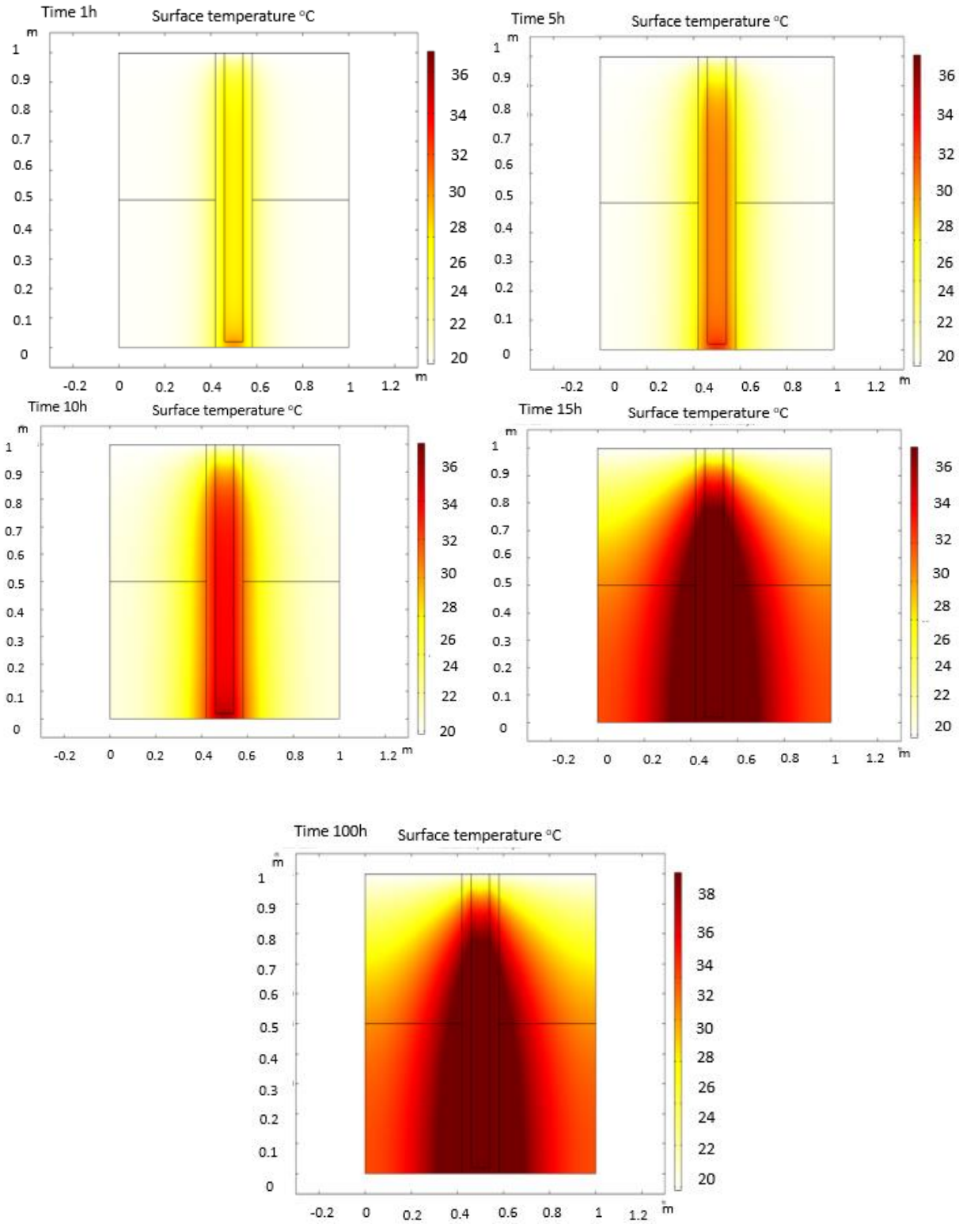

Fig. 4.12. Modelled temperature variation for GPC pile test.

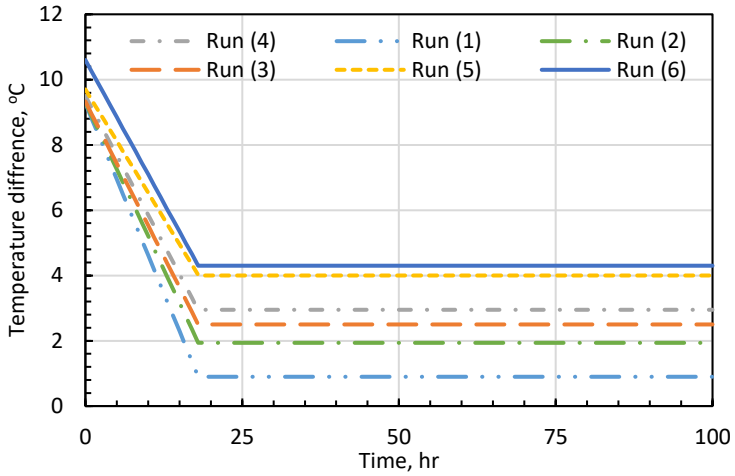

Fig. 4.13. Numerical results for $\Delta T_{(in\text{-}out)}$ with different K values

4.6.3 Wall heat transfer test

To study the thermal performance of geo-energy walls, two tests were carried out; one tested GPC wall and the other conducted on OPCC wall. Both walls were installed inside partly saturated sand. According to Fig. 4.14a, the temperature measurements were taken for the circulating fluid at Inlet, T1, and outlet points of the heat exchanger. The temperature differences between inlet and outlet data for GPC and OPCC walls are presented in Fig. 4.14b. For steady state condition, the data obviously indicated that the GPC wall produced a higher temperature dissipation of 7 ^{o}C compared with the temperature difference of 5.77 ^{o}C dissipated by OPCC wall. These results demonstrated that the thermal performance of geo-energy wall increased by 21% in comparison with wall made out of OPC . This can be justified by the fact that the used GPC can offer higher thermal conductivity than that for OPCC, reporting 17% improvement in the current study. Elkezza et al. (2022) stated that by doubling the thermal conductivity of the concrete used to produce the GEW, the thermal efficiency of the geo-energy wall installed in partly saturated sand would increase by 66% .

The measurement of the liquid temperature was taken at T1, which is located at 4950 mm away from the inlet point Ti (Fig. 4.14b). Fig. 4.14c illustrates data for temperature measurement at 3 points including inlet, T1 and outlet for both types of walls; GPC and OPCC . The results also showed that the temperature dropped

from that recorded at the inlet was almost the same (59% and 61%) in both tests; GPC wall and OPCC wall. As can be Seen from the results presented in Fig. 4.14c and Table 4.10, the fluid temperature gradient along the 9900 mm embedded heat exchanger was considered to uniformly decline. In addition, the heat exchange between the geo-energy wall and the soil was also calculated by equation 3.2, and the results showed that the dissipation heat from the GPC wall was clearly higher than that found in OPCC wall by 20%, while the calculated dissipated heat was 482 W and 400 W.

The vertical temperature profile was measured at two vertical sections (V1 and V2), located at 100mm and 300mm away from the experimented energy wall, respectively as shown in Fig. 3.4. The measurements of temperature along V1 and V2 were taken at depths of 150mm, 300mm, 450mm, and 750mm. The data for soil temperature after steady-state at V1 and V2 were plotted in Fig. 4.15. The data clearly showed that the soil temperature at section V1 was significantly higher than that measured further away at section V2.

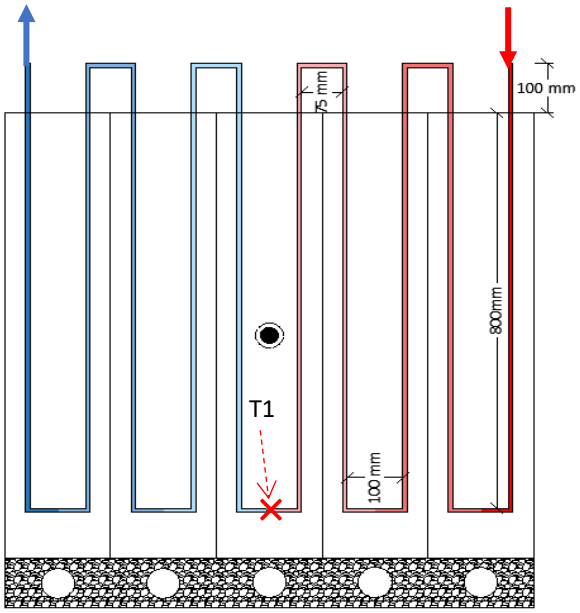

(a)

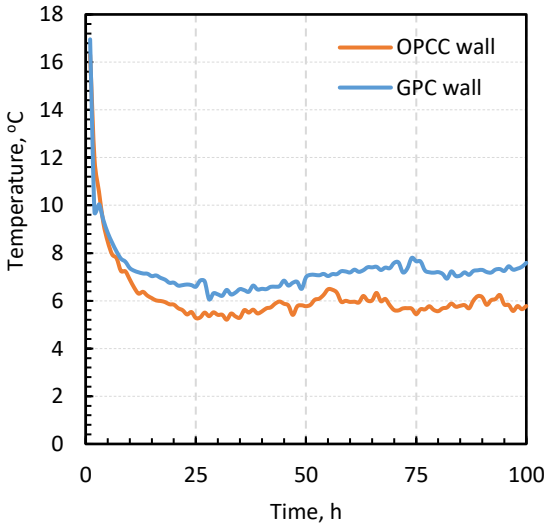

(b)

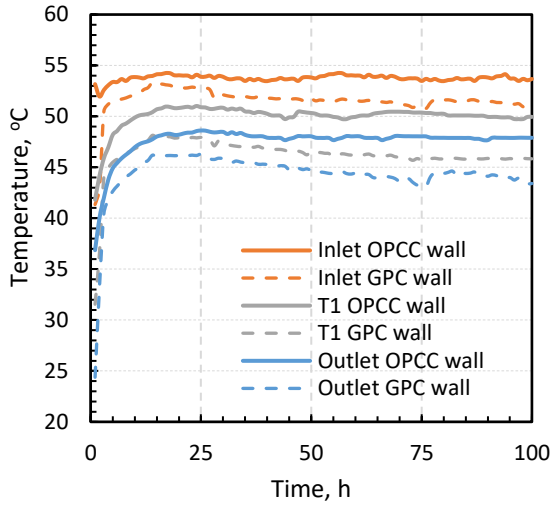

(c)

Fig. 4.14. (a) Cross section of the experimental wall shown the measurement point T1. (b) temperature difference between inlet and outlet. (c) The measurement of the liquid temperature was taken at inlet, T1and outlet.

Table 4.10. Circulating fluid temperature along the heat exchanger for wall tests

TEST CODE	INLET POINT	POINT 1 (T_1)			OUTLET POINT		DISSIPATED ENERGY
	T_i °C	T_1 °C	Δt_1 °C	HD %	T_O °C	Δt_{in-out} °C	q watts
OPCC wall	53.78	50.26	3.58	61	48.01	5.77	400
GPC wall	51.59	46.79	4.10	59	43.51	7	482

Where; T_i = inlet temperature, T_1 = Circulating fluid temperature at 4950 mm, T_O = Outlet temperature, $\Delta t_1 = T_i - T_1$, $\Delta t_{in-out} = T_i - T_o$, HD = percentage of temperature dissipation, q = dissipated energy.

Furthermore, it can also be observed that the influence of the GPC wall on soil temperature was more significant in comparison with that produced by GEP made by OPCC. Fig. 4.15 also indicates that the change of the soil temperature increases with the increase of depth. It is worth to note that the change of soil temperature is significantly affected by water table, and the vertical soil changes above the water table are more significant than below the water level, which can be explained by the higher heat capacity of the fully saturated soil.

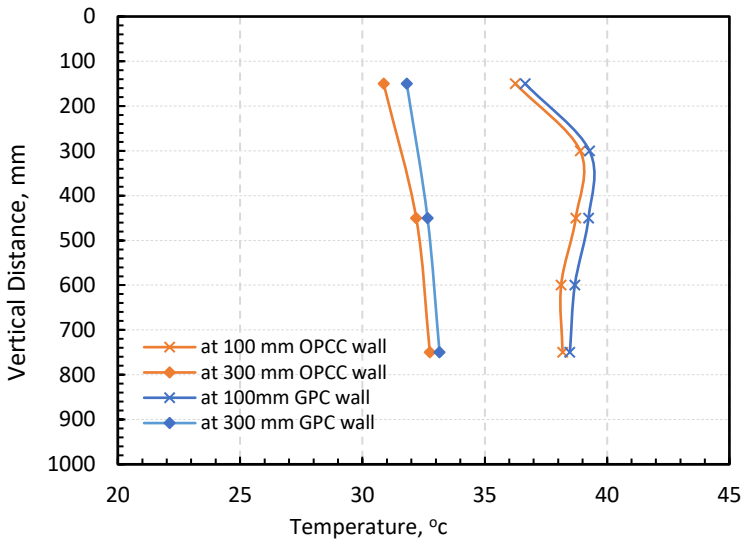

Fig. 4.15. Vertical soil temperature at V1 and V2 for GPC wall and OPCC wall.

The horizontal soil temperature profile measured at mid-height of the wall is presented in Fig. 4.16. Soil temperature was measured at 50 mm, 100 mm, 200 mm, 300 mm, 400 mm, 500 mm, 600 mm and 880 mm away from the wall. Initially, the soil temperature was 21°C, which intensely increased to reach almost 40.1 °C at 50 mm away from the wall after reaching steady-state conditions for GPC wall. For the same measurement point the temperature gradient reduced by 2 °C to be almost 39.1 °C when OPCC was used. The figure indicated the steady-state soil temperature reduced when increasing the horizontal distance from the wall. For instance, the soil temperature in GPC wall at 200mm away from the wall was recorded to be 34.57 °C, whereas further increasing in the horizontal distance 300mm led to a reduction in soil temperature to be 32 °C. Also, it was also observed that the interference region between the wall and soil can be considered as the most affected region in the experimental tank, and the soil-wall interference region was identified to be around 400 mm.

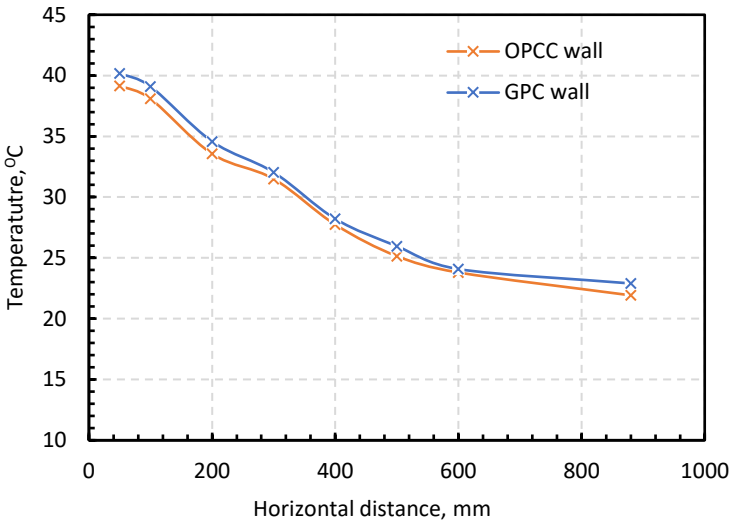

Fig. 4.16. Horizontal soil temperature for GPC wall and OPCC wall.

The measured lateral pressure at mid-height of the wall in case of a GPC and OPCC wall was measured and the results are presented in Fig. 14.17. The experimental results confirmed that heating the geo-energy wall prompted a thermal expansion, which in turn rose the lateral earth pressure applied on the wall surface. In other words, the lateral earth pressure increased with the increase in wall temperature irrespective of the concrete type until reaching almost a constant value after running the tests for 40 hours. The maximum lateral earth pressure was double that measured at the onset of the experiment. According to Dong et al. (2019), the increase in lateral earth pressure might cause a significant contribution to the vertical stress within the wall. In the case of the GPC wall, the excess lateral earth pressure was 7.4 kPa to 14 kPa whilst for OPCC wall, 8 kPa to 15 kPa. The results suggested that the GPC wall produced 6% lower lateral earth pressure than that measured on a normal concrete wall. To clarify this behaviour, Equation 3.3 was utilised to determine the thermal strain for both walls as a function of temperature. The thermal strain results were presented in Fig. 4.18, and demonstrated that when the temperature of the wall increased, correspondingly strain also increased. For OPCC wall, the maximum thermal strain was founded to be 119 με while for the GPC wall, and the maximum thermal strain was reduced by 10% to 108 με , highlighting that the CTE of GPC is 17% times less than the OPCC. In contrast with the pile, the wall generated a higher lateral earth pressure,

which could be attributed to the relative volume of concrete used for the construction of pile and wall. Thus, when the pile subjected to thermal load, it would slightly expand, but due to the cylindrical shape of the pile, the adjacent sand would arch around it partially absorbing the effect of thermal expansion. While in case of geo-energy walls, the lateral expansion was greater than that observed on the piles, and the whole wall would unidirectional push the sand, and thus producing a higher lateral earth pressure (Elkezza et al., 2021).

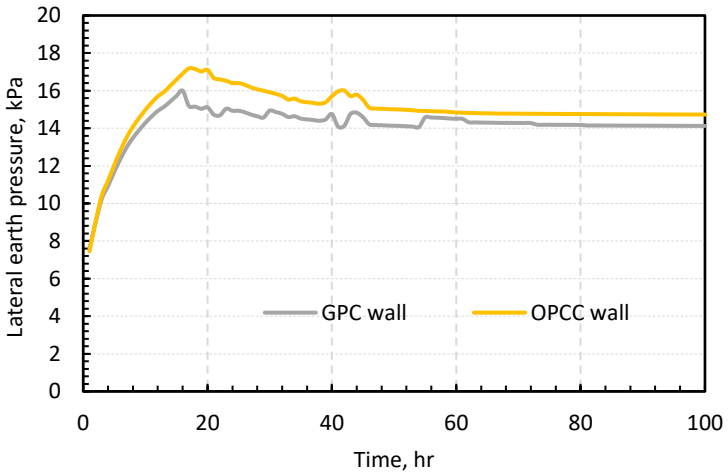

Fig. 4.17. Lateral earth pressure on walls made of GPC and OPCC.

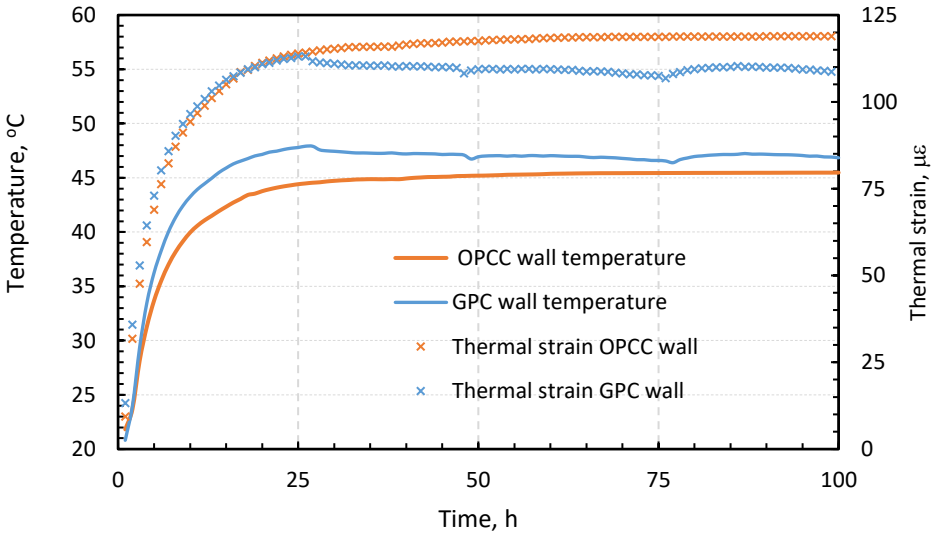

Fig. 4.18. Wall temperature and thermal strain versus time.

4.7 Assessment of CO_2 emissions

Fig. 4.19 presents the estimated emissions resulted from one cubic meter of GPC and OPCC. GPC resulted 44.5% less CO_2 emissions, compared to that for OPCC. The high emissions were mainly credited to OPC (ordinary Portland cement), which responsible for 92% of the total emission of OPCC as shown in Fig. 4.19a. In contrast, the combination of the alkaline activators (sodium hydroxide(NaOH) and sodium silicate (Na_2Sio_3)) occupied 68% of the total emission of GPC as shown in Fig. 4.19b. Na_2Sio_3 itself produces 37% of the total emission. Yang et al. (2013) reported different CO_2 emission values than that reported by Alsalman et al., (2021). According to Yang et al. (2013) the CO_2 emissions produced by one kg of Na_2Sio_3 and NaOH are 1.32 kg-CO2/kg and 1.22 kg-CO2/kg, respectively. If these values of the emission generated from sodium silicate and sodium hydroxide were accounted, the emission of GPC would further be reduced by only 9% compared to those reported by (Alsalman et al., 2021). The binder materials of GPC (FA and EAFS) are responsible for approximately 2% and 5% of the total emission of GPC, respectively. The effect of coarse and fine aggregates on the emission of OPCC and GPC is minimal, whilst the production of Concrete seems does not have a obvious influence on the CO_2 emission generated from OPCC and GPC as shown on Fig. 4.19. Detailed calculations can be found in Appendix B.

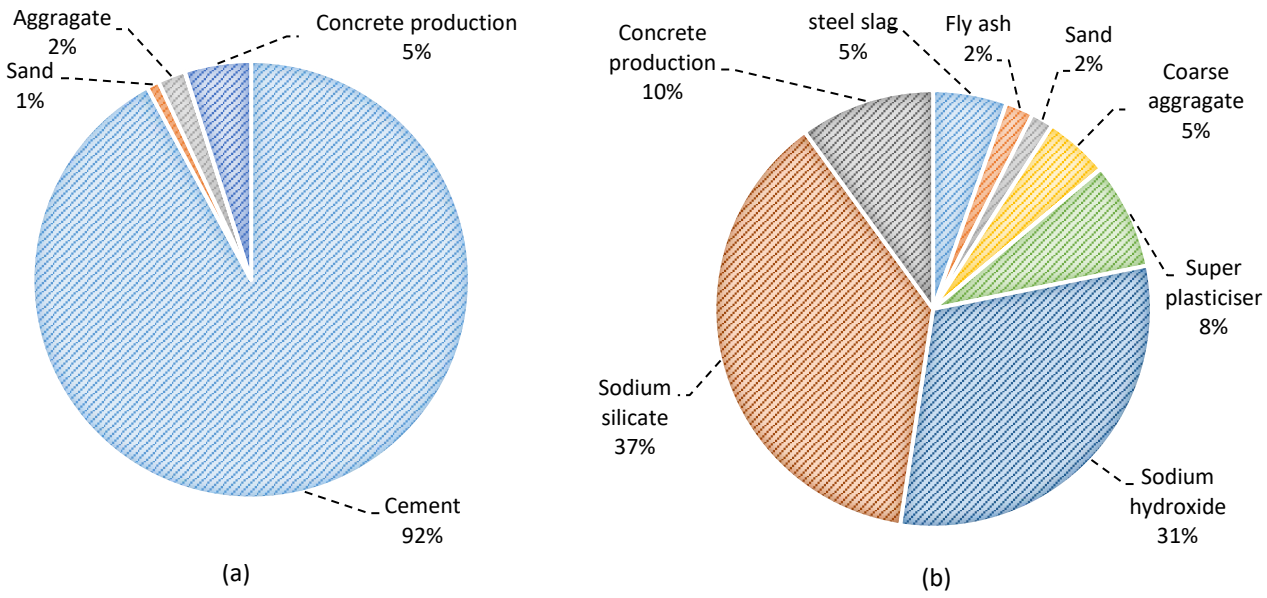

Fig. 4.19. CO2 emissions (a). OPCC and (b). GPC.

4.5. Summary of findings

The thermal performance of GPC geo-energy structures in partly saturated sand was experimentally and numerically investigated and compared with that of OPCC geo energy structures. The environmental foot-print of using GPC for geo-energy piles and walls was also evaluated by calculating the CO_2 emissions, and compared with those resulted from OPCC piles and walls. The following conclusion were drawn:

- The thermal conductivity of GPC was considerably increased with the increase of EAFS percentage and reached the peak when EAFS about 0.3 of the total binders.
- Significant improvement in GPC compressive strength was achieved when EAFS/ FA ratio was increased up to 0.3, while a decline in the measured compressive strength for GPC was observed with higher ratios used.
- The stiffness of OPCC was 11% greater than that for GPC, and the CTE of OPCC is 17% higher than that measured for GPC. As result experienced less lateral earth pressure in GPC geo-energy structures.
- In comparison to OPCC geo-energy pile, the thermal performance of GPC geo-energy pile installed in partly saturated soil improved by 14%.
- The thermal efficiency of GPC geo-energy walls was higher by 21% when compared with OPCC wall.
- The CO_2 emissions associated with GPC geo-energy piles and walls showed a significant reduction, reaching up to 44.5% lower in comparison with n that reported with OPCC piles and walls.

Chapter 5: Thermal enhancement of soil-geo-energy structure interaction using conductive additives.

5.1 Highlights

- Enhancing the thermal contact properties is critical to improve the heat transfer efficiency of geo-energy structures.
- Conductive additives such as graphTHERM and carbon fibre were found effective to enhance the thermal properties of sand and reduce contact thermal resistance.
- Heat transfer efficiency of geo-energy piles and walls remarkably improved by 81 % and 100 % when thermally enhanced sand by the addition of 10 % graphTHERM was used at the interface within a finite region.
- The use of thermally enhanced sand by the addition of 10 % carbon fibre by weight around the geo-energy piles and walls increased the heat transfer rate by 54 % and 80 % respectively.
- Placing thermally enhanced sand in direct contact with the geo-energy structures led to enhance the heat flux and enlarge the thermally active soil zone.

5.2 Introduction

Over the last decade, the effect of traditional backfill and thermally enhanced backfill on the thermal performance of GSHP boreholes were investigated in many research (e.g. Jobmann and Buntebarth. 2009; Delaleux et al., 2012; Erol and Fracois, 2014; Zhou et al., 2012; Liu et al., 2019). Jobmann and Buntebarth (2009) studied the potential of enhancing the thermal conductivity of the bentonite-based backfill materials using two conductive additives (quartz sand and graphite). It was stated that the addition of 50% quartz sand to the bentonite increases the thermal conductivity by about 50 %, while adding 50 % graphite to the bentonite increases the thermal conductivity by almost 8.5 folds in comparison with those reported when raw backfill materials were used. Graphite is, therefore, considered as an effective additive in improving the thermal conductivity of the backfill material and hence the performance of ground heat exchanger. It is worth noting that graphite is characterised by its low chemical reactivity with the

ecosystem. Nevertheless, adding graphite with a high content to the backfill materials could be detrimental to grout viscosity which would lead to forming gaps between buried tubes and borehole grout material. Delaleux et al. (2012) concluded that the addition of 10 % graphite enhances the thermal conductivity of bentonite grout about five folds'. Accordingly, Erol and Francois (2014) suggested a maximum blending ratio of 10 % graphite to avoid potential adverse effects. Liu et al. (2019) used TICA GSHP Design software to evaluate the applicability of using quartz sand–bentonite–carbon fibre mixture as a borehole backfill material. It was found that the total area and cost of ground buried pipes were reduced when a backfill made from quartz sand–bentonite–carbon fibre was used. These results concerning the effect of backfill material properties on the thermal performance of boreholes were promising, which would motivate researchers to work on and explore potential approaches to improve the thermal recovery using geo-energy structures. Nevertheless, the effect of backfill material on the thermal performance of geo-energy structures might be complex due to the complexity of some types of geo-energy structure geometry and the requirement to carry out coupled mechanical and thermal loads (Brandl, 2006).

Research studies on evaluating the effect of adjacent soil properties on the performance of GESs seem scarce and existing ones are carried out numerically. Qi et al. (2020) carried out a numerical investigation to evaluate the thermal response of the pile/soil interface. This study illustrated that heat transfer coefficient *(h)* at the pile-soil interface can be different during cooling and heating modes. Thus, for a proper design of the system, accurate and reliable heat transfer values at the interface must be deduced. It is also reasonable to conclude that experimental investigations are also imperative to complement and confirm the outcomes of previously limited numerical research studied.

Performance of energy walls was assessed primarily using numerical methods (see, Bourne-Webb et al., 2016; Nasilio et al., 2016; Di Donna et al., 2017; Barla et al., 2020; Rammal et al., 2020; Di Donna et al., 2021). It was revealed that analysis and design method of geo-energy walls currently lack comprehensive design guidelines which in turn could lead to difficulties in calculating thermal energy supply without full numerical simulations which is time consuming. The first

proposal to design energy walls by analytical methods was introduced by (Sun et al., 2013). Their model proposed 2D plane heat conduction between geo-energy wall and surrounding ground. Although the model was validated using data collected from the Shanghai Museum of Nature History, the model results poorly matched the collected data. Kurten et al. (2015) established an analytical model to design geo-energy walls based on the based on the thermal resistances of the structure (Rx), they simplified the calculation of (Rx) considering the heat problem as delt electrical resistance connection. Shafagh and Rees (2019) also established a thermal resistance model for energy walls. They assumed the shape factors as rectangle wall with pipe which represented at an offset hole. This approach led to achieving an acceptable accuracy for many design purposes such as choosing the number of pipes inside the wall. Furthermore, Shafagh et al. (2020) proposed numerical finite volume model to represent geo-energy wall with surrounded ground and basement boundary conditions using dynamic thermal network (DTN), the model was validated by imposing Thermal Response Test (TRT). Acceptable relative errors between measured and predicted heat transfer rates were achieved. The proposed thermal response model showed to be very efficiently when utilised to simulate the wall response over long timescales. Consequently, Di Donna et al. (2021) provided the only design chart for energy walls based on ground properties e.g. hydraulic and thermal properties and ground conditions including ground water and flow velocity. According to the presented design chart, the ground thermal conductivity with the absence of groundwater flow can increase the available energy by almost 150 %. Despite these attempts to provide practical design guidelines, none of these studies covered the effect of wall-soil interface properties on the thermal performance of geo-energy walls.

In the current Chapter, sand samples were initially prepared and tested to ascertain the effect of adding thermal enhancement additives e.g. graphTHERM and carbon fibre on the thermal properties of thermally enhanced sand. These results assisted with the determination of an optimum additive ratio to achieve favourable mechanical and thermal performance of the thermally enhanced sand. Then, the selected ratio of additives was utilised to prepare thermally enhanced materials that were placed at the soil-structure interface. Experiments using a relatively large-scale experimental rig with dimensions of 1 m x 1 m x 1 m were carried out

to assess the impact of enhancing the soil's thermal properties at the GES-soil interface using graphTHERM and carbon fibres on the performance geo-energy piles and walls and to evaluate the impacts on ground temperature. All results were compared against a control test where GESs were installed in virgin soils.

5.3 Significance of this chapter

Currently, all available numerical studies used to design GESs assume perfect interface between GES and adjacent soil which is capable to pass through conductive heat transfer. However, Qi et al. (2020) proved that poor interface thermal properties between concrete structure and soil could lead to a deleterious impact on the heat transfer efficiency for large size GESs which in turn might lead to losing its ability to transfer heat. This chapter proposes an innovative way to enhance the thermal performance of geo-energy structure and thermal interaction with surrounding soils. The chapter provides a deeper understanding for the effect of thermal properties at the interface between geo-energy structures and adjacent soils on the thermal performance of geo-energy structures which would help improving the design and efficiency of geo-energy structures. Data generated from this comprehensive investigation could be used to validate numerical and analytical models. It should be noted that it becomes paramount to consider possible ways to transform this method to reality so that it can be applied in real-world application/projects. This can be applied through deep mixing method and injection technology so that the thermal and mechanical properties of the near soil zone can be improved. The outcomes of this study seem promising and provide a strong rationale for practicing engineers and client to apply such techniques in real projects.

5.4 Methodology

In order to investigate the performance of geo-energy structures installed in thermally enhanced soils with particular dimensions, a fully instrumented testing rig was designed and manufactured as shown in Fig. 5.2 and 5.3. The following sections demonstrated the thermal and physical properties of the material used in the experimental program as well as described the experimental rig that have

been used to evaluate the thermal performance of geo energy structures (piles and walls).

5.4.1 Materials

The ground soil in this study was simulated by using standard building with a mean particle size D_{50} of 250 µm, a coefficient of uniformity (C_u) of 1.38 and a coefficient of curvature of 0.89. Further details about the used sand can be found in section 3.3.1.1.

GraphTHERM and Carbon fibre were selected as additives to enhance the thermal properties of sand. GraphTHERM is a special type of graphite powder which have a high thermal conductivity value up to 100 W/m.k, more information about this material composition, particle size and surface area are presented in Elkezza et al. 2022. Carbon fibres are a recycled carbon fibre powdered to 80µ - 100µ. This type of fibres are normally used in the applications that required to increase the mechanical properties. Also, it can contributes customise the electrical and thermal conductivity of selected matrix. The selected carbon fibre was provided by ELG carbon fibre Ltd. Table 5.1 presents the main properties of carbon fibre that were provided by the supplier.

Table 5.1 The main properties of Carbon fibre.

property	Value
Carbon fibre content, %	>98
Fibre diameter, µm	7
Bulk density (ton/m^3)	0.40
Thermal conductivity, dry (W·m^{-1}.k^{-1})	Up to 30
Metal contaminations*	<0.5x10^{-3}
Tensile strength, MPa**	4150
Tensile modulus, GPa**	320-255

Ordinary Portland cement concrete OPCC was designed for target compressive strength of 45 MPa was used to produce the geo energy piles and walls that been used in this study. Further information about the preparation procedure can be found in section 3.3.1.3 in this thesis.

5.4.2 Mechanical and Thermal assessment

Although data provided by the supplier indicated that these additives were designed to cause very minor influence on the mechanical properties even at a high filling degree of greater than 60 %, it was found essential that experiments are conducted to assess the impact of mixing additives with sand on the shear strength behaviour of the mix. Shear strength tests were then conducted to determine friction angle, (Ø) of pure sand and mixes of sand with different percentages of the highly conductive additives (graphTHERM and Carbon fibre) with ratio of 2.5 %, 5.0 %, 10.0 %, 15.0 % and 20.0 % by weight to examine the effects on the shear strength of thermally enhanced sand. Direct shear tests were conducted in accordance with BS 1377:7 (1990) to obtain both normal and shear stresses at failure for each sand mix. All test samples were compacted to the same unit weight of 1.85 gm/cm^3.

In addition, to determine an optimum percentage for the additives based on the thermal properties, samples were prepared by mixing sand with different percentages of additives (2.5 %, 5 % and 10 %) by dry weight. The thermal properties of the mixes were determined using KD2 Pro thermal analyser. In total, 84 samples were prepared and tested for sand mixed with predetermined amounts of carbon fibre and graphTHERM powder. Table 5.2 summaries the testing programme to assess the thermal properties of thermally enhanced sand. The materials were initially mixed by hand until obtaining a homogenous mixture and then predetermined amounts of water was added to produce mixtures with moisture content of 5 %, 10 % and 15 %. Subsequently, the mixtures were poured into a designed mould shown in Fig. 5.1. All samples were compacted to a unit weight of 18. 5 KN/m^3. This achieved by compacting each sample in 5 layers starting with a central layer with a thickness of 50 mm and successive layers with thickness of 12.5 mm from both sides. This approach was found useful to avoid and/or minimise the discrepancy in the density along the height. All samples were conducted according to the recommendations of (Saad et al., 2012). The thermal properties were measured using dual-needle sensor SH-1 of the K2D Pro thermal meter device that was inserted in the sample for 2 to 5 min. Data presented for each sample was obtained as an average value of three measurement readings.

Table 5.2 Experimental program for sand thermal enhancement tests

Series	Material	Parameters		Note
		Variable	Fixed	
1	Pure sand	w_c= 0 %, 5 %, 10 %, 15 %	γ_d=18.5 KN/m^3	12 samples
2	Sand + GT	w_c= 0 %, 5 %, 10 %, 15 % GT = 2.5 %, 5 %, 10 %	γ_d=18.5 KN/m^3	36 samples, 12 for each % of GT
3	Sand +CF	w_c= 0 %, 5 %, 10 %, 15 % CF= 2.5 %, 5 %, 10 %	γ_d=18.5 KN/m^3	36 samples, 12 for each % of CF

Note: GT =grapTHERM, CF=Carbon Fibre, wc=water content and γ_d= dry density.

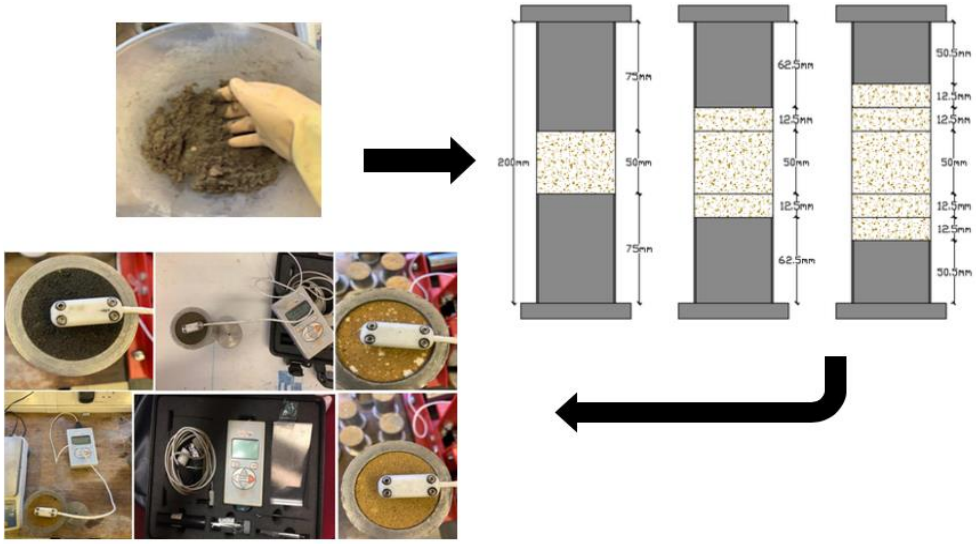

Fig. 5.1. The procedure of testing the thermal enhanced sand.

5.4.3 Heat transfer of geo-energy piles and walls

This experimental work was designed to simulate the installation of geo-energy structures in thermally enhanced soils with a particular zone around the GES so as to study the effects of the thermal properties at the soil-GES interface on the thermal performance of geo-energy structures. In order to determine the effective size of a thermally enhanced sand zone, a preliminary investigation was carried out using hot plate setup. Six cylindrical layered samples with a diameter of 100 mm and height of 200 mm were prepared and tested as shown in Fig. 5.2. The

thermally enhanced sand layers were prepared by mixing sand with optimum values of graphTHERM and carbon fibre additives. Samples were then constructed by compacting the thermally enhanced sand into layers with predetermined heights of 10 %, 20 %, 30 %, 40 % and 50 % of the total sample height. The unit weight of all samples was kept constant at 18.5 kN/m^3. Each sample was subjected to a hot end source of heat to allow heat flux through the layered sample and measuring the temperature at the cold end as shown in Fig. 5.2 (a and b). Measured temperature values at the cold end of samples were presented in Fig. 5.2 c after reaching steady state conditions. It was very clear that by increasing the height of thermally enhanced sand layer, heat flux was increased resulting in rising the temperature at the cold end. The data revealed that there is a unique relationship between the thickness of thermally enhanced sand layer and the temperature at the cold end which was characterised by showing two stages performance. The first stage showed a rapid increase in the temperature at the cold end from 30.3 ^{o}C to 32.4 ^{o}C with a slight change in the thickness of thermally enhanced layer up to a thickness of 23 % whilst less impact on the temperature at the cold end was observed when the thickness of thermally enhanced layer was increased beyond it. The results suggested that a ratio of 25 % and 24 % of thermally enhanced sand with graphTHERM and carbon fibres, respectively are practically effective distances to enhance the thermal interaction with adjacent soils. As a result, it was decided to place 100 mm of thermally enhanced sand all around the geo-energy piles and 200 mm of thermally enhanced sand in front of geo-energy walls.

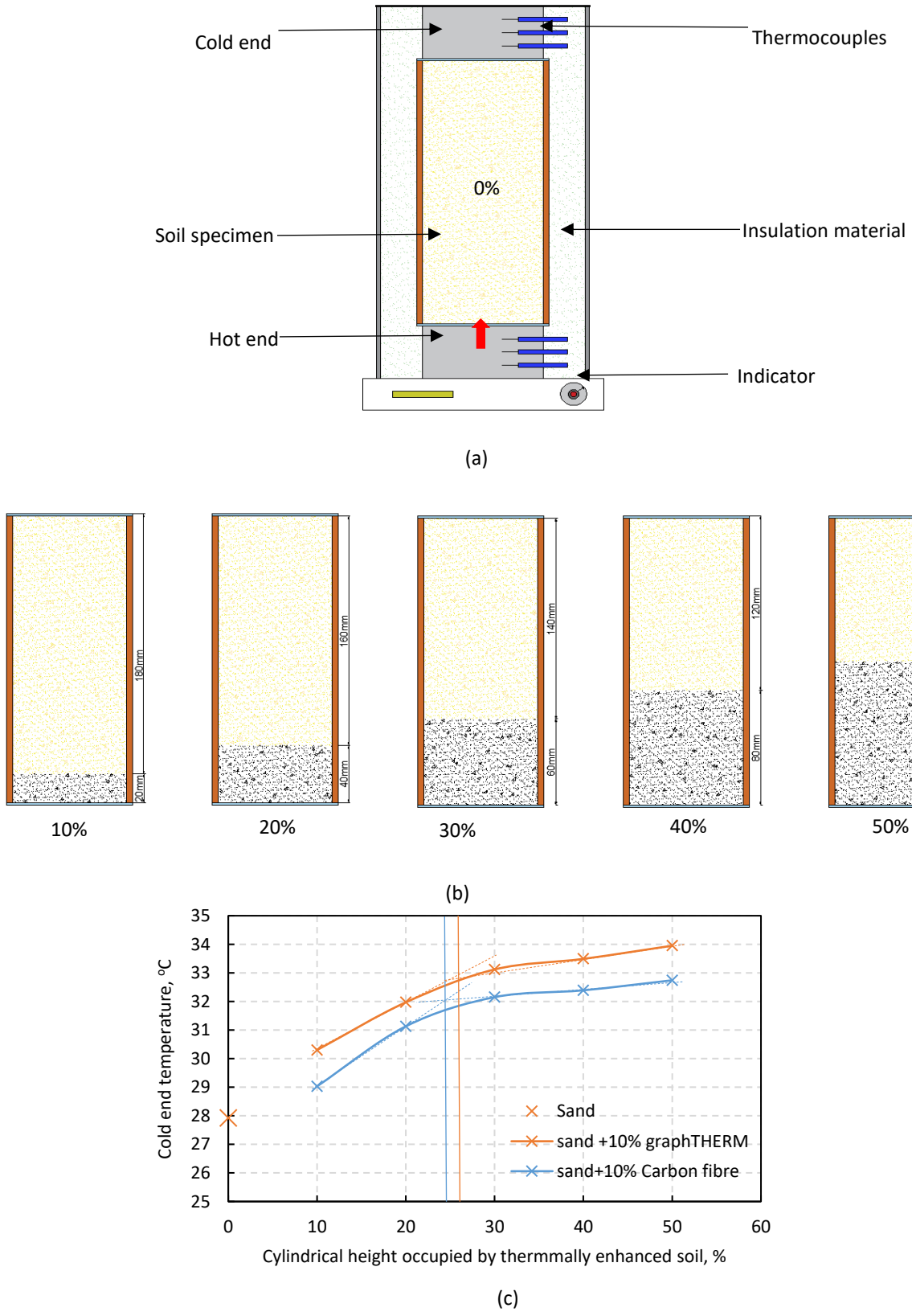

Fig. 5.2. (a). Hot plate setup for heating the samples, (b). The variation of the thermally enhanced layer for each test and (c). The relationship between cylindrical height occupied by thermally enhanced soil and cold end temperature.

The piles and walls were experimented using the experimental rig that have been explained in section 3.3.3 in this thesis. Figs. 5.3 and 5.4 showed schematic diagrams of the testing rig for geo-energy piles and walls respectively. In total, six experiments were carried out to assess the performance of geo-energy piles and walls with fixed and variable parameters as demonstrated in Table 5.3. To create a particular zone around the geo-energy pile filled with thermally enhanced sand whilst the rest of the tank is filled with natural sand, a filling method was proposed utilising a wooden box with dimensions of 350 mm x 350 mm x 1000 mm to set out boundaries of each zone around the geo-energy piles. Both the geo-energy pile and box were centred in the experimental tank. Then the thermal enhanced sand was filled around the geo-energy pile inside the wooden box whilst natural sand was poured outside the wood box. After filling the wooden box, it was gently lifted to form a natural boundary between the two zones. In case of tests on geo-energy walls a wooden sheet was used during the filling process to create a thermally enhanced sand zone with a width of 200 mm as can be seen in Fig. 5.3 and 5.4.

Table 5.3. Fixed and variable parameters for piles and walls heat transfer experiments

Series		Test coding	Fixed parameters	Variable parameters
Series 1	(piles)	S/S/P1	FR = 67 l/h, GWL = 500 mm, IT = 52.41 ^{O}C	Normal sand
		S/C/P2	FR = 67 l/h, GWL = 500 mm, IT = 52.54 ^{O}C	Sand + 10 % Cf boundaries
		S/G/P3	FR = 67 l/h, GWL = 500 mm, IT = 52.36 ^{O}C	Sand + 10 % GT boundaries
Series 2	(walls)	S/S/W1	FR = 67l/h, GWL = 500mm, IT = 52.61 ^{O}C	Normal sand
		S/C/W2	FR = 67 l/h, GWL = 500 mm, IT = 52.19 ^{O}C	Sand + 10 % Cf boundaries
		S/G/W3	FR = 67l/h, GWL = 500 mm, IT = 52.30 ^{O}C	Sand + 10 % GT boundaries

GT=grapTHERM, CF=Carbon fibre, GWL= ground water level, IT= inlet temperature.

5.5 Results and discussions

Data presented in this section were organised and discussed to provide a deeper understanding for i. the effects of conductive additives on shear strength and thermal behaviour of sand, ii. the performance of the geo-energy structures installed in thermally enhanced soils and iii. the impacts of using thermally enhanced soils on ground temperature.

5.5.1 Sand shear strength assessment

Data from shear strength experiments were collected on sand samples prepared with different percentage of additives e.g. GT and CB. Fig. 5.5 showed the relationship between the percentage of additive content e.g. GT and CF in the sand sample and the determined friction angle. A reference point showing the friction angle of natural sand was also plotted.

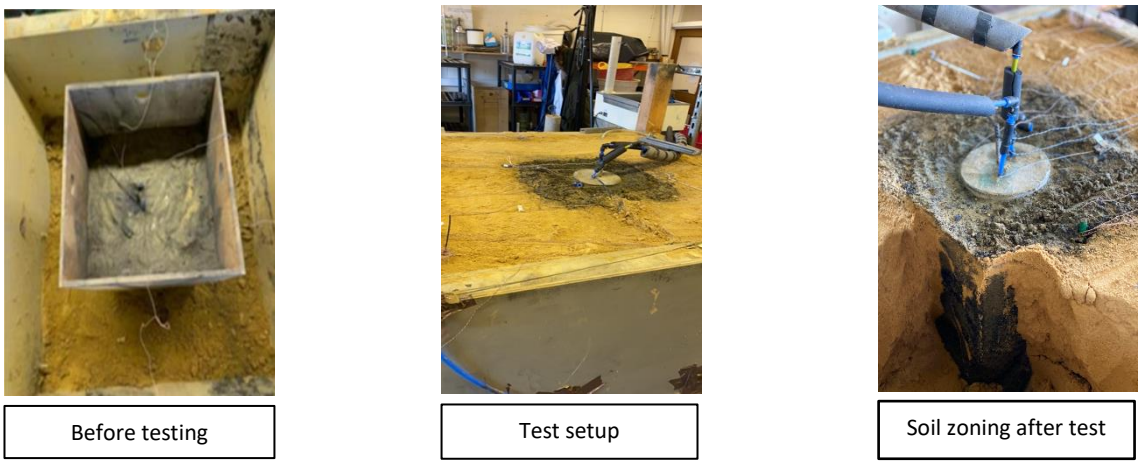

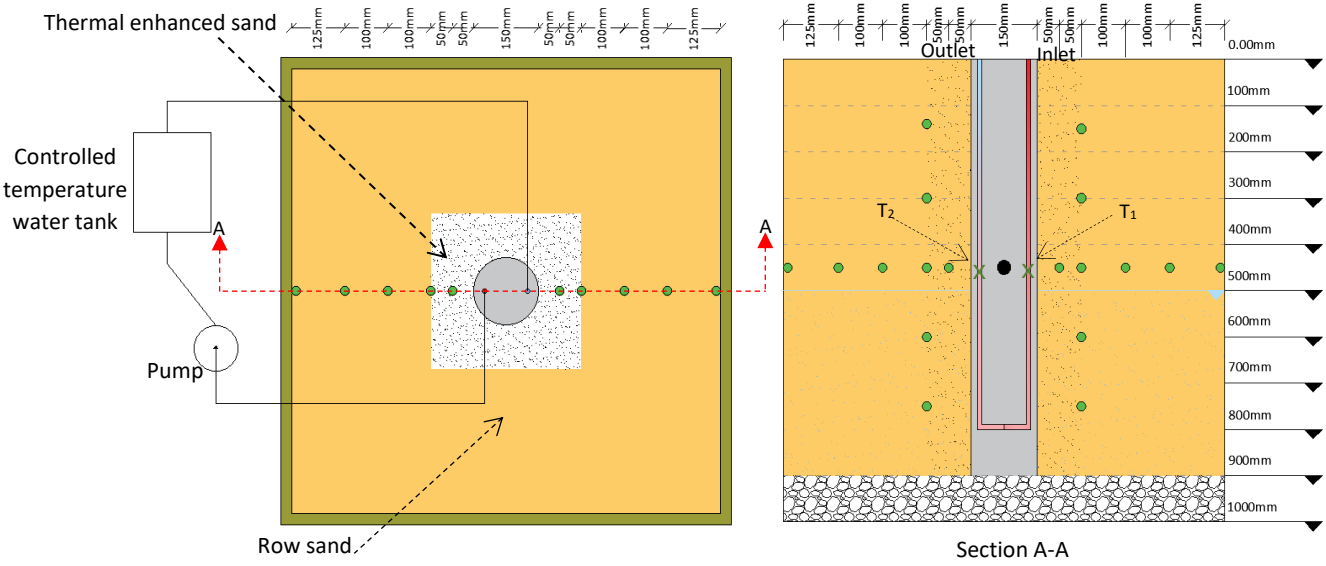

Fig. 5.3. Heat transfer experimental model for geo energy pile.

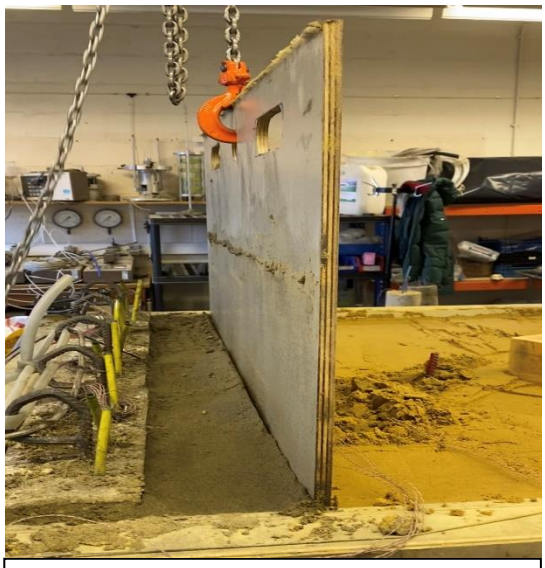

Creating a thermally enhanced soil zone

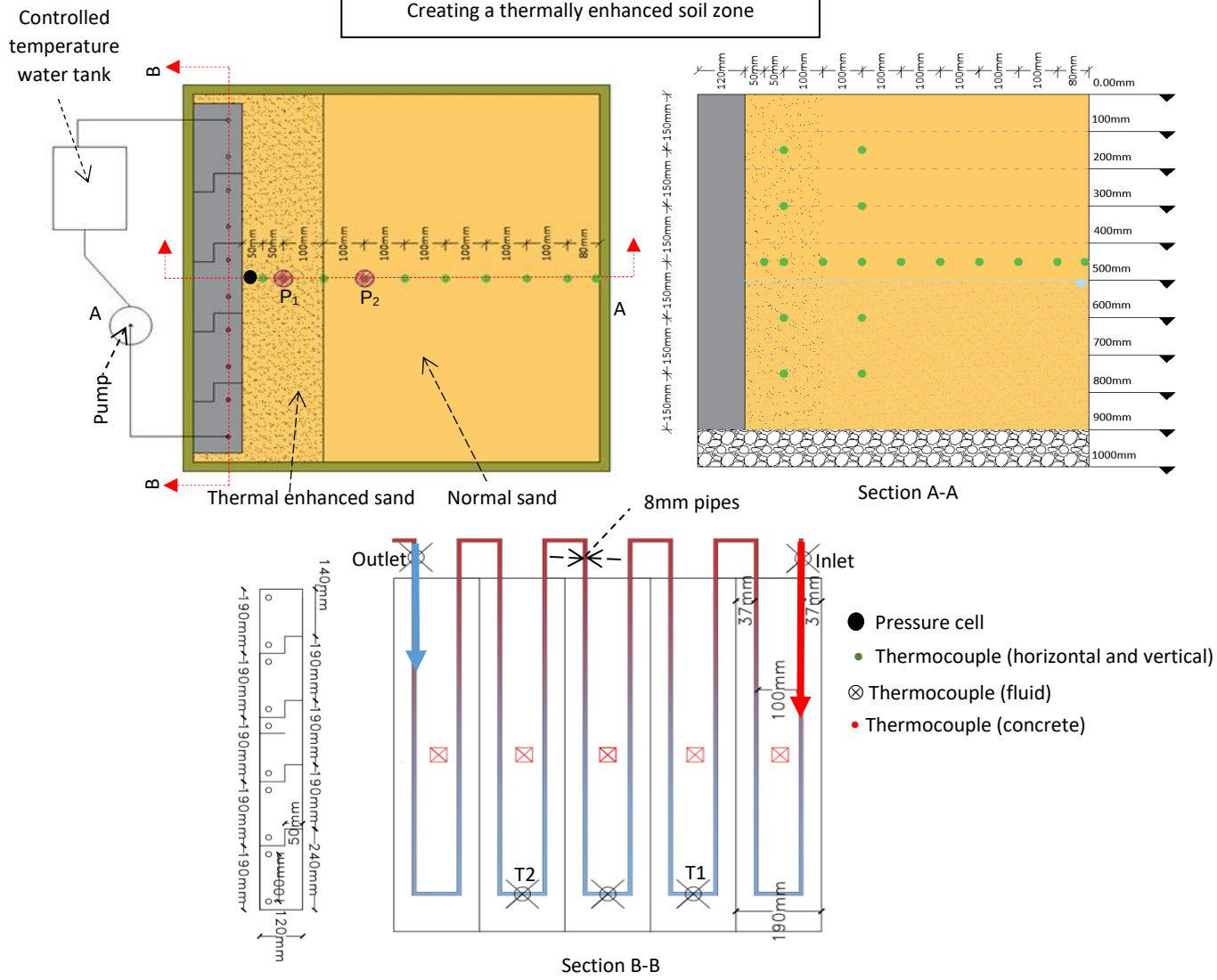

Fig. 5.4. Heat transfer experimental model for geo energy wall.

The data suggested that adding GT and CB with a content of up to 15 % resulted in an improved shear strength above which a decline in the angle of friction was observed. This could be contributed to the size distribution of GT and CF which is finer than the mean diameter of the sand. Therefore, one would anticipate that the added GT and CF filled the pore voids, increased particle contacts and interlocking hence leading to an increased friction angle. Nevertheless, exceeding 15 % content of GT and CF caused an adverse impact on the overall shear strength since the additives started to dominate the behaviour of composite soil developing weaker contact surfaces. The results clearly suggested that the behaviour of sand mixed with GT and CB peaked at the addition of 10 resulting in attaining a higher friction angle by a value of 8 % and 15 % respectively. Thus 10 % additive was considered to be an optimum value to enhance effectively the shear strength of pure sand. Further tests were therefore limited to 10 % to avoid any determinantal impacts on the stability of geo-energy structures.

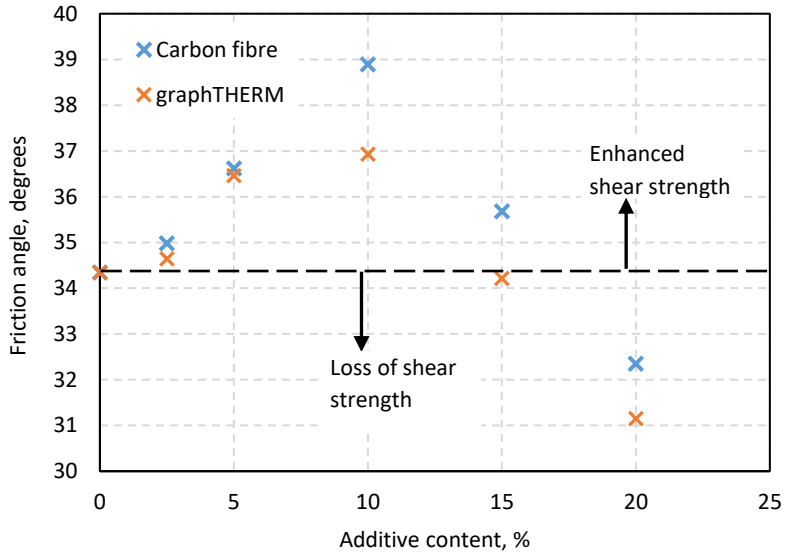

Fig. 5.5. Friction angle against additive content.

5.5.2 Thermal enhancement of sand

The KD2 Pro thermal analyser device was utilised to measure the thermal properties including thermal conductivity, volumetric heat capacity and thermal diffusivity of sand samples. Samples of sand were mixed with predetermined amounts of additives e.g.GT and CF as illustrated in Table 4 and prepared with different

water content of 0 %, 5 %, 10 %, and 15 % that are equivalent to degree of saturations of 0 (dry state), 28 %, 59 % and 88 %. These samples generated enormous data for the thermal performance of thermally enhanced sands as a function of the additive type and moisture content. It is worth noting that all samples were compacted to the same dry unit weight of 18.5KN/m^3 and actual water content was determined at the end of test. Figs. 5.6a and b showed the results of thermal conductivity as a function of GT and CF content at different moisture content. The data showed linear relationships between the additive content and the attained thermal conductivity of sand mixes at different moisture contents. As presented in Figs. 5.6a and b, sand mixed with the addition of 10 % graphTHERM powder and water at 88 % saturation showed high thermal conductivity of 4.20 W/m.k. Whereas when sand samples prepared with exactly the same CF and moisture content showed a 12 % reduction in the overall thermal conductivity coefficient which was found to be 3.7 W/m.k. Careful inspection of the data in Fig. 5.6a and b illustrated that addition of GT and CF to moist sands would improve the thermal conductivity by an average rate of 13.6 % and 8.8 % respectively related to the additive content. This indicated that the addition of GT powder was more effective to enhance the thermal conductivity of sands which could be due to the fact that the thermal conductivity of grapTHERM particles was three times higher than that of carbon fibre. Data shown in Fig. 5.6 a and b revealed that the degree of saturation played a major role in enhancing the thermal conductivity of sand mixes. Despite the additive type and content, insignificant improvement could be achieved for the thermal conductivity of dry sands. This could be attributed to inability of additives to form an effective conductive matrix through the whole sand sample. Preparing sand samples at low moisture content e.g. 28 % degree of saturation that is close to the residual saturation of the sand coupled with the addition of additives showed a remarkable improvement of almost 6-fold increase in the magnitude of thermal conductivity. This could be attributed to the gradation of the sand used and its water retention, resulting in a high suction head at low degrees of water saturation. This would in turn lead to a strong particle bonding and bridging the gaps between particles, hence enhancing the conductive heat transfer capability (Tarnawski and Leong, 2000; Abdel-Aal et al., 2015; Mostafa et al., 2015; Alrtimi et al., 2016; Elkezza et al., 2022). Nevertheless, the positive contribution of increasing the moisture content in the sand samples

deemed to decline with further increase in the moisture content above the residual saturation. The thermal conductivity increased roughly by 30 % on samples prepared with water moisture at near full saturation.

Measurements taken for the volumetric heat capacity of natural sand and sand mixed with different percentages of graphTHERM and carbon fibre at different degrees of saturation were presented in Figs. 5.7a and b. Data presented for the volumetric heat capacity illustrated that adding both additives to a dry sand would not cause a substantive degree of improvement in the heat capacity of mixed sand. Nevertheless, the addition of graphTHERM to sand, generally, led to a higher heat capacity than that observed when carbon fibre was added irrespective of the amount of water. The effect of graphTherm on the volumetric heat capacity was more prominent at higher moisture content reaching a degree of improvement of 4 % with 1 % increase in the graphTherm content which was double that was deduced on sand samples mixed with carbon fibres.

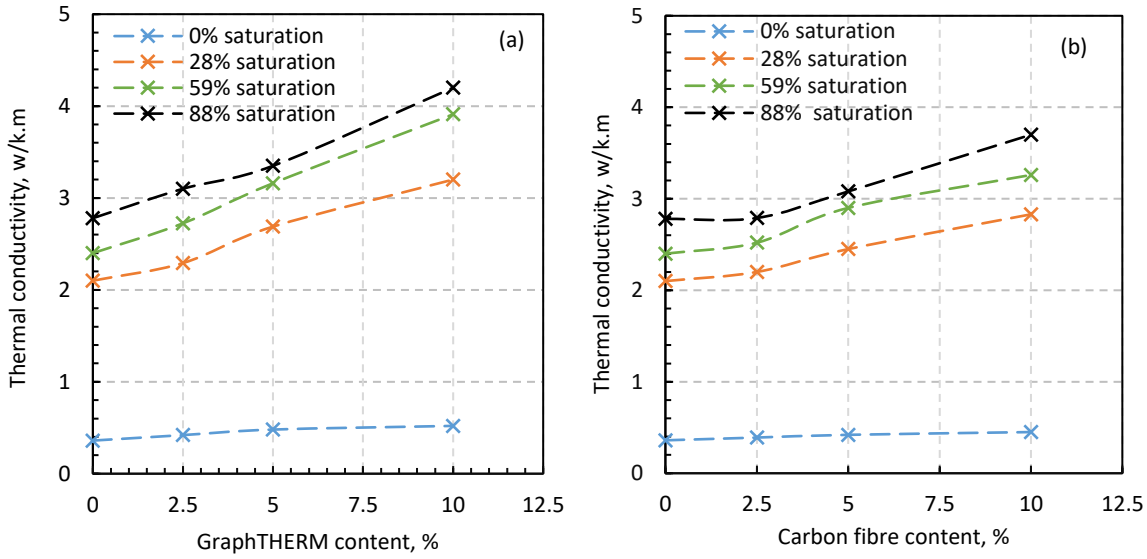

Fig. 5.6.Thermal conductivity relationships as function of a) graphTHERM and b) carbon fibre content

Moreover, data presented in Figs. 5.7a and b suggested that direct increase in the volumetric heat capacity was noticeable with the increase in the degree of saturation for both additives. Studies carried out by Yadav and Saxena (1973); Ghuman and Lal (1985) and Abu-hamdeh (2003) agreed on direct relationship between water content and the volumetric heat capacity of pure sand. Based on

the attained results even with the addition of the two different additives, the measured volumetric heat capacity seems to be directly related to the moisture content despite the amount of the additive.

Values for the thermal diffusivity of the tested sand samples mixed with graphTherm and carbon fibre were exhibited in Figs. 5.8a and b respectively. The thermal diffusivity was slightly reduced with the addition of the thermally conductive fillers at 2.5 % followed by a gradual increase with further addition of additives. The initial drop in the thermal diffusivity with the addition of small quantity of additive can primarily be attributed to the relative changes in the thermal conductivity and thermal capacity. The thermal diffusivity of sand mixed with carbon fibre seemed to improve at a considerably higher rate than that recorded on sand samples mixed with graphTherm powder. Mathur et al. (2015) numerically investigated the performance of EATHE (earth air tunnel heat exchanger) systems in soils with three thermal diffusivities. The study revealed that the soil with a higher thermal diffusivity would be able to transfer heat to nearby soils more quickly in comparison with the soil that has a lower thermal diffusivity.

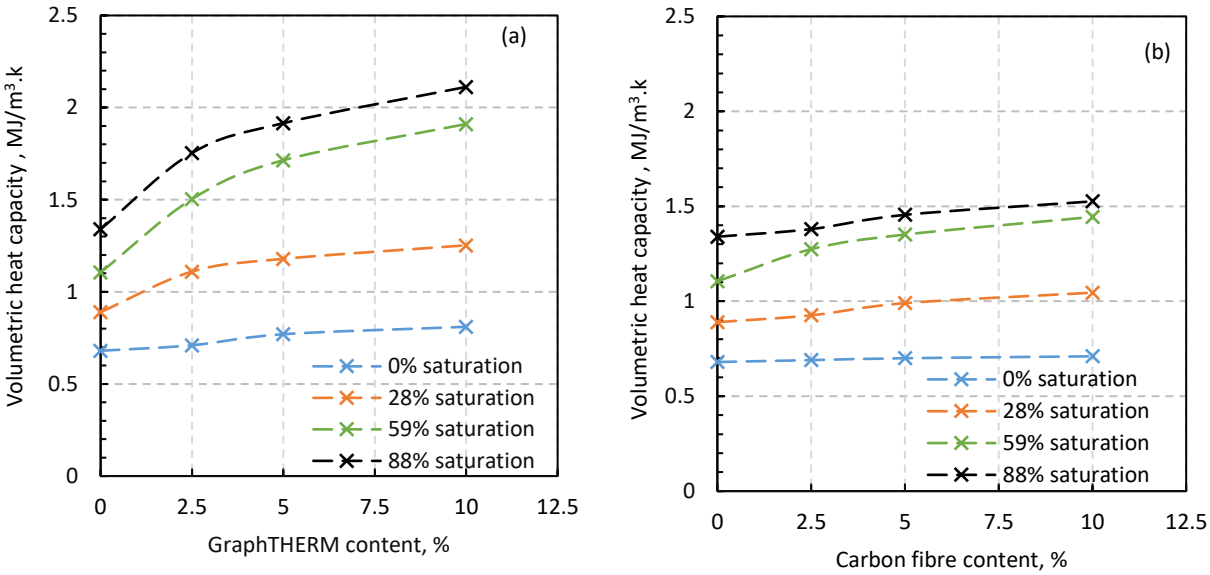

Fig. 5.7. Volumetric heat capacity relationship at different water saturation as function of a) graphTHERM content and b) carbon fibre content

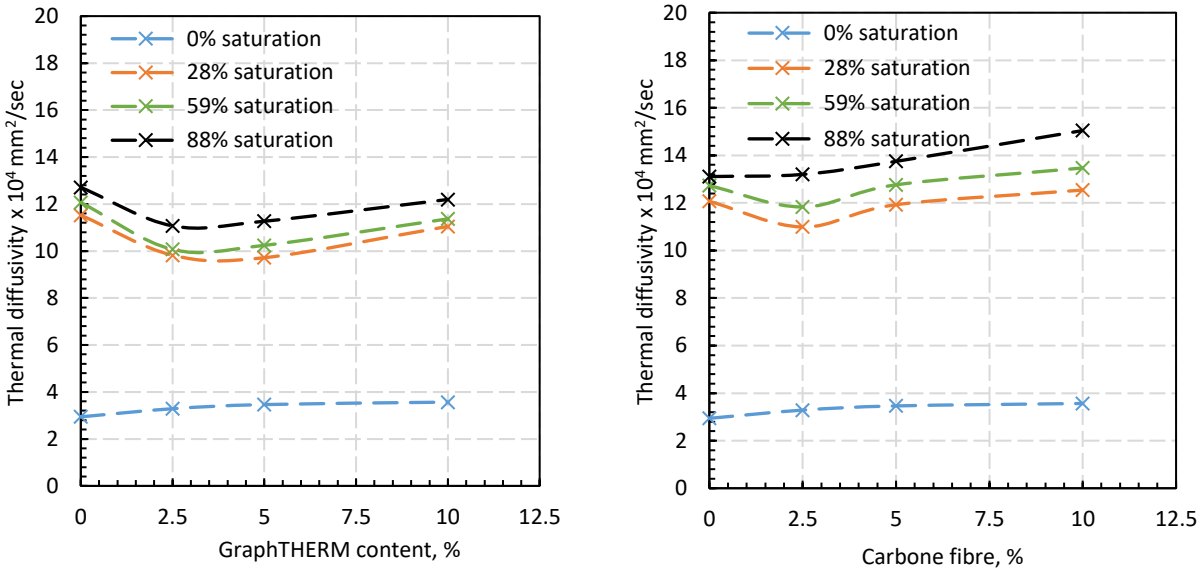

Fig. 5.8. Thermal diffusivity as a function of a) graphThHERM and b) carbon fibre.

5.5.3 Heat transfer experiments

In order to assess the performance of geo-energy structures and impact on soil temperature, the temperature of the circulating fluid at the inlet and outlet points of the HE as well as the horizontal and vertical soil temperature profiles at predetermined locations in the soil surrounding the geo-energy structure were recorded as shown in Figs. 5.3 and 5.4. The inlet-outlet temperature difference (Δt) would indicate the highest amount of heat energy that the geo-energy structures were able to dissipate into the soil. Figs.5.9 and 5.10 presented data for the temperature difference between inlet and outlet points ($T_{inlet} - T_{outlet}$) measured for modelled geo-energy piles and walls respectively. It can be seen from the data in Figs.5.9 and 5.10 that at the onset of the cooling process, there was a clear unsteady thermal structure-soil interaction illustrated by a relatively clear variable temperature difference between inlet and outlet which lasted for about 20 hrs until reaching the steady state equilibrium. The measured temperature difference between inlet and outlet were 2.16 ^{o}C, 3.33 ^{o}C and 3.92 ^{o}C for geo-energy piles installed in pure sand, thermally enahnced sand by CF and thermally enehnaced sand by GT respectively. Whereas for geo-energy walls, the measured

temperature difference were 5.8 ^{o}C, 10.5 ^{o}C and 12.0 ^{o}C for the same soil types respectively. It was therefore evident that the recorded temperature difference between inlet and outet was dependent on the thermal properties of the nearby soil to thegeo-energy structure. It was also noted that the use of thermally enhanced sand with GT showed the highest temperatre difference, followed by that enhanced by CF which was consistent with the measured thermal properties of soils as illustrated in Table 5.4. This suggested that the greater the thermal properties of near backfill soil e.g thermal conductivity, heat capacity, the higher temperature difference between inlet and outlet. Fig. 5.11 showed results for the dissipated heat energy for geo-energy piles and walls installed in different soils (calculated using equation 3.2). The heat transfer rate for the geo-energy pile reached its highest value of 269.84 W when installed in a thermally enhanced sand by GT which was 18 % higher than that recorded when thermally enhanced sand by CF was used and 91% increase over that recoded for a control geo-energy pile in pure sand. Similarily data deduced for geo-enregy walls demonstarted that heat transfer rate for walls installed in thermally enhanced sand by GT is the highest and higher by 15 % and 108 % in comparison with those recorded for geo-energy structure installed in a thermally enhanced sand by CF and pure sand.

This outcome is in agreement with previous conclusions made for horizontal loops and boreholes. Song et al. (2006) based on a numerical study revealed that increasing soil thermal conductivity from 1.1 w/m.k to 2.5 w/m.k led to almost 100 % increase in the heat transfer rate by horizontal loops. Studies by Javadi et al. (2018); Omer (2016) and Dulaleux et al. (2012) reported that the higher thermal conductivity of the borehole backfill resulted in a greater heat transfer rate.

In addition, as illustrated in Fig. 5.3, the circulating fluid temperature was measured at two additional points; points 1 and 2 inside the HE at a distance of 450 mm and 1450 mm from the inlet point respectively. The total length of pipe within the HE was 1900 mm. Data for the measured temperature, temperature difference from that measured at the inlet point and the percentage of temperature dissipation at the two points after reaching steady state conditions are presented in Table 5.4 . The data demonstrated that the fluid temperature

reduced by about 20 % and 90 % from the total dissipated temperature at points 1 and 2 respectively. Furthermore, around 70% of the total temperature dissipation was found to occur between point 1 and point 2. This could be attributed predominantly to the fact that the soil in the bottom half of the tank was fully saturated with water, leading to a remarkably high thermal conductivity and heat capacity. To confirm this observation, measurements for unit weight, moisture content (degree of saturation), thermal conductivity and volumetric thermal heat capacity of soil were taken at predetermined heights after the completion of tests S/C/P2 and S/G/P3. Tables 5.5 and 5.6 presented measured values for the degree of saturation which confirmed that sand in the bottom half of the tank is fully saturated with water. There was a significant drop in the degree of saturation in the top 300 mm of the sand, reaching almost a dry condition at the surface of the sand. Then, the obtained value of the soil degree of saturation was used in conjunction with Figs. 5.6 and 5.7 to measure the thermal conductivity and the volumetric heat capacity of the sand along the tank height. The measurements revealed that thermal conductivity and heat capacity retained high values in the bottom half of the tank, and decreased gradually towards the sand surface (top of the tank).

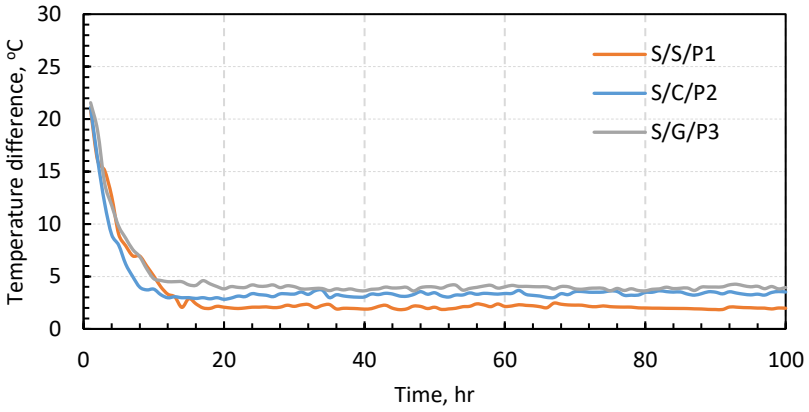

Fig. 5.9. Temperature difference Inlet-Outlet for geo energy piles with three soil boundaries.

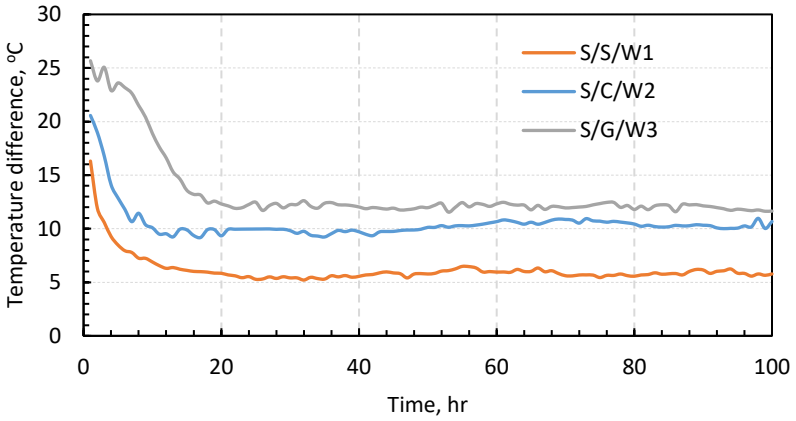

Fig. 5.10. Temperature difference Inlet-Outlet for geo energy walls with three soil boundaries.

Table 5.4. Circulating fluid temperature along the heat exchanger for pile test

	INLET POINT	POINT 1 (T_1)			POINT 2 (T_2)			POINT 2-POINT 1		OUTLET POINT		DISSIPATED ENERGY
	T_i °C	T_1 °C	Δt_1 °C	TD %	T_2 °C	Δt_2 °C	HD %	Δt_{1-2} °C	TD %	T_O °C	Δt_3 °C	q watts
S/S/P1	52.01	51.6	0.46	22	50.07	1.94	95	1.53	75	49.96	2.05	141.10
S/C/P2	52.71	51.83	0. 87	26	49.56	3.14	94	2.27	68	49.36	3.35	229.10
S/G/P3	52.28	51.42	0.89	21	48.49	3.78	96	2.93	73	48.30	3.98	269.80

where, Ti = inlet temperature, T1 = Circulating fluid temperature at 450 mm, T2 = Circulating fluid temperature at 1450mm, T_O = Outlet temperature, $\Delta t_1 = T_i - T_1$, $\Delta t_2 = T_i - T_2$, $\Delta t_3 = T_i - T_O$, $\Delta t_{1-2} = T_1 - T_2$, T_D = percentage of temperature dissipation, q = dissipated energy.

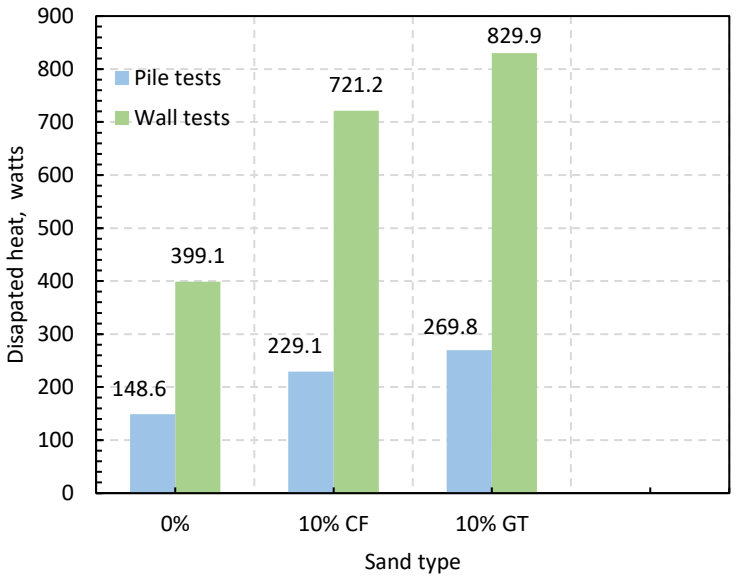

Fig. 5.11. Dissipated heat energy from geo energy walls and piles with different soil boundaries.

Table. 5.5. Measured degree of saturation and thermal properties along the experimental tank for test S/C/P2.

Depth	Normal sand				Thermally enhanced sand by CF			
	γ_d (KN/m^3)	S_r (%)	K (w/m.k)	C_v MJ/m^3.k	γ_d (KN/m3)	S_r (%)	K (w/m.k)	C_v MJ/m^3.k
0-100mm	16	3	0.4	0.6	16.4	2.1	0.45	0.72
100-200 mm	16.2	6.7	0.56	0.65	16.5	7.5	0.91	0.81
200-300 mm	16.5	12.6	1	0.81	16.8	10.4	1.1	0.95
300-400 mm	16.7	91.8	2.65	1.4	17.1	90.2	3.5	1.5
400-900 mm	16.8	99.6	2.78	1.44	17.3	99.1	3.7	1.52

where; γ_d = the unit weight of sand, Sr = degree of saturation, K = thermal conductivity, Cv= volumetric heat capacity.

Table 5.6. Measured degree of saturation and thermal properties along the experimental tank for test S/G/P3.

Depth	Normal sand				Thermally enhanced sand by GT			
	γ_d (KN/m^3)	S_r (%)	K (w/m.k)	C_v MJ/m^3.k	γ_d (KN/m3)	S_r (%)	K (w/m.k)	C_v MJ/m^3.k
0-100mm	16.8	3	0.4	0.6	16.7	3	0.54	0.81
100-200 mm	16.9	6.7	0.56	0.65	16.8	6.7	1.2	0.89
200-300 mm	17.1	12.6	1	0.81	16.9	12.6	2.5	1
300-400 mm	17.3	91.8	2.65	1.4	17.2	91.8	4.15	2
400-900 mm	17.7	99.6	2.78	1.44	17.5	99.6	4.20	2.1

where, γ_d = the unit weight of sand, Sr = degree of saturation, K = thermal conductivity, Cv= volumetric heat capacity.

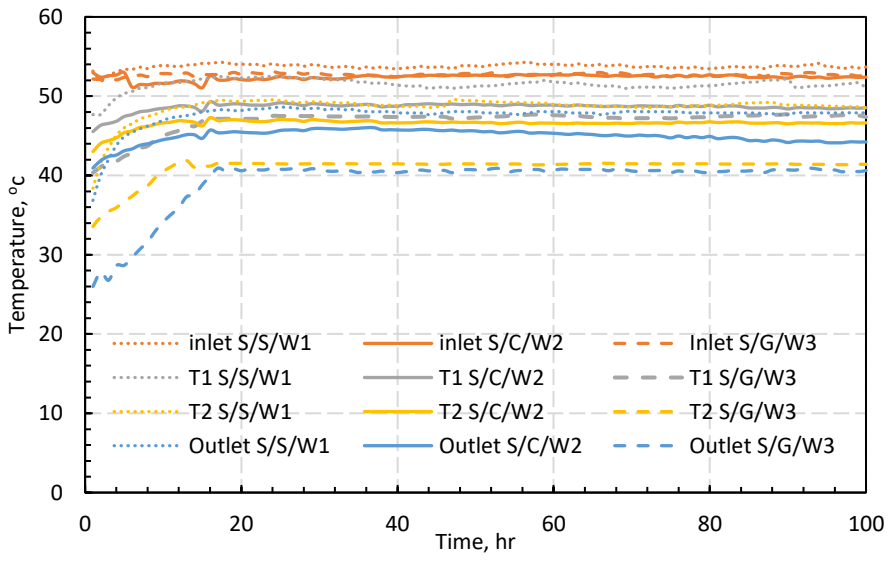

Fig. 5.12. Circulating fluid temperature along the heat exchanger for wall tests.

In case of geo-energy walls, circulating fluid temperature were measured at two intermediate points T_1 and T_2 at distances of 2950mm and 6950mm along the 9900mm long embedded heat exchanger (see Fig. 5.4). Fig. 5.12 shows the data for the temperature measurements at four points on the geo-energy wall tests (S/S/W1, S/C/W2, S/G/W3). The results showed the measured circulating fluid temperature reduced by about 30 % at T_1 and 80% at T_2. The fluid temperature at the embedded heat exchanger was considered to be uniformly reduced.

Figs. 5.13 and 5.14 displayed the change in soil temperature at a height of 450 mm along the horizontal direction after reaching the steady state conditions for geo-energy piles and walls respectively installed in pure sand, thermally enhanced sand by 10 % GT and thermally enhanced sand by 10 % CF.

For geo-energy pile tests, measurements for the soil temperature were taken at horizontal locations of 50 mm, 100 mm, 200 mm, 300 mm and 425 mm on both sides of the pile at exactly the same height of 450 mm from the tank base (see Fig. 5.3). In the case of geo-energy walls, the horizontal soil temperature profile was recorded at horizontal locations of 50 mm, 100 mm, 200 mm, 300 mm, 400 mm, 500 mm, 600 mm and 880 mm at a height of 450 mm above the tank base (see Fig. 5.4). Due to the high-temperature gradient between the experimental model of geo-energy structures including (piles and walls) and soil, the soil temperature increased rapidly during the early stage of cooling until reaching a steady state then remained almost constant.

The maximum increase in soil temperature measured on geo-energy pile tests was recorded at 50 mm from the pile surface and found to be 8 ^{o}C, 11 ^{o}C, 12 ^{o}C when geo-energy piles installed in pure sand, thermally enhanced sand by CF and thermally enhanced sand by GT respectively. The soil temperature gradually declined with the increase in the horizontal distance away from the pile. Fig. 5.13 clearly showed that the soil temperature at the tank boundary remained almost the same as the initial one measured at 0 hr when the geo-energy pile was installed in pure sand. However, in case of using thermally enhanced sands by CF and GT around the geo-energy pile, the soil temperature at the tank boundary was considerably higher by 3 ^{o}C and 5 ^{o}C respectively. This suggested that enhancing the thermal properties of adjacent soils led to improved thermal interaction and higher heat flux to the surrounding soils. Furthermore, it can be observed

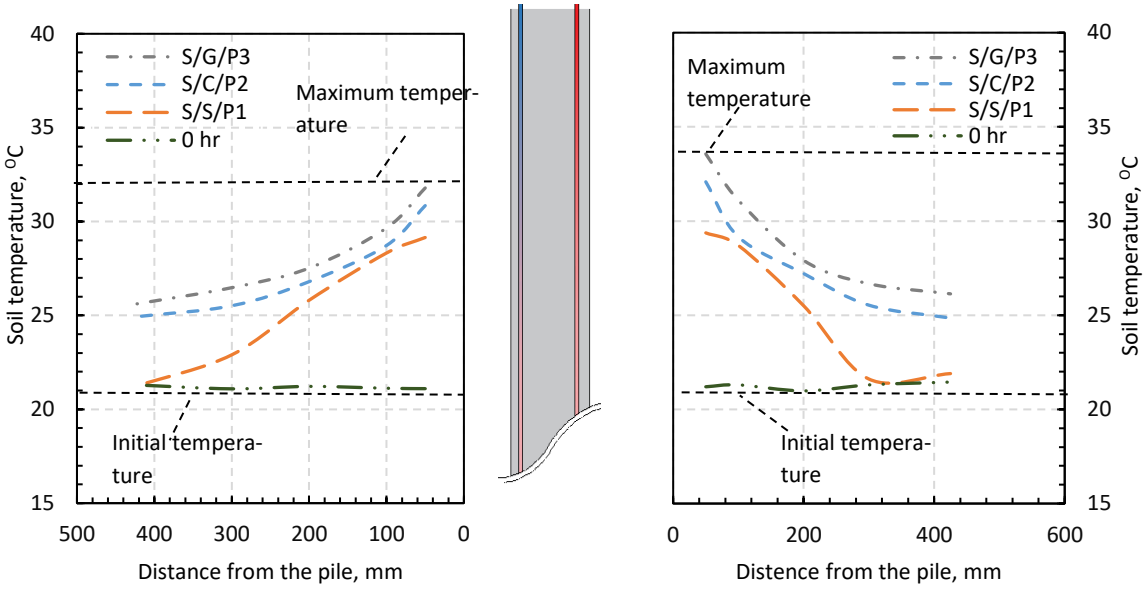

Fig. 5. 13. Horizontal soil temperature profile at depth 450mm at both sides of geo-energy pile model

that the use of thermally enhanced sand by GT around the pile led to producing the highest temperature change in the soil temperature. Fig. 5.14 presented measured temperature data on geo-energy walls which showed that i. the maximum temperature increase in eth adjacent soil was found to be 18^{o}C, 19^{o}C and 20.5 ^{o}C at a horizontal distance of 50 mm away from the wall when pure sand, thermally enhanced sand by CF and thermally enhanced sand by GT were placed in front of the wall respectively. Furthermore, the change in soil temperature at the boundaries of the experimental tank was found to be 0^{o}C, 4.2^{o}C, 7.52^{o}C corresponding to the same three tests which again suggested that the best thermal interaction occurred when thermally enhanced sand by GT was placed in front of the geo-energy wall. The use of thermally enhanced sand by GT resulted in 20 % higher temperature at the tank boundary on comparison with that measured for pure sand. The results, therefore, suggested that the use of thermally enhanced sand at the GES-soil interface resulted in a higher heat flux from the GES into the surround soils which in turn would lead to enlarging the thermally active soil zone. These results are in line with those previously reported by Zhou et al. (2020) for U-shaped HE installed in sand/graphite backfill. This could be attributed to the amount of dissipated energy that could the adjacent soil at the interface of geo-energy structure transfer from the pile to the surroundings.

Vertical soil temperature profiles were recorded at 100 mm away from both sides of the geo-energy piles and presented in Fig. 5.15. The data clearly showed that there was a gradual increase in the soil temperature with depth which is consistent with previously presented data for the temperature difference between the two intermediate points T1 and T2. This could be attributed to the increase in thermal conductivity with depth and the fact that the bottom half of the geo-energy pile existed in fully saturated sand. In addition, the increase in soil temperature with depth was also found to be dependent on the type of soil at the geo-energy pile interface e.g. whether it was thermally enhanced. The data in Fig. 5.15 demonstrated that the lowest temperature change was recorded when geo-energy pile was installed in pure sand (test S/S/P1) whereas the highest soil temperature change was experienced when the geo-energy pile was installed in thermally enhanced sand by GT (test S/G/P3).

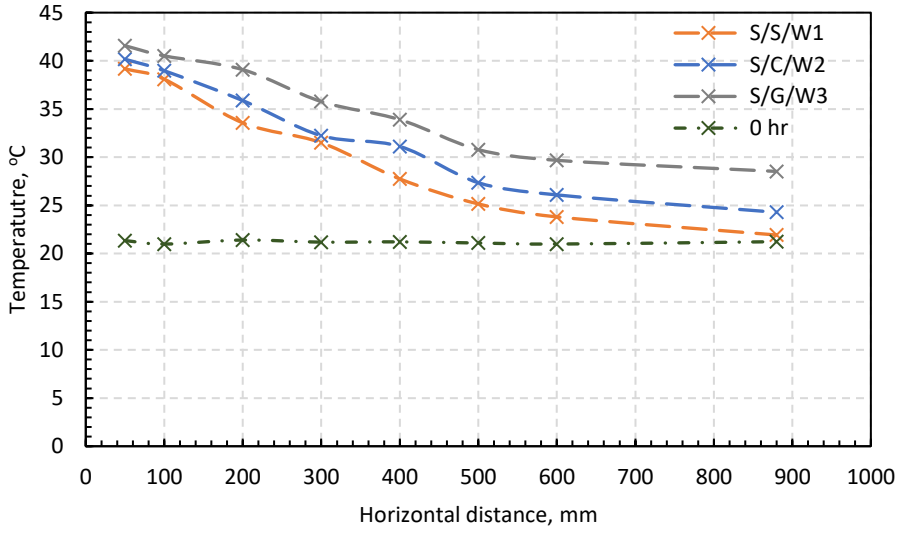

Fig. 5.14. Horizontal Soil temperature profile at depth 450mm in front of geo-energy wall model.

This is primarily due to the higher thermal conductivity of thermally enhanced sand by GT which was placed around the pile. The change in soil temperature above the water table is highly significant than that below the water table. In the case of geo-energy pile installed in thermally enhanced sand with GT (test S/G/P3), the soil temperature above the WL rose from 28.21 ^{0}C at a depth of 150 mm to 29.75 ^{0}C at a depth of 300 mm. Whereas below WL, a lower increase in soil temperature was recorded from 32.50 ^{0}C at a depth of 600 mm to 33.18 ^{0}C at a depth of 750 mm. This can be justified by the fact that saturated sand has a

greater heat capacity than that of the partially saturated and dry sand. Therefore, more rejected thermal energy would be required by geo-energy pile to observe an identical temperature change in fully saturated sand.

The results of the vertical soil temperature profile at two vertical locations named P_1 at 100 mm and P_2 at 300 mm (see Fig. 5.4) away from the geo-energy structure wall are presented in Fig. 5.16. It is worth noting that the vertical soil temperature profile at P_1 is within the thermally enhanced soil whereas the second vertical soil temperature profile is in the pure sand. Data presented in Fig. 5.16 illustrated that higher temperature change was recorded at the location P_1 compared to that recorded at P_2. Moreover, it can be observed that using thermally enhanced sand by GT produced the highest temperature change over the other two studied cases (CF and pure sand).

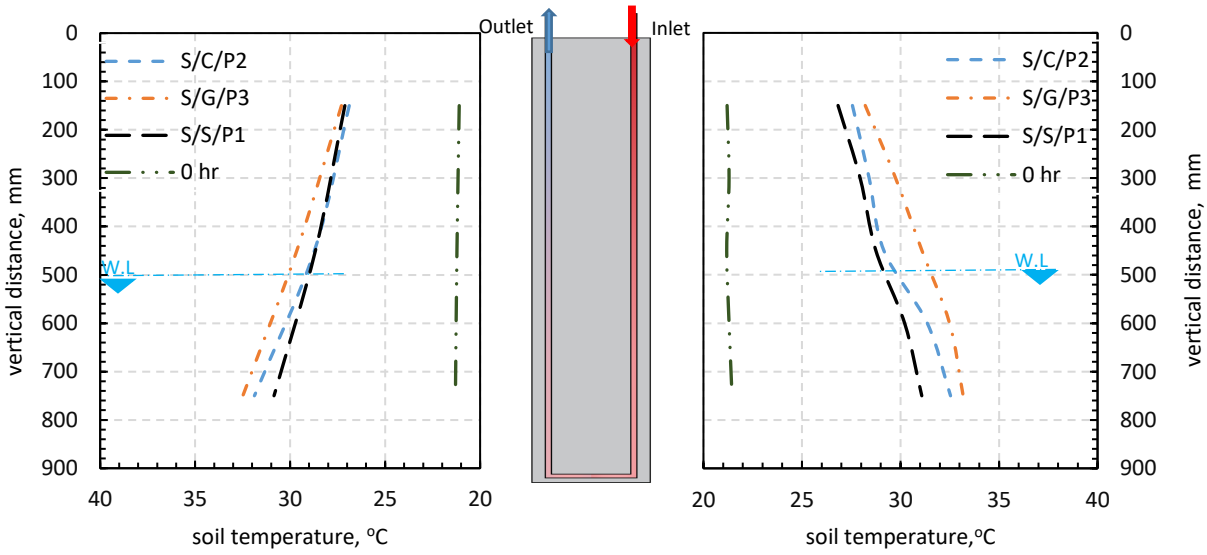

Fig. 5.15. Vertical Soil Temperature profile along the geo-energy pile at 100mm at both sides (inlet & outlet).

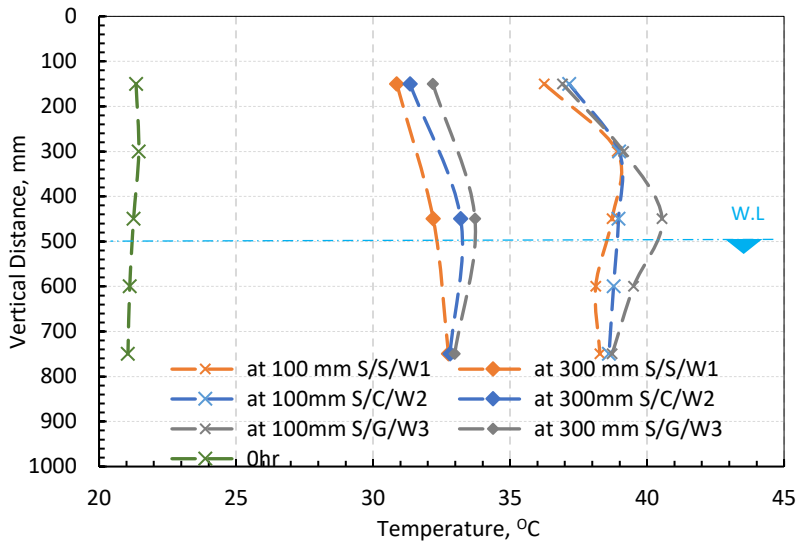

Fig. 5.16. Vertical soil temperature profile at 100mm & 300mm in front of the geo-energy wall

Figs. 5.17a and b showed measured data for the lateral earth pressure at mid-height of the geo-energy piles and walls respectively. In tests on geo-energy piles, the pressure cell was placed at the pile/soil interface on the inlet side (see Figs. 5.3 and 5.4). Results recorded on geo-energy piles demonstrated a very minor effect on the lateral earth pressure reporting an increase of around 7 Pa. However, measurements taken on geo-energy walls showed higher effect on the lateral earth pressure. For instance, the lateral pressure increased with elevating the wall temperature over the time from 8 kPa to 15 kPa in the case of using pure sand (0 % additive). There was a slight drop in the passive lateral earth pressure to 14.5 KPa and 14.0 kPa when thermally enhanced sand by GT and CF used in front of the wall respectively. This behaviour can be attributed to the increase in friction angle by the addition of 10 % GT and CF (see Fig. 5.5). Furthermore, thermal strain due to thermal expansion of the geo-energy structures was calculated in accordance with EN 1992-1-2 as given by Equation 3.3. To accurately calculate the thermal strain, it was crucial to determine the coefficient of thermal expansion. Experiments were conducted in accordance with TI-B 101 (94) on samples of concrete that used to produce the geo- energy piles and walls. The coefficient of thermal expansion was found to be 5.024 $x10^{-6}$ $^{o}C^{-1}$. Fig. 5.18 illustrated the increase in thermal strain as a function of the temperature difference. The thermal strain determined for geo-energy piles were 82 με, 80 με and 73 με

when the geo-energy piles were installed in thermally enhanced sand by GT, thermally enhanced sand by CF and pure sand respectively. Whereas the thermal strains were 123 με,116 με and 115 με on walls installed in the similar soils respectively. It can be clearly observed that the use of thermally enhanced sand by GT produced the highest thermal strain.

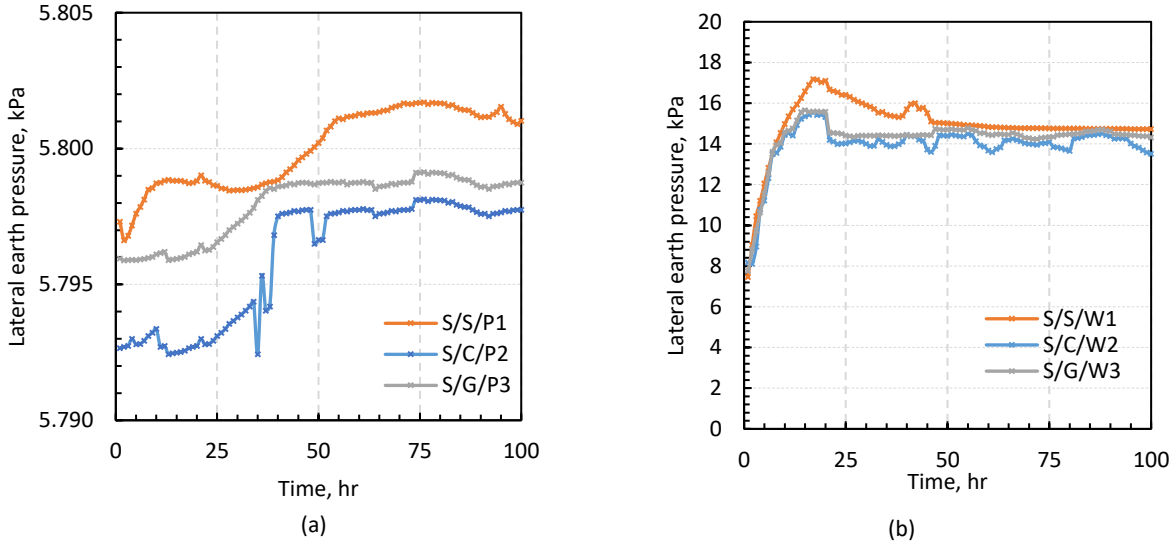

Fig. 5.17. (a). Lateral earth pressure at 450mm along the pile, (b). Lateral earth pressure at 450mm in front of the wall.

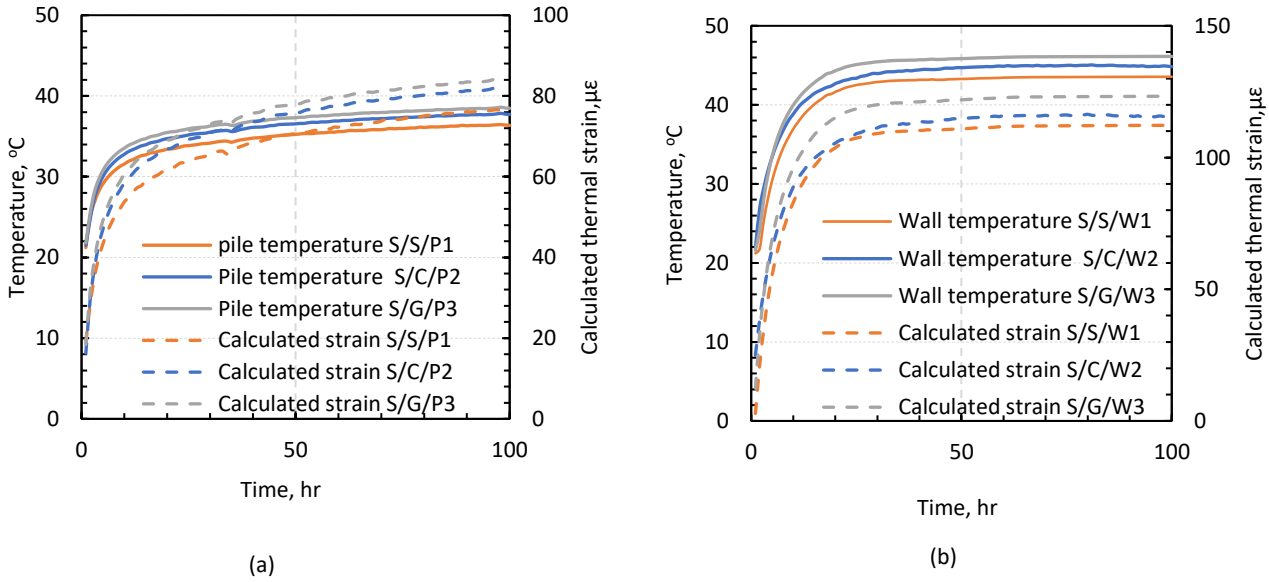

Fig. 5.18. (a). Calculated thermal strain and pile temperature, (b). Calculated thermal strain and wall temperature.

5.6 Summary of outcomes

This chapter was designed to examine experimentally the effects of soil thermal properties at geo-energy-soil interface on the thermal performance of geo-energy structures. Thorough experimental programme was carried out to assess the thermal and mechanical properties of thermally enhanced sands by graphTherm and carbon fibre as well as to evaluate the thermal performance of geo-energy structures placed in pure and thermally enhanced sands and impact on ground temperature using large scale testing rig. The following findings can be attained from this chapter:

- Significant improvement on the sand thermal properties can be achieved by the addition graphTherm and carbon fibres.
- Adding 10 % of grapTHERM and 10 % carbon fibre to pure sand by weight was found to increase the thermal conductivity by 62 % and 35 % respectively. This is coupled by experiencing a considerable increase in the shear strength parameter by 15 % and 8 % respectively.
- Volumetric heat capacity of sand was increased by 73 % and 30 % by the addition of 10 % of graphTHERM and 10 % carbon fibre to the sand respectively which would assist geo-energy structures to dissipate and extract more thermal energy with a lower effect on soil temperature.
- The composite soils after the addition of CF showed a slightly higher thermal diffusivity than that of pure sand indicating that the thermally enhanced sands are capable of provide faster heat transfer rate to surroundings. on the other hand, the addition of GT seems to cause a little reduction on the value of the thermal diffusivity resulting in slowing the heat transfer rate.
- The heat transfer rate by geo-energy piles and walls remarkably increased by 54 % and 80 % respectively when a thermally enhanced soil by 10 % CF was placed at the soil/structure interface.
- Using thermally enhanced sand by GT at the soil-geo-energy structure interface led to an enhancement in heat transfer rate of 81 % and 100.7 % for geo-energy piles and walls respectively.

- It is evident that placing thermally enhanced sand at the interface of geo-energy structure enlarged the thermally active soil zone, hence leading to enhancing the thermal performance of geo-energy structures.
- The use of thermally enhanced sands at the interface of the geo-energy structure did make insignificant impact on the lateral earth pressure.

Chapter 6: the use of PCM heat exchangers in geo-energy piles and walls.

6.1 highlights

- Use of PCM heat exchangers was found to significantly enhance the thermal performance of geo-energy piles and walls.
- The use of PCM heat exchanger increased the heat transfer efficiency of geo-energy piles by 75 % and 43% in heating and cooling operations respectively in comparison with those achieved using a standard heat exchanger.
- The use of PCM heat exchanger led to 43 % and 32 % enhancement in the heat transfer performance of geo-energy walls during heating and cooling cycles respectively compared with those achieved using standard heat exchangers.
- The use of PCM heat exchangers was found to reduce the impact on geo-energy strains, soil temperature and the thermal interference radius.

6.2 Introduction

The geometry of geo-energy structures is generally designed in accordance with the building structural loads which might result in a limited thermal storage capacity for GES (Mehrizi et al., 2015; Musa et al., 2020; Lee et al., 2015). Therefore, thermal storage systems are highly recommended as possible solutions for GES to increase the thermal storage capacity and reduce the associated influence to soil temperature without the need to increase the size of structural elements (Musa et al., 2020). In building applications, Phase Change Materials (PCMs) are commonly used to increase the thermal energy storage due to the ability of absorb and/or release latent heat due to its solid-liquid phase translation (Peng et al., 2020).

Several studies were performed using the PCM as a thermal storage system in GSHP's applications but with different approaches including: i. mixing PCM with backfill materials in boreholes (Pu et al., 2019; Chen et al., 2017; Li et al., 2016; Qi et al., 2016; Wang et al., 2014; Bottarelli et al., 2015; Kong et al., 2017;

Dehdezi et al., 2012 ; Benli, 2010), around horizontal GHE (Pu et al., 2019; Bottarelli et al., 2015; Dehdezi et al., 2012; Benli, 2008) and surrounding vertical GHE (Chen et al., 2018; Kong et al., 2017; Li et al., 2016; Qi et al., 2016; Wang et al., 2014), ii. encapsulating PCM inside the energy pile (Han et al., 2018; Musa et al., 2020; Yang et al., 2021a, Cao et al., 2022; Bao et al., 2022; Yang et al., 2021b) and iii.

using a PCM slurry as a heat transfer fluid (Pu et al. 2019; Kong et al. 2017). Tables 6.1 and 6.2 summarise the methods and outcomes of available studies into the use of PCM in geo-energy piles.

Table 6.1. The available studies of using PCM for GSHPs

Method	Outcome	Reference
Numerically studied the effect of replacing 12.6 % backfill with PCM (paraffin wax) and compared it with standard grout.	>>The study concluded that PCM reduced the thermal radius. However, the thermal conductivity of paraffin wax led to a lower thermal efficiency of the grout.	Chen et al., 2017
Shape stabilized PCM material made of silica, graphite and deconic acid with mass of 10 %,6 % and 60 % respectively was used as backfill material for bore hole of 50 m depth and 150 mm diameter.	>>The study revealed that the use of proposed backfill increased the heat storage and heat transfer rate of the tested borehole by 35.9 and 22.3 respectively, compared to normal grout.	Li et al., 2016
Numerically compared the influence of 3 different PCMs (RT27, mixture of capric acid and lauric acid as 66:34 and enhanced acid with metal particles) as backfill materials on the thermal performance of borehole with 2 m diameter and 3 m depth.	>>It was revealed that a smaller thermal radius occurs whereas the heat transfer rate is reduced.	Qi et al., 2016
Numerically studied the performance of GSHP for 300 hrs at constant inlet temperature. Considering the effect of PCM backfill with	>>It was found that PCM could reduce the thermal radius but the heat transfer would be reduced as well.	Wang et al., 2014
Numerically examined the effect of mixing microencapsulated PCM into the backfill material and determined the thermal performance of horizontal GHE for two cases with and with out PCM backfill.	>>the results suggested that inclusion of micro capsulated PCM enhanced the heat pump performance by decreasing the temperature of GHE, which allows to smooth the thermal wave. However, the enhancement percentage was not reported.	Bottarelli et al., 2015
Studied the effect of the use of microencapsulated PCM on the thermos-physical properties of soil, using 5 different ratios of 10 %, 20 %, 30 %, 40 % and 80 % by volume.	>>The result showed that the addition of 40 % and 80 % PCM decreased the temperature variation in the soil at a depth 1 m by 2 ^{o}C and 3 ^{o}C respectively. In addition, COP of the horizontal GHE was enhanced by 17%.	Dehdezi et al., 2012
Experimentally investigated a GSHP coupled with PCM storage tank for greenhouse heating model. The study was conducted between October 2005 and May 2006.	>>The COP was found to be between 2.3 to 3.8 depending on the ambient temperature. However, there was no compassion between the experimented system and a conventional GSHP system without PCM tank.	Benli, 2010

Table 6.2. The available studies of using PCM for GEP.

Method	Outcome	Reference
Experimentally and numerically studies into the effect of PCM on the thermal performance of GEP with different flow rates.	>> It was revealed that the presence of PCM increased the extracted and rejected heat for the same flow rate by 16%.	Musa et al. 2020
Numerical analysis study aimed to elucidate the potential use PCM GEP as a renewable snow melting system.	>> The PCM modified GEP provided higher thermal energy extraction and therefore it would significantly reduce the required number of piles by 25-35 %.	Han et al.2018
Experimentally investigated the thermo-mechanical behaviour of PCM energy piles made with expanded perlite which impregnated with decly acid and lauric acid 66 % to 34 %, respectively and coated with epoxy resin then compared with traditional GEP.	>> During a continuous 10 hrs operation, the heat transfer rate increased from 2900 to 3162 KJ for traditional pile and PCM pile respectively. The displacement at the top of the pile, the internal peak stress and the maximum tip pressure were decreased for the PCM pile in comparison with the traditional pile.	Yang et al. 2021a
Numerical simulations were conducted to compare the influence of traditional and enhanced PCM backfill materials on the thermal performance of precast high strength GEP.	>> The result indicates that the thermal conductivity of the PCM backfill has extraordinary effect on the heat transfer rate of the energy pile. It shows that by increase the thermal conductivity of the PCM backfill by 0.2 W/(m.^{o}C) and 0.4 W/(m.^{o}C) the heat exchange rate of the GEP increased by 17 % and 32.6 %.	Cao et al. 2022
Experimentally investigated an innovative method to enhance the thermal performance of GEP using phase change steel balls as concrete aggregates.	>> The heat transfer rate of PCM pile was always larger than that measured for traditional pile. Also, the PCM pile showed more uniform temperature and restoration and a smaller temperature difference between soil and pile. This would produce lower internal stresses and deformation in the pile body.	Bao et al. 2022
Numerically studied the effect of thermal conductivity and phase change temperature of the PCM energy pile on it's thermal and mechanical behaviour.	>> From a thermal energy prospective: by increasing the thermal conductivity of the PCM GEP 2.1 to 3.1 w/m.k the thermal performance increased from 135.6 to 175.9 w/m, which led to increasing the soil influence radius. Concerning the mechanical behaviour,	Yang et al. 2021b

	increasing the thermal conductivity led to an increased thermal deformation, axial force and displacement. Thermo-mechanical behaviour is greatly affected by the phase change temperature of PCM for cooling mode. Decreasing the phase change temperature can improve the heat exchange rate and decrease the thermal influence radius. Also it would reduce the deformation and the axial forces.	
Experimentally investigated the thermal performance of GEPs modified with bio-based phase change materials impregnated in glass aggregates and fly ash aggregates.	The heat storage capacity of GEP was increased with the increase of PCM %. And concluded that incorporating biobased PCM in GEP is a promising and sustainable way of enhancing its thermal performance.	Olawoore, 2020

Based on the above critical review of the technical literature, it can be concluded that the majority of the research studies were carried out numerically to assess the effects of incorporating PCM in the backfill material for GHE. The three studies that were experimentally conducted to evaluate the influence of incorporating the PCMs into GES were performed using three different techniques including adding PCM steel balls as a replacement to aggregate Bao et al. (2022), using phase change material aggregate which made out of expanded perlite Yang et al. (2021a) encapsulating the PCM inside enclosed tubes at the centre of the pile Musa et al. (2020). However, to the best of the author's knowledge there are no available laboratory studies in the open technical literature to date into applying PCM in geo-energy wall (GEW). Therefore, the current chapter aims to address this gap by presenting a new concept for the development of PCM heat exchanger inside the GES e.g. piles and walls. The thermal performance of geo-energy piles and walls prepared with PCM-HE and standard-HE during cooling and heating processes are experimented and assessed. Moreover, the earth pressure and thermal deformation for the geo-energy piles and walls incorporating PCM-HE and standard HE are evaluated.

6.3 Significance

Worldwide spread use of renewable energy sources are encouraged to enable the UK and EU countries to meet their carbon emissions targets and assist with achieving the UN Sustainable Goals. The results obtained from this chapter are

expected to provide engineers and researchers with an innovative approach on how to enhance the thermal performance and thermal energy storage (TES) of geo-energy structures and reduce changes in the soil temperature, which consequently may reduce the thermal deformations resulted from the changes in GES temperature. In addition, the findings would offer a greater grasp of applying of PCM in GES applications for design practitioners and researchers who work in the related area.

6.4 Experimental work

In order to precisely investigate the thermal performance of geo-energy walls and piles with phase change materials (PCM) heat exchangers (HE), a PCM HE was manufactured and fastened inside GEP and GEW at the casting stage. The thermal performance of GEP and GEW with PCM HE was tested using fully instrumented testing. The heat transfer experiments consisting of three main parts, a testing tank, geo-energy structure and a data acquisition system. Details of the materials used in this experimental approach are demonstrated and discussed in the following sections.

6.4.1 Material properties

6.4.1.1 Sand

Standard building sand was selected to simulate the ground soil in this experimental study further details about the thermal and mechanical properties of the used sand can be found in section 3.3.1.1 in this thesis.

6.4.1.2 Concrete

All concrete batches were designed in compliance with the British Standards (BS 8500). The mixtures were designed with water/cement (w/c) ratio of 0.45 to achieve a target compressive strength ranging between 45 - 48 MPa after 28 days. special cylindrical concrete samples with an internal diameter of 100 mm and a height of 50 mm and 100 mm cubical concrete samples were prepared. The former was used to measure thermal conductivity using a hotplate testing setup, whereas the latter was used to assess the compressive strength of concrete. Furthermore, a concrete prisms with dimensions of 40 x 40 x 160 mm and

cylindrical concrete samples with a diameter of 100 mm and height of 300 mm were also prepared to measure the concrete thermal expansion coefficient in accordance with TI-B 101 (94), and to determine the concrete stiffness in accordance with EN 1992-1-2, 2004. Further information about the measurements of concrete properties can be found in section 3.3.1.3 and Table 6.3.

6.4.1.3 Phase Change Material (PCM) properties

Two different types of paraffin- based PCMs were considered in this study, namely: i. RT26, used for geo-energy pile test and ii. RT42, used for geo-energy wall test. Both materials are pure PCM with high heat storage during the phase transition to store/release substantial heat at nearly constant temperature. These utilising the process of phase change between solid and liquid (melting and congealing) PCM materials were selected primarily based on the results of Elkezza et al. 2022. where the ultimate steady state of soil temperature during cooling tests on identical geo-energy piles and walls were found to occur at 26 ^{o}C and 42 ^{o}C. Table 6.4 and Fig. 6.1 presented the detailed properties of the PCM provided by the supplier (Rubitherm Technologies GmbH). It is worth noting that the used PCMs are characterised by their high heat storage, releasing and storing heat at relatively constant temperature, no supercoiling effect, chemically inert and their stable performance through thousands of phase change cycles.

Table 6.3. Main properties of the used PCM.

Property	Value	Test Method
Thermal conductivity (W/m.k)	1.44	BS EN 12664:2001
Compressive strength (MPa)	45	
Stiffness (GPa)	28.2	EN 1992-1-2, (2004)
CTE ($^{o}C^{-1}$)	5.024 x10^{-6}	TI-B 101 (94)

where; CTE= coefficient of thermal expansion.

Table 6.4. Thermal and mechanical properties of concrete

Properties	RT26	RT42
Melting area (^{o}c)	25-28	38-43
Congealing area (^{o}c)	27-25	37-43
Heat storage capacity (kj/kg)	180	165
Specific heat capacity (kj/kg.k)	2	2
Density solid (kg/l)	0.88	0.88
Density liquid (kg/l)	0.75	0.76

Heat conductivity (both phase) (w/m.k)	0.2	0.2
Volume expansion (%)	12.5	12.5
Flash point	150	150

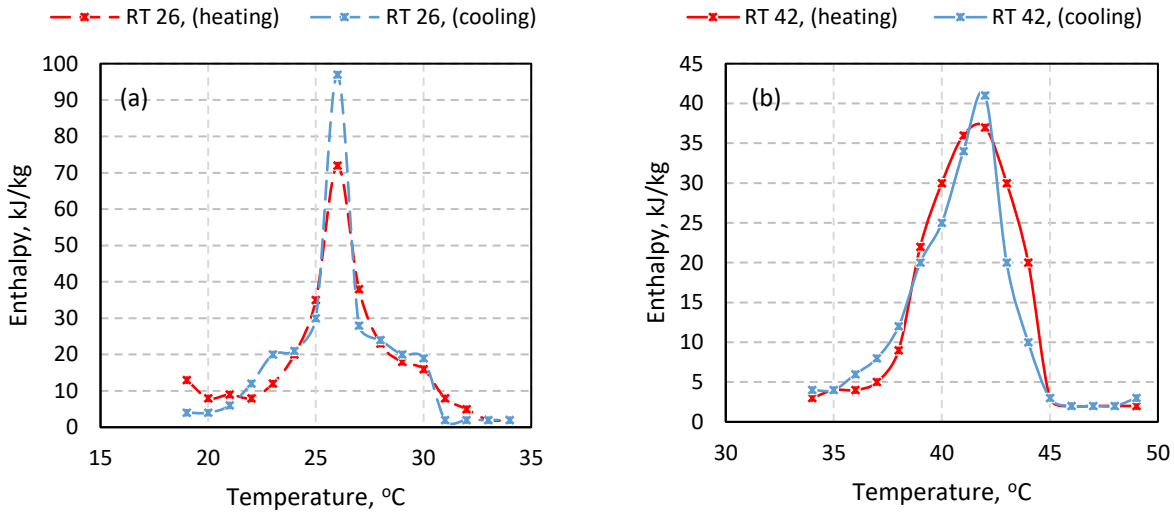

Fig. 6.1. Enthalpy of a). RT26 and b). RT42.

6.4.2 Heat transfer experiments

6.4.2.1 Fabrication of HE's

For a precise assessment of the thermal response of geo-energy piles and walls made out with PCM heat exchangers, geo-energy piles and walls were made using i. strandared heat exchanger (HE) and ii. phase change material heat PCM

(HE). The standard HE is a U-shaped heat exchanger [HE] made from nylon with a total length of 1700 mm and outer and inner diameters of 8 mm and 6 mm respectively. Whereas the PCM (HE) is made of double pipes where a smaller diameter pipe was held concentrically inside a larger pipe. The inner pipe acts as a heat transfer fluid carrier, whearas the outer pipe hosts the PCM around the inner pipe as shown in Fig. 6.2. The inner pipe is made from nylon and with the same size as those of standard HE whilst the outer pipe is made of polybutylene with inner and outer diameters of 19 mm and 22 mm respectively. However, selecting different materials for the outer pipe could lead to a better thermal performance. Faizal et al. (2016), revealed that the higher thermal conductivity pipe

materials can result in a positive impact on the thermal performance of GEP. A 560.49 cm^3 and 2802.45 cm^3 of RT26 and RT42 were used to fill the space between the inner and outer pipes which was used in geo-energy piles and walls respectively.

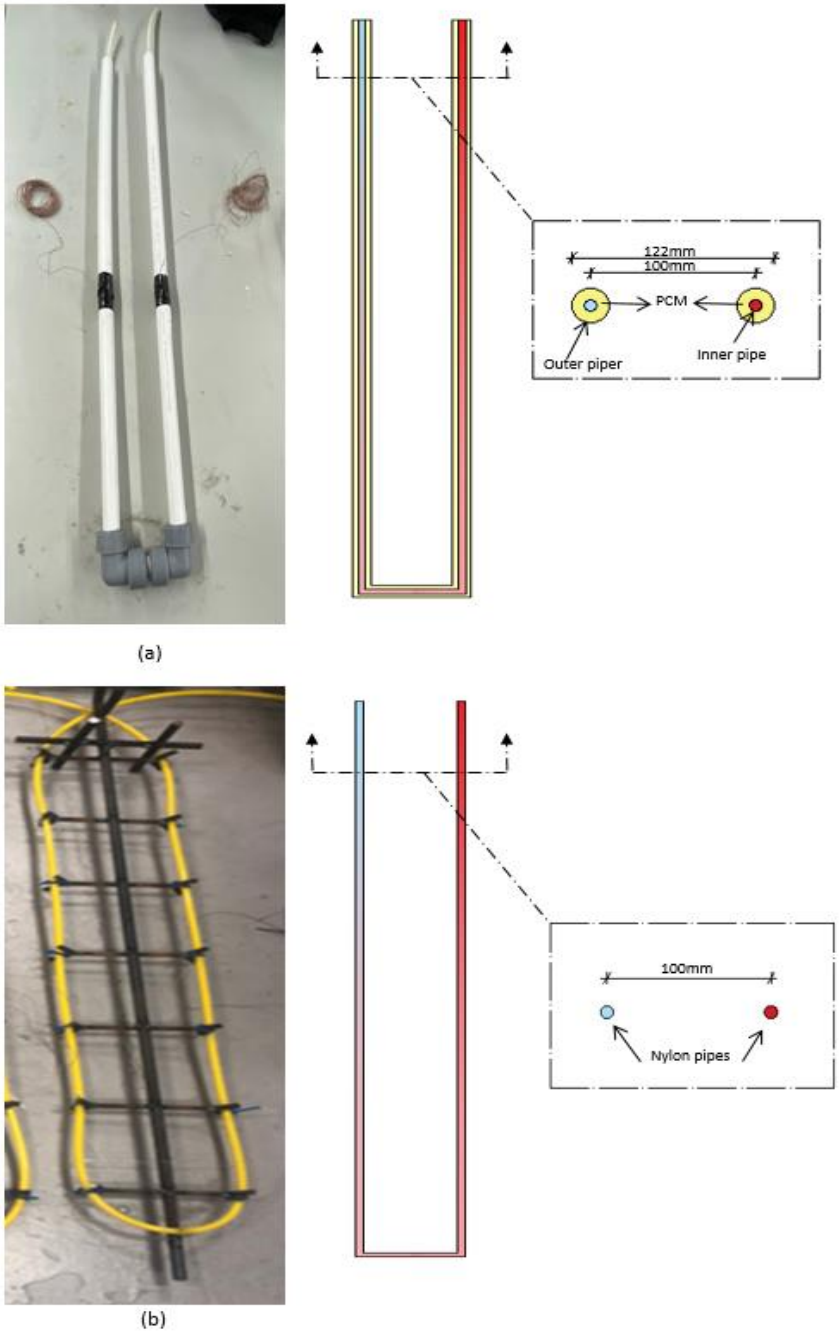

Fig. 6.2. Heat Exchangers used in geo-energy pile (a) PCM HE and (b) standard HE.

6.4.2.2 Geo-energy structures expermintal setup

To evaluate the thermal performance of geo-energy piles and walls with PCM heat exchangers, a fully instrumented heat transfer testing rig with internal dimensions of 1 m x 1 m x 1 m was designed and manufactured. the schematic

diagrams of the testing rig and configuration of the geo-energy piles and walls are presented in Figs. 6.3 and 6.4, respectively. The experimental rig consisted of, fully insulated experimental tank, drainage system, geo-energy piles and walls, and sand . Thermos couples connected to data acquisition system were utilised to measure the temperature at pre-determined location as shown in Figs. 6.3 and 6.4.

In total 4 experiments were carried out including 2 tests on energy piles and 2 tests on energy walls with fixed and variable parameters demonstrated in Table 6.5. The first two tests were conducted on piles using standard heat exchanger and PCM heat exchanger. Two more experiments were carried out on energy walls with standard heat exchanger and PCM heat exchanger. All thermocouples were calibrated against an accurate thermocouple, achieving an accuracy around ± 0.25 ^{o}C Prior to their use.

Table 6.5. Fixed and variable parameters for GEP and GEW tests.

Series		Fixed parameters	Variable parameters
GEP	1	FR = 67 l/h, PSS, WL=500 mm	Standard HE
		FR = 67 l/h, PSS, WL=500 mm	PCM HE
GEW	2	FR = 67 l/h, PSS, WL=500 mm	Standard HE
		FR = 67 l/h, PSS, WL=500 mm	PCM HE

Where, PCM= phase change materials, HE= heat exchanger, PSS= Partly Saturated Sand, FR = Flow Rate, and WL= Water Level.

6.4.2.3 Testing procedure

After the installation of all devices and completing sand-filling, a mix of degradable glycol-water ratio (1:3) was circulated in the HE. The flow rate of the circulating fluid was controlled using a pump at a rate of 67 l/h throughout the tests. Each test was kept running continuously for 100 hrs so as to undertake two cycles of cooling and heating. In the cooling cycle, a hot glycol-water with an inlet temperature of 52 ^{o}C was continuously circulated in the heat exchanger within the geo-energy structure for 24 hrs. The heating cycle is then carried out by circulating cold glycol-water mix with an inlet temperature of -2 ^{o}C for 24 hrs. It should be noted that all tests were performed whilst the sand surrounding the geo-energy

structural was partly saturated with water by keeping the water level inside the tank at 500 mm above the base, resulting in a steady hydrostatic water pressure which simulates a real-world scenario where geo-energy piles and walls are installed in grounds with a stagnant groundwater level at a particular height. All measurements were taken every 10 seconds using a data acquisition system and saved automatically in a computer, while an hourly average was then determined and presented hereafter.

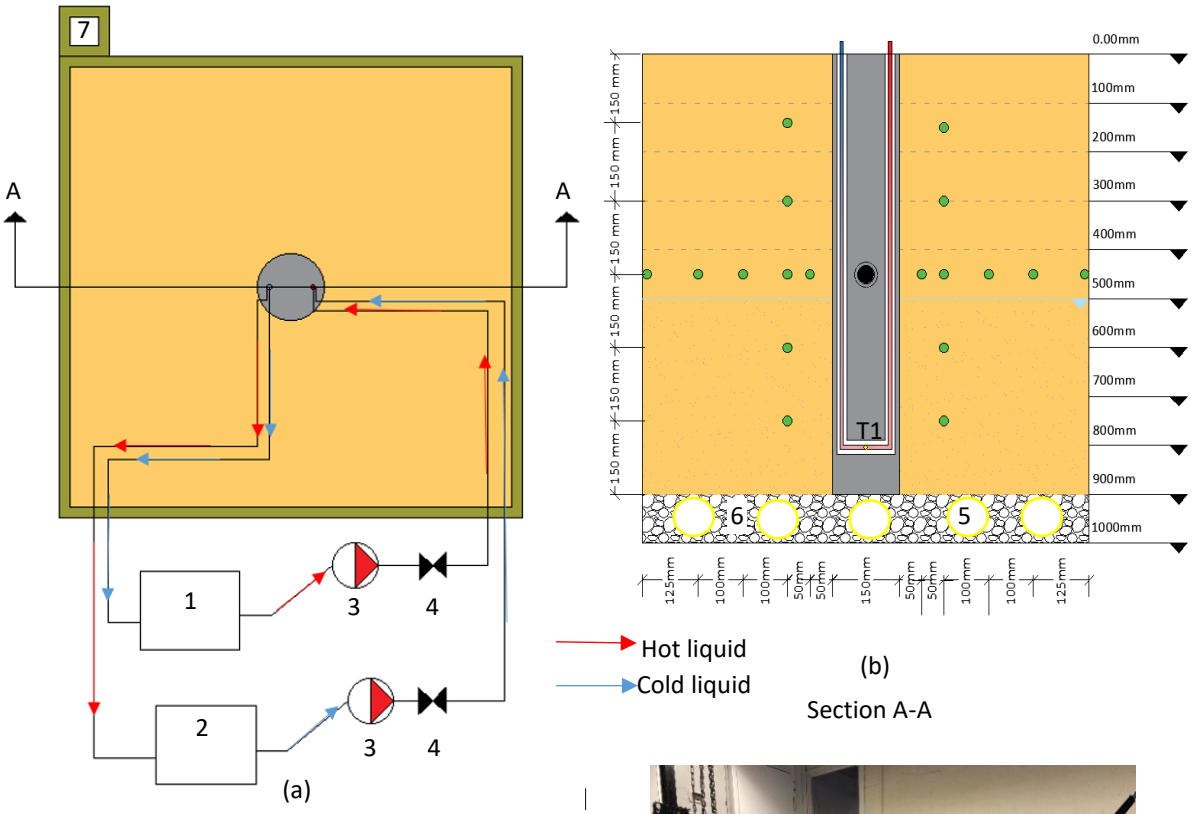

●	Thermocouples in soils
T1	Thermocouples inside HE
●	Thermocouples in concrete
◌	Pressure cell
1	Control temperature tank (heater)
2	Chiller
3	Central heating pump
4	Flow control
5	Perforated pipes
6	Gravel bed
7	Well
– –	Synthetic filter

(c)

Fig. 6.3. Experimental rig for geo-energy pile tests: (a) Plan view, (b) Vertical cross section of the testing tank showing location of thermocouples and (c) Image of the testing rig.

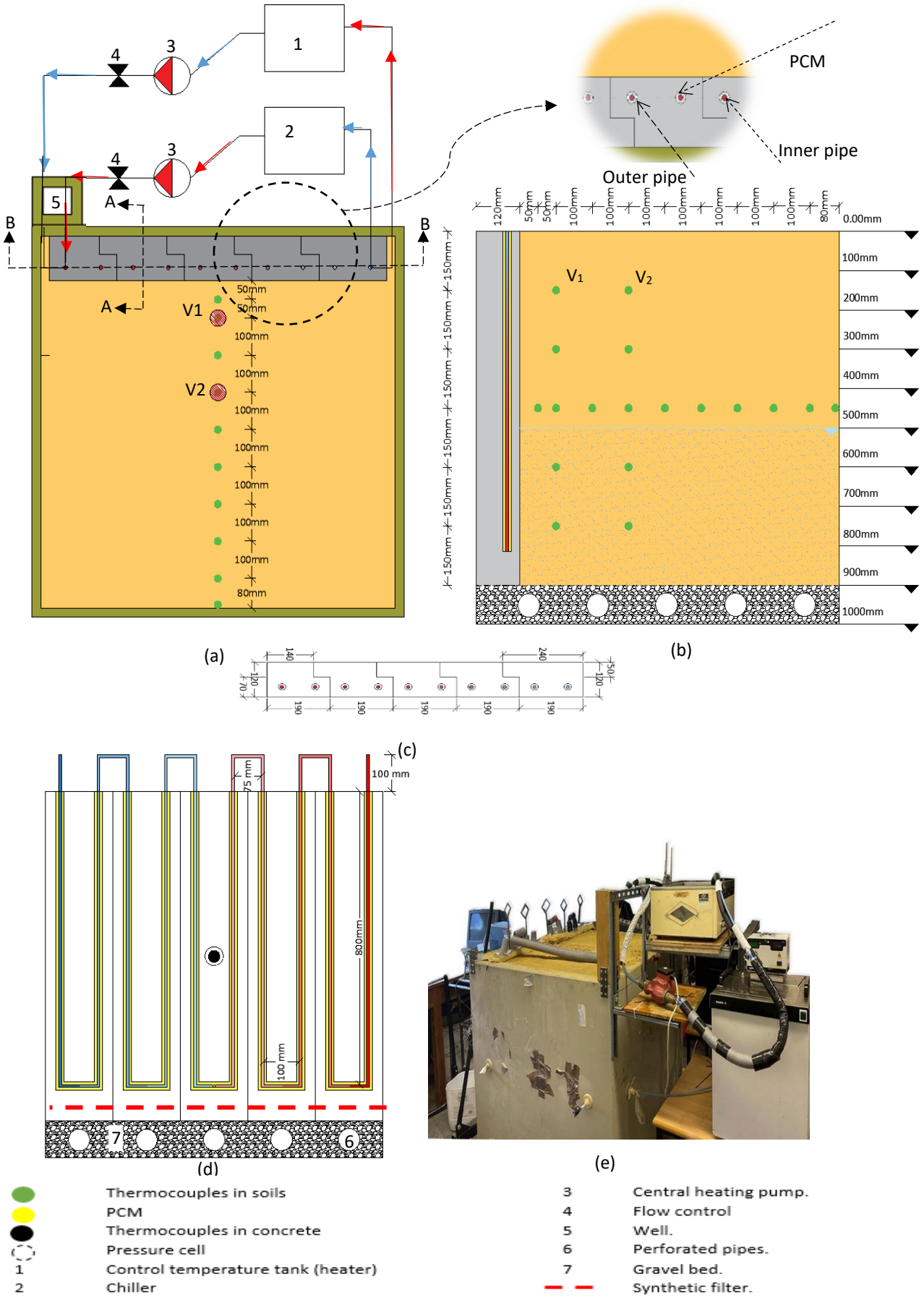

Fig. 6.4. Experimental rig for geo-energy wall tests: (a) Plan view, (b) Vertical cross section of the tested energy wall, (d) section B-B, location of thermocouples, e) image of real test rig.

6.4.3 Evaluation of experimental data

To assess the extracted/rejected thermal energy from and to the geo-energy structure, total heat exchange rate expressed by Equation 3.2 was determined. Furthermore to assess the change in soil temperature due to heat extraction and rejection from the geo-energy structures, excess soil temperature (EST) which is defined as the diffrence between actual soil temperature during the test and original soil temperature. EST can be possitive (+ve) value during the cooling cycles or negative (–ve) value during the heating cycles and can be deduced as given by Equation 6.1:

$$EST = T_{t_i} - T_O \tag{6.1}$$

The unconstrained thermal strain of the geo-energy structure caused by the temperatures change of the concrete was defined and measured using equation 3.3. In addition, the thermal stress due to the temperature change of concrete can be expressed by the general Hook's law as following:

$$\rho_{thermal} = \pm E * \varepsilon_{thermal} \tag{6.2}$$

where; $\rho_{thermal}$ is the thermal stress of the geo-energy structure due to temperature change, E refers to young's modulus of the concrete and the negative sign means the concrete of the geo-energy structure is cooled.

6.5. Results and discussions

6.5.1 Heat transfer in geo-energy pile

Fig. 6.5a shows the variation in the temperature of the circulating fluid at inlet point, base of the HE (T1) and Outlet point for geo-energy piles equipped with a standard HE and PCM HE during a continuous cooling-heating operation. The flow rate of the circulating fluid was kept constant through the test at 67L/hr. A temperature difference is notable in Fig. 6.5b which clearly reflects the degree of heat exchange between the geo-energy piles and surrounding soil. It is worth mentioning that during cooling tests the circulating fluid was circulated with an inlet temperature of 52^{o}C whilst during the heating stages the circulating fluid was circulated with an inlet temperature of -2 ^{o}C. Careful inspection of Fig. 6.1 illustrated that PCM RT26 generates about 34 % higher energy during cooling than heating.

Fig. 6.5b demonstrates the temperature difference between inlet and outlet that was recorded in geo-energy piles equipped with standard HE and PCM HE. It can be observed that the pile equipped with a PCM HE gave a higher temperature difference. For both pile tests, the temperature difference in the heating cycle is slightly higher than that recorded during the cooling cycle, which reveals a better heat exchange performance of the piles during the heating operation. The results demonstrated that a geo-energy pile with a standard HE has temperature difference of about 2.15 ^{o}C and 2.11 ^{o}C in heating and cooling cycles respectively after reaching steady-state conditions which was reached after 16 hrs of continuous operation. Whereas in the case of geo-energy pile with a PCM HE, the temperature difference recorded after reaching steady state conditions was 3.77 ^{o}C and 3.10 ^{o}C in heating and cooling cycles respectively. This could be attributed primarily to the impact of PCM (RT26) which generates about 34 % higher energy during cooling than heating (see Fig. 6.1). The average of temperature difference of the last eight hours of heating and cooling cycles have been calculated to determine the percentage of improvement, the results revealed that the thermal performance of geo-energy pile tends to enhance during heating and cooling by about 75 % and 43 %, respectively when PCM HE was embedded inside the GEP.

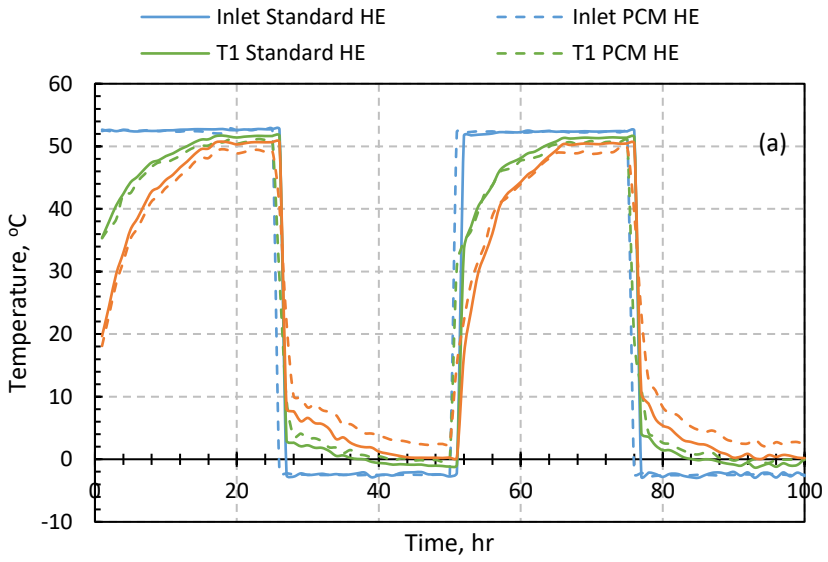

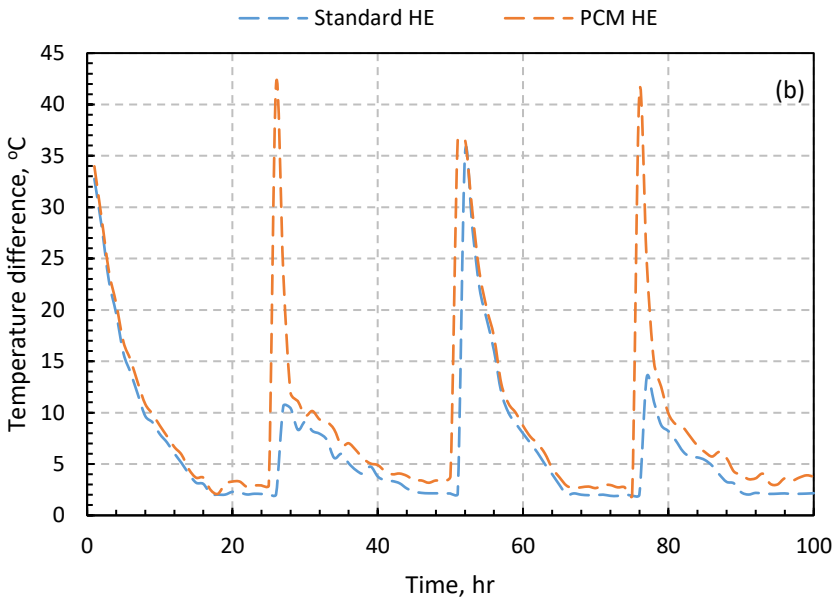

Fig. 6.5. Measured circulating fluid temperature a). inlet, T1 and outlet temperature b). Temperature difference between inlet and outlet.

In order to aid the discussion, the heat exchange between the geo-energy pile and soil was calculated using Equation 3.2 and presented in Fig. 6.6. It is obvious that the dissipated and extracted heat in a geo-energy pile with PCM HE is higher than that reported for a geo-energy pile with a standard HE. This could be attributed to the use of PCM which enhanced heat transfer from and to the pile by i. sensible heat due to temperature change and ii. storing the latent heat during phase transition of PCM. Therefore, the total amount exchanged heat due to PCM incorporation increased remarkably.

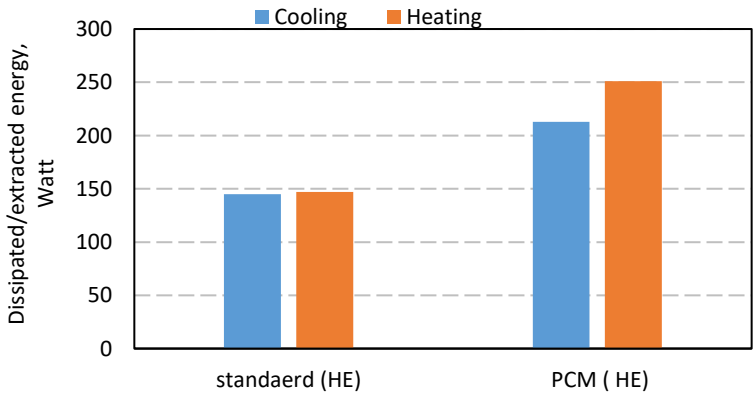

Fig. 6.6. Dissipated or extracted energy in a geo-energy pile with a standard HE and PCM HE.

The influnce of PCM HE on the temperature of soil surounding the GEP is assessed based on the results recorded by 24 thermocouples that were installed in the soil in pre-determined locations (see Fig. 6.3). Fig. 6.7 shows the soil temperature that was recoreded during the two cycles of continuous cooling and heating operation for 100 hrs. Temperature measurements were taken at horizontal distances of 50 mm, 100 mm, 200 mm, 300 mm and 425 mm in both sides of the pile at a depth of 450mm from the tank base. The results clearly illustrate that in both tests with a standard HE and PCM HE a similar trend was recorded where temperature dropped with increasing the distance from the pile. In addition, maximum temperature difference after reaching a steady state condition was observed at 50 mm from the pile and gradually decreased with the increase in horizontal distance. However, it is very notable that the changes in soil temperature are much lower in the case of geo-energy pile equipped with a PCM HE. Precisely, during the cooling cycle, the excess soil temperature (EST) after reaching steady state conditions at radial distances of 50 mm, 100 mm, 200 mm, 300 mm, 425 mm were 10.6, 8.29, 4.8, 3.29 and 1.44 ^{o}C respectively in case of GEP with a standard HE whereas the corresponding values for GEP with a PCM HE were found to be 3.22, 1.43, 0.9, 0.86 and 0.58 ^{o}C respectively. This illustrates a remarkable impact for encapsulating PCM around the HE in reducing the temperature difference in the soil surrounding the geo-energy pile which is attributed to the capacity of PCM to store thermal energy between the cooling and heating cycles. In heating tests where surrounding soil is likely to drop its temperature, the temperature difference at radial distances of 50 mm, 100 mm, 200 mm, 300 mm, 425 mm were recorded and found to be 11.9, 9.29, 3.44, 1.28, and 0.20 ^{o}C respectively for GEP with a standard HE and 4.24, 1.06, 0.38, 0.21, and 0.08 ^{o}C respectively for GEP with a PCM HE. Based on data presented in Fig. 6.7, it can be also observed that the interference region between the pile and soil can be considered as the most affected region which is often given by the radius of interference. From the results of the two tests, a soil-pile interference radius was identified to be around 300 mm and 100mm for geo-energy piles with a standard HE and a PCM HE respectively. This could be attributed to the latent heat that released and absorbed by the PCM which can not only enhance the thermal performance but also can reduce the soil temperature changes and the thermal interference radius of GEP.

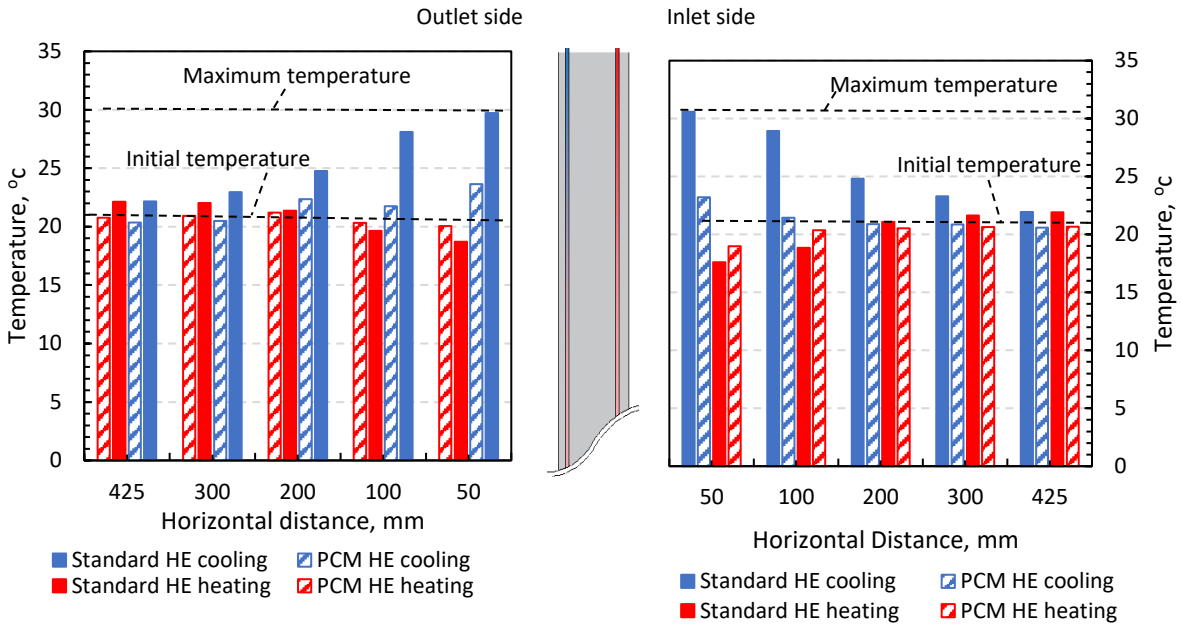

Fig. 6.7. Soil horizontal temperature profile at mid-height of GEP with a standard HE and a PCM HE.

Fig. 6.8 shows the variation in soil temperature along the depth of pile after reaching steady state conditions in case of GEP with a standard HE and a PCM HE. Data in Fig. 6.8 demonstrate that during the heating cycle, soil temperature increased with the depth of GEP as the circulating fluid travelled inside the HE but with a different temperature range depending on the type of HE. Furthermore, during the cooling stages, the changes in soil temperature were observed to be less prominent in case of GEP with a PCM HE than that recorded for a GEP with a standard HE. Data recorded showed that temperature changed from 20.88 ^{o}C at 150mm to 22.33 ^{o}C at 750 mm for GEP with a PCM HE, whereas for a GEP with a standard HE, the soil temperature was found to change from 26.20 ^{o}C to 29.38 ^{o}C at the same measurement points. In contrast with the heating stages, the vertical soil temperature between 150 mm and 750 mm was found to increase from 20.17 ^{o}C to 21.92 ^{o}C for GEP with a PCM HE and from 16.86 ^{o}C to 20.33 ^{o}C for GEP with a standard HE.

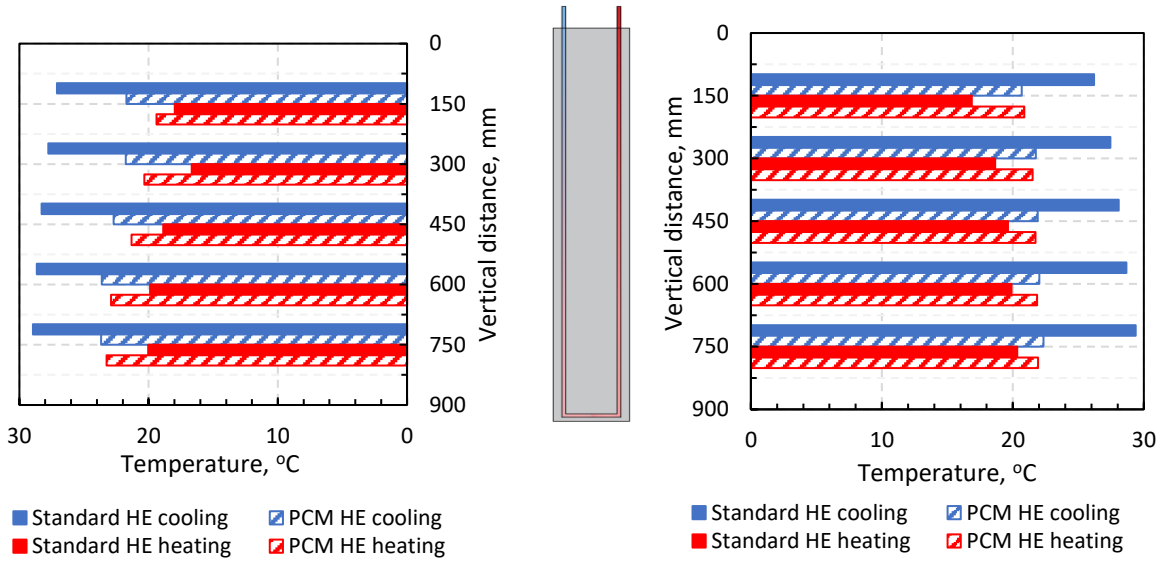

Fig. 6.8. Soil vertical temperature profile at 100mm from standard HE and PCM HE GEP.

Fig. 6.9a displays the lateral earth pressure measured at mid-height of pile for GEP with a standard HE and a PCM HE. The pressure cell was placed at the soil-pile interface on the inlet side. According to Fig. 6.9a, the initial value of lateral earth pressure was approximately 5225.80 Pa for GEP with a standard HE and 5115.70 Pa for GEP with a PCM HE. During the cooling stage, the pile is heated and the lateral earth pressure gradually increased until reaching a peak pressure of 5551.20 Pa and 5320. 10 Pa for GEP with a standard HE and a PCM HE respectively at the end of cooling stage. Then the lateral pressure started to decrease to reach 5293.22 Pa and 5106.40 Pa for GEP with a standard HE and a PCM HE respectively. This could be a result of the induced thermal expansion/shrinkage due to heating/ cooling of concrete which led to an increase/ decrease in the lateral earth pressure at the soil pile interface. To assist the discussion, Equation 3.3 was used to determine the thermal strain that caused by the thermal expansion/ shrinkage of both piles. It is worth mentioning that to precisely estimate the thermal strain, it was essential to determine the coefficient of thermal expansion. An experiment was conducted in accordance with TI-B 101 (94) on concrete samples to determine the coefficient of thermal expansion which was found to be 5.024×10^{-6} ^{o}C-1. Fig. 6.9b and c show that the increase in pile temperature led to an increase in the thermal strain which caused an increase in the soil pressure at the pile side. On the other hand, reducing the pile temperature

would lead To a decrease in the thermal strain which in turn would cause a drop in the soil pressure at the pile-soil interface. Therefore, values for the lateral pressure in the case of GEP with a PCM HE were lower than those measured for GEP with a standard HE under the same conditions of flow rate and inlet temperature. Further analysis, to determine the internal thermal stress that generated in the pile due to temperature changes was deduced using Equation 6.2. In order to precisely estimate the thermal stress, it is essential to determine the modules of elasticity of concrete. The modulus of elasticity (E) was determined from the measured data in accordance with EN1992-1-2, (2004). The result revealed that the stiffness of the concrete was 28.2GPa. Consequently, the thermal stress is determined and presented in Fig. 6.9d. It can be seen that peak stresses are −270 and – 100.6 kPa for GEP with a standard HE and a PCM HE respectively. This can be attributed to that higher temperature rise in standard HE energy pile caused larger thermal strain compared with the PCM HE. This indicates that the PCM HE energy pile can reduce the thermal deformation of geo-energy pile caused by thermal stress intensity at the middle of GEP.

6.5.2 Heat transfer in geo-energy wall

Two tests were carried out using geo-energy walls made with a standard HE and a PCM HE and installed at the side of the experimental tank. Measurements for the circulating fluid temperature were taken at inlet, T1 and Outlet for a standard HE geo-energy wall and a PCM HE geo-energy wall. Fig. 6.10 presents measured temperature data and temperature difference for geo-energy wall with the two types of HE. It should be noted that both walls were installed in a partly saturated soil and tested whilst maintaining the same circulating fluid flow rate at a value of 67L/hr. Furthermore, the cooling test was performed by circulating the fluid with an inlet temperature of 52^{o}C whilst during the heating stages the fluid was circulated with an inlet temperature of -2^{o}C. It can be seen from Fig. 6.10 that there is a notable difference between inlet and outlet temperatures in both the PCM HE and standard HE energy walls during the cooling stages during cooling and heating cycles.

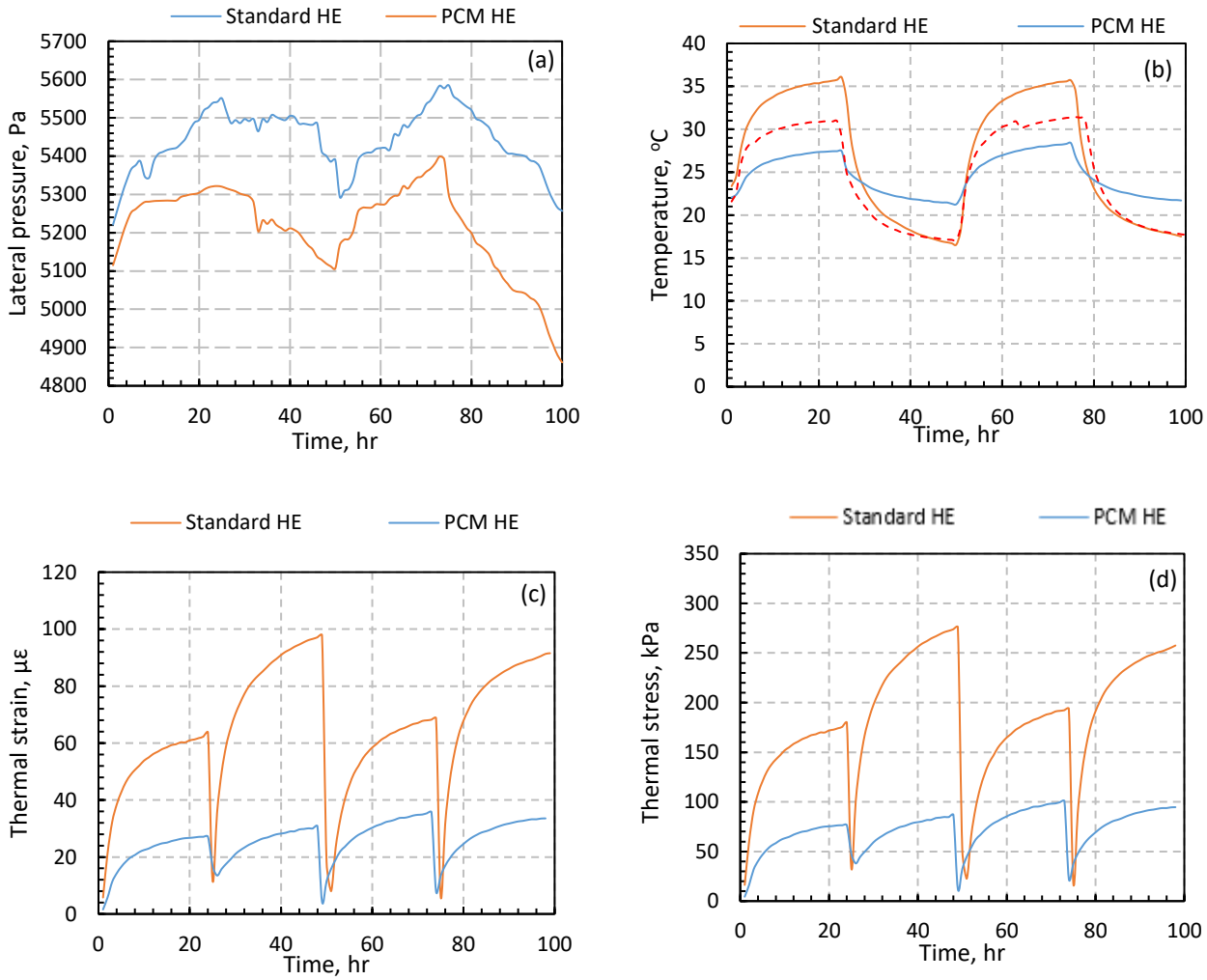

Fig. 6.9. a) Lateral earth pressure at the mid height of standard HE and PCM HE GEP; b) Change of temperature for standard HE and PCM HE GEP and the PCM; c) The calculated thermal strain for standard HE and PCM HE GEP; d) The calculated thermal stress for both.

This temperature difference indicates heat exchange between the wall and the surrounding soil. It can clearly be observed from Fig. 6.10b that GEW equipped with a PCM HE experienced the highest differences in temperature. Moreover, The heat exchange between the geo-energy wall and soil was calculated using Equation 3.2 and presented in Fig. 6.11. It is obvious that the dissipated and extracted heat from the PCM HE pile is higher than that reported for a geo-energy wall with a standard HE. This is attributed to the use of PCM HE for the energy walls which allows the wall to transfer the heat by two mechanisms sensible heat cauced by the change in temperature, and by stores the latent heat energy due

to PCM phase transition, consequently, the amount exchanged heat can be greatly increase.

Furthermore, Fig. 6.10 (b) shows that for both wall tests, the temperature difference in the heating cycles is slightly larger than that in the cooling cycles, which revealed a better heat exchange performance of the wall during the heating operation. On average, for standard HE wall heating and cooling cycles, about 5.47^{o}C and 5.72 ^{o}C differences were recorded after reaching steady-state conditions (after 16 hrs of operation), respectively. For PCM HE wall, the steady state temperature difference was 8.18 ^{o}C and 7.23 ^{o}C in heating and cooling cycles respectively. This could be attributed to that the used PCM (RT42) generates about 13% higher energy during cooling than heating see Fig. 6.1.These results provide reliable proof that the thermal performance of geo-energy wall tends to enhance by about 43 % and 32 % for heating and cooling cycles respectively when PCM was encapsulated around the heat exchanger in the GEW.

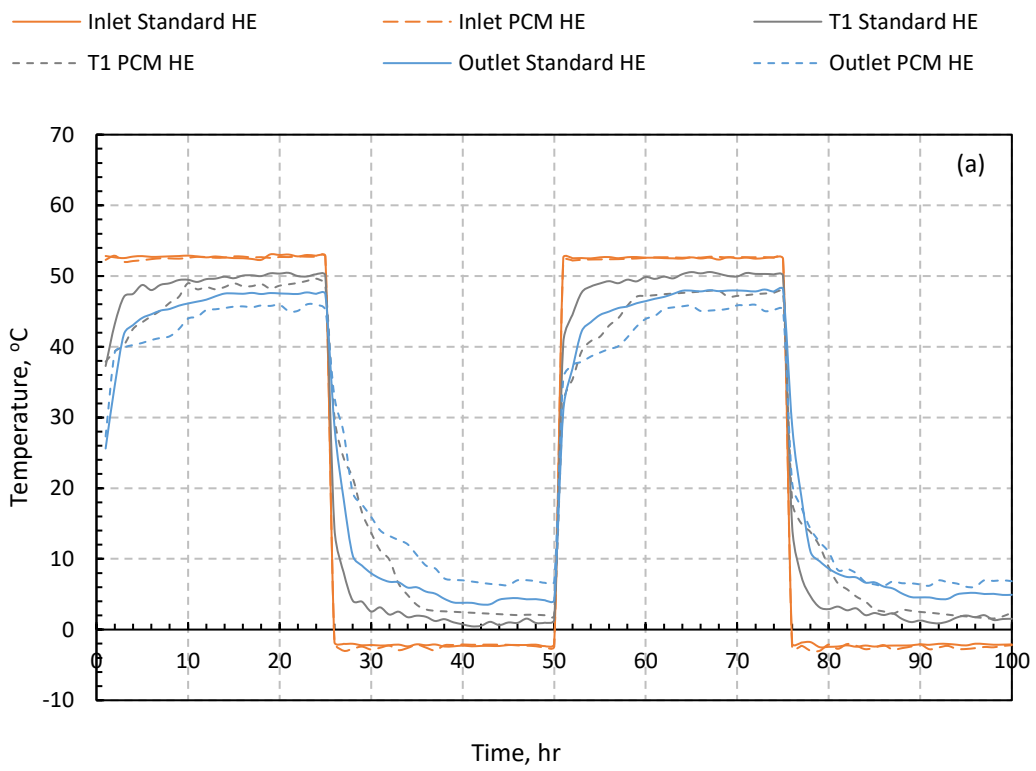

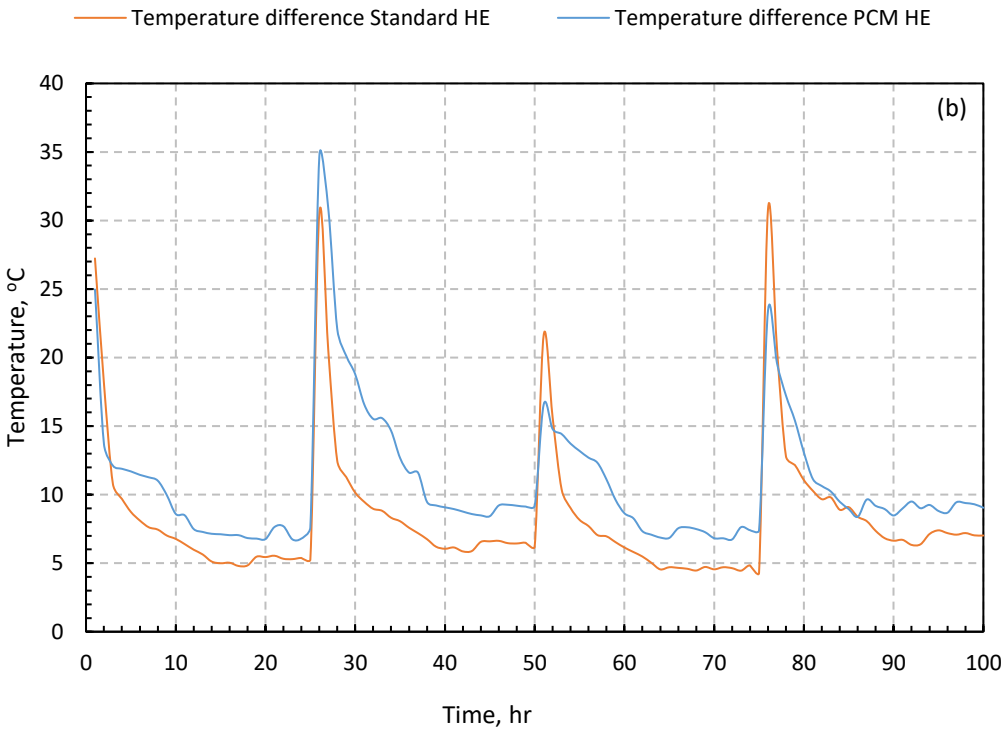

Fig. 6.10. Data for measured circulating fluid temperature in GEW a) Temperature measurements at inlet, T1 and outlet temperature, b) Temperature differences between inlet and outlet.

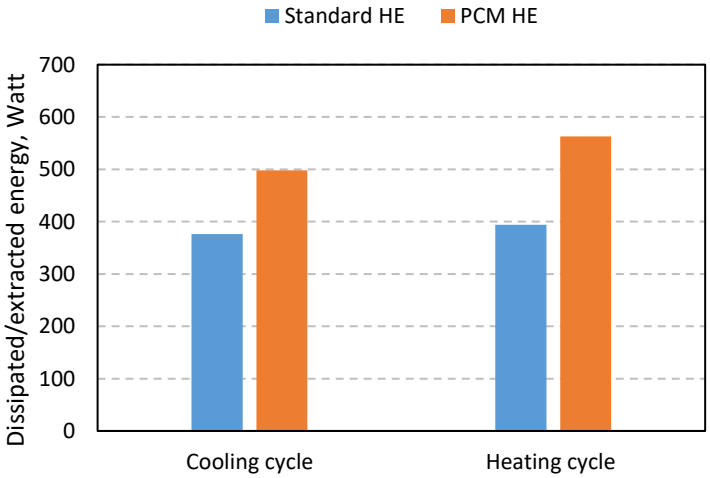

Fig. 6.11. Dissipated/ extracted energy from standard, (HE) and PCM, (HE) GEW.

The horizontal soil temperature profile measured at mid-height of the wall is presented in Fig. 6.12. The soil temperature was measured at 50 mm, 100 mm, 200 mm, 300 mm, 400 mm, 500 mm, 600 mm and 880 mm away from the wall. It was observed that an interference region between the wall and soil can be considered

as the most affected region in the experimental tank. From the results of the two tests, a soil-wall interference region was identified to be around 600 mm and 400mm for geo-energy walls with a standard HE and a PCM HE respectively. The pattern of temperature variation with distance was similar irrespective of the type of the HE. It is also observed that maximum temperature excess after reaching steady state conditions was observed at 50 mm from the wall and gradually decreased with the increase in horizontal distance. During cooling cycle, the steady state excess in soil temperature (EST) at horizontal distance of 50 mm, 100 mm, 200 mm, 300 mm, 400 mm, 500 mm, 600 mm, 700 mm, 880 mm are respectively 17.64, 17.41, 12.65, 11.56, 6.86, 4.37, 1.96, 1.96,and 1.44 ^{o}C for geo-energy wall with a standard HE, whilst the corresponding values for geo-energy wall with a PCM HE were 11.17, 8.85, 6.05, 2.56, 2.44, 1.47, 1.47, 1.47 and 1.47 ^{o}C respectively. Data for the EST during the heating cycle at the same measurement points were found to be -10.73, -10.13, -8.3, -6.74, -5.46, -3.77, -2.77, -2.77 and -2.77 ^{o}C respectively for a geo-energy wall with a standard HE wall and -3.95, -3.05, -2.1, -1.54, -0.75, -0.47, -0.47, -0.47, and -0.47 ^{o}C respectively for a geo-energy wall with a PCM HE. From the results of the horizontal soil temperature profile can clearly conclude that the soil temperature rise and the thermal interference region of PCM HE wall are without doubt smaller than those for the standard HE wall. This could be attribute to the latent heat that releasing and absorbing of the PCM which can not only enhance the thermal performance, but also can reduce the soil temperature changes and the thermal interference zone of GEW.

The influence of PCM HE inclusion in GEW on the vertical soil temperature profile is also assessed and compared with the standard GEW. The soil temperature profile was recorded at two vertical sections (V1 and V2) which were located at 100 mm and 300 mm away from the experimented energy wall, respectively as shown in Fig. 6.4.

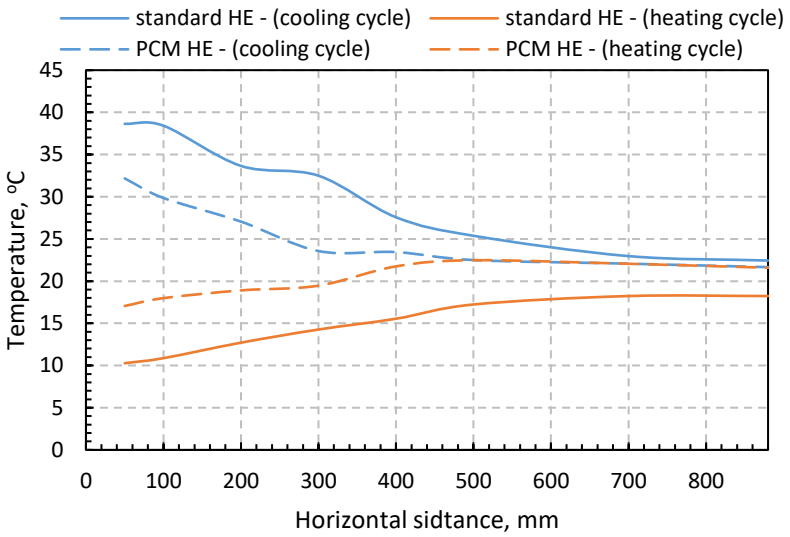

Fig. 6.12. Soil horizontal temperature profile at the mid-height of standard HE and PCM HE GEW.

The measurements of temperature along V1 and V2 were taken at depths of 150 mm, 300 mm, 450 mm, and 750 mm. The data for soil temperature after reaching steady-state conditions at V1 and V2 were plotted in Fig. 6.13. The data clearly showed that the soil temperature at section V1 was significantly higher than that measured further away at section V2. During the cooling stages, the steady state temperature changes for GEW with a PCM HE was found to be less than those measured for GEW with a standard HE. Soil temperature changed from 30.45 ºC at 300 mm to 27.63 ºC at 750 mm for GEW with a PCM HE, whereas for a GEW with a standard HE, the soil temperature changed from 35.82 ºC to 36.02 ºC exactly at the same measurement points. In contrast during heating stages, the vertical soil temperature changed from 18.55 ºC at 300 mm to 18.48 ºC at 750 mm for GEW with a PCM HE whereas those measured for GEW with a standard HE were 14.08 ºC and 14.85 ºC at 150 mm and 750 mm respectively. Furthermore, it can be observed that the influence of the PCM HE on reducing the soil temperature changes around GEW was significant in comparison with the case of using standard HE. This can be justified by the ability PCM to store or reject more energy, hence reduce the energy that might be extracted or rejected into the ground (Mousa et al., 2020).

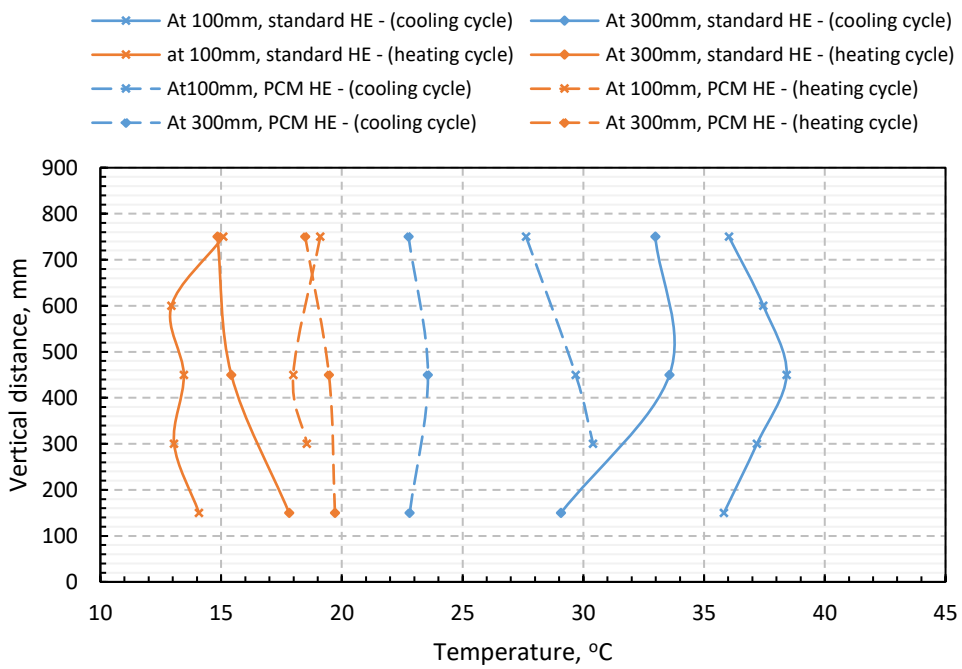

Fig. 6.13. Soil vertical temperature profile at 100mm and 300mm from GEW with a standard HE and a PCM HE.

A pressure cell was installed at mid-height of the soil-wall interface to measure the lateral earth pressure. Fig 6.14a shows the measured lateral earth pressure at mid-height of the wall. According to the data captured, the initial value of lateral earth pressure was approximately 5.56 kPa for GEW with a standard HE and 4.29 kPa for GEW with a PCM HE. During the cooling stage the wall is heated and the lateral earth pressure increased gradually until reaches a peak pressure of 14.73 kPa and 13.56 kPa for standard HE and PCM HE wall respectively, at the end of cooling stage. Then it starts to decrease to reach 13.44 kPa (standard HE) and 12.72 kPa (PCM HE). According to Dong et al. (2019), this could be attributed to the induced thermal expansion/shrinkage due to heating/ cooling which leads to increase/ decrease in the earth pressure at the soil wall interface. To explain this behaviour, Equation 3.3 was utilised to determine the thermal strain for both walls as a function of temperature changes. Data for the thermal strain and temperature of the walls and PCM were presented in Fig. 6.14 (b) and (c) and demonstrate that when the temperature of the wall increased, the correspondingly strain increased (expansion) reversely, when the temperature of the wall reduced, strain decreased (shrinkage). Generally, for the same flow rate tests the PCM HE wall shows smaller temperature rise and thermal strain than the standard HE.

Also, it worth to mention that the change of the temperature in GEW produces internal stress which can be determined using Equation 6.2. The calculated thermal stresses are presented in Fig. 6.14d, according to data in Fig. 6.14d, the peak thermal stress of GEW with a PCM HE and a standard HE are 253.33 kPa and 333.01 kPa respectively during cooling stages. Whereas, during the heating stages the peak thermal stress of PCM HE wall is 393.32 kPa and that for standard HE wall is 477.09 kPa. This can be justified by the higher temperature change in the standard pile when compared with that for PCM HE pile.

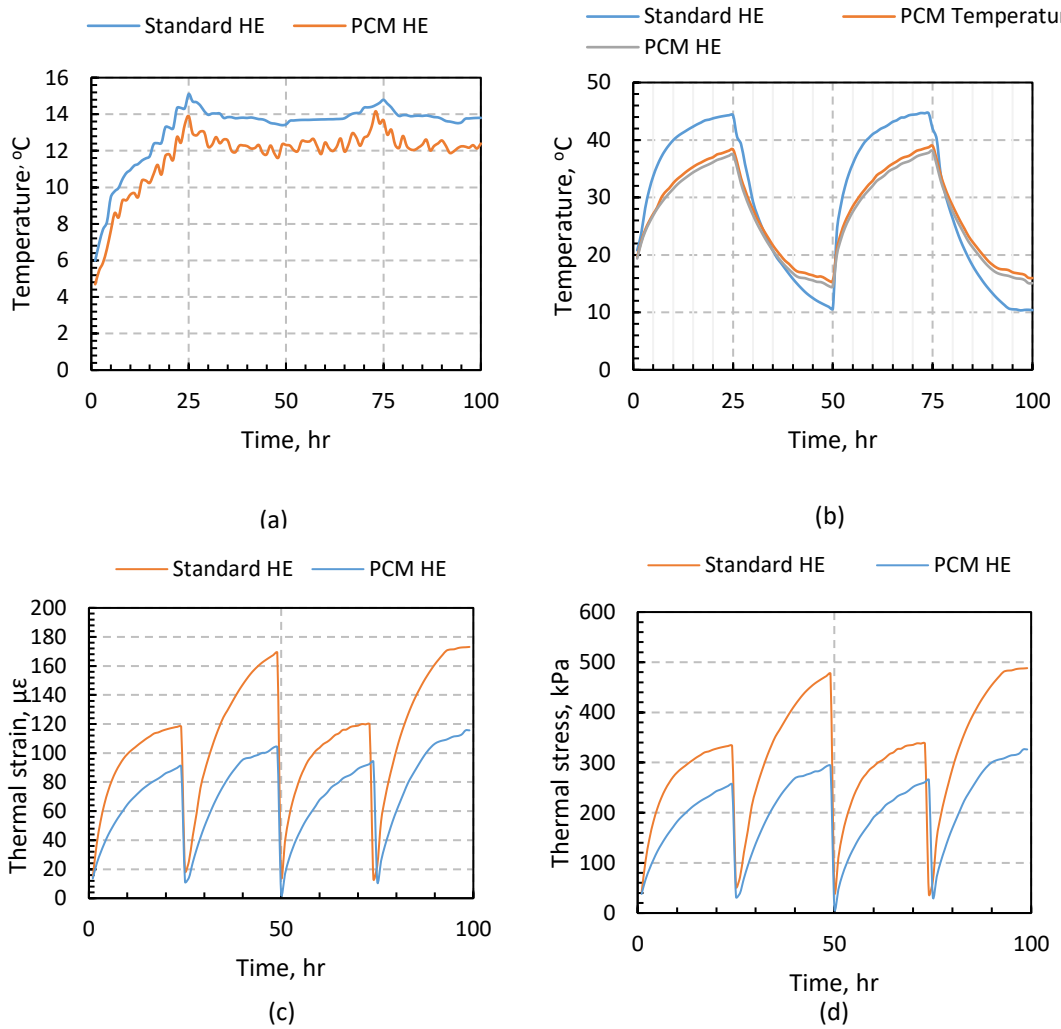

Fig. 6.14. Lateral earth pressure at the mid height of standard HE and PCM HE GEW; b). Change of temperature for standard HE and PCM HE GEW and the PCM; c). The calculated thermal strain for standard HE and PCM HE GEW; d). The calculated thermal stress for both walls.

6.6 Summary

The current chapter assesses the thermal performance of geo-energy piles and walls fabricated with phase change material (PCM) heat exchangers in comparison with the performance of the same energy structure but with standard heat exchangers. Two types of PCM were used for piles and walls in the current study based on their melting points, namely RT26 and RT42, respectively. The main conclusions that could be drawn from the chapter are as follows:

- The inclusion of PCM immediately around heat exchangers has an effective positive impact on enhancing heat transfer for GEP by 75 % and 43 % for heating and cooling, respectively and for GEW by 43 % and 32 % for heating and cooling cycles.
- The PCM heat exchanger significantly reduced the changes in soil temperature and thermal interference zone of geo-energy piles and walls.
- Due to low temperature rise of PCM HE GES, the lateral earth pressure at the pile side and the wall face is reduced in comparison with the standard HE.
- Also, the thermal strain and stresses that produced by the change of GES temperature are decreased when the PCM HE is used.

Chapter 7: Assessment of using the phase change lightweight aggregate to enhance the thermal and mechanical interaction between soil and geo energy structures.

7.1 highlights

- Milled Carbon fibre showed the best performance and durability for sealing PCM impregnated LWA's.
- Adding PCM impregnated LWA's to sand led to dropping the MDUW and OMC, while it increased the permeability coefficient and the friction angle of the soil mix.
- The thermal energy storage of the soil and PCM LWA's mixes increased by increasing the percentage of PCM in the mix.
- The use of 35% by volume ratio at the soil/GES interface showed significance increase in the efficiency of Geo-energy piles and wall.
- The inclusion of PCM LWA's at soil/GES interface reduces the thermal stress and strains at the GES body.
- GES operation thermal effect on surrounded soils was also reduced when PCM LWA's was used.

7.2 Introduction

Thermal energy storage (TES), often known as heat storage, enables storage of heat energy in a material, so that can be used in the future . TES can be applied mainly through two techniques, namely sensible heat storage and latent heat storage (Mehling and Cabeza, 2008). Sensible heat storage, which is the most prevalent technique applied, is fundamentally based on storing the thermal energy by raising the temperature of the storage medium in the range of sensible heat storage (See Fig. 7.1). For example, storage of heat in the ground is one of the common applications where sensible TES method can be applied. Heat is stored or released not only due to the change in temperature but also can be through the change in material's phase. The latter is known as latent heating, and its principle based on storing the heat during the phase change material without any shift in temperature, as shown in Fig. 7.1. The amount of heat that is retained when a substance goes through a phase shift without affecting its temperature is

known as latent heat (See Fig. 7.1). The term "phase change materials" (PCM) refers to the substances that are able to transform from solid to liquid, and appropriate for temperature-sensitive heat storage.

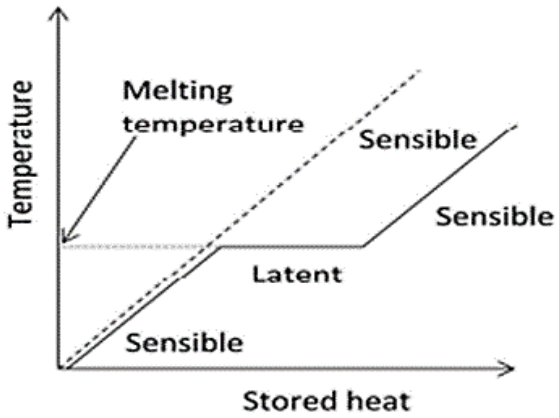

Fig. 7.1. Sensible and latent heat storage.

Since 1980, PCM has been used as a potential source for thermal storage in construction materials (Mehling and Cabeza, 2008). Temperature stabilisation and the storage/delivery of heat with minimal temperature differences are two potential uses for PCMs. The ability of PCM to minimise the heating and cooling loads inside buildings has been investigated by several researchers. For instance, Feldman et al. (1995) found that the storage capacity of PCM prepared from 1 m^2 gypsum wallboard impregnated with 23% by weight of methyl stearate and methyl palmitate in a temperature range of 3.5 ^oC was approximately 12 times higher than that found in wallboard alone. By using a different PCM made from Gypsum board with 25% weight Butyl stearate, Athientis et al. (1997) indicated that PCM could lower the maximum room temperature in passive solar structures by about 4°C throughout the day. Cabeza et al. (2007) highlighted that concrete wall contained almost 5%wt of microencapsulated paraffin wax as PCM was able to minimising the maximum interior dry bulb air temperature by around 2 °C during summer period. According to Hunger et al. (2009), adding 5%wt of microencapsulated paraffin wax to the concrete mix saved almost 12% of the energy needed for running air conditioners and keep the internal temperature inside a building constant at 23.5°C. Castell et al. 2010 pointed that the inclusion of PCM in brick walls used in establishing and regulating the interior temperature led to saving around 15% of the energy, compared with the same walls made

without any PCM. Lightweight aggregate can also be employed as a PCM carrier in concrete application, allowing a considerable amount of PCM to be used (up to 8% by weight of concrete) without impairing the mechanical qualities (Ramakrishna et al., 2015; Pongsopha et al., 2021). However, one significant disadvantage is the leakage of PCM to the concrete's surface over time (Sukontasukkul et al., 2020; Pongsoph et al., 2019).

PCM has also been involved in the ground source heat pump systems (GSHP's), in the applications of boreholes and geo-energy piles. Recent studies indicated that the incorporation of PCM in boreholes applications can highly enhance the thermal storage capacity and heat transfer efficiency, in addition to reducing the thermal influence radius in soils (Wang et al., 2014; Li et al., 2016; Chen et al., 2018).

Recently the use of PCM for geo energy piles got extensive attention and it has been investigated in many studies (Han and Yu, 2018; Mousa et al., 2020; Yang et al., 2021a; Yang et al., 2021b; Cao et al., 2022; Bao et al., 2022). Yang et al. (2021a) examined the thermos-mechanical behaviour of PCM energy piles prepared with expanded perlite (impregnated with 66% of lauric and 34% of decly acids), and coated by epoxy resin. The heat transfer rate rose during a continuous 10-hour operation from 2900 to 3162 KJ, compared to the conventional piles. Also, their results showed a reduction in the displacement of PCM piles at the top-of-pile, internal peak stress, and maximum tip pressure. Another computational analysis to examine the thermal performance of the PCM energy pile in terms of phase change temperature and thermal conductivity was conducted by Yang et al. (2021b), The findings showed that the thermal performance of the PCM GEP rose from 135.6 to 175.9 w/m due to the thermal conductivity improvement of the PCM. Also Increased thermal deformation, axial force, and the top displacement. Han and Yu (2018) conducted numerical analysis to clarify the possible use of PCM GEP as a renewable snow melting technology. The results indicated that number of required piles would be greatly decreased by 25–35% because the PCM-modified GEP significantly increased the thermal energy extraction. Mousa et al. (2020) investigated the thermal performance of GEP incorporated with PCM at various flow rates using both experimental and numerical

methods. It is found that the extracted and rejected heat for the same flow rate were found to rise by 16% in the presence of PCM.

More recently, phase change steel balls were used as concrete aggregates in an experimental study by Bao et al. (2022) to improve the thermal performance of GEP. The heat transmission rate of PCM pile was reported always higher Compared to traditional piles. In addition, the temperature and restoration in the PCM pile were more consistent, and the temperature difference between the pile and the soil was lower. As a result, the internal tensions and deformation in the pile body could be clearly reduced. The thermal performance of precast high strength GEP was recently simulated by Cao et al. (2022) to evaluate the performance of PCM backfill materials. The outcome showed that the thermal conductivity of PCM backfill significantly affected the heat transmission rate of energy piles. The heat exchange rate of the GEP rose by 17% and 32.6 % when the thermal conductivity of the PCM backfill increased by 0.2 and 0.4%, respectively.

Based on the critical review of the literature and aforementioned discussion, it can be noted that although several studies have been carried out on the effect of the inclusion of PCM in geo-energy piles applications, no comprehensive work has been found in the literature regarding the use of PCM in geo-energy walls. Furthermore, none of these studies have investigated the use of PCM at the soil/GES interface. Nevertheless, a numerical investigation was conducted by Qi et al. (2020) to assess the thermal behaviour at a pile/soil interface. This study demonstrated that the heat transfer coefficient (h) at the pile-soil interface can be varied during cooling or heating. Therefore, accurate heat transfer values at the interface must be calculated properly during the design of system, and experimental studies are necessarily needed to support and validate the findings obtained from the limited numerical research. According to Bourne-Web et al. (2020), the geo contact thermal resistance is sensitive to sand density, and it can be decreased between loose and thick sand by 0.02 and 0.005 m2/kW, respectively.

The purpose of this chapter was to use coated-PCM-impregnated LWAs to enhance the thermal energy storage surrounded geo-energy piles and walls. The main objectives of this study are to: i. produce coated PCM impregnated light-

weight aggregate, ii.mix the produced PCM LWA's with soil and evaluate the improvement of the TES for the mixes, iii. Apply the enhanced TES soil mix at the soil/GES interface and assess the heat transfer efficiency of geo energy piles and walls and iv. Study the thermal expansion and the lateral earth pressure on the GES.

7.3 Experimental work

In order to enhance the thermal energy storage (TES) of the sand and evaluate the effect of thermally enhanced sand on the thermal performance of geo-energy piles and walls, the experimental work was divided into three main stages. The first stage covered the production of PCM impregnated light weight aggregates, while the second stage has focused on the enchantment of the TES of sand using PCM Impregnated lightweight aggregates. The final stage presented the thermal and mechanical performance of the geo-energy piles and walls after the inclusion of PCM impregnated LWA at the soil/structure interface see Fig 7.2.

7.3.1 Production of PCM LWAs

7.3.1.1 Materials.

In this section, the main properties of various materials such as PCMs, LWAs, and coating materials are discussed.

7.3.1.1.1 PCM

Two different types of paraffin-based PCMs were considered in this study, namely: I. RT26, used for geo-energy pile testing and ii. RT42, used for geo-energy wall test. Both materials are pure PCM with high heat storage at the phase transition temperature. These PCM materials were selected primarily based on the results of Elkezza et al. 2022, where the ultimate steady state of soil temperature during the cooling tests of identical geo-energy piles and walls was found to occur at 26 ^{o}C and 42 ^{o}C. Table 6.4 and Fig. 6.1 a and b presented the detailed properties of the PCM provided by the supplier (Rubitherm Technologies GmbH). It is worth noting that the used PCMs are characterised by their high heat storage, releasing and storing heat at a relatively constant temperature, no super-coiling effect, chemically inert and their stable performance through thousands of phase change cycles. The thermal stability (PCM weight change during different

temperatures) of the PCM has been examined using thermogravimetric analysis (TGA) Q500 V3.17 Build 265 equipment.

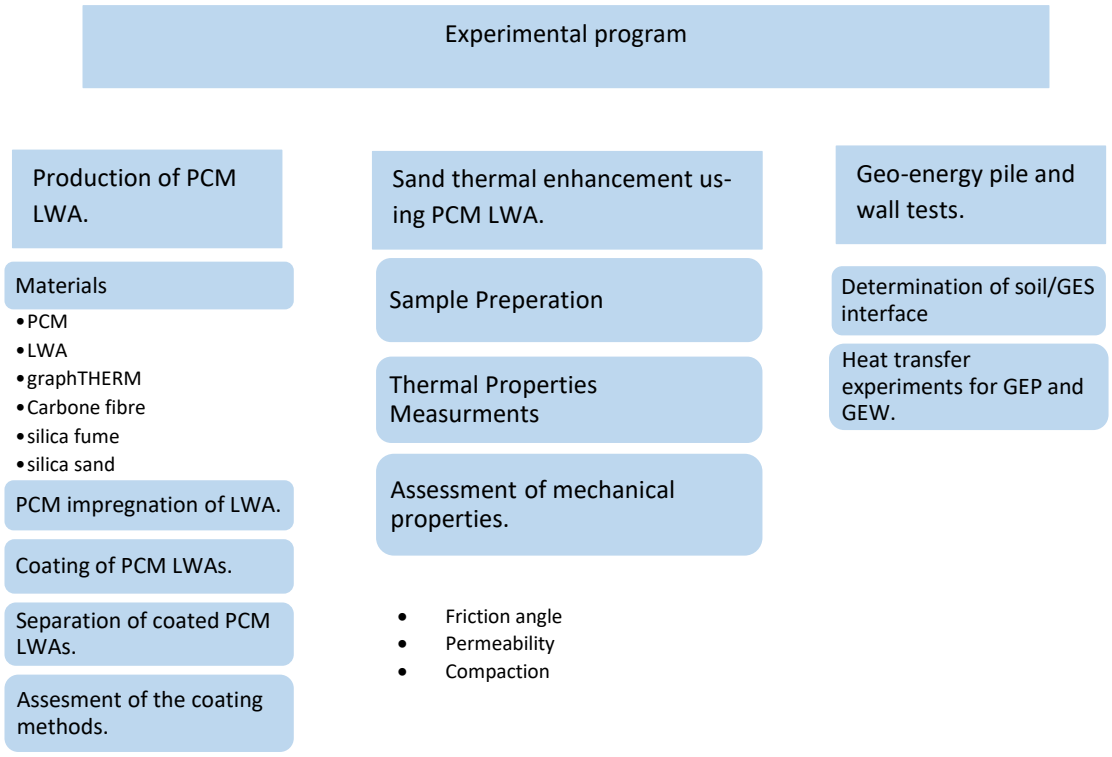

Fig. 7.2. Experimental work stages.

About 40 ±10mg of each PCM (RT26 & RT42) was loaded in the TGA and subjected to a temperature ranges from 15 ^{o}C to 60 ^{o}C at a temperature change rate of 5 ^{o}C/minute under air flow rate of 10ml/min (Bensharada et al. 2021). The results obtained from the TGA test were presented in Fig. 7.3 and revealed that there were little or no weight losses of both PCMs during and after the test. Therefore, the PCMs can be considered as thermally stable and reliable to be used for soil thermal energy storage enhancement.

7.3.1.1.2 light weight aggregates (LWAs)

LWA is an aggregate type that is characterised by a very low bulk density with a range of 100 - 1000 kg/m^3 and low specific gravity (0.1 to 1.5) (Shendy, 1991). It can also be considered as a highly porous medium which helps in absorbing more liquid than normal aggregate. In this study, lightweight expanded clay ag-

gregate (LECA), as shown in Fig. 7.4, was used to host the PCM due to its availability and low cost. The particle size of the used LECA ranged from 4 mm to 10 mm, while the bulk density was 500 kg/m^3.

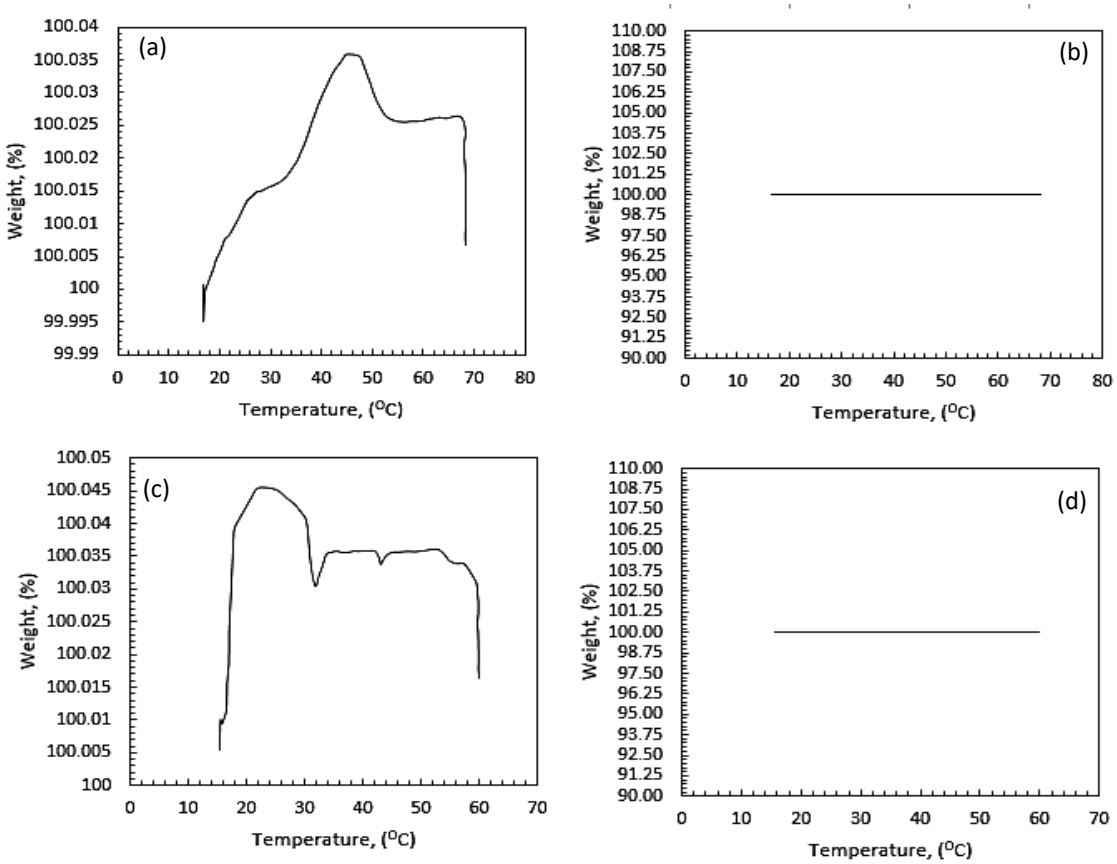

Fig. 7.3. TGA curve (a), (b) for RT42; (c), (d) for RT26.

Fig. 7.4. Typical LECA.

7.3.1.1.3 graphTHERM

The thermally enhanced graphite powder was developed by georg h. luh gmbh, further information about this material can be found in section 3.3.1.2.

7.3.1.1.4 Milled Carbon fibre

This material made from recycled carbon fibre milled to 80µ/100µ made from standard modulus fibre. This material have thoroughly explained in chapter 5, section 5.4.1 and Table 5.1.

7.3.1.1.5 Silica Fume

This type of densified silica fume (micro silica) is produced in the electric furnace during the production of silicon metals and other ferrosilicon alloys. The silica fume consists of a high percentage of amorphous (non-crystalline) silicon dioxide, and it has a density of 500-700 kg/m^3 and a particle size of less than 45 microns. The chemical analysis, as provided by the supplier, is shown in Table 7.1.

Table 7.1. Chemical analysis of silica fume (Westbrook resource Ltd)

Constituents	**Percentage (%)**
SiO_2	92% min
Fe_2O_3	2% max
MgO	3% max
Al_2O_3	1% max
LOI*	6% max
K_2O	3% max
CaO	3% max
Moisture	Not specified
Na_2O	3% max
C	3% max

*Loss on ignition representing organic matter content.

7.3.1.2 PCM impregnation of LWAs

Fig. 7.5 illustrates the experimental setup that was used in this chapter to impregnate the PCM in LWA's. The setup consists of vacuum chamber, A vacuum pump, water path and pipes. The vacuum chamber was used to host the lightweight aggregate and the melted PCM during the process of suction. Furthermore, the vacuum pump was unlisted to provide 75 kPa suction pressure throughout the impregnation process.

A 1 kg of oven dried LWA' was placed inside the vacuum chamber. Then, a perforated plate was putted inside the chamber to cover the LWA's, a 5kg steel weight was also putted on the top of the plate inside the chamber, to keep the LWA's under the plate to prevent it from floating to the surface during the impregnation process. After that, the melted PCM was poured inside the chamber and the vacuum pump was switched on in order to begin air suction from the LWA's pore space, which took around 4 hrs from LWA's absorption till the PCM reached the peak. At the end of the impregnation process, the vacuum was turned off, and the impregnated LWA's were taken out of the chamber and immediately put inside a fridge for 24 hrs to allow the PCM to solidify. Table 7.2 shows the quantities and the percentage of PCM that was impregnated in the LWA's used in this study.

Table 7.2. The quantities and the % of PCM impregnation.

Constituents	RT26	RT42
Original weight of LWA'S (gm)	3200	3100
Weight after PCM impregnation (gm)	58062.81	55368.96
Percentage of impregnated PCM (%)	82	78
Weight after coating (gm)	67338.30	64033.80
Percentage of PCM after coating (%)	61.08	62.12

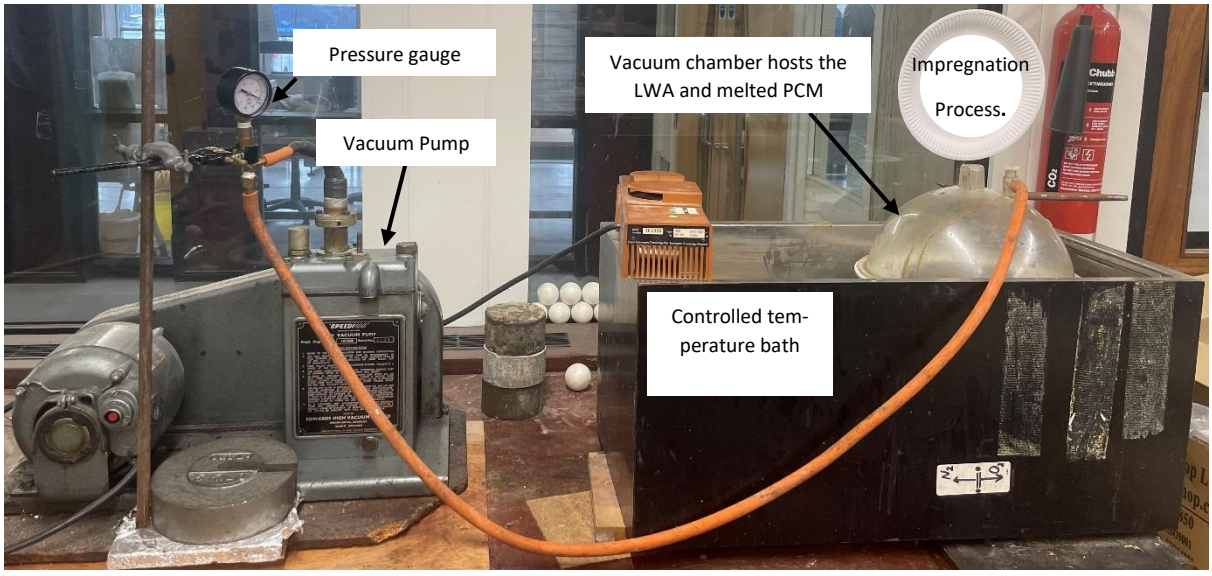

Fig. 7.5. PCM impregnation of LWAs setup.

7.3.1.3 Coating of PCM impregnated LWAs

In a recent study by Sani et al. (2021), to the use of epoxy resin for coating the PCM impregnated LWA's with graphite powder has been proposed to avoid the concern of coalescing of the coated LWA's. Similarly, Kastiukas et al. (2016), suggested the use of polyester resin to cover the surface of PCM impregnated LWA's, and the findings showed that this method reduced PCM leakage up to 3%. Also, kheradmand et al. (2015) coated the PCM impregnated LWA's with three different methods by using sikalastic-490T (waterproofing liquid membrane), makote 3 (bituminous emulsion) and weber dry lastic (liquid used for water proofing the building roofs). From the results, they observed that the coating thickness was not homogenising and the PCM still leaked. In this study, to prevent the issue of PCM leaking from impregnated LWA's, flexilon 457 (resin) and flexilon 1117 (dilution) were mixed with a mixing ratio of 60% and 40%, respectively. Both materials were supplied by Rosehill Polymers.Ltd. Firstly, flexilon 457 and flexilon 1117 were combined inside a container to form the coating material. Then, the PCM impregnated LWA's were taken from the fridge and placed inside the coating solution for about 5 minutes. While the PCM aggregates were in the coating solution. It was manually turned around to ensure that all the aggregates were uniformly coated and soaked with coating. It has been observed, that the coated PCM LWA's tends to stick to one another, while the hardening of the coating material, as shown in Fig. 7.6. it worth mentioning that the separation of the coated PCM LWA's at this stage was impossible and any force would result in damaging the coating of the LWA's.

7.3.1.4 Separation of coated PCM LWA's

Kheradmand et al. (2015); Memon et al. (2015); Kastiukas et al. (2016) and Sani et al. (2021) Experienced a problem where the coated PCM LWA's sticked together during the coating hardening. To solve the issue, Kastiukas et al. (2016) sprinkled different materials such as glass powder, quartz and granite over the sticked PCM LWA's. it was stated that after sprinkling the coated PCM LWA's with the materials before the coating material fully hardened, it was easy to separate the coated PCM LWA's. the assessment of these thress separation material

shows that the granite powder provided the best choice in terms of ease of separation and uniform coating however, about 3% PCM leakage was reported. Memon et al. (2015), used silica fume to separate the coated paraffin-LWA how ever it dosit show a great performance for sealing the PCM LWA's. Kheradmand et al. (2015), suggested the use of four different waterproof materials such as sikalastic-490T, Makote 3 and Weber dry lastic as coating materials. They also reported that there is no method has solved the issue of PCM LWA's sticking together. In the study of Sani et al. (2021), two materials were used, namely Redhill sand and graphite powder, to help the separation of coated PCM LWA's during the hardening of the epoxy resin. They observed that using Redhill sand produced a non-uniform coating surface and most of the coated PCM LWA's were coalesced together. Also, they added that the graphite powder coated PCM LWA's yielded a product with a uniform coating layer and were separated from each other. In this study, to separate the particles of PCM LWA's during the hardening of the coating material, graphTHERM, milled Carbon fibre and silica fume were chosen to be sprinkled over the PCM LWA's five minutes after the coating with the coating materials, and manually sieved, and left to totally dry for 24 hrs (See Fig.7.6).

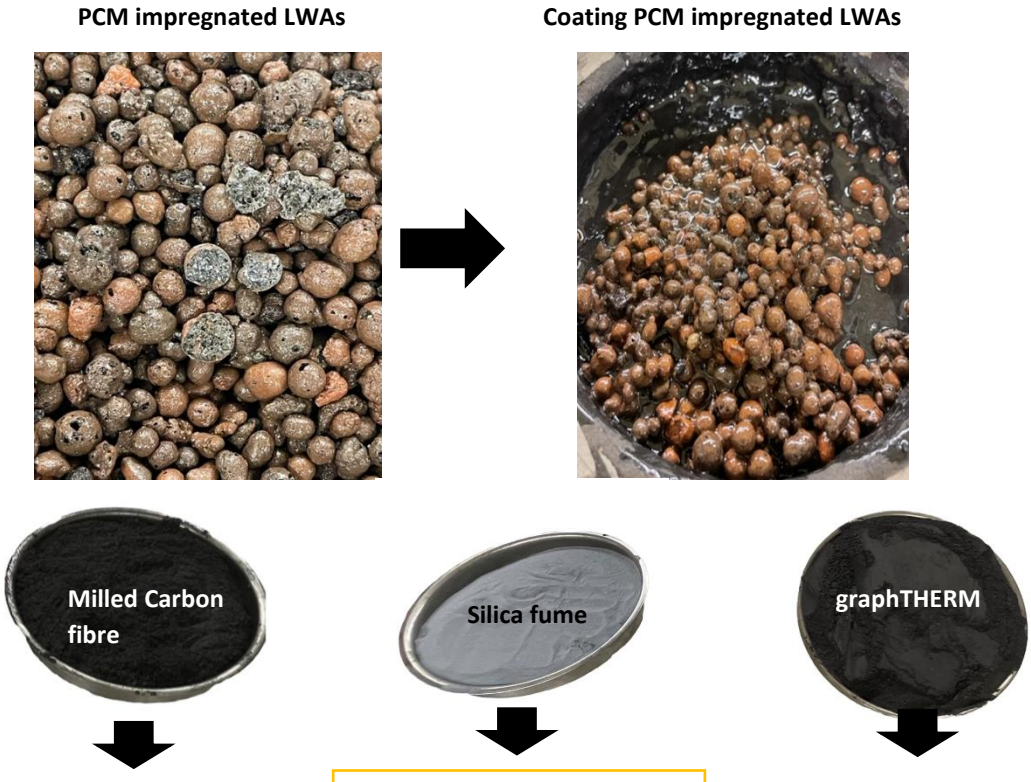

Figure continued in next page

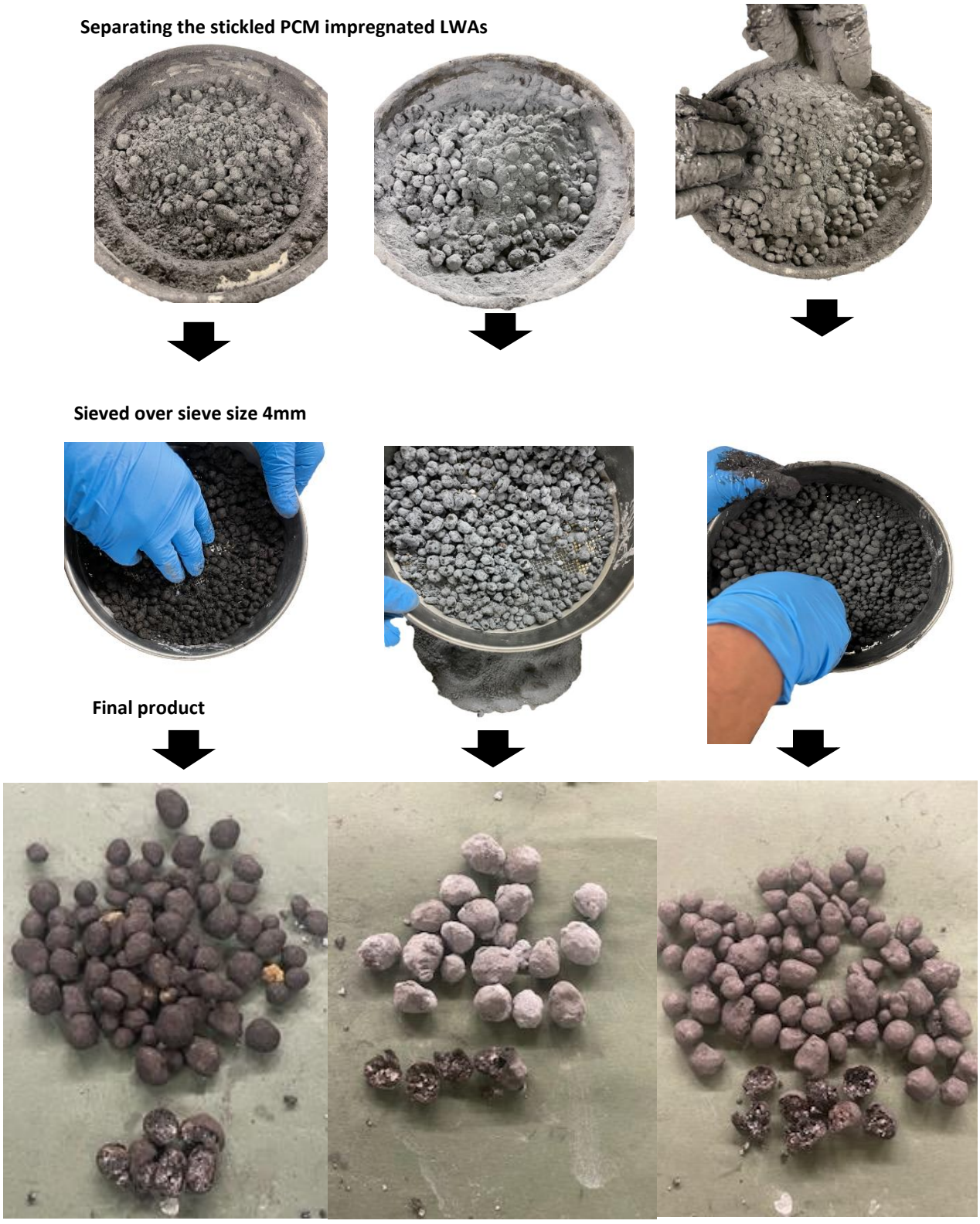

Fig. 7.6. Procedure PCM impregnated LWAs preparation

7.3.1.5 Assessment of coating methods

Following the coating and drying process, the assessment of the best coating method took a place by determining the PCM leakage with time under two conditions, which are below the melting point environment and above the melting point condition. A 1000 gm of RT26 PCM LWA's and 1000 gm of RT42 PCM LWA's were placed in the same container and kept in the oven at 20 ^{o}C (below the melting point) for 30 days. During this period, the changes in mass was observed at 1st day,7th days and 30th day. Similarly, 2000 gm of PCM LWA'S (50% RT26 and 50% RT42) was placed in the oven at 60 ^{o}C (above the melting point) and tested similar to the case of 20^{o}C. The results obtained from this measurement were presented in Fig. 7.7. According to the figure, the mass of the tested PCM that is coated LWA's unchanged when it was kept in an environment temperature below the melting point. The exposure to a temperature above the melting point led to a leakage from the LWA's. Fig. 7.7 also displays the assessment of the three coating methods including graphTHERM, Milled Carbone fiber, and silica fume. The results indicated that that the use of Carbone fiber as a separating material seems the best option to confine and seal the aggregate particles to prevent the PCM from leaking out the LWA's in both conditions below and above the melting point of the PCM.

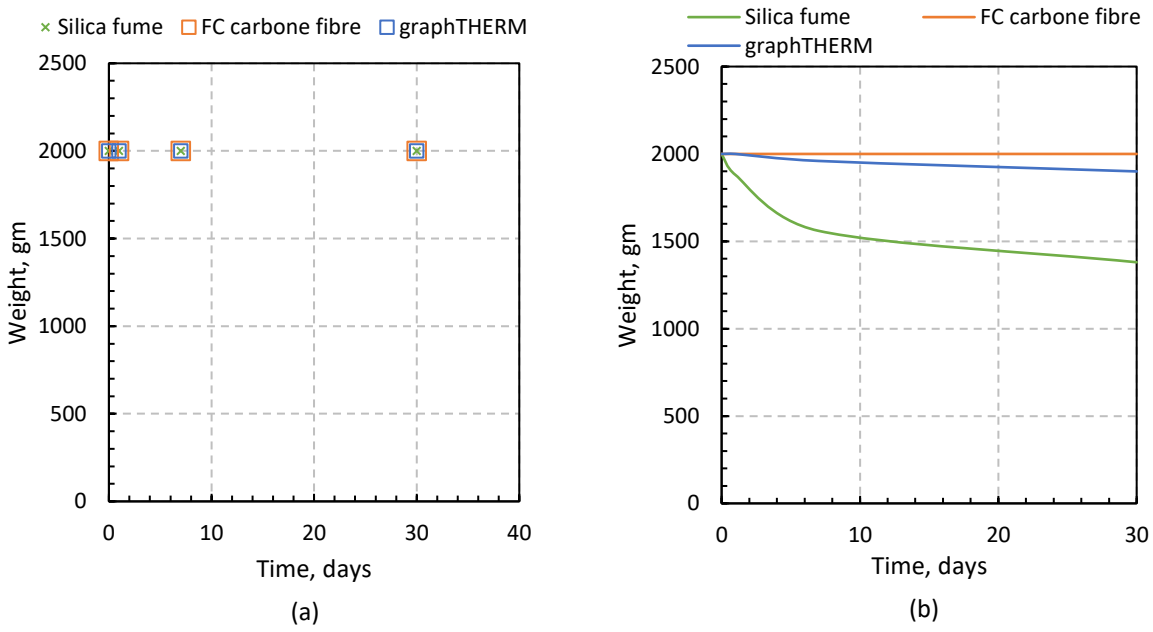

Fig. 7.7. Assessment of the coating method a). below melting point, b). above melting point.

7.3.1.6 Durability of the chosen coating method

As mentioned in the previous section, that the use of Milled Carbon fibre as a separation material for the coated PCM LWA's provided the best selection of the coating methods, and therefore, it becomes essential to carry out a further investigation to discuss the durability of the selected option. For this reason, the selected PCM impregnated LWAs were subjected to a salty environment to reflect the case of using the PCM LWAs in saline soils. Soil salinity is the quantity of salt that is dissolved in soil water, it can be measured by using electrical conductivity (EC) (Maximillian et al., 2019). Paul and Rashid (2016) classified the soils in accordance with their salinity and named the soils that have EC ≥ 16 dS/m the strongly saline soils. To convert the EC (dS/m) to TDS (total dissolved solids) (mg/L) , the following equation was used (Boman and Stover, 2002):

$$\text{TDS (mg/L)} = \text{EC (dS/m)} * 640 \quad (7.1)$$

In this research, the PCM impregnated LWAs in a strong saline environment was tested with EC =16dS/m to present harsh environmental conditions. A 1000gm RT26 PCM LWA's and 1000gm RT42 PCM LWA's were placed in one container filled with saline water (10.24 gm/L) and kept in the oven at 20 ^{o}C (below the melting point). Another 2000 gm of PCM LWA'S (50% RT26 and 50% RT42) was similarly placed in a container filled with saline water and was kept in the oven at 60 ^{o}C (above the melting point). The measurements of the dry mass of PCM LWA'S were taken at 1 day,7 days and 30 days and the difference in the mass of the PCM LWA'S was used to measure the durability of the impregnated LWAs. The results of the durability tests are illustrated in Fig. 7.8. From the results, it can be noted that no changes in the coated PCM-impregnated LWAs weight at both temperatures 20 ^{o}C and 60 ^{o}C. Thus, the use of Mf Carbon fibre as a separation material for the coated PCM impregnated LWAs supplied a strong enough protection to shield the impregnated PCM inside the LWAs at both states of the PCM (solid & melting) as well as, from any subjection to severe environmental conditions (salt attack). The final finished product of the coated PCM impregnated LWAs was used later to enhance the thermal energy storage of sands and to increase the thermal energy storage at the soil/ geo-energy structures interface.

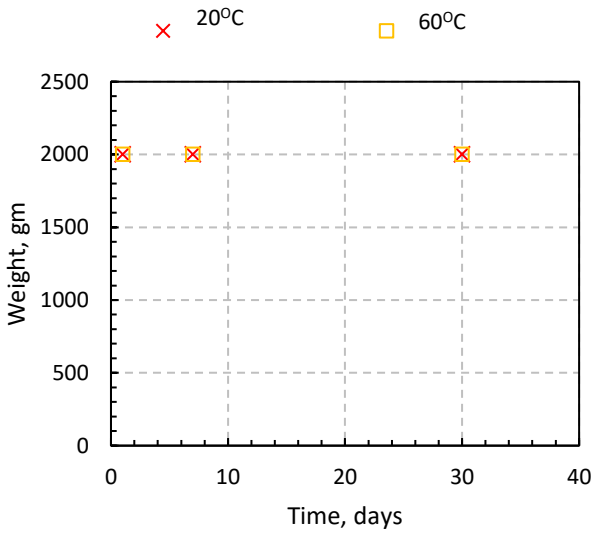

Fig. 7.8. Durability of the coating method.

7.3.2 Sand thermal enhancement using PCM LWA.

7.3.2.1 Sample preparation and thermal properties measurements.

The used sand, which was already described in section 3.3.1.1, was mixed with different percentages of its volume (7%, 14%, 21%, 28% and 35%) with coated PCM impregnated LWAs. The sand and certain amounts of the PCM LWA's were initially mixed by hand until obtaining an even distribution of PCM LWA'S. Amount of water (5%, 10% and 15%) was added, and then mixed to ensure the uniform distribution of moisture. All specimens were prepared at constant unit weight of 15 KN/m^3 by controlling the volume and the weight of LWA/sand to fill cubic moulds. The mould was made of transparent acrylic with dimensions of 100mm× 100mm×100mm and has two holes in each side of the mould, as shown in Fig. 7.9. Subsequently, the mixture was poured into the designed mould. Each sample was compacted in 3 layers and ensuring no excesses soil remainined. Then, the thermal properties were measured by K2D Pro thermal meter device using the dual-needle sensor SH-1 by inserting the needle in the sample for 2 to 5 min through two holes see Fig. 7.9. An average reading of three measurements from three different faces was recorded for each sample. All tests were carried out at different temperatures:10 ºC, 20 ºC, 25 ºC, 26 ºC,27 ºC, 30 ºC, 40 ºC and 50 ºC for soil mixes with coated RT26 impregnated LWAs and at 20 ºC, 30 ºC, 40 ºC,

42 ^{o}C, 43 ^{o}C, 45 ^{o}C, 50 ^{o}C, 60 ^{o}C for soil mixes with coated RT42 impregnated LWAs. Tables 7.3 and 7.4 summarise the testing programme for thermal enhancement of sand using coated PCM impregnated LWAs

Table 7.3. Sample design parameters for soil and RT26 LWA's mixes

Series	Parameters		
	Variable (w_c)	Variable (ST)	Fixed (γ)
Sand	w_c= 5%,10%,15%	(20, 30, 40, 42,43, 45, 50, 60) ^{O}C	γ=15 KN/m^3
Sand +7% PCM LWA's	w_c= 5%,10%,15%	(20, 30, 40, 42,43, 45, 50, 60) ^{O}C	γ=15 KN/m^3
Sand +14% PCM LWA's	w_c= 5%,10%,15%	(20, 30, 40, 42,43, 45, 50, 60) ^{O}C	γ=15 KN/m^3
Sand +21% PCM LWA's	w_c= 5%,10%,15%	(20, 30, 40, 42,43, 45, 50, 60) ^{O}C	γ=15 KN/m^3
Sand +28% PCM LWA's	w_c= 5%,10%,15%	(20, 30, 40, 42,43, 45, 50, 60) ^{O}C	γ=15 KN/m^3
Sand +35% PCM LWA's	w_c= 5%,10%,15%	(20, 30, 40, 42,43, 45, 50, 60) ^{O}C	γ=15 KN/m^3

Wc= water content, γ= density of the sample, ST= sample temperature

Table 7.4. Sample design parameters for soil and RT42 LWA's mixes

Series	Parameters		
	Variable (w_c)	Variable (ST)	Fixed (γ)
Sand	w_c= 5%,10%,15%	(10, 20, 25, 26,27, 30, 40, 50) ^{O}C	γ=15 KN/m^3
Sand +7% PCM LWA's	w_c= 5%,10%,15%	(10, 20, 25, 26,27, 30, 40, 50) ^{O}C	γ=15 KN/m^3
Sand +14% PCM LWA's	w_c= 5%,10%,15%	(10, 20, 25, 26,27, 30, 40, 50) ^{O}C	γ=15 KN/m^3
Sand +21% PCM LWA's	w_c= 5%,10%,15%	(10, 20, 25, 26,27, 30, 40, 50) ^{O}C	γ=15 KN/m^3
Sand +28% PCM LWA's	w_c= 5%,10%,15%	(10, 20, 25, 26,27, 30, 40, 50) ^{O}C	γ=15 KN/m^3
Sand +35% PCM LWA's	w_c= 5%,10%,15%	(10, 20, 25, 26,27, 30, 40, 50) ^{O}C	γ=15 KN/m^3

Wc= water content, γ= density of the sample, ST= sample temperature

7.3.2.2 Assessment of mechanical properties.

Fig. 7.10 displays the procedures used to assess the friction angle, maximum dry density, optimum water content and permeability coefficient. All tests were performed on pure sand and sand mixes with different percentages of coated PCM-impregnated LWAs, the coated PCM-impregnated LWAs have been added as a percentage of volume.

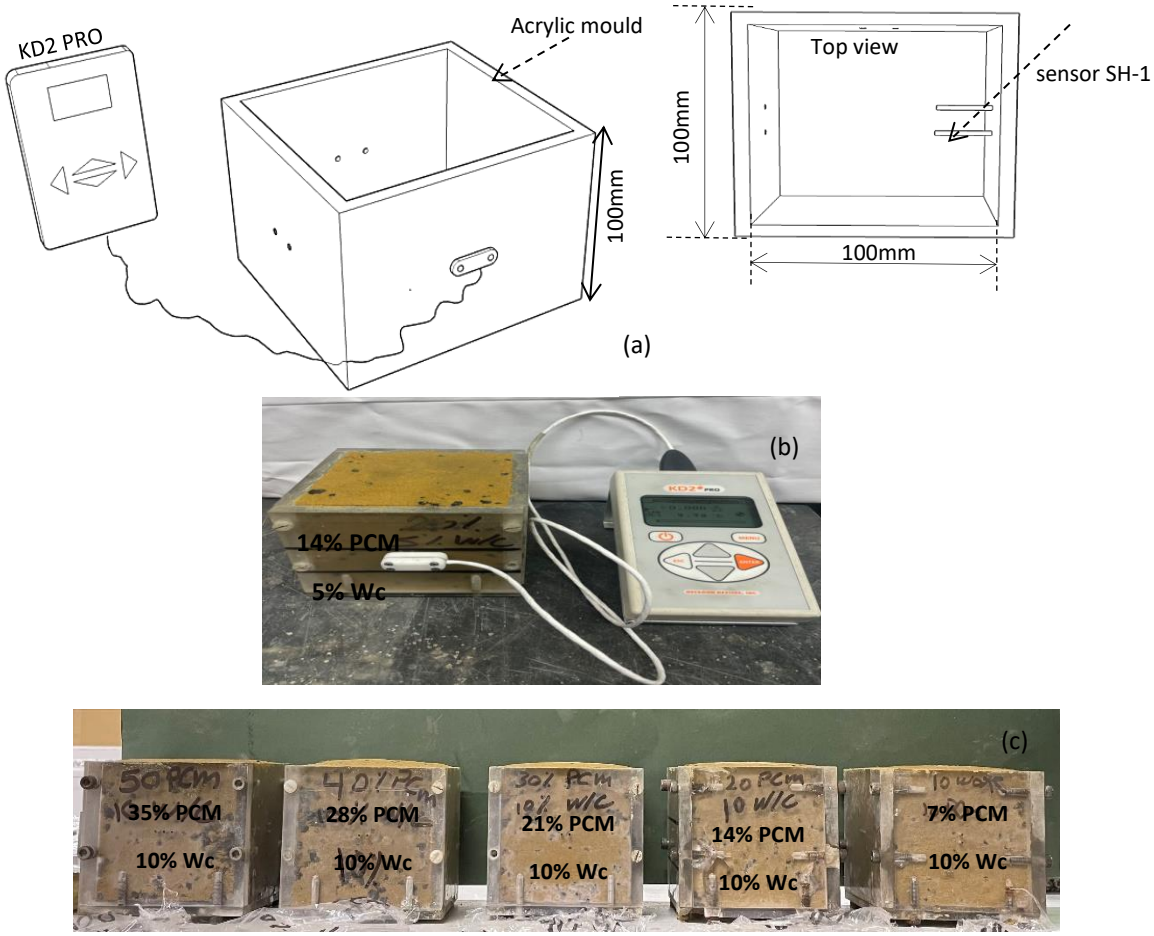

Fig. 7.9. Schematic diagram fir the thermal enhancement, (b). image of real test, (c). Acrylic mould fill with soil mixes.

7.3.3 Geo-energy pile and wall tests

7.3.3.1 Determination of soil/GES interface

In order to determine the soil/geo-energy structure interface, which will be occupied by coated PCM impregnated LWAs soil mix, six cylindrical sand specimens with a diameter of 100 mm and height of 200 mm were tested. Around 35% of coated PCM impregnated LWAs soil mix was added in various percentages (i.e., 10%, 20%, 30%, 40% and 50%) of the cylinder height and the rest of the cylinder was filled with normal soil (See Fig. 7.11). The unit weight of the five samples was kept constant at 15 kN/m^3. Each of these samples was subjected to a hot

end source of heat to allow the heat to transfer along the sample to the cold end as shown in Fig. 7.11 (a and b). From Fig. 7.11 (c), it was very clear that by increasing the cylindrical height, which occupied by PCM LWAs soil, the steady state temperature at the cold end decreased.

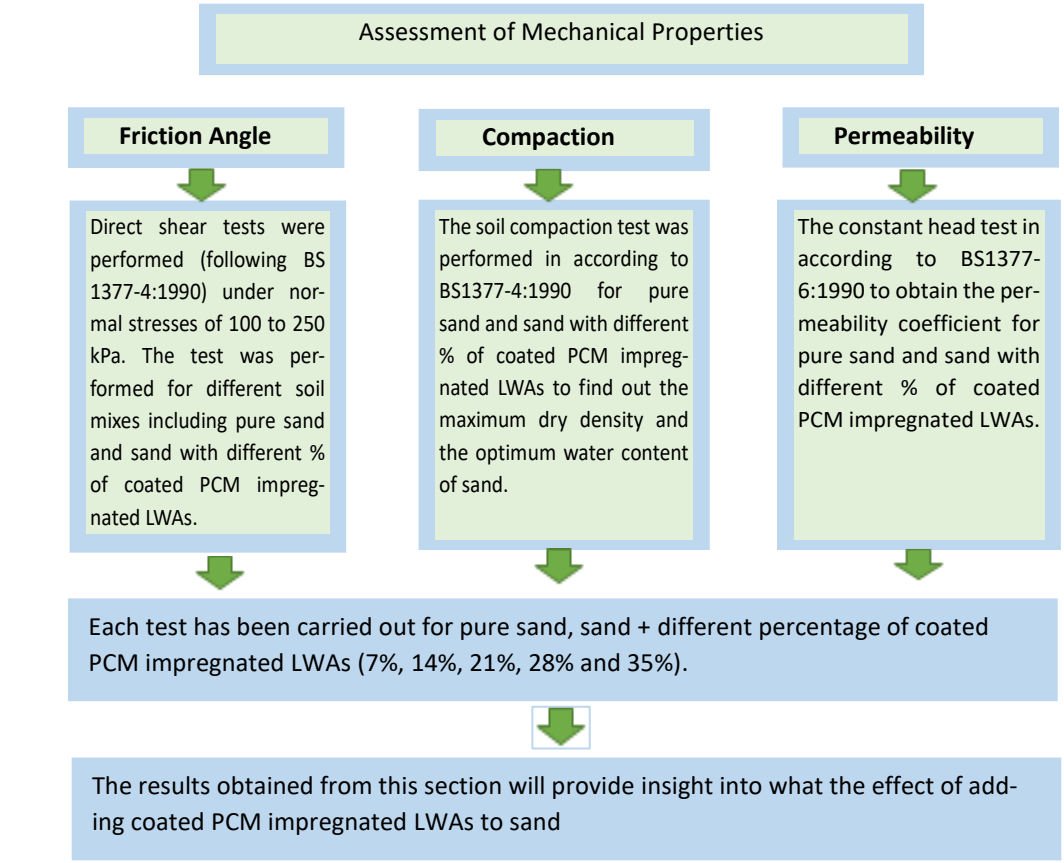

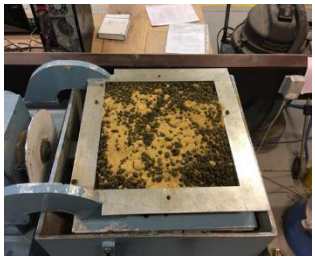

Direct shear box

Compaction test

Constant head test

Fig. 7.10. Assessment of mechanical properties follow chart

It also revealed that, for the case of using 10% of the cylinder height filled with PCM LWAs soil mix (50% soil and 50% PCM LWAs), the temperature of the cold end reduced by about 12% compared with the case of pure soil. In the case of 50% of the cylinder height was occupied by coated PCM impregnated LWAs soil mix, the temperature at the cold end dropped by about 68%, in comparison with the pure soil case. This indicates a reduction in the thermal conductivity of the soil column when the coated PCM impregnated LWAs soil mix was increased. Zhang et al. (2021), reported that the key element in enhancing the short-and-long-term heat transfer capacity of GEP is the thermal conductivity of backfill soil. Also, an experimental and numerical analysis were carried out by Shafagh et al. 2022 to study the thermal regime of buried pipes. The results demonstrated that the thermal conductivity of backfill is the dominant heat transfer mechanism. So, it becomes essential to not negatively affect the thermal conductivity of the back-fill. Therefore, the results suggested the ratio of 10% of the soil height as it pre-sents a decrease of 10% only on the thermal conductivity of the soil mix, to be equipped by coated PCM-impregnated LWAs soil mix. For PCM LWA's pile test, the pile was placed in the centre of the experimental tank and the soil domain covered 425 mm in all directions of the tank wall. For PCM LWA's wall test, the wall was installed at one of the tank sides, offering 880mm of soil domain to the tank wall. Hence, 42.5 mm of coated PCM-impregnated LWAs soil mix was placed around the pile and 8.8 mm of coated PCM-impregnated LWAs soil mix was used in front of the wall.

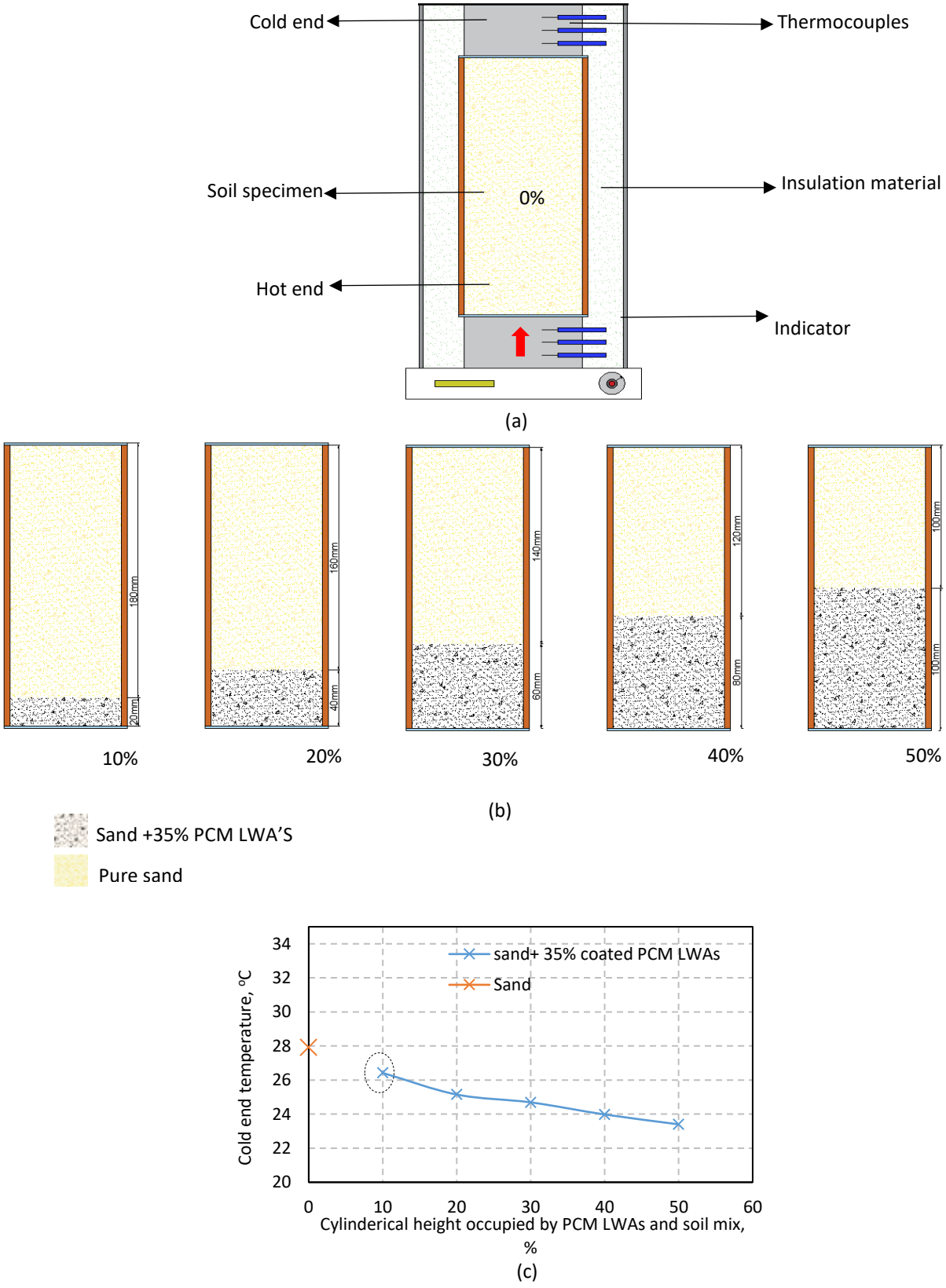

Fig. 7.11. (a). Hot plate setup for heating the samples, (b). The variation of coated PCM LWA's for each test and (c). The relationship between cylindrical height occupied by coated PCM LWA's and cold end temperature.

7.3.3. 2 Heat transfer experiments for GEP and GEW

In total, four experiments were carried out with fixed and variable parameters using a fully instrumented test rig, as explained in section 3.3.3 and shown in Fig. 7.12 and 7.13. The first two experiments were conducted on energy pile using normal sand and sand + 50% coated PCM-impregnated LWAs. The challenge with these tests was how to fill the tank with coated PCM-impregnated LWAs sand mix in 42.5 mm boundaries around the pile and how to maintain the other part of the experimental tank filled with normal sand. For this reason, a filling method was proposed using 235×235×1000 mm of the wooden box to create the required boundaries. After placing the wooden box at the centre of the experimental tank, it was filled with the coated PCM LWAs sand mix and the neutral sand was filled outside the wood box. Once tank was totally filled, the wooden box was gently removed using an airframe fixed around the experimental tank. two more tests were carried out on geo energy walls. The first test was conducted using pure sand and the second test used coated PCM LWAs sand mix. A filling method was used to fill the coated PCM LWAs sand mix additive up to the 88.8mm in front of the wall using a wooden barrier, that was placed at 88.8 mm away from the wall location to separate the experimental tank into two parts; the coated PCM LWAs sand mix was filled inside the barrier, while natural was filled outside that barrier (See Fig. 7.13.). Table 7.5 presents the test coding, fixed and variable parameters in the experimental program applied in this study.

Table 7.5. Fixed and variable parameters for GEP and GEW tests

GES	Test Name	Fixed parameters	Variable parameters
GEP	Standard Test	FR =67l/h, GWL=500mm.	Pure Sand
GEP	PCM Test	FR =67l/h, GWL=500mm.	Coated PCM LWAs sand mix at 42.5mm around the pile.
GEW	Standard Test	FR =67l/h, GWL=500mm.	Neutral Sand
GEW	PCM Test	FR =67l/h, GWL=500mm.	Coated PCM LWAs sand mix at 88.8mm in front of the wall.

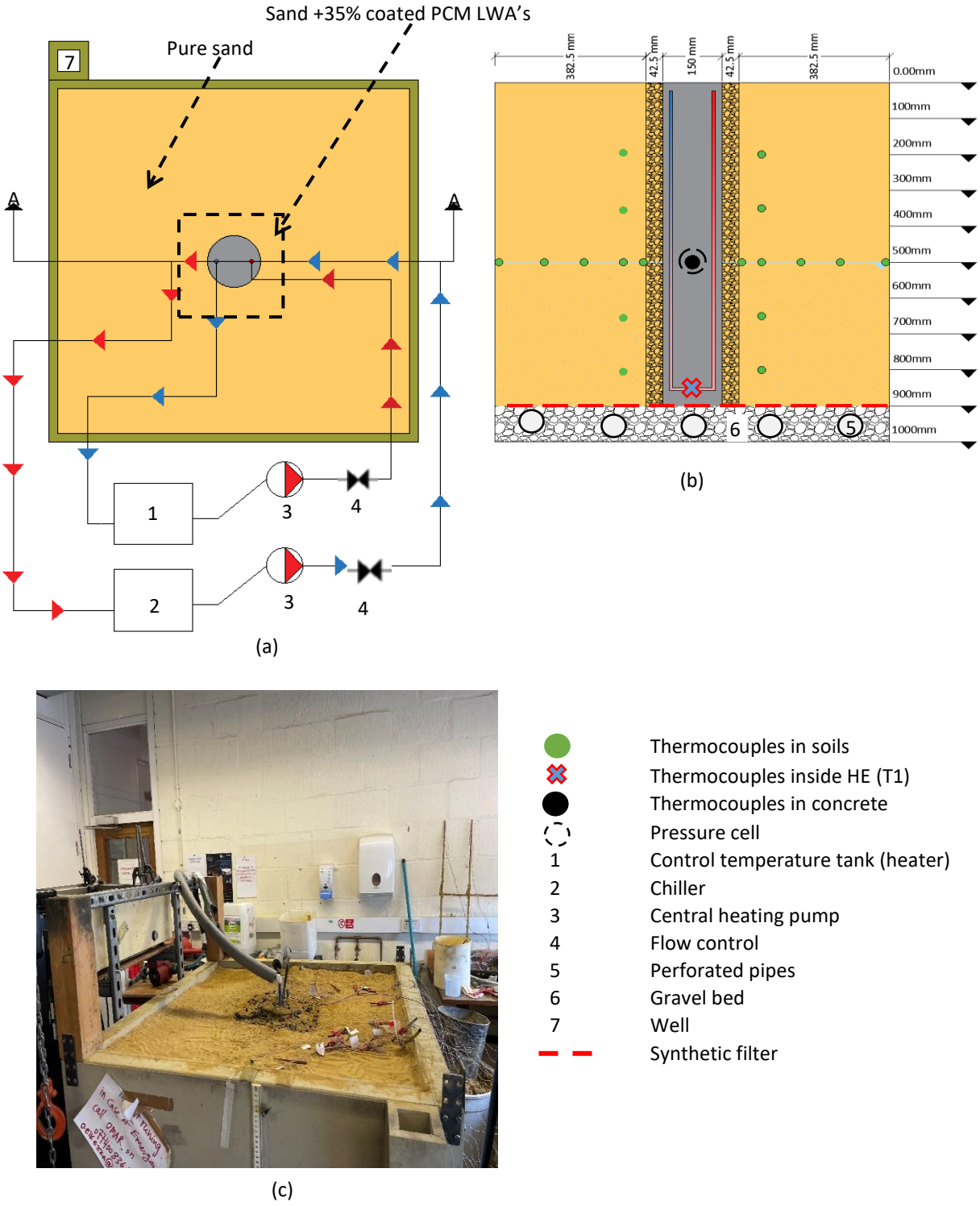

Fig. 7.12. Schematic diagram of the experimental rig for energy pile tests:(a) Plan view, (b) Location of thermocouples, and Vertical cross section of the testing tank. (c) Image of real testing rig.

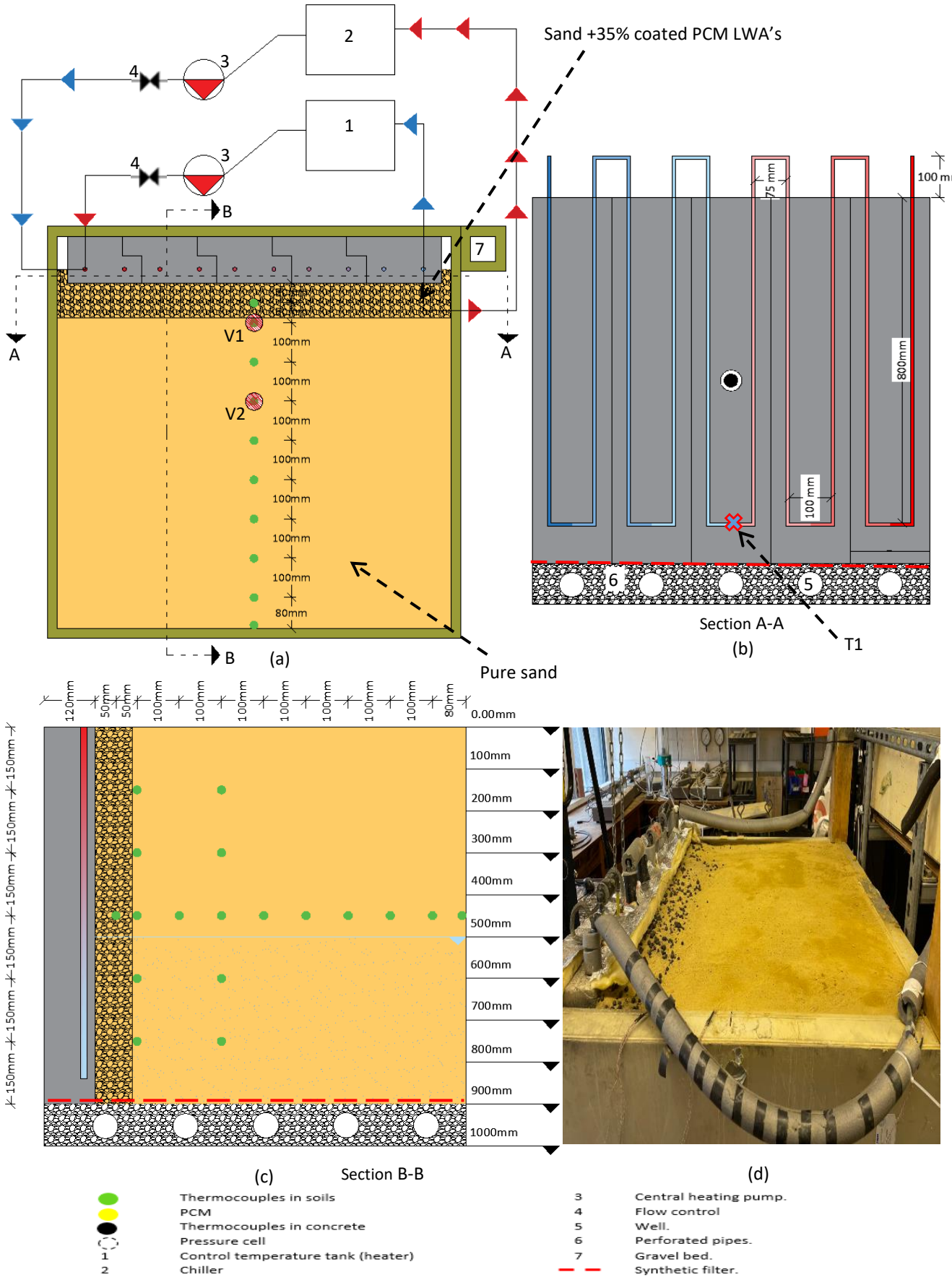

Fig. 7.13. Schematic diagram of the experimental rig for energy wall tests: (a) Plan view, (b) Section A-A, Vertical cross section of the tested energy wall, (c) wall geometry details, (d) section B-B, location of thermocouples, e) image of real test rig.

7.4 Results and discussions

7.4.1 Thermal enhancement of sand using PCM LWAs

The specific heat capacity of pure sand and sand mixed with different percentages of coated PCM impregnated LWA's at different water contents has been experimentally measured using KD2 PRO thermal analysis device. The detailed sample design at the percentage of PCM LWA's can be found in Tables 7.3 and 7.4. Fig. 7.14 , shows the specific heat capacity of the soil PCM mixes was slightly increased with the increase of the sample temperature until reached a range of temperature, where the specific heat capacity significantly rocked to create a peak which is known as the phase change point, where the paraffin transforms from a solid to a liquid phase. The increase beyond the melting point showed a sudden drop in the value of the specific heat until reaching almost a constant value after the melting range of temperature. Moreover, Fig. 7.14, (a, b and c) were carried out using RT26 PCM, whereas Fig. 7.14 (d, e and f) used RT 42 and carful inspection of these figures demonstrated that the use of RT 42 PCM always gives a lower value of the specific heat capacity than the use of RT 26. This could be attributed to the low ability of RT42 to store or release heat (see Fig .6.1).Fig. 14 also, shows the effect of water content on the measurement of the specific heat capacity of sand mix. In order to evaluate this effect, it is worth looking at 0% PCM series. As shown in the figure for zero percent PCM, the specific heat capacity at 5%, 10% and 15% water content was measured and found to be 0.85, 1.05 and 1.15 kj/kg.k, respectively. The area under the peak of the specific heat capacity vs temperature is equal to the quantity of latent energy stored in the PCM soil mix (Dehdezi et al. 2012). Hence, the area under Fig. 14 (a and d) was estimated and the data was presented in Table. 6.6 (Further information about the measurements can be found in Appendix C). worth mentioning that the estimated values for both graphs were considered 10^{o}C from 20^{o}C to 30^{o}C for Fig.14a and from 40^{o}C to 50^{o}C Fig.14d and the obtained data are presented in Table. 6.6. demonstrating the quantity of the latent energy that stored in the six soil mixes with deferent percentages of PCM LWA's and the value ΔT (^{o}C) needed to store the same quantity of energy as sensible heat in soil (0% PCM case). As shown in Table 6.6 , adding 35% PCM LWA's to soils

allows storeing about 30.84 kj/kg at only ΔT =10°C and to achieve similar energy storage, ΔT =36.28°C is needed for sensible storage only. Furthermore, Table 7.6, illustrates that sensible heat storage causes an excessive variation in the ground temperature which is undesirable for ground-source heat pump applications. The thermal conductivity of soil mixes was also measured, and the data is presented in Fig. 7.15. The figure clearly shows that the inclusion of PCM LWA's in soil resulted in a reduction of its thermal conductivity. This reduction could be due to the lower thermal conductivity of RT26 and RT42 also might be caused by the significant drop in the porosity of the soil mixes when the PCM LWA's is used in soils. The maximum reduction of soil mix thermal conductivity was obtained when 35% of PCM LWA's was added, resulting in a reduction of about 34.8% compared with the 0% PCM LWA's case. These resulted in line with outcomes obtained from a study carried out by Dehdezi et al. (2012), when the addition of 80% microencapsulated PCM led to a reduction of the thermal conductivity of the soil mix by 100%. The thermal diffusivities of different soil and PCM LWA's mixes at different water saturations were measured, and plotted in Fig. 17.16. as shown in Fig. 17.16, the thermal diffusivity decreased with the increase of the PCM LWA's percentage in the soil mix, and reached its lowest value when the specific heat capacity was at the peak. This reduction is due to the slight reduction of thermal conductivity and the extreme increase in specific heat capacity. The reduction of the thermal diffusivity indicated that the heat transfer would be slower at the temperature of phase change of PCM.

Table 7.6. Latent energy stored in the mixes considering ΔT =10°C

Mix	RT 26		RT42	
	Energy stored at ΔT= 10 °C (kj/kg)	ΔT needed to store same quantity of energy as sensible heat in soil (°C)	Energy stored at ΔT = 10 °C (kj/kg)	ΔT needed to store same quantity of energy as sensible heat in soil (°C)
0% PCM	8.5	-	8.5	-
7% PCM	14.52	17.08	9.86	11.6
14% PCM	19.28	22.68	14.68	17.2
21% PCM	22.32	26.25	18.50	21.76
28% PCM	24.64	28.98	21.74	25.57
35% PCM	30.84	36.28	24.46	28.77

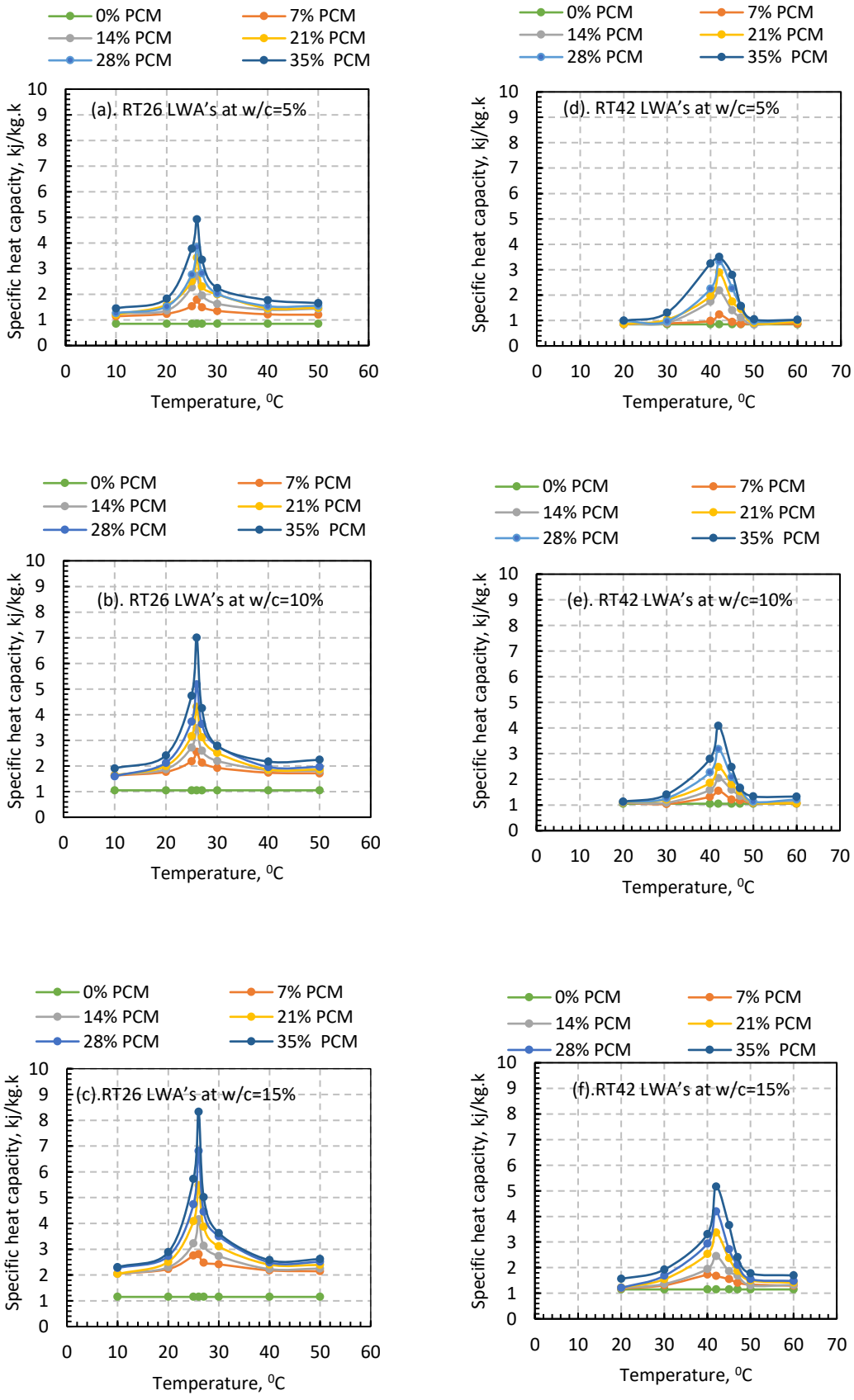

Fig. 7.14. Specific heat capacity of the PCM-modified soil at different temperatures.

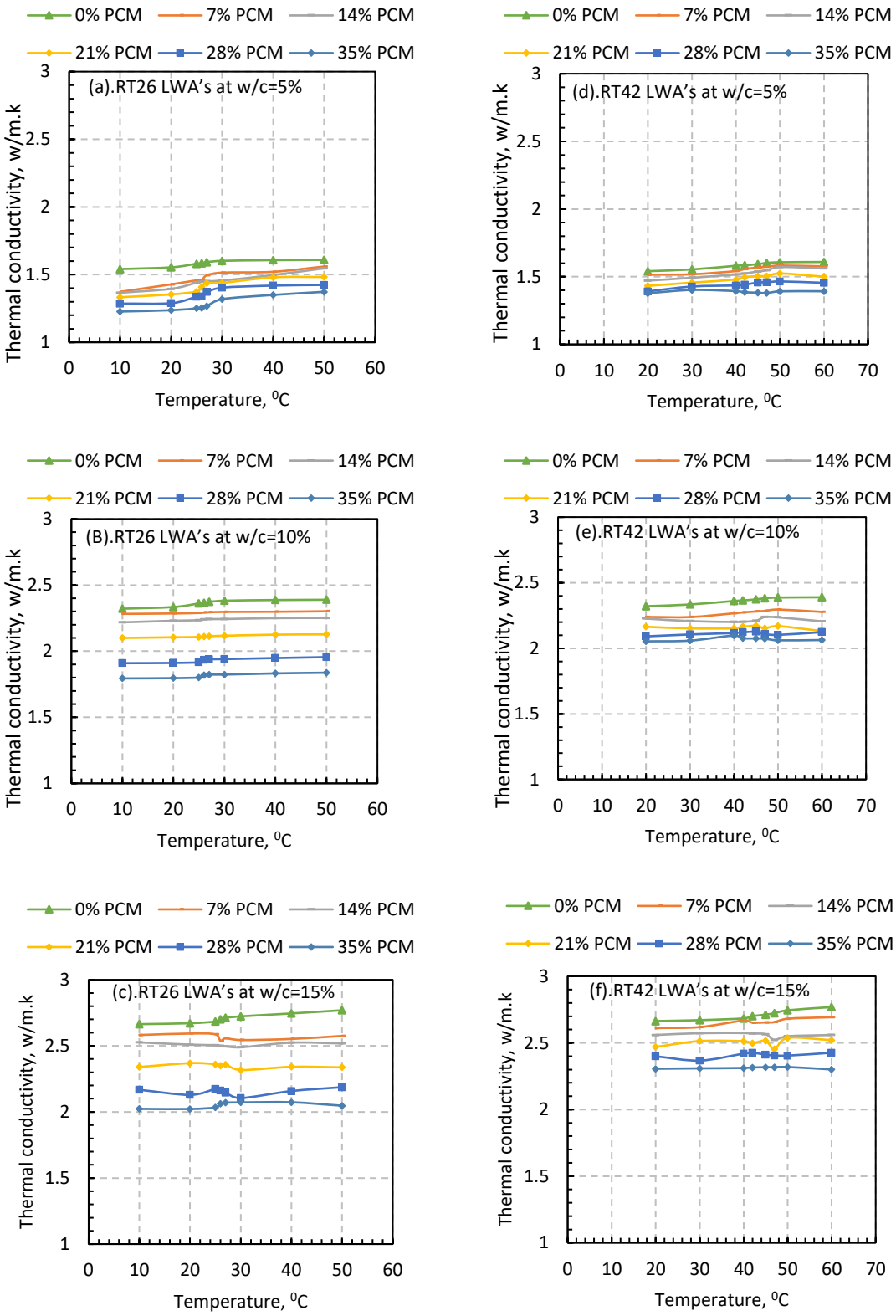

Fig.7.15. Thermal conductivity of PCM- modified soils at different temperatures.

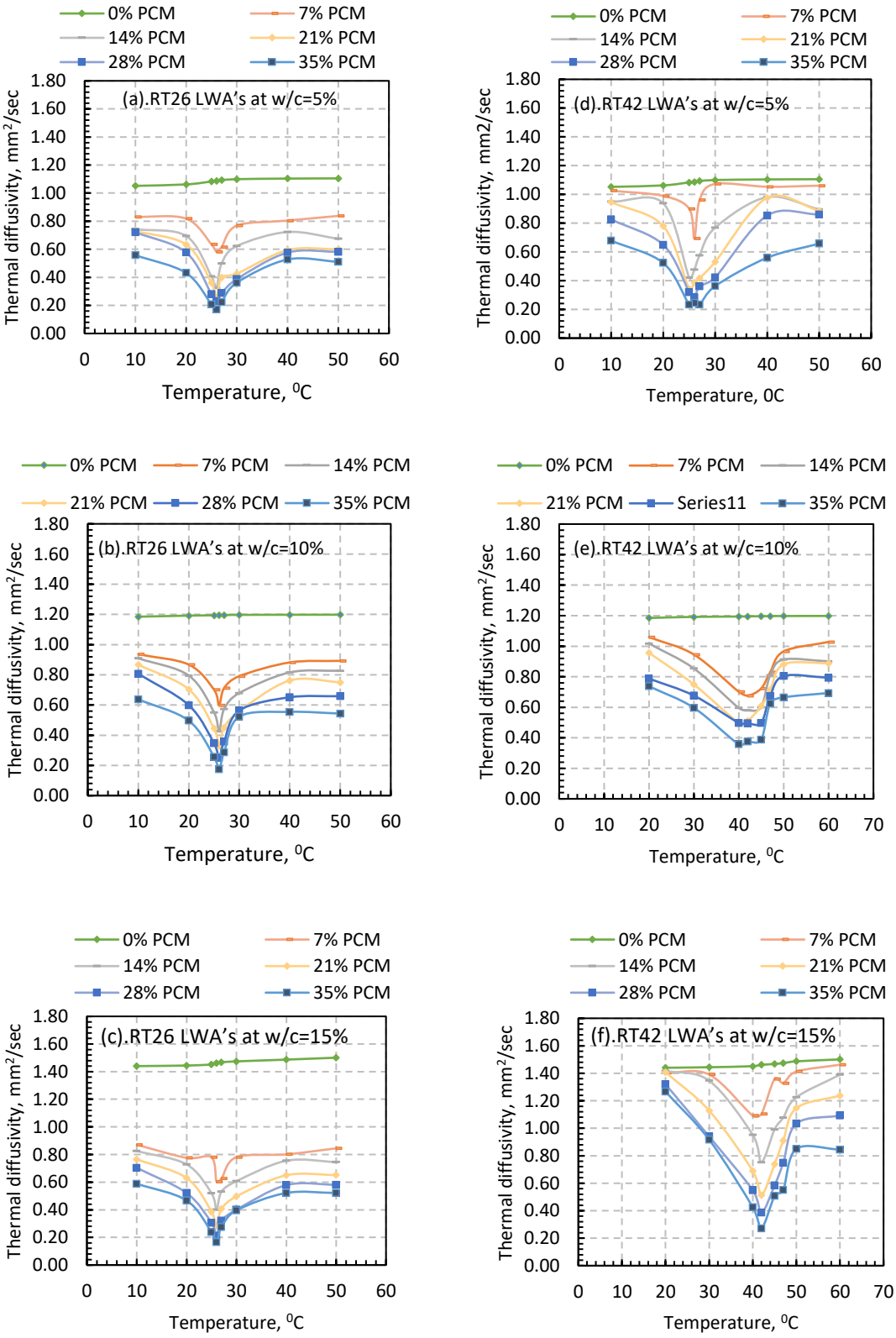

Fig. 7.15. Thermal diffusivity of the PCM-modified soil at different temperatures.

7.4.2 Assessment of mechanical properties

4.4.2.1 Compaction characteristics

The sand was mixed with different percentages of coated PCM-impregnated LWAs, considering the volume of sand, the maximum dry unit weight (MDUW) and optimum moisture content (OMC) were evaluated using proctor compaction test. Fig. 7.17 shows the typical compaction curve for pure sand and sand with 7%, 14%, 21%, 28%, and 35% of coated PCM impregnated LWAs. It could be observed that the addition of coated PCM impregnated LWAs has dropped the

MDUW and the OMC of the compacted sand mixes. The inclusion of 7% coated PCM impregnated LWAs, reduced the MDUW and the OMC by 8% and 7%, respectively. Moreover, the addition of more than 7% coated PCM impregnated LWAs has flattened the compaction curve of the tested mixes, demonstrating that the density variation with moisture content is relatively steady. In other words, with the addition of coated PCM-impregnated LWAs, the maximum density of the soil can be obtained over a wide range of moisture content.

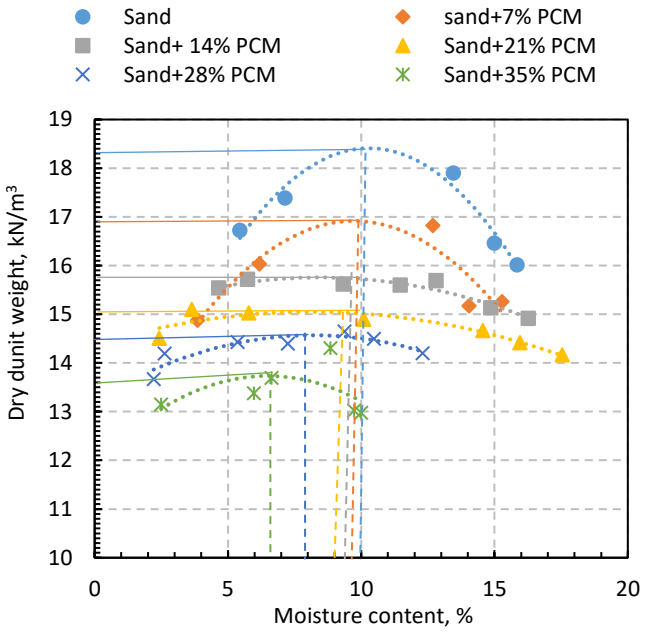

Fig. 7.16. Compaction curve for different sand and PCM LWA's mixes.

7.4.2.2 Permeability characteristics

The permeability test was conducted for the pure and five coated PCM-impregnated LWAs soil mixes (with different percentages of 7%, 14%, 21%, 28%, and 35% of the soil volume). Each test was performed with three different flows (low, medium and high) and an average value of the hydraulic conductivity was calculated. As shown in Fig. 7.18, the inclusion of coated PCM-impregnated LWAs in sand increases the coefficient of permeability compared with the pure sand case. In the case of increasing the coated PCM impregnated LWAs in the sand mix, the coefficient of Permeability increased until reaching the maximum value (35% of coated PCM impregnated LWAs). This could be attributed to the fact that by increasing the coated PCM-impregnated LWAs percentage in the sand mix, the porosity of the soil mix significantly increases.

7.4.2.3 Friction angle characteristics

A large direct shear box was carried out on pure sand and sand with different percentages of coated PCM impregnated LWA's. The findings for all soil mixes indicated that, by adding the coated PCM-impregnated LWA's, the friction angle of the mix increased (See Fig. 7.19). this can be explained by the higher friction behaviour of the coated PCM LWA's. To confirm this behaviour, a sample with 100% PCM LWA's was tested using the shear box, and the result revealed that the friction angle was 39.7 ^{o}. This value is about 15% higher than that for pure sand.

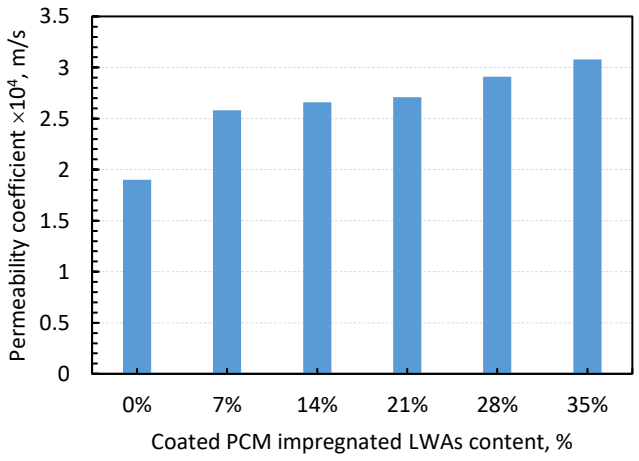

Fig. 7.17. Coefficient of Permeability for different sand and PCM LWA's mixes.

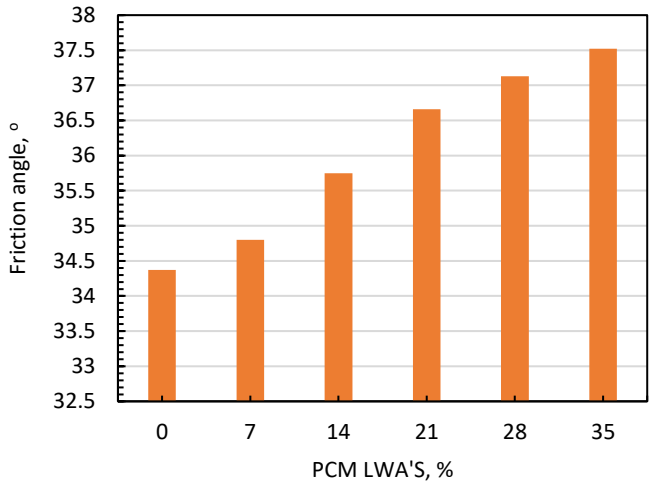

Fig. 7.18. The friction angle for different sand and PCM LWA's mixes.

7.4.3 Heat transfer experiments

For the same flow rate of 67L/hr, the variation in temperature of the circulating fluid at the inlet point, based on the HE (T1) and the outlet point for geo-energy piles and walls with two different soil conditions at the thermal interference zone were measured and the data was presented in Figs. 7.20 and 7.21, respectively. It is worth mentioning that the tests were carried out for the continuous cooling-heating operation of 100hrs and during cooling tests, the circulating fluid was circulated with an inlet temperature of 52^{o}C whilst during the heating stages the circulating fluid was circulated with an inlet temperature of -2^{o}C. For pile tests, the measurements of the temperature difference at T1 after reaching the steady state during the cooling and heating stages, showed that for the standard pile test with the pure sand about 53% and 58% of the total temperature difference was recorded, respectively. In the case of using PCM LWA's soil mix at the pile soil interface, the temperature difference at T1 was recorded 52% and 53% for the cooling and heating respectively, (See Fig. 7.20a).

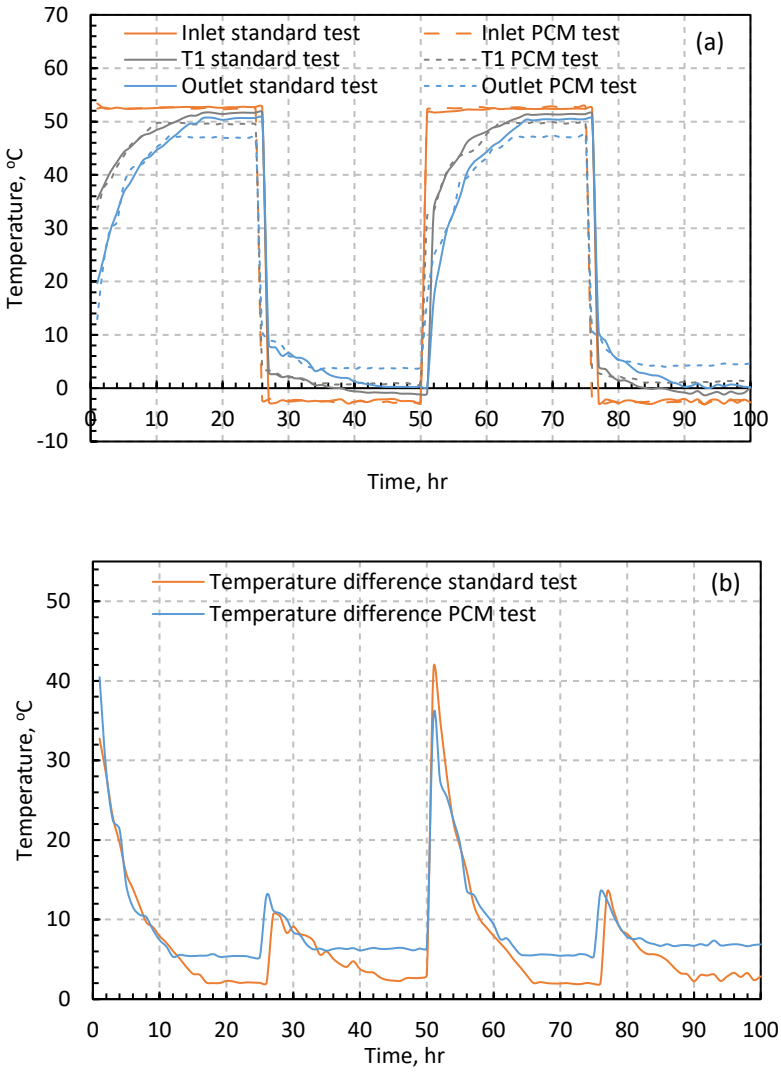

Fig. 7.19. (a). Circulating fluid temperature of inlet, T1 and outlet of the heat exchanger for pile tests, (b). Temperature differences between inlet and outlet.

The measurements for the liquid at T1 of the two wall tests were also taken. The measurements indicated that about 51% and 50% of the total temperature differences were obtained for the cooling and heating of standard wall test, respectively. Furthermore, the measurements of T1 when the PCM LWA'S soil mix was used were 52% and 51% for the cooling and heating, respectively (Fig 7.21a). The measurements of T1 for the piles and walls tests showed that there was a uniform heat transfer behaviour as the temperature of the liquid at the half length of the heat exchanger gained around 50% of the total temperature difference.

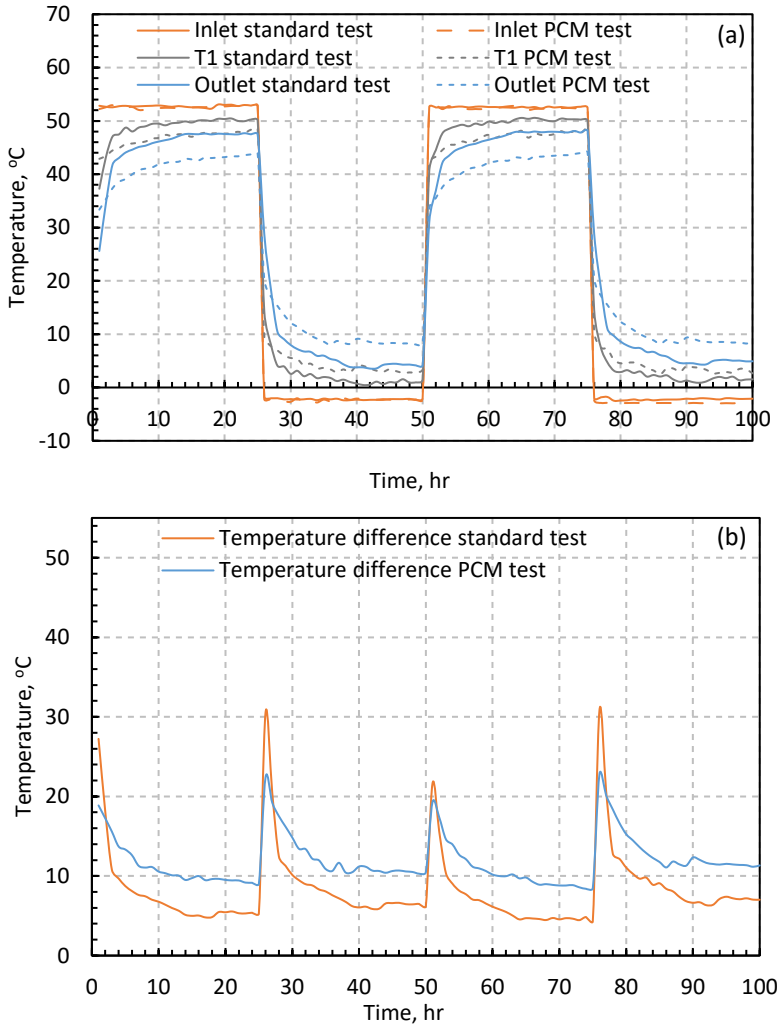

Fig. 7.20. (a). Circulating fluid temperature of inlet, T1 and outlet of the heat exchanger for wall tests, (b). Temperature differences between inlet and outlet.

Fig. 7.20. (b) exhibits the ΔT (Inlet-Outlet) for the two pile tests (standard test and PCM test). It was observed that the use of PCM LWA's soil mix at the interface between the pile and the soil in the experimental tank presented a higher temperature difference. The results established that the standard geo-energy pile test has a temperature difference of about 2.10°C and 2.25°C in cooling and heating cycles , respectively, after reaching steady-state conditions. In the case of using PCM LWA's soil mix at the interface of pile and soil, the temperature difference recorded at steady state was 5.38°C and 6.34°C in the cooling and heating cycles, respectively. The figure also reveals that, for both pile tests, the temperature difference in the heating cycle is slightly higher than that recorded during the

cooling cycle, which reveals a better heat exchange performance of the piles during the heating operation. This could be primarily attributed to the impact of PCM (RT26), which generated about 34 % more energy during cooling than heating (see Fig. 6.1). These results provide reliable proof that the thermal performance of geo-energy pile tends to enhance during cooling and heating by about 156 % and 181%, respectively, when PCM LWA's soil mix was used at the interface between the GEP and the soil.

ΔT (Inlet-Outlet) for the two wall tests was also measured and the data presented in Fig. 7.21b. According to the figure, the case of using the PCM LWA's soil mix experienced the highest temperature differences. The figure also indicated that, similar to the pile the use of PCM LWA's soil mix at the interface zone for GEW has shown better performance during the heating test (inlet temperature =-2^{o}C). Moreover, for standard wall cooling and heating cycles a difference of about 5.47^{o}C and 5.72^{o}C, respectively, was recorded after reaching steady-state conditions. while for the case of using PCM LWA's soil mix, the steady state temperature deference was 9.37^{o}C and 10.52^{o}C cooling and heating cycles respectively. The heat exchange between the geo-energy structure and soil per unit was calculated using Equation (3.2) which indicates that the quantity of transferred heat is connected to the temperature difference between the inlet and outlet, which is evidenced to be directly dependent on the thermal properties of nearby soils. Fig. 7.22 showed results for the dissipated heat energy for geo-energy piles and walls installed in different soils (with and without PCM LWA's. The heat transfer rate for the geo-energy pile reached its highest value of 436 W at the heating cycle when 35% of PCM LWA's was installed in the GEP/soil interface. The results also showed that the contribution of the pcm inclusion to enhance thermal performance of GEP is more signficant (18% higher) during the heating mode (extruction of heat from ground). This could be due to the ability to store/ extracte heat for the RT26. Similarily, the data deduced for geo-enregy walls demonstrated that the heat transfer rate for walls with PCM LWA's used in the interface zone extracted and dissipated more heat from/to the ground of about 72% and 83%, respectivelly, when compared with the standard walls.

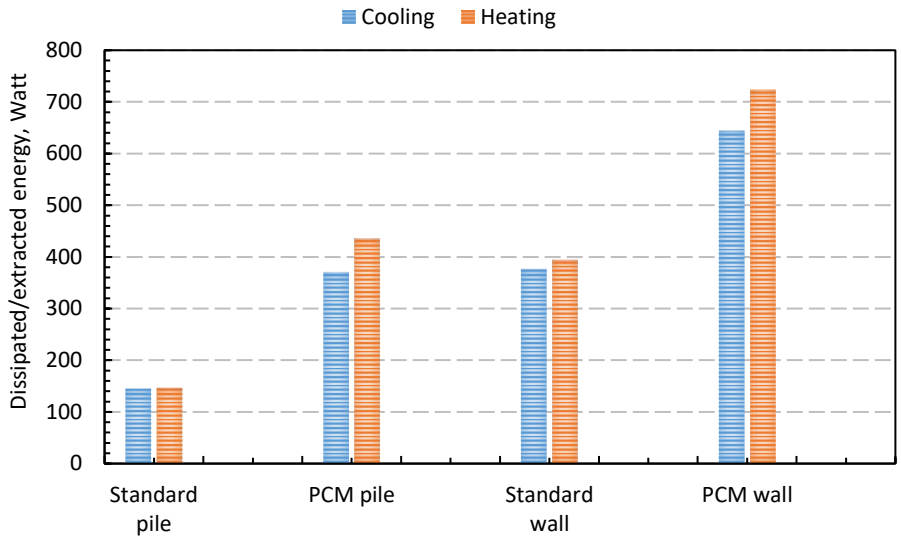

Fig. 7.21. Dissipated/ extracted energy from standard and PCM GEP and GEW.

Mousa et al., (2020), Yang et al., (2021a) and Bao et al., (2022) have justified the previous founding to that the use of PCM for the energy structures (GEP) allows the structure to transfer the heat not only by sensible heat due to temperature change, but also can transfer and store the latent heat during phase transition of PCM, and therefore, the amount of heat that can be exchanged increased significantly.

The horizontal soil temperature profile measured at mid-height for piles and walls is presented in Fig. 7.23. Fig. 7.23a shows the temperature variation in the surrounding soil measured at horizontal distances of 50 mm, 100 mm, 200 mm, 300 mm and 425 mm on both sides of the pile at a depth of 450 mm from the tank base. Fig. 7.23b shows the measurements of THE soil temperature at 50 mm, 100 mm, 200 mm, 300 mm, 400 mm, 500 mm, 600 mm and 880 mm away from the wall.

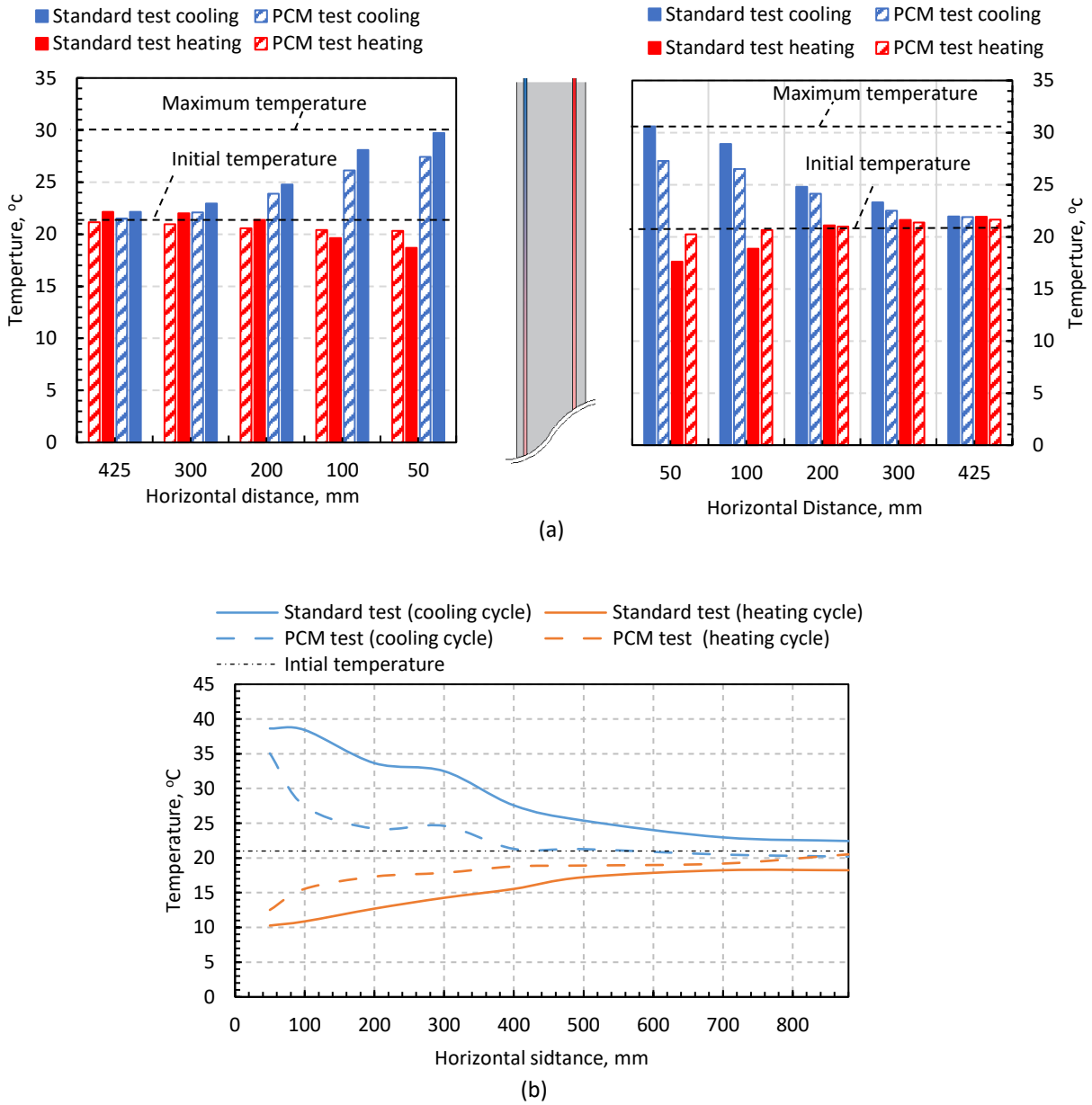

Fig. 7.22. (a). Soil horizontal temperature profile at mid-height of standard GEP test and PCM GEP test, (b). soil horizontal temperature profile at the mid-height of standard GEW test and PCM GEW test.

For piles, the results evidently showed that in both tests (standard test and PCM test) a similar trend was recorded, where the temperature dropped with increasing the distance from the pile. In addition, the maximum temperature difference after reaching a steady state was observed at 50 mm from the pile and gradually decreased with the increase in horizontal distance. However, it was very notable that the changes in soil temperature were much lower in the case pile PCM test.

To precisely prove this, the excess soil temperature (EST) at steady state conditions measured at radial distances of 50 mm, 100 mm, 200 mm, 300 mm and 425 mm were calculated using Equation (6.1).

In the case of standard GEP, the excess soil temperature (EST) at steady state conditions measured at the radial distance of 50 mm, 100 mm, 200 mm, 300 mm and 425 mm was 10.6, 8.29, 4.8, 3.29 and 1.44^{o}C, respectively, whereas the corresponding values for GEP in the case of using PCM LWA's at the interface was 6.29, 5.5, 2.12, 1.50 and 0.68^{o}C respectively. The impact of using PCM LWA's at the interface between GEP and soils is significant in reducing the temperature difference in the soil surrounding the geo-energy pile, which is attributed to the capacity of PCM to store thermal energy between the cooling and heating cycles. In heating tests, where the surrounding soil is probable to drop its temperature, the temperature differences at a radial distance of 50 mm, 100 mm, 200 mm, 300 mm and 425 mm was 11.9, 9.29, 3.44, 1.28, and 0.20^{o}C, respectively for standard GEP test and 6.9, 5.1, 3.1, 1.2, and 0.2^{o}C, respectively for GEP with a PCM LWA's at the interface. The measurement of horizontal soil temperature for both wall tests are presented in Fig. 7.23b. It was observed that an interference region between the wall and soil can be considered as the most affected region in the experimental tank. From the results of the two tests, a soil-wall interference region was identified to be around 600 mm and 400 mm for Standard wall test and PCM wall test, respectively. Both wall tests have shown the same trend as the maximum temperature excess after the steady state reached was observed at 50mm from the wall and gradually decreased with the increase of horizontal distance. It can also be further seen that heat was release into soil (cooling test), the steady state excess in soil temperature (EST) at horizontal distance of 50 mm, 100 mm, 200 mm, 300 mm, 400 mm, 500 mm, 600mm, 700 mm,880 mm are respectively 17.64, 17.41, 12.65, 11.56, 6.86, 4.37, 1.96, 1.96, and 1.44^{o}C for the standard wall test, while the corresponding values are respectively 13, 6.3, 4.21, 2.2, 0.38, 0.47, 0.42, 0.43, and 0.44^{o}C for the PCM wall test (using PCM LWA's at the interface). For heating tests (soil absorbs cool), the EST at the same measurement points are respectively -10.73, -10.13, -8.3, -6.74, -5.46, -3.77, -2.77, -2.77 and -2.77^{o}C for the standard GEW test wall and -8.48, -5.45, -3.7, -1.09, -0.92, -0.57, -0.77, -0.27, and -0.67^{o}C for the wall test with using

PCM LWA's at the interface. From the results of the horizontal soil temperature profile for both GEP and GEW, can clearly conclude that the soil temperature rises and the thermal interference region of GEP and GEW with using PCM LWA's at the interface are without a doubt smaller than those for the standard HE wall. This could be attributed to the latent heat that is released and absorbed by the PCM which can not only enhance the thermal performance but also reduce the soil temperature changes and the thermal interference zone of GEW.

Fig. 7.24a shows the variation in soil temperature along the depth of the pile after reaching a steady state in the case of standard GEP and for pile with PCM LWA's at the pile-soil interface. Data in Fig. 7.24a demonstrated that during the cooling cycle (inlet =52^{o}C), soil temperature increased with the depth of GEP as the circulating fluid travelled inside the HE but with different temperature ranges, depending on the type of soil at the interface zone. In case of standard pile test (during heating cycles), the recorded Data showed that the temperature changed from 26.2^{o}C at 150mm to 29.38^{o}C at 750mm. Furthermore, the changes in soil temperatures were observed to be less prominent in the case of GEP with PCM LWA's at the interface with the soil for heat cycles. In the case of PCM pile test the temperature dropped along the depth from 24.12^{o}C at 150mm to 27.28^{o}C at 750mm.

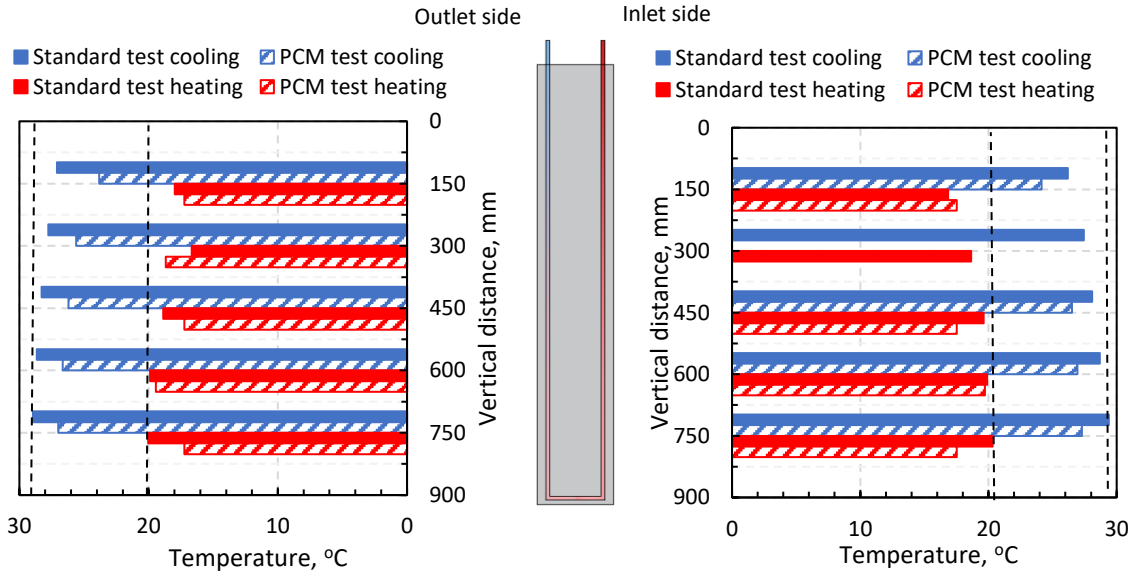

(a)

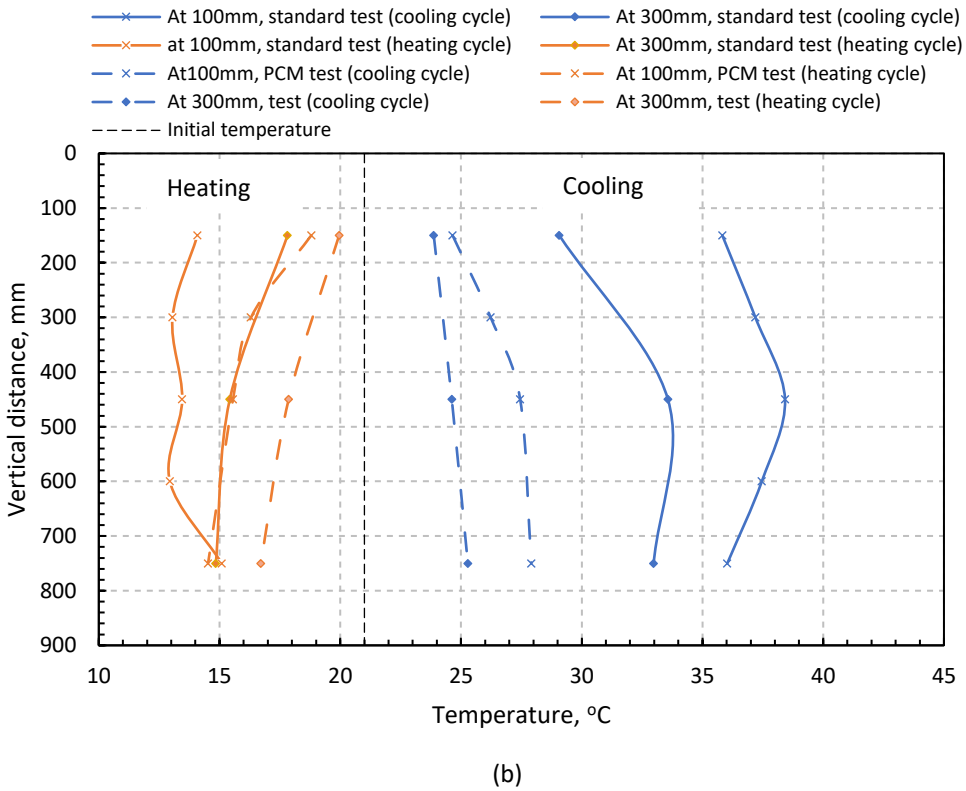

(b)

Fig. 7.23. (a). Soil vertical temperature profile at 100mm from GEP, (b). soil vertical temperature profile at 100mm and 300mm from GEW.

The influence of the inclusion of PCM LWA's at the interference zone between geo-energy wall and soil was also assessed and compared with the standard GEW. The vertical temperature profile was measured at two vertical sections (V1 and V2), located at 100 mm and 300 mm away from the experimented energy wall, respectively, as shown in Fig. 7.13. The measurements of temperature along V1 and V2 were taken at depths of 150 mm, 300 mm, 450 mm, and 750 mm. The data for soil temperature after reaching steady-state conditions at V1 and V2 were plotted in Fig. 7.24b. The figure clearly showed that the soil temperature at section V1 was significantly higher than that measured further away at section V2. In the cooling stages of the 100 hrs continuous operation, the steady state temperature changes for the PCM wall test was considered less significant than that the standard wall. The temperature changes at V1 from 24.65ºC at 150mm to 27.70ºC at 750 mm for PCM wall test, whereas for of the standard wall test, wall the temperature changes from 35.82ºC to 36.02ºC for the same measurement points. In contrast with the heating stages (where the soil is cooled), the vertical soil temperature changes at v1 were from 18.75ºC at 150 mm to 14.52ºC at 750ºC for PCM, wall test and 19.59ºC to 16.17ºC at 150mm

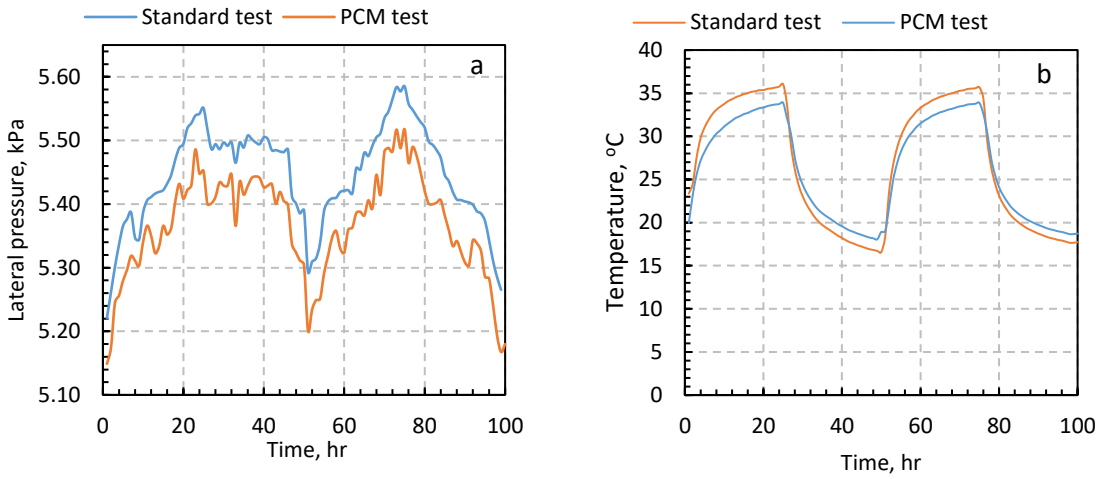

Fig. 7.24.a). Lateral earth pressure at the mid height of standard test and PCM test GEP; b). Change of temperature for GEP standard test and PCM test.

and 750mm respectively, for the standard wall test. Furthermore, it can be observed that the influence of the PCM inclusion at the wall/soil interface reduced the soil temperature changes around GEW significantly, in comparison with the case of using standard soil. This can be justified by the ability of PCM to store or reject more energy, and hence reducing the energy that might be extracted or rejected into the ground (Mousa et al., 2021).

The lateral earth pressure (LEP) at mid-height of the pile for both pile tests was measured, and the data is presented in Fig. 7.25a. As shown in the figure, the initial value of LEP was about 5.22 kPa and 5.174 kPa for the standard pile test and PCM pile test, respectively. At cooling cycles (where the pile was heated), the LEP increased gradually to reach peak pressure of 5.551k Pa and 5.486 kPa at the end of cooling stage for standard pile test and PCM pile test, respectively. Then, during the heating cycle LEP started to decrease, reaching 5.293 kPa and 5.201 kPa for the standard test and PCM test. The slight increase in LEP can be justified by the fact that the increase and decrease of pile temperature lead to thermal expansion/ shrinkage which will lead to an increase or decrease in LEP at the GEP/soil interface.

To verify this result, the thermal strain was calculated at the end of heating and cooling cycles using Equation (3.3).The calculation of $\varepsilon_{thermal}$ revealed that at

the end of cooling stage the peak strain was 63.71 με and 60.95με for standard and PCM pile tests. On the other hand, reducing the pile temperature leads to decrease the thermal strain to 97 με and 75 με for the standard and PCM pile tests. Furthermore, the internal thermal stresses were also calculated at the end of each heating and cooling stage using Equation (6.2). $\rho_{thermal}$ = 179 and 171 kPa for standard pile and PCM pile test at the end of cooling cycle and 271 and 211 kPa at the end of heating stage. These results indicated the GEP with PCM LWA's at the interface with soil has always smaller thermal deformation when compared with the standard pile test.

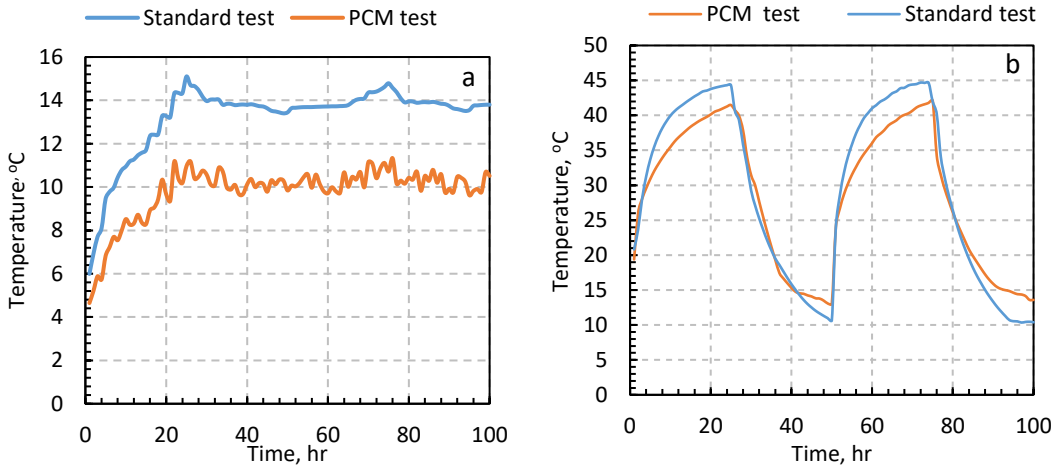

Fig. 7.25. a). Lateral earth pressure at the mid height of standard test and PCM test GEW; b). Change of temperature for GEW standard test and PCM test.

A pressure cell was installed at the centre point of the wall on the GEW/soil interface to measure the lateral earth pressure at the face of the wall. The capture data was presented in Fig. 7.26. The initial value of LEP was approximately 5.56 kPa for standard GEW and 4.734 kPa for the case of using PCM LWA's at the interface. During the cooling stage, the wall was heated and the LEP was gradually increased until reaching the peak pressure of 14.73 kPa and 11.18 kPa for the standard test and PCM test, respectively, at the end of cooling stage. Then, it started to decrease when the heating stage reached the lowest value of 13.44 kPa and 9.67 kPa at the end of heating stage, for the standard wall and PCM wall tests. The fluctuation of the LEP between heating and cooling was justified by

Dong et al., (2019), to the induced of thermal expansion/shrinkage due to heating/ cooling can lead to an increase or decrease in the earth pressure at the soil wall interface. In overall, the case of using PCM LWA's at the GEW/soil interface offered about 32% lower values for LEP, in comparison with the standard case. This could be due to the excellent drainage property and the ability of LWA to control ground water pressure through the drainage surface water and ground water. Similar results were obtained by Sherif et al., (2017) when the LEP was significantly reduced by up to 25% when the expanded polystyrene (EPS) is used at the interface between sand and concrete.

7.5 Summary of findings

This paper aimed to study the thermal performance of geo-energy piles and walls by using PCM LWA's soil mix at the interface between the structure and the soil. In the case of GEP, RT26 was impregnated in the LWA's, and mixed with the soil to form highly TES soil mix, while RT42 was used for the wall test. The following conclusions are drawn:

- The use of MF- Carbon fibre showed the best performance and durability compared with the other two methods for sealing the impregnated LWA's.
- The addition of PCM impregnated LWA's to sand led to dropping the MDUW and the OMC, while it increased the permeability coefficient and the friction angle of the soil mix.
- The thermal energy storage of the soil and PCM LWA's mixes increased by increasing the percentage of PCM in the mix. Soil with 35% PCM LWA's stored 30.84 kj/kg at $\Delta T = 10^{o}C$, which can be equivalent to $\Delta T = 37^{o}C$ in the neutral soil case.
- The results showed a reduction in the thermal conductivity and thermal diffusivity with the increase of PCM LWA's amount in the soil mix.
- in the case of geo-energy pile, the inclusion of 35 % PCM LWA's at the GEP/soil interface increased the temperature difference (inlet-outlet) by 156% and 181% during cooling and heating, respectively.

- In comparison with the standard GEW, the addition of PCM LWA's at the wall/ soil interface rose ΔT by 72% and 83% for cooling and heating, respectively.
- The results showed that the effect of PCM inclusion to enhance the thermal performance was more significant during the heating mode (PCM was cooled down) than that for the cooling mode (PCM was heated up).
- For the case of using PCM LWA's, the thermal deformation in terms of thermal stress and strain was always smaller than that reported in the standard case.
- The soil temperature significantly reduced when the PCM LWA's was used in the GES/ soil interface.

Chapter 8: Conclusions and future work

8.1 Summary

The main aim of this research was to enhance the thermal performance of geo-energy piles and walls through improving: i. Thermal properties of concrete. ii. Thermal properties of GES/soil interface. iii. Thermal energy storage of these structures. In order to achieve the aim, different enhancement approaches were proposed and thoroughly presented in the previous five chapters. The main purpose of this chapter is to summarise the main findings obtained these approaches and provide a number of suggestions for future work.

8.2 Conclusions

The findings achieved from each approach for geo energy piles and walls were stated in full details at the end of each chapter. Hence, this section presents the main findings drawn from this research work as follows:

- The impacts of using graphTHERM concrete on the thermal performance of geo-energy structures was significant. The Results illustrated that adding 36% of graphTHERM powder to concrete by weight of cement was found to double the thermal conductivity of concrete, and improve the stiffness by 15% without detrimental effects on the compressive strength. The heat transfer efficiency of energy pile and energy diaphragm wall made from graphTHERM concrete was considerably enhanced by 50% and 66% respectively, in comparison with the efficiency of the same type of energy structure made from a normal concrete.

- The heat transfer efficiency of GPC geo energy piles and walls was higher by 14% and 21% respectively, in comparison with the efficiency of geo energy structure that was made from OPCC. Also, the use of geopolymer concrete reduced the coefficient of thermal expansion by 17% in compression with that for OPCC, providing less lateral earth pressure. From environmental point view, the GPC produced almost 44.5% less CO2 emissions than OPPC.

- Placing 100 mm of thermally enhanced sands by graphTherm and carbon fibre powders resulted in experiencing a remarkable improvement in the heat transfer efficiency of the geo-energy piles by 81 % and 54 %, respectively. Furthermore, an extraordinary increase (100 % and 80 %) in the heat transfer efficiency was reported when 200 mm of thermally enhanced sands were placed in front of geo-energy. The findings of using thermally enhanced soils with a finite size at the GES-soil interface also suggested that the use of thermally enhanced sands at GES-soil interface did not cause unfavourable impacts in the lateral earth pressure on the GES but it was effective in enlarging the thermally active soil zone.

- The use of PCM heat exchanger increases the heat transfer efficiency of geo-energy piles by 75 % and 43% in heating and cooling operations respectively in comparison with those achieved using a standard heat exchanger. Also, the heat transfer performance of geo-energy walls with PCM heat exchanger was enhanced by 43 % and 32 % in heating and cooling tests respectively. Interestingly, the use of PCM heat exchangers not only enhance the thermal performance but also reduced the possible impact of using GES on soil temperature and the thermal interference radius. Furthermore, the findings also indicated that the PCM heat exchangers were able to reduce potential damage due to thermal stress, in comparison with traditional energy wall structure.

- Increasing the thermal energy-storage of geo energy structures by incorporating PCM-impregnated LWA’s at the interface of structure soil, showed that the inclusion of 35 % PCM LWA’s at the GES/soil interface, extensively increased the temperature difference (inlet-outlet) for cooling and heating. It is also illustrated that the effect of PCM inclusion to enhance the thermal performance is more significant during the heating mode (PCM is cooled down) than the cooling mode (PCM is heated up). Furthermore, the findings indicated that the use of PCM LWA’s has reduced the thermal deformation of GES and has a positive impact on soil temperature and interference radius.

8.3 Contribution to knowledge

- My PhD research has contributed to developing knowledge in different aspects of engineering. In addition to testing experimentally large scales of thermally enhanced geo-energy piles and walls for the first time, this research revealed the feasibility of using geopolymer concrete as an alternative material to replace the traditional ones in GES applications.
- The research also provided a new concept about enhancing the thermal performance of GES through mixing conductive fillers (graphTHERM and Carbon fibre) with soils at the interface between GES and soils.
- This study also enhanced thermal energy storage of geo-energy structures via two new techniques, namely PCM heat exchanger, and PCM impregnated LWA'S , which allows developing the thermal performance and reducing the thermal deformation of GES.

8.4 Limitations

The study used fixed inlet temperatures of 52°C for cooling tests and -2°C for heating tests. These temperatures may not accurately represent real-world conditions of geo-energy structure (GES) operations. The chosen temperatures were intended to create a reasonable temperature gradient, considering the constant room temperature of 21°C. However, the results and conclusions drawn from the study may not fully reflect the performance enhancement under different inlet temperatures and ambient temperatures that are encountered in actual GES operations. It's important to acknowledge that this study findings and conclusions may be influenced by the selected temperature conditions. Extrapolating the results to real-world scenarios with different temperature conditions should be done with caution, as the performance of GES systems can vary significantly based on temperature differentials and operating conditions.

8.5 Recommendations for future work

This research has delivered new insights into the enhancement of the thermal performance of geo-energy piles and walls. However, it has also revealed that

further studies are required to be addressed in future research. These studies can be summarised as follows:

- **Measurement of thermal elongation and thermally induced bending for thermally enhanced piles and walls.**

Further investigations on the effect of graphTHERM concrete and Geopolymer concrete on the thermally induced elongation for geo-energy piles and walls and the thermally induced bending for the geo-energy wall are highly required.

- **investigations into the producing the geopolymer concrete from other by-product material.**

The current investigation conducted in geo-energy piles and wall made of geo-polymer concrete are limited to by-product materials such as slag and fly ash. Testing the thermal performance of geopolymer concrete piles and walls pre-pared from other sources (e.g construction demolition waste (CDW)) are highly required due to the high demand and limited resource of by-product material.

- **The thermal contact resistance between the geo-energy structure and the surrounded soils.**

It would be great benefit to carried out further experimental and numerical studies to acquire better understanding of the contact thermal resistance at the interface between the geo energy structures and the soil considering different parameters (e.g. concrete and soil mineralogy, contact roughness, compaction level, and other parameters).

- **Optimising the thermal performance of PCM heat exchanger.**

In this research the PCM HE was made out from two pipes, the inner pipe acts as a heat transfer fluid carrier, whearas the outer pipe hosts the PCM around the inner pipe. The inner pipe is made from nylon, whilst the outer pipe is made of polybutylene. Using pipes from different materials can lead to achieving better thermal performance, and hence, investigations in this area seems an essential practise.

- **PCM LWA's as thermally storage enhancement technique at GES/soil interface.**

The use of PCM LWA's at the interface between GES and soils has showed positive influence on the thermal and mechanical performance of GES during cooling and heating operations. Therefore, it become essential to carried out further research to propose a method for executing this method of enhancement in real projects.

- **Combination between different thermal enhancement approaches.**

In this thesis, different approaches to enhance the thermal performance of geo energy piles and walls were thoroughly studied. However, combination of two or more enhancement approaches may lead to better thermal and mechanical performance. Therefore, more relevant studies are needed:

1- Using of PCM heat exchanger with thermally enhanced concrete, this could provide considerable thermal enhancement with significant reduction in GES temperatures.
2- Using the thermally enhanced concrete with thermally enhanced interface, the expected benefit of carrying out this method, can be extreme enhancement of the thermal performance. However, this method would more likely lead to cause extraordinary increase in the GES and the surrounded soil temperatures.
3- Using thermally enhanced concrete with highly thermally storage interface (using PCM LWA's at the interface between soils and GES).
4- Enhancing the thermal energy storage and the thermal properties of the interface GES/ soil by using PCM LWA's and conductive additives.

Also, the critical review of the available up-to-date literature review have revealed that there are many research gaps regarding the performance of geo energy structures need to be covered and some these can be as follows:

- **The behaviour of corroded geo energy structures.**

Energy piles and other types of geo energy structures are commonly cast in place, which can potentially subject these structures to either concrete faults or reinforcement installation issues. In the case of concrete faults voids in concrete piles might be formed due to insufficient of concrete which might resulted from the non-even finish of the borehole. Furthermore, steel bars are more likely to be laterally moved or dragged down during compaction. Consequently, the steel bars will be exposed to the surrounding environments and the piles are mostly buried in wet soils, provides an ideal environment for steel corrosion.

The corrosion of steel reinforcement in concrete is an electrochemical process which occurs in the presence of moisture, oxygen and some catalyst to start the electrochemical process. In this process, the iron in the steel is oxidized to produce rust, which can increase the volume of steel two to four times. This can create a week interface layer between concrete and steel. The consequences of the steel corrosion in concrete might lead to internal tensile stresses, causing loss in bonding. Followed by cracking, spalling, which in turn significantly affects the load carrying capacity.

The limited studies conducted on pile foundation after exposure to corrosion indicated that, corrosion can significantly accelerate the formation of the cracks within three to seven years after initiation (Weyers, 1998). Feng et al. 2021 carried out a laboratory and numerical study to investigate the corrosion damage and the bearing capacity characteristics of bridge pile foundations. Interestingly, the result revealed that the increase of corrosion depth leads to gradually decrease the pile bearing capacity after 8 years. They also highlighted that the bearing capacity of the pile will decreased by 34.5% in the 20th years of operation. However, no studies have been evaluated the thermal and mechanical behaviour of geo energy piles or other types after the exposure to corrosion. Therefore, its required to evaluate the influence of different corrosion levels on the thermal and mechanical performance of geo energy piles and other GES.

- **Self-sensing geo energy piles**

Monitoring the mechanical deformation of geo energy structures is common practice in real projects. Currently, vibrating wire strain gauges or other types and load sensors are used to measure these deformations. However, the durability, cost and the none-linear behaviour of those sensors motivates researchers to develop new methods for monitoring the concrete health. Recently, concrete can be modified to be self- monitoring concrete using smart materials such as carbon nanofibers. Those smart materials have the ability to sense and respond the changes in strain, temperature, electrical shield and moisture through the measurement of the change in the thermal resistivity. The self-monitoring property of the concrete have been covered in many researches such as (Li et al. 2006; Wen and Chung. 2007; Han et al. 2007; Azhari and Banthia. 2012; Howser Roberts, 2013; Materazzi et al. 2013; Ding et al. 2013; Han et al. 2014; Dalla et al. 2016; D'Alessandro et al. 2016; Azhari and Banthia.2017). however, none of these studies have applied the self-sense property for geo energy piles, hence, examine the self monitoring property of geo-energy pile is required.

Bibliography

A. A. Mehrizi, S. Porkhial, B. Bezyan, and H. Lotfizadeh, “Energy pile foundation simulation for different configurations of ground source heat exchanger,” Int. Commun. Heat Mass Transf., vol. 70, pp. 105–114, 2016, doi: 10.1016/j.icheatmasstransfer.2015.12.001.

A. Zarrella, M. De Carli, and A. Galgaro, “Thermal performance of two types of energy foundation pile: Helical pipe and triple U-tube,” Appl. Therm. Eng., vol. 61, no. 2, pp. 301– 310, 2013, doi: 10.1016/j.applthermaleng.2013.08.011.

AbdelSalam, S. S., Azzam, S. A., & Fakhry, B. M. (2017). Reliability and 3D modeling of flexible walls with EPS inclusion. *International Journal of Geomechanics*, *17*(7), 04016153.

Abu-Hamdeh, N. H. (2003). Thermal properties of soils as affected by density and water content. Biosystems engineering, 86(1), 97-102.

Adesina, A. (2020). Performance and sustainability overview of alkali-activated self-compacting concrete. Waste Disposal & Sustainable Energy, 1-11.

Adesina, A. (2021). Performance and sustainability overview of sodium carbonate activated slag materials cured at ambient temperature. Resources, Environment and Sustainability, 100016.

Akrouch, G. (2014). Energy piles in cooling dominated climates (Doctoral dissertation).

Alhawat, M., Ashour, A., Yıldırım, G., Aldemir, A. and Sahmaran, M., 2022. Properties of geopolymer sourced from construction and demolition waste: A review. Journal of Building Engineering, p.104104.

Ali, I. M., Naje, A. S., & Nasr, M. S. (2020). Eco-friendly chopped tire rubber as reinforcements in fly ash based geopolymer concrete. Glob. NEST J., 22, 342-7.

Almutairi, A. L., Tayeh, B. A., Adesina, A., Isleem, H. F., & Zayed, A. M. (2021). Potential applications of geopolymer concrete in construction: A review. Case Studies in Construction Materials, e00733.

aloui, L, Di Donna, A, 2013. Energy Geostructures: Innovation in Underground Engineering. ISTE Ltd, London, UK and John Wiley & Sons Inc, Hoboken, NJ, USA. Book.

Alrtimi, A., Rouainia, M., & Haigh, S. (2016). Thermal conductivity of a sandy soil. *Applied Thermal Engineering*, *106*, 551-560.

Alrtimi, A., Rouainia, M., & Manning, D. A. C. (2014). An improved steady-state apparatus for measuring thermal conductivity of soils. *International Journal of Heat and Mass Transfer*, *72*, 630-636.

Alsalman, A., Assi, L. N., Kareem, R. S., Carter, K., & Ziehl, P. (2021). Energy and CO2 emission assessments of alkali-activated concrete and Ordinary Portland Cement concrete: A comparative analysis of different grades of concrete. Cleaner Environmental Systems, 3, 100047.

Amran, Y. M., Alyousef, R., Alabduljabbar, H., & El-Zeadani, M. (2020). Clean production and properties of geopolymer concrete; A review. journal of cleaner production, 251, 119679.

Arora, A., Aguayo, M., Hansen, H., Castro, C., Federspiel, E., Mobasher, B., Neithalath, N., 2018. Microstructural packing-and rheology-based binder selection and characterization for Ultra-high Performance Concrete (UHPC). Cem. Concr. Res. 103, 179–190.

Athienitis AK, Liu C, Hawes D, Banu D, Feldman D. Investigation of the thermal performance of a passive solar test-room with wall latent heat storage. Building and Environment. 1997;32(5):405-10.

Banks, D. (2008) 'An introduction to thermogelogy: Ground source heating and cooling', 1edn. oxford: Black well publishing LTD.

Bao, X., Li, Y., Feng, T., Cui, H. and Chen, X., (Bao, Li et al. 2019)2019. Investigation on thermo-mechanical behavior of reinforced concrete energy pile with large cross-section in saturated sandy soil by model experiments. Underground Space.

Bao, X., Qi, X., Cui, H., Tang, W., & Chen, X. (2022). Experimental study on thermal response of a PCM energy pile in unsaturated clay. Renewable Energy, 185, 790-803.

Barla, M., Di Donna, A., & Santi, A. (2020). Energy and mechanical aspects on the thermal activation of diaphragm walls for heating and cooling. *Renewable Energy*, *147*, 2654-2663.

Barnard, A.C.L., Hunt, W.A., Timlake, W.P., Varley, E., 1966. A theory of fluid flow in compliant tubes. Biophysical Journal 6, 717–724.

Barrios, M.N., Choi, Y.S. and Van Sciver, S.W. (2008) 'Thermal conductivity of powder insulations below 180 k', AIP Conference Proceedings, American Institute of Physics. pp. 788-795.

Bas, B. E. (2020). Study on The Thermal Properties of Concrete Containing Ground Granulated Blast Furnace Slag, Fly Ash and Steel Reinforcement.

Bensharada, M., Telford, R., Stern, B., & Gaffney, V. (2022). Loss on ignition vs. thermogravimetric analysis: A comparative study to determine organic matter and carbonate content in sediments. *Journal of Paleolimnology*, *67*(2), 191-197.
BniLam, N.; Al-Khoury, R.; Shiri, A.; Sluys, L.J. A semi-analytical model for detailed 3D heat flow in shallow geothermal systems. Int. J. Heat Mass Transf. 2018, 123, 911–927

Boman, B. J., & Stover, E. W. (2002). Managing salinity in florida citrus. *Univ. of Florida, IFAS, Coop. Ext. Circ*, *1411*.
Bourne-Webb, P., Burlon, S., Javed, S., Kürten, S., & Loveridge, F. (2016). Analysis and design methods for energy geostructures. Renewable and sustainable energy reviews, 65, 402-419.

Bourne-Webb, P.J., Freitas, T.B., da Costa Gonçalves, R.A., 2016. Thermal and mechanical aspects of the response of embedded retaining walls used as shallow geothermal heat exchangers. Energy Build. 125, 130–141.

Bowen, A., & Rydge, J. (2011). Climate-change policy in the United Kingdom.

Brandl, H. (2006). Energy foundations and other thermo-active ground structures. Géotechnique, 56(2), 81-122.

Brandl, H. (2016). Geothermal geotechnics for urban undergrounds. Procedia engineering, 165, 747-764.

Brandl, H. Energy foundations and other thermo-active ground structures. Géotechnique 2006, 56, 81–122.

Brandl, H., 2006. Energy foundations and other thermo-active ground structures. G´eotechnique 56 (2), 81–122.

Brandon, T.L. and Mitchell, J.K. (1989) 'Factors influencing thermal resistivity of sands', Journal of geotechnical engineering, 115(12), pp. 1683-1698.

BSI, 2001. BS EN 12664:2001 Thermal performance of building materials and products. BSI, London. buildings. J. Sol. Energy Eng. 135 (4), 040907.

C. J. Wood, H. Liu, and S. B. Riffat, “Comparative performance of ‘U-tube’ and ‘coaxial’ loop designs for use with a ground source heat pump,” Appl. Therm. Eng., vol. 37, pp. 190– 195, May 2012, doi: 10.1016/j.applthermaleng.2011.11.015.

Cabeza LF, Castellón C, Nogués M, Medrano M, Leppers R, Zubillaga O. Use of micro-encapsulated PCM in concrete walls for energy savings. Energy and Buildings. 2007;39(2):113-9.

Cao, S.-J., Kong, X.-R., Deng, Y., Zhang, W., Yang, L., Ye, Z.-P., 2016. Investigation on the thermal performance of steel heat exchanger for ground source heat pump systems using full-scale experiments and numerical simulations. Appl. Therm. Eng. 115, 91–98.

Cao, Z., Zhang, G., Liu, Y., Zhao, X., & Li, C. (2022). Influence of backfilling phase change material on thermal performance of precast high-strength concrete energy pile. Renewable Energy, 184, 374-390.

Cao, Z., Zhang, G., Liu, Y., Zhao, X., & Li, C. (2022). Influence of backfilling phase change material on thermal performance of precast high-strength concrete energy pile. *Renewable Energy*, *184*, 374-390.
Castell A, Martorell I, Medrano M, Pérez G, Cabeza LF. Experimental study of using PCM in brick constructive solutions for passive cooling. Energy and Buildings. 2010;42(4):534-40.

Cecinato, F, Loveridge, FA., 2015. Influences on the thermal efficiency of energy piles. Energy 1021-1033, 82.

Cercel, J., Adesina, A. and Das, S., 2021. Performance of eco-friendly mortars made with alkali-activated slag and glass powder as a binder. Construction and Building Materials, 270, p.121457.

Cercel, J., Adesina, A., & Das, S. (2021). Performance of eco-friendly mortars made with alkali-activated slag and glass powder as a binder. Construction and Building Materials, 270, 121457.

Chen, S. (2008) 'Thermal conductivity of sands', Heat and Mass Transfer, 44(10), pp. 1241-1246.

Chiasson, A.D. Geothermal Heat Pump and Heat Engine Systems; Wiley: Hoboken, NJ,

USA, 2016

Churchill, S.W., 1997. Friction factor equations spans all fluid-flow regimes. Chemical Engineering 84, 91–92.

D. Qi, L. Pu, F. Sun, and Y. Li, “Numerical investigation on thermal performance of ground heat exchangers using phase change materials as grout for ground source heat pump system,” Appl. Therm. Eng., vol. 106, pp. 1023–1032, 2016, doi: 10.1016/j.applthermaleng.2016.06.048.

Das, S. K., Singh, S. K., Mishra, J., & Mustakim, S. M. (2020). Effect of Rice Husk Ash and Silica Fume as Strength-Enhancing Materials on Properties of Modern Concrete—A Comprehensive Review. Emerging Trends in Civil Engineering, 253-266.

Das, S.K. and Shrivastava, S., 2021. Influence of molarity and alkali mixture ratio on ambient temperature cured waste cement concrete based geopolymer mortar. Construction and Building Materials, 301, p.124380.

Das, S.K., Choi, S.U., Patel, H.E., 2006. Heat transfer in nanofluids—a review. Heat Transfer Eng. 27 (10), 3–19.

Delaleux, F., Py, X., Olives, R., & Dominguez, A. (2012). Enhancement of geothermal borehole heat exchangers performances by improvement of bentonite grouts conductivity. *Applied Thermal Engineering*, *33*, 92-99.

Di Donna, A., 2016. Energy walls for an underground car park. In: 25th European Young Geotechnical Engineering conference. Sibiu, Romania, 21-24 June 2016.

Di Donna, A., Cecinato, F., Loveridge, F., & Barla, M. (2017). Energy performance of diaphragm walls used as heat exchangers. *Proceedings of the Institution of Civil Engineers-Geotechnical Engineering*, *170*(3), 232-245.

Di Donna, A., Loveridge, F., Piemontese, M., & Barla, M. (2021). The role of ground conditions on the heat exchange potential of energy walls. *Geomechanics for Energy and the Environment*, *25*, 100199.

Dimov, D., Amit, I., Gorrie, O., Barnes, M.D., Townsend, N.J., Neves, A.I., Craciun, M.F., 2018. Ultrahigh performance nanoengineered graphene–concrete composites for multifunctional applications. Adv. Funct. Mater. 28 (23), 1705183.

Dong, S., Li, X., Tang, A. M., Pereira, J. M., Nguyen, V. T., Che, P., & Xiong, Z. (2019). Thermo-mechanical behavior of energy diaphragm wall: Physical and numerical modelling. *Applied Thermal Engineering*, *146*, 243-251.

Dong, S., Li, X., Tang, A.M., Pereira, J.M., Nguyen, V.T., Che, P., Xiong, Z., 2019. Thermo-mechanical behavior of energy diaphragm wall: Physical and numerical modelling. Appl. Therm. Eng. 146, 243–251.

Dorrian, D., & Mumm, S. M. (2011). U.S. Patent Application No. 12/835,404. EN 1992-1-2, 2004. Eurocode 2: Design of Concrete Structures - Part 1-2, 1st ed. BSi, Brussels.

Drysdale, B., Wu, J., & Jenkins, N. (2015). Flexible demand in the GB domestic electricity sector in 2030. Applied Energy, 139, 281-290.

EC, A. (2018). Clean Planet for all: a European strategic long-term vision for a prosperous, modern, competitive and climate neutral economy. *COM (2018) 773-communication from the commission to the european parliament, the european council, the council, the european economic and social committee, the committee of the regions and the european investment bank*.

Egg, J.; Howard, B.C.; Bass, J.; Otte, N.; Hassman, K. Geothermal HVAC. In Green Heating and Cooling; McGraw-Hill: New York, NY, USA, 2011

Elkezza, O., Mohamed, M., & Khan, A. (2022). Performance of thermally enhanced geoenergy piles and walls. Geothermics, 98, 102274.

Elzeadani, M., Bompa, D. V., & Elghazouli, A. Y. (2021). Preparation and properties of rubberised geopolymer concrete: A review. Construction and Building Materials, 313, 125504.

Erol, S., & François, B. (2014). Efficiency of various grouting materials for borehole heat exchangers. *Applied Thermal Engineering*, *70*(1), 788-799.

F. Chen et al., “Restoration performance and operation characteristics of a vertical U-tube ground source heat pump system with phase change grouts under different running modes,” Appl. Therm. Eng., vol. 141, no. February, pp. 467–482, 2018, doi: 10.1016/j.applthermaleng.2018.06.009 .

F. Chen, J. Mao, S. Chen, C. Li, P. Hou, and L. Liao, “Efficiency analysis of utilizing phase change materials as grout for a vertical U-tube heat exchanger coupled ground

source heat pump system," Appl. Therm. Eng., vol. 130, pp. 698–709, 2018, doi: 10.1016/j.applthermaleng.2017.11.062.

Faizal, M., Bouazza, A., & Singh, R. M. (2016). Heat transfer enhancement of geothermal energy piles. Renewable and Sustainable Energy Reviews, 57, 16-33.

Faroki, O.T., 1986. Thermal Properties of Soils "; Series on Rock and Soil Mechanics, 11. Trans Tech Publications.

Farooq, F., Jin, X., Javed, M. F., Akbar, A., Shah, M. I., Aslam, F., & Alyousef, R. (2021). Geopolymer concrete as sustainable material: A state of the art review. Construction and Building Materials, 306, 124762.

Feldman D, Banu D, Hawes DW. Development and application of organic phase change mixtures in thermal storage gypsum wallboard. Solar Energy Materials and Solar Cells. 1995;36(2):147-57.

Fillion, M-H., Cote, J. & Konrad, J-M. (2011) Thermal radiation and conduction properties of materials ranging from sand to rock-fill, Canadian Geotechnical Journal, 48, 532-542.

Gashti, E.H.N., Uotinen, V.M., Kujala, K., 2014. Numerical modelling of thermal regimes in steel energy pile foundations: A case study. Energy Build. 69, 165–174.

Ghacham, A. B., Pasquier, L. C., Cecchi, E., Blais, J. F., & Mercier, G. (2016). CO 2 sequestration by mineral carbonation of steel slags under ambient temperature: parameters influence, and optimization. Environmental Science and Pollution Research, 23(17), 17635-17646.

Ghozatloo, A., Rashidi, A., Shariaty-Niassar, M., 2014. Convective heat transfer enhancement of graphene nanofluids in shell and tube heat exchanger. Exp. Therm. Fluid Sci. 53, 136–141.

Ghuman, B. S., & Lal, R. (1985). Thermal conductivity, thermal diffusivity, and thermal capacity of some Nigerian soils. Soil Science, 139(1), 74-80.

Godson, L., Deepak, K., Enoch, C., Jefferson, B., Raja, B., 2014. Heat transfer characteristics of silver/water nanofluids in a shell and tube heat exchanger. Arch. Civ. Mech. Eng. 14 (3), 489–496.

Guerrieri, M. and Sanjayan, J.G., 2010. Behavior of combined fly ash/slag-based geopolymers when exposed to high temperatures. Fire and Materials: An International Journal, 34(4), pp.163-175.

Guo, C., Zhu, J., Zhou, W., Chen, W., 2010. Fabrication and thermal properties of a new heat storage concrete material. J. Wuhan Univ. Tech.-Mater. Sci. Ed. 25 (4), 628–630.

H. Benli and A. Durmuş, "Evaluation of ground-source heat pump combined latent heat storage system performance in greenhouse heating," Energy Build., vol. 41, no. 2, pp. 220– 228, 2009, doi: 10.1016/j.enbuild.2008.09.004.

H. Benli, "Energetic performance analysis of a ground-source heat pump system with latent heat storage for a greenhouse heating," Energy Convers. Manag., vol. 52, no. 1, pp. 581– 589, 2011, doi: 10.1016/j.enconman.2010.07.033.

H. Park, S. R. Lee, S. Yoon, and J. C. Choi, "Evaluation of thermal response and performance of PHC energy pile: Field experiments and numerical simulation," Appl. Energy, vol. 103, pp. 12–24, 2013, doi: 10.1016/j.apenergy.2012.10.012.

Hall, M. and Allinson, D. (2009a) 'Analysis of the hydrothermal functional properties of stabilised rammed earth materials', Building and Environment, 44(9), pp. 1935-1942.

Hamada, H., Tayeh, B., Yahaya, F., Muthusamy, K. and Al-Attar, A., 2020. Effects of nano-palm oil fuel ash and nano-eggshell powder on concrete. Construction and Building Materials, 261, p.119790.

Hammond, G., Jones, C., Lowrie, F., & Tse, P. Building Services Research and Information Association, & University of Bath.(2011). Embodied carbon: the inventory of carbon and energy (Ice). Bracknell: BSRIA.

Han, C., & Yu, X. B. (2018). An innovative energy pile technology to expand the viability of geothermal bridge deck snow melting for different United States regions: Computational assisted feasibility analyses. Renewable Energy, 123, 417-427.

Hasanbeigi, A., Price, L., & Lin, E. (2012). Emerging energy-efficiency and CO2 emission-reduction technologies for cement and concrete production: A technical review. Renewable and Sustainable Energy Reviews, 16(8), 6220-6238.

He, R., Dai, N. and Wang, Z., 2020. Thermal and mechanical properties of geopolymers exposed to high temperature: a literature review. Advances in Civil Engineering, 2020.

Hellstrom, G. (1991) Ground Heat Storage, Thermal Analysis of Duct Storage Systems, Theory, Department of Mathematical Physics, University of Lund, Sweden

Hills, T., Florin, N., & Fennell, P. S. (2016). Decarbonising the cement sector: a bottom-up model for optimising carbon capture application in the UK. Journal of cleaner production, 139, 1351-1361.

Hu, P., Zha, J., Lei, F., Zhu, N., & Wu, T. (2014). A composite cylindrical model and its application in analysis of thermal response and performance for energy pile. Energy and buildings, 84, 324-332.

Hunger M, Entrop AG, Mandilaras I, Brouwers HJH, Founti M. The behavior of self-compacting concrete containing micro-encapsulated Phase Change Materials. Cement and Concrete Composites. 2009;31(10):731-43.

J. Gao, X. Zhang, J. Liu, K. S. Li, and J. Yang, “Thermal performance and ground temperature of vertical pile-foundation heat exchangers: A case study,” Appl. Therm. Eng., vol. 28, no. 17–18, pp. 2295–2304, Dec. 2008, doi: 10.1016/j.applthermaleng.2008.01.013.

J. L. Wang, J. De Zhao, and N. Liu, “Numerical simulation of borehole heat transfer with phase change material as grout,” Appl. Mech. Mater., vol. 577, pp. 44–47, 2014, doi: 10.4028/www.scientific.net/AMM.577.44.

J. U. Lee, T. Kim, and S. B. Leigh, “Applications of building-integrated coil-type ground-coupled heat exchangers - Comparison of performances of vertical and horizontal installations,” Energy Build., vol. 93, pp. 99–109, 2015, doi: 36 10.1016/j.enbuild.2015.02.020.

Jalaluddin, A. Miyara, K. Tsubaki, S. Inoue, and K. Yoshida, “Experimental study of several types of ground heat exchanger using a steel pile foundation,” Renew. Energy, vol. 36, no. 2, pp. 764–771, Feb. 2011, doi: 10.1016/j.renene.2010.08.011.

Javadi, H., Mousavi Ajarostaghi, S. S., Rosen, M. A., & Pourfallah, M. (2018). A comprehensive review of backfill materials and their effects on ground heat exchanger performance. *Sustainability*, *10*(12), 4486.

Jiao, W., Sha, A., Liu, Z., Jiang, W., Hu, L., & Li, X. (2020). Utilization of steel slags to produce thermal conductive asphalt concretes for snow melting pavements. Journal of Cleaner Production, 261, 121197.

Jobmann, M., & Buntebarth, G. (2009). Influence of graphite and quartz addition on the thermo–physical properties of bentonite for sealing heat-generating radioactive waste. *Applied Clay Science*, *44*(3-4), 206-210.

Johansen, O. (1975) 'Thermal conductivity of soils', Trondheim University, Norway.

K. Sani, R. M. Singh, T. Amis, and I. Cavarretta, “A review on the performance of geo-thermal energy pile foundation, its design process and applications,” Renew. Sustain. Energy Rev., vol. 106, no. March, pp. 54–78, 2019, doi: 10.1016/j.rser.2019.02.008.

Kaltreider, C., Krarti, M., McCartney, J., 2015. Heat transfer analysis of thermo-active foundations. Energy Build. 86, 492–501.

Kamseu, E., Nait-Ali, B., Bignozzi, M.C., Leonelli, C., Rossignol, S. and Smith, D.S., 2012. Bulk composition and microstructure dependence of effective thermal conductivity of porous inorganic polymer cements. Journal of the European Ceramic Society, 32(8), pp.1593-1603.

Kastiukas, G., Zhou, X. and Castro-Gomes, J. (2016) ‘Development and optimisation of phase change material-impregnated lightweight aggregates for geopolymer composites made from aluminosilicate rich mud and milled glass powder’, Construction and Building Materials. Elsevier Ltd, 110, pp. 201–210. doi: 10.1016/j.conbuildmat.2016.02.029.

Kavanaugh, S.P.; Rafferty, K. Ground-Source Heat Pumps: Design of Geothermal Systems for Commercial and Institutional Buildings; American Society of Heating, Refrigerating and Air-Conditioning Engineers: Atlanta, GA, USA, 1997.

Kersten, M.S. (1949) 'Laboratory research for the determination of the thermal properties of soils', University of Minnesota, Minneapolis, Engineering Experiment Station.

Kheradmand, M. et al. (2015) ‘Assessing the feasibility of impregnating phase change materials in lightweight aggregate for development of thermal energy storage systems’, Construction and Building Materials. Elsevier Ltd, 89, pp. 48–59. doi: 10.1016/j.conbuildmat.2015.04.031.

Kong, L.P., Qiao, L., Xiao, Y.Y., Li, Q.W., 2019. A study on heat transfer characteristics and pile group influence of enhanced heat transfer energy piles. J. Build. Eng. 24, 100768.

Kovaˇcevi´c, M.S., Baˇci´c, M., Arapov, I., 2012. Prospects of underground engineering in the use of shallow energy. Građe- vinar 64 (12), 1019–1028.

Kovačević, M. S., Bačić, M., & Arapov, I. (2013). Possibilities of underground engineering for the use of shallow geothermal energy. Gradevinar, 64(12), 1019-1028.

Kramer, C. A., MSc in civil engineering (2013). An experimental investigation on performance of a model geothermal pile in sand. The Pennsylvania State University

Krishnaiah, S. and Singh, D.N. (2003) 'Determination of influence of various parameters on thermal properties of soils', International Communications in Heat and Mass Transfer, 30(6), pp. 861-870.

Kumar, S., Kumar, R., & Mehrotra, S. P. (2010). Influence of granulated blast furnace slag on the reaction, structure and properties of fly ash based geopolymer. Journal of materials science, 45(3), 607-615.

Kumar, S., Murugesan, K., 2020. Optimization of geothermal interaction of a double Utube borehole heat exchanger for space heating and cooling applications using Taguchi method and utility concept. Geothermics 83, 101723.

Kurten S, D. Mottaghy, Ziegler M. A new model for the description of the heat transfer for plane thermo-active geotechnical systems based on thermal resistances. Acta Geotech. 2015;10(2):219–229.

Kurten, S., Mottaghy, D., Ziegler, M., 2015. Design of plane energy geostructures based on laboratory test and numerical modelling. Energy Build. 107, 434–444.

Kwag, B.C., Krarti, M., 2013. Performance of thermoactive foundations for commercial

L. Pu, L. Xu, S. Zhang, and Y. Li, “Optimization of ground heat exchanger using micro-encapsulated phase change material slurry based on tree-shaped structure,” Appl. Energy, vol. 240, no. January, pp. 860–869, 2019, doi: 10.1016/j.apenergy.2019.02.088.

L. Rybach and W. J. Eugster, “Sustainability aspects of geothermal heat pump operation, with experience from Switzerland,” Geothermics, vol. 39, no. 4, pp. 365–369, 2010, doi: 10.1016/j.geothermics.2010.08.002.

Laloui and Di Donna A (2013) Energy Geostructures: Innovation in Underground Engineering. ISTE Ltd, London, UK and John Wiley & Sons Inc, Hoboken, NJ, USA. Book

Laloui, L., & Di Donna, A. (2011, November). Understanding the behaviour of energy geo-structures. In Proceedings of the Institution of Civil Engineers-Civil Engineering (Vol. 164, No. 4, pp. 184-191). Thomas Telford Ltd

Lee, S., Van Riessen, A., Chon, C.M., Kang, N.H., Jou, H.T. and Kim, Y.J., 2016. Impact of activator type on the immobilisation of lead in fly ash-based geopolymer. Journal of hazardous materials, 305, pp.59-66.

Li, Q., Chen, L., Ma, H., Huang, C.H., 2018. Enhanced Heat Transfer Characteristics of Graphite Concrete and Its Application in Energy Piles. Adv. Mater. Sci. Eng. 2018.

Li, Y., Mao, J., Geng, S., Han, X., Zhang, H., 2014. Evaluation of thermal short-circuiting and influence on thermal response test for borehole heat exchanger. Geothermics 50, 136.

Lin, Y., & Chen, H. L. (2015). Thermal analysis and adiabatic calorimetry for early-age concrete members. Journal of Thermal Analysis and Calorimetry, 122(2), 937-945.

Liu, L., Cai, G., Liu, X., Liu, S., & Puppala, A. J. (2019). Evaluation of thermal-mechanical properties of quartz sand–bentonite–carbon fiber mixtures as the borehole backfilling material in ground source heat pump. *Energy and Buildings*, *202*, 109407.

Lloyd, J. W. (1991). PA Domenico & FW Schwartz 1990. Physical and Chemical Hydrogeology. xxii+ 824 pp. New York, Chichester, Brisbane.

Loria, A. F. R. (2020). Energy geostructures: Theory and application. In E3S Web of Conferences (Vol. 205, p. 01004). EDP Sciences.

Loria, A. F. R., & Laloui, L. (2016). The interaction factor method for energy pile groups. Computers and Geotechnics, 80, 121-137.

Loria, A. F. R., & Laloui, L. (2017). Displacement interaction among energy piles bearing on stiff soil strata. Computers and Geotechnics, 90, 144-154.

Loveridge, F., McCartney, J. S., Narsilio, G. A., & Sanchez, M. (2020). Energy geostructures: a review of analysis approaches, in situ testing and model scale experiments. Geomechanics for Energy and the Environment, 22, 100173.

Loveridge, F., Powrie, W., 2014. 2D thermal resistance of pile heat exchangers. Geothermics 50, 122–135.

Lund, J.W.; Boyd, T.L. Direct utilization of geothermal energy 2015 worldwide review. Geothermics 2016, 60, 66–93.

Lyu, W., Pu, H., Xiao, H., Hu, D., Ma, Q., 2021. Thermal performance of energy pile with deeply penetrating 1-U-shape heat exchanger. Geothermics 91, 102023.

M. Abdel-Aal, M. Mohamed, R. Smits, R. E. Abdel-Aal, K. De Gussem, A. Schellart and S. Tait (2015) “Predicting wastewater temperatures in sewer pipes using abductive network models” Water Science & Technology, 71:1, 89-96.

M. Bottarelli, M. Bortoloni, Y. Su, C. Yousif, A. A. Aydın, and A. Georgiev, “Numerical analysis of a novel ground heat exchanger coupled with phase change materials,” Appl. Therm. Eng., vol. 88, pp. 369–375, 2015, doi: 10.1016/j.applthermaleng.2014.10.016.

M. Kong, J. L. Alvarado, C. Thies, S. Morefield, and C. P. Marsh, “Field evaluation of microencapsulated phase change material slurry in ground source heat pump systems,” Energy, vol. 122, pp. 691–700, 2017, doi: 10.1016/j.energy.2016.12.092.

Martynov (1959) Heat and Moisture Transfer in Freezing and Thawing Soils. In: Principles of Geocryology. National Research Council of Canada, Technical Translation 1065, Chapter VI.

Mathur, A., Srivastava, A., Mathur, J., Mathur, S., & Agrawal, G. D. (2015). Transient effect of soil thermal diffusivity on performance of EATHE system. *Energy Reports*, *1*, 17-21.

Maximillian, J., Brusseau, M., Glenn, E., & Matthias, A. (2019). Environmental and Pollution Science.
Mehling H, Cabeza LF. Heat and cold storage with PCM. Berlin: Springer; 2008.

Memon, S. A., Cui, H., Lo, T. Y., & Li, Q. (2015). Development of structural–functional integrated concrete with macro-encapsulated PCM for thermal energy storage. *Applied energy*, *150*, 245-257.
Meng, W., Khayat, K.H., 2016. Mechanical properties of ultra-high-performance concrete enhanced with graphite nanoplatelets and carbon nanofibers. Compos. Part B Eng. 107, 113–122.

Mikulčić, H., Klemeš, J. J., Vujanović, M., Urbaniec, K., & Duić, N. (2016). Reducing greenhouse gasses emissions by fostering the deployment of alternative raw materials and energy sources in the cleaner cement manufacturing process. Journal of cleaner production, 136, 119-132.

Mimouni, T., & Laloui, L. (2015). Behaviour of a group of energy piles. Canadian Geotechnical Journal, 52(12), 1913-1929.

Mohamed, M., El Kezza, O., Abdel-Aal, M., Schellart, A., & Tait, S. (2015). Effects of coolant flow rate, groundwater table fluctuations and infiltration of rainwater on the efficiency of heat recovery from near surface soil layers. *Geothermics*, *53*, 171-182.

Mousa, M. M., Bayomy, A. M., & Saghir, M. Z. (2020). Experimental and numerical study on energy piles with phase change materials. Energies, 13(18), 4699.

Mousa, M. M., Bayomy, A. M., & Saghir, M. Z. (2022). Long-Term Performance Investigation of a GSHP with Actual Size Energy Pile with PCM. Applied Thermal Engineering, 118381.

Mustafa Omer, “Ground-source heat pumps systems and applications,” Renew. Sustain. Energy Rev., vol. 12, no. 2, pp. 344–371, 2008, doi: 10.1016/j.rser.2006.10.003.

Narsilio, G. A., Bidarmaghz, A., Disfani, M., Makasis, N., & Johnston, I. (2016). Geothermal exchange feasibility study—stage 1, p 60. *Report to the Melbourne Metro Rail Authority, Victorian Government*

Neupane, K. (2016). Investigation on modulus of elasticity of powder-activated geopolymer concrete. International Journal of Structural Engineering, 7(3), 262-278.

Nicholson, D. P., Chen, Q., de Silva, M., Winter, A., & Winterling, R. (2014, June). The design of thermal tunnel energy segments for Crossrail, UK. In Proceedings of the Institution of Civil Engineers-Engineering Sustainability (Vol. 167, No. 3, pp. 118-134). Thomas Telford Ltd.

Nikbin, I.M., Beygi, M.H.A., Kazemi, M.T., Vaseghi Amiri, J., Rahmani, E., Rabbanifar, S. and Eslami, M. (2014) 'A comprehensive investigation into the effect of aging and coarse aggregate size and volume on mechanical properties of self-compacting concrete', Materials & Design, Vol. 59, pp.199–210.

Nikliоć, I., Marković, S., Janković–Častvan, I., Radmilović, V. V., Karanović, L., Babić, B., & Radmilović, V. R. (2016). Modification of mechanical and thermal properties of fly ash-based geopolymer by the incorporation of steel slag. Materials Letters, 176, 301-305.

Noorollahi, Y., Saeidi, R., Mohammadi, M., Amiri, A., Hosseinzadeh, M., 2018. The effects of ground heat exchanger parameters changes on geothermal heat pump performance–a review. Appl. Therm. Eng. 129, 1645–1658.

Nusier, O., & Abu-Hamdeh, N. (2003). Laboratory techniques to evaluate thermal conductivity for some soils. *Heat and mass transfer*, *39*(2), 119-123.

Omer, A. M. (2016). Experimental investigation of the performance of a ground source heat pump system for buildings heating and cooling. *Int. J. Innov. Math. Stat. Energy Policies*, *4*(1), 10-44.

Olawoore, I. O. (2020). Study of thermal performance enhancement of geothermal energy pile using PCM (Doctoral dissertation, University of Surrey).

P. K. Dehdezi, M. R. Hall, and A. R. Dawson, "Enhancement of soil thermo-physical properties using microencapsulated Phase Change materials for ground source heat pump applications," Appl. Mech. Mater., vol. 110–116, pp. 1191–1198, 2012, doi: 10.4028/www.scientific.net/AMM.110-116.1191.

Pagola, M. A., Madsen, S., Jensen, R. L., & Poulsen, S. E. (2018). Thermo-mechanical aspects of pile heat exchangers: background and literature review.

Paul, B., & Rashid, H. (2016). *Climatic hazards in coastal Bangladesh: non-structural and structural solutions*. Butterworth-Heinemann.

Peng, G., Dou, G., Hu, Y., Sun, Y., & Chen, Z. (2020). Phase change material (PCM) microcapsules for thermal energy storage. Advances in polymer technology, 2020.

Q. Zhao, B. Chen, M. Tian, and F. Liu, "Investigation on the thermal behavior of energy piles and borehole heat exchangers: A case study," Energy, vol. 162, pp. 787–797, Nov. 2018, doi: 10.1016/j.energy.2018.07.203.

Qi, H. Thermal Performance of the Energy Geotechnical Structures. Ph.D. Thesis, University of Cambridge, Cambridge, UK, 2016.

Qi, H., Zhou, Y., Zhang, Z., Wang, B., Zhang, Y., Cui, H., & Wang, X. (2020). Heat Transfer Performance in Energy Piles in Urban Areas: Case Studies for Lambeth College and Shell Centre UK. *Applied Sciences*, *10*(17), 5974.

Rammal, D., Mroueh, H., & Burlon, S. (2020). Thermal behaviour of geothermal diaphragm walls: Evaluation of exchanged thermal power. *Renewable Energy*, *147*, 2643-2653.

Rashad, A.M., 2019. Insulating and fire-resistant behaviour of metakaolin and fly ash geopolymer mortars. Proceedings of the Institution of Civil Engineers-Construction Materials, 172(1), pp.37-44.

Ravera, E., Sutman, M., & Laloui, L. (2020). Load transfer approach for the geotechnical analysis of energy piles in a group with slab. In E3S Web of Conferences (Vol. 205, p. 05008). EDP Sciences.

Raymond, J., et al., 2015. Designing coaxial ground heat exchangers with a thermally enhanced outer pipe. Geothermal Energy 3 (1), 7.

Rees, S. W., Adjali, M. H., Zhou, Z., Davies, M. & Thomas, H. R. (2000) Ground heat transfer effects on thermal performance of earth contact structures, Renewable and Sustainable Energy Reviews, 4, 213-265

Rybach, L. The future of geothermal energy and its challenges. In Proceedings of the World Geothermal Congress, Bali, Indonesia, 25–29 April 2010.

S. Lee, S. Park, D. Kim, D. Ahn, and H. Choi, “Dual performance of novel steel pipe heat exchangers equipped in cast-in-place energy pile,” Energy Build., vol. 234, p. 110725, 2021, doi: 10.1016/j.enbuild.2021.110725. 35

S. Li, W. Yang, and X. Zhang, “Soil temperature distribution around a U-tube heat exchanger in a multi-function ground source heat pump system,” Appl. Therm. Eng., vol. 29, no. 17–18, pp. 3679–3686, 2009, doi: 10.1016/j.applthermaleng.2009.06.025.

Saad, S., Mirzababaei, M., Mohamed, M., Miraftab, M., 2012. Uniformity of density of compacted fibre reinforced clay soil samples prepared by static compaction. In: The 5th Eurpean Geosynthetics Congress. Valencia, Spain.

Sailer, E., Taborda, D. M., Zdravković, L., Potts, D. M., & Cui, W. (2021). Thermo-hydro-mechanical interactions in porous media: Implications on thermo-active retaining walls. Computers and Geotechnics, 135, 104121

Sailer, E., Taborda, D.M., Zdravkovi´c, L., Potts, D.M., Cui, W., 2021. Thermo-hydromechanical interactions in porous media: Implications on thermo-active retaining walls. Comput. Geotech. 135, 104121.

Sakaguchi, I., Momose, T. and Kasubuchi, T. (2007) 'Decrease in thermal conductivity with increasing temperature in nearly dry sandy soil', European Journal of Soil Science, 58(1), pp. 92-97.

Samal, S., Thanh, N.P., Petríková, I., Marvalová, B., Vallons, K.A. and Lomov, S.V., 2015. Correlation of microstructure and mechanical properties of various fabric reinforced geo-polymer composites after exposure to elevated temperature. Ceramics International, 41(9), pp.12115-12129.

Sani, A. K., Olawoore, I. O., & Singh, R. M. (2021). Assessment of impregnating phase change materials into lightweight aggregates for development of thermal energy storage aggregate composites. *Construction and Building Materials*, *305*, 124683.

Sani, A. K., Singh, R. M., Amis, T., & Cavarretta, I. (2019). A review on the performance of geothermal energy pile foundation, its design process and applications. Renewable and Sustainable Energy Reviews, 106, 54-78.

Sanjuán, M. Á., Andrade, C., Mora, P., & Zaragoza, A. (2020). Carbon dioxide uptake by cement-based materials: A Spanish case study. Applied Sciences, 10(1), 339.

Sbia, L.A., Peyvandi, A., Soroushian, P., Balachandra, A.M., Sobolev, K., 2015. Evaluation of Modified- Graphite Nanomaterials in Concrete Nanocomposite Based on Packing Density Principles. Constr. Build. Mater. (76), 413–422.

Selamat, S., Miyara, A., Kariya, K., 2016. Numerical study of horizontal ground heat exchangers for design optimization. Renew. Energy 95, 561–573.

Self, S.J.; Reddy, B.V.; Rosen, M.A. Geothermal heat pump systems: Status review and comparison with other heating options. Appl. Energy 2013, 101, 341–348.

Sepaskhah, A.R. and Boersma, L. (1979) 'Thermal conductivity of soils as a function of temperature and water content', Soil Science Society of America Journal, 43(3), pp. 439-444.

Shafagh I, Rees S, Mardaras IU, Janó MC, Carbayo MP. A model of a diaphragm wall ground heat exchanger. Energies. 2020;13(2):1–23.

Shafagh I, Rees SJ. Analytical investigations into thermal resistance of diaphragm wall heat exchangers. In: Proceedings of the European Geothermal Congress, EGC 2019, (11–14 June); 2019:1–6.

Shafagh, I., Shepley, P., Shepherd, W., Loveridge, F., Schellart, A., Tait, S., & Rees, S. J. (2022). Thermal energy transfer around buried pipe infrastructure. *Geomechanics for Energy and the Environment*, *29*, 100273.

Shao, D., Jiang, G., Zong, C., Xing, Y., Zheng, Z., & Lv, S. (2021). Global sensitivity analysis of behavior of energy pile under thermo-mechanical loads. Soils and Foundations, 61(2), 283-302.

Shendy, M. E. (1991). A comparative study of LECA concrete sandwich beams with and without core reinforcement. *Cement and Concrete Composites*, *13*(2), 143-149.
Singh, D.N. and Devid, K. (2000) 'Generalized relationships for estimating soil thermal resistivity', Experimental Thermal and Fluid Science, 22(3–4), pp. 133- 143.

Singh, R. M., Sani, A. K., & Amis, T. (2019). An overview of ground-source heat pump technology. Managing Global Warming, 455-485.

Smith, W.O. (1942) 'The Thermal Conductivity of Dry Soil', Soil Science, 53(6), pp. 435-460.

Snell, C., Tempest, B. and Gentry, T., 2017. Comparison of the thermal characteristics of portland cement and geopolymer cement concrete mixes. Journal of Architectural Engineering, 23(2), p.04017002.

Soga, K., & Rui, Y. (2016). Energy geostructures. In Advances in ground-source heat pump systems (pp. 185-221). Woodhead Publishing.

Sterpi, A.Coletto, Mauri, L., 2017. Investigation on the behaviour of a thermoactivediaphragm wall by thermo-mechanical analyses. Geomech. Eng. Environ. 9, 1–20.

Sun M, Xia C, Zhang G. Heat transfer model and design method for geothermal heat exchange tubes in diaphragm walls. Energy Build. 2013;61:250–259.

Suryatriyastuti, M. E., Mroueh, H., & Burlon, S. (2012). Understanding the temperature-induced mechanical behaviour of energy pile foundations. Renewable and sustainable energy reviews, 16(5), 3344-3354.

T. Sliwa, A. Sojczyńska, M. A. Rosen, and T. Kowalski, “Evaluation of temperature profiling quality in determining energy efficiencies of borehole heat exchangers,” 34 Geothermics, vol. 78, no. October 2018, pp. 129–137, 2019, doi: 10.1016/j.geothermics.2018.12.005.

Takeda, M., Onishi, T., Nakakubo, S., & Fujimoto, S. (2009). Physical properties of iron-oxide scales on Si-containing steels at high temperature. Materials transactions, 50(9), 2242-2246.

Tanabe, T.A., Sakata, K., Mihashi, H., Sato, R., Maekawa, K., Nakamura, H., 2008. In: Creep, Shrinkage and Durability Mechanics of Concrete and Concrete Structures, Two Volume Set: Proceedings of the CONCREEP 8 conference held in Ise-Shima, Japan, 30 September-2 October 2008, Vol. 1. CRC Press.

Tarnawski, V. R., & Leong, W. H. (2000). Thermal conductivity of soils at very low moisture content and moderate temperatures. *Transport in porous media*, *41*(2), 137-147.

Tarnawski, V.R., Leong, W.H., Gori, F., Buchan, G.D. and Sundberg, J. (2002) 'Interparticle contact heat transfer in soil systems at moderate temperatures', International journal of energy research, 26(15), pp. 1345-1358.

Tavman, I.H. (1996) 'Effective thermal conductivity of granular porous materials', International Communications in Heat and Mass Transfer, 23(2), pp. 169-176.

Tayeh, B. A., Zeyad, A. M., Agwa, I. S., & Amin, M. (2021). Effect of elevated temperatures on mechanical properties of lightweight geopolymer concrete. Case Studies in Construction Materials, 15, e00673.

Thomas, H.R. and Sansom, M.R. (1995) 'Fully coupled analysis of heat, moisture, and air transfer in unsaturated soil', Journal of Engineering Mechanics - ASCE, 121(3), pp. 392-405.

Thomas, H.R., Rees, S.W., 2009. Geotechnique 59 (4), 365–375. https://doi.org/10.1680/geot.2008.59.4.365.

TI-B 101 (94), 1994. Testing and Sampling Method Concrete: Thermal Expansion Coefficient. Danish Technological Institute, Denmark.

UK DECC. The Future of Heating: Meeting the Challenge; UK Department of Energy and Climate Change: London, UK, 2013.

UNFCCC, V. (2015). Adoption of the Paris Agreement. I: proposal by the president (Draft Decision). United Nations Office, Geneva (Switzerland).

Van rooyen, M. and Winterkorn, H.F. (1957) 'thoretical and practical aspects of the thermal conductivity of soils and similar granular systems', Highway Research Board Bulletin, 168.

Weil, M., Dombrowski, K. and Buchwald, A., 2009. Life-cycle analysis of geopolymers. In Geopolymers (pp. 194-210). Woodhead Publishing.

Wright, P. M. (1998). Geothermal energy-harnessing heat from the centre of the Earth. Chemistry and Industry.

X. Li, C. Tong, L. Duanmu, and L. Liu, “Research on U-tube Heat Exchanger with Shape’’stabilized Phase Change Backfill Material,” Procedia Eng., vol. 146, pp. 640–647, 2016, doi: 10.1016/j.proeng.2016.06.420.

X. Zheng, “Long-term Effects of Ground Source Heat Pumps on Underground Temperature,” pp. 1–6, 2013.

Y. Deng, Z. Feng, J. Fang, and S. J. Cao, “Impact of ventilation rates on indoor thermal comfort and energy efficiency of ground-source heat pump system,” Sustain. Cities Soc., vol. 37, no. September 2017, pp. 154–163, 2018, doi: 10.1016/j.scs.2017.11.014.

Y. Song, Y. Yao, W. Na, Impacts of soil and pipe thermal conductivity on per- formance of horizontal pipe in a ground-source heat pump, in: Proc. Sixth Int. Conf. Enhanc. Build. Oper. ICEBO2006, Shenzhen, China, 2006.

Yadav, M. R., & Saxena, G. S. (1973). Effect of compaction and moisture content on specific heat and thermal capacity of soils. Journal of the Indian Society of Soil Science, 21(2), 129-132.

Yadav, M.R., Saxena, G.S., 1973. Effect of compaction and moisture content on specific heat and thermal capacity of soils. J. Indian Soc. Soil Sci. 21 (2), 129–132.

Yang, K. H., Song, J. K., & Song, K. I. (2013). Assessment of CO2 reduction of alkali-activated concrete. Journal of Cleaner Production, 39, 265-272.

Yang, W., Sun, T., Yang, B., & Wang, F. (2021). Laboratory study on the thermo-mechanical behaviour of a phase change concrete energy pile in summer mode. Journal of Energy Storage, 41, 102875.

Yang, W., Yang, B., Wang, F., & Jing, N. (2021). Numerical evaluations on the effects of thermal properties on the thermo-mechanical behaviour of a phase change concrete energy pile. Energy and Built Environment.

Ye, C.M., Shentu, B.Q., Weng, Z.X., 2006. Thermal conductivity of high density polyethylene filled with graphite. J. Appl. Polym. Sci. 101 (6), 3806–3810.

Zagorscak, R., & Thomas, H. R. (2016). A review on performance of energy piles and effects on surrounding ground. Inzenjerstvo Okolisa (Environmental Engineering), 3(1), 33-45.

Zarrella, A., De Carli, M., Galgaro, A., 2013. Thermal performance of two types of energy foundation pile: helical pipe and triple U-tube. Appl. Therm. Eng. 61 (2), 301

Zhang, G., Cao, Z., Liu, Y., & Chen, J. (2021). Field test and numerical simulation on the long-term thermal response of PHC energy pile in layered foundation. *Sensors*, *21*(11), 3873.

Zhao, R. and Sanjayan, J.G., 2011. Geopolymer and Portland cement concretes in simulated fire. Magazine of Concrete research, 63(3), pp.163-173.

Zhihe, D., Zimu, Z., Yan, L., Guozhi, L., Ting'an, Z., & Xiaoli, J. (2014). Study on Utilization of Cyclic Heat Stewed Steel Slag Washing Water to Mineralize CO2. Energy Technology 2014: Carbon Dioxide Management and Other Technologies, 97-102.

Zhou, D., Zhao, C. Y., & Tian, Y. (2012). Review on thermal energy storage with phase change materials (PCMs) in building applications. *Applied energy*, *92*, 593-605.

Zhou, T., Chen, M., & Liang, B. (2020). Thermal performance of a ground U-shaped tube with twisted tapes in sand/graphite backfill materials. *Experimental Heat Transfer*, 1-15.

Appendix (A)

Numerical simulation for geothermal wall temperature.

The wall model has been utilised to predict the changes of wall temperate and soil temperature during the experiment run time for GPC and OPCC geo-energy walls, finite element analysis using COMSOL multiphysics was undertaken. The simulation of GEW have been executed to solve time dependant heat transfer and heat transfer problem, which was solved by calculating the temperature at each node of the finite element mesh. Pure conduction heat transfers in solids with the generation of internal heat energy model have used which governed by the following equation:

$$\rho C_p \frac{\partial T}{\partial t} + \nabla.(\lambda \nabla T) = q$$

Where ρ represents the density of solid materials (sand and concrete), C_p and λ are the specific heat capacity and the thermal conductivity of solids, T represents the temperature of the solids and q is line heat flux which have been defined in COMSOL interface by watts by just draw line and assign line heat source with desired power per unit length.

Geometry and boundary condition

The experimental models which have been described in Fig 1 was modelled in 2D using COMSOL. Side cross-section of the experimental tank like the section presented in Fig 5 (d). The heat exchanger has been assigned to the wall as a line heat flux (see Fig 1). A similar method for representing the heat exchanger for geo-energy wall in 2D was published by Dong et al. (2019), and showed great potential in modelling the wall and soil temperature as well as the thermomechanical behaviour of the GEW.

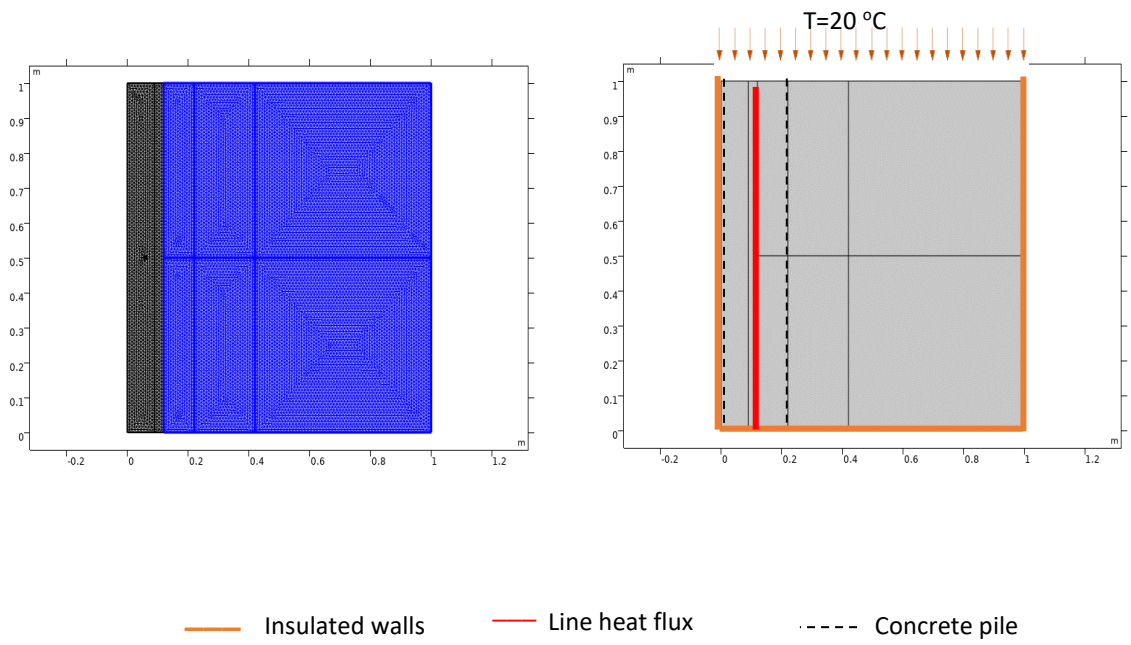

Fig.1. geometry and boundary condition of the wall module.

All boundary conditions were applied using the as have been described in section 4.5.1 The ambient temperature of 20°C has been assigned to the top (soil surface) of the module domain while the sides and the bottom have been insulated. The simulation was carried out using finite element mesh with a maximum element size of 0.067 m and minimum element size of 0.0003 m and a maximum growth rate of 1:1. Table 4.6 shows the material properties that have been used in the numerical model.

To simulate the wall temperature and the soil temperature for the current experimental work, two numerical runs were performed (run 1 predicts the OPCC geo-energy wall with thermal conductivity of 1.44 w/m.k, and run 2 considers the GPC wall with a thermal conductivity value of 1.69 w/m.k).

Results

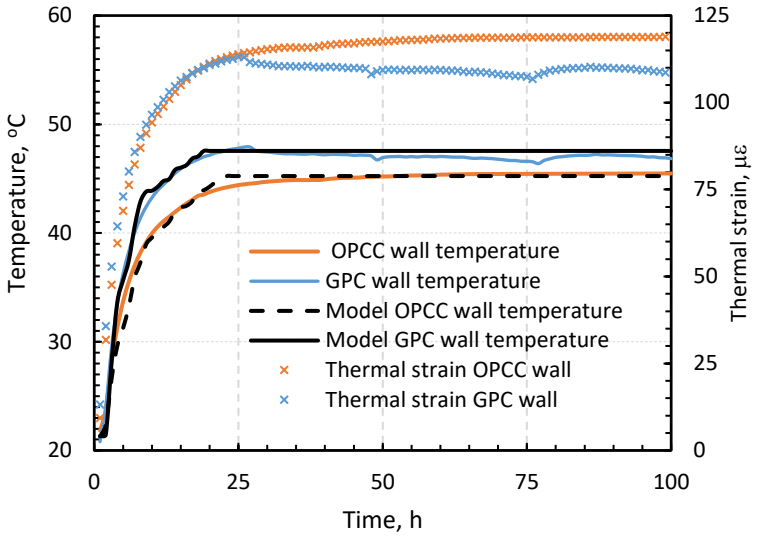

Wall temperature and thermal strain versus time

Model run	Experimental data		Numerical data		RMSE	Errmax
	$T_{at\ 100\ mm}$ °C	$T_{at\ tank\ boundary}$ °C	$T_{at\ 100\ mm}$ °C	$T_{at\ tank\ boundary}$ °C		
1	38.08	21.9	39	20	1.49	0.095
2	39.09	22.8	40	21	1.42	0.085

Appendix (B)

CO_2 Emissions Calculation

Ingredient	OPCC proportions kg/m³	GPC-Mix1 proportions kg/m³	GPC-Mix2 proportions kg/m³	GPC-Mix3 proportions kg/m³	GPC-Mix4 proportions kg/m³
Cement	343	-	-	-	-
Flay ash	-	360	320	280	240
Slag	-	40	80	120	160
NaOH (14 M)	-	66.5	66.5	66.5	66.5
Na_2SiO_3	-	163	163	163	163
Coarse aggregate 10mm	1199	1209	1209	1209	1209
Fine aggregate	783	650	650	650	650
Water	155	20	20	20	20
Super plasticiser	-	10	10	10	10
weight	2480	2518.5	2518.5	2518.5	2518.5

	A Geopolymer	A NORMAL	B	geo-polymer	normal con-crete
Item	kg/m³	kg/m³	CO_2 .Kg/kg	A.B	A.B
OPC	*	343	0.84		288.120
EAFS	120	*	0.052	6.240	
Fly ash	280	*	0.0196	5.488	
Sand	650	783	0.0048	3.120	3.758
Coarse aggregate	1209	1199	0.0075	9.068	8.993
Water	20	155	0.000196	0.004	0.030
Super plasticiser	10	*	1.88	18.800	
Sodium hydroxide	32.1195	*	1.23	39.507	
Sodium silicate	58.68	*	1.22	71.590	
Concrete production	2518.5	2480	0.008	20.148	19.840
Total Co2 emissions				173	312

Appendix (C)

Calculation of the area under curve Fig 7.14 a

	yo	y1	x0	x1		
	1.83	3.78	20	25		14.025
35%	3.78	4.928	25	26		4.354
	4.928	3.315	26	27		4.1215
	3.315	2.25	27	30		8.3475
					TOTAL	30.848

	yo	y1	x0	x1		
	1.52	2.772	20	25		10.73
28%	2.772	3.84	25	26		3.306
	3.84	2.825	26	27		3.3325
	2.825	2.026	27	30		7.2765
					TOTAL	24.645

	yo	y1	x0	x1		
	1.5	2.511	20	25		10.0275
21%	2.511	3.434	25	26		2.9725
	3.434	2.306	26	27		2.87
	2.306	1.995	27	30		6.4515
					TOTAL	22.3215

	yo	y1	x0	x1		
14%	1.36	2.264	20	25		9.06
	2.264	2.72	25	26		2.492
	2.72	1.962	26	27		2.341
	1.962	1.632	27	30		5.391
					TOTAL	19.284

	yo	y1	x0	x1		
7%	1.241	1.531	20	25		6.93
	1.531	1.789	25	26		1.66
	1.789	1.498	26	27		1.6435
	1.498	1.354	27	30		4.278
					TOTAL	14.5115

Calculation of the area under curve Fig 7.14 d

	yo	y1	x0	x1		
35%	3.243	3.5	40	42		6.743
	3.5	2.796	42	45		9.444
	2.796	1.567	45	47		4.363
	1.3057	1.041	47	50		3.52005
					Total	24.07005

	yo	y1	x0	x1		
28%	2.427	3.317	40	42		5.744
	3.317	2.262	42	45		8.3685
	2.262	1.567	45	47		3.829
	1.567	0.971	47	50		3.807
					Total	21.7485

	yo	y1	x0	x1		
21%	1.966	2.885	40	42		4.851
	2.885	1.742	42	45		6.9405
	1.742	1.453	45	47		3.195
	1.453	0.895	47	50		3.522
					Total	18.5085

	yo	y1	x0	x1		
14%	1.741	2.172	40	42		3.913
	2.172	1.395	42	45		5.3505
	1.395	1.11	45	47		2.505
	1.11	0.837	47	50		2.9205
					Total	14.689

	yo	y1	x0	x1		
7%	0.979	1.231	40	42		2.21
	1.231	0.941	42	45		3.258
	0.941	0.858	45	47		1.799
	0.858	0.877	47	50		2.6025
					Total	9.8695

Appendix (D)

Papers Produced from This Thesis

Published

Elkezza, O., Mohamed, M., & Khan, A. (2022). Performance of thermally enhanced geo-energy piles and walls. Geothermics, 98, 102274.

Elkezza, O., Mohamed, M., & Khan, A. Influence of graphite addition on the thermal performance of energy pile. ICESF, DTAEnergy and Nottingham Trent university, sep 2019.

Currently under review

El Kezza, O., Mohamed, M. Thermal enhancement of soil-geo-energy structure interaction using conductive additives. Under review ‘’Renewable energy’’.

Elkezza, O., Mohamed, M., Alhawat,M., Khan, A., Shewehdi,H. Experimental study into the use of PCM heat exchangers in geo-energy piles and walls. Under review ‘’ Geomechanics of energy and the environment’’.

Elkezza, O., Mohamad, A., Mohamed, M., Alhawat,M., Khan, A. Feasibility of using Geo-polymer concrete for Geo-energy piles applications. Under review ‘’ Geothermics’’

Elkezza, O., Mohamed, M. Experimental study into the enhancement of the thermal energy storage of soil surrounding the geo-energy piles and walls. Under review ‘’building and the environment’’